Table des matières

Nomenclature

Alphabet latin   –   Variables physiques correspondantes

A	contraste de réactivité
C	concentration molaire des gaz, $mol \cdot m^{-3}$
d	distance ou diamètre, m
D	coefficient de diffusion, $m^2 \cdot s^{-1}$
Da	nombre de Damköhler
h	hauteur, m
j	densité de flux massique, $kg \cdot m^{-2} \cdot s^{-1}$
J	densité de flux molaire, $mol \cdot m^{-2} \cdot s^{-1}$
k	réactivité chimique, $m \cdot s^{-1}$
Kn	nombre de Knudsen
l	largeur de la section des fils, m
L	longueur de la section des fils, m
m	masse, kg
n	ordre de réaction chimique
$\mathcal{M}$	masse molaire, $kg \cdot mol^{-1}$
p	pression, Pa
P	probabilité de collage
q	flux molaire, $mol \cdot s^{-1}$
r	taux de perte de masse, $g \cdot g^{-1} \cdot s^{-1}$
R_f	rayon des fibres, μm
Re	nombre de Reynolds
S	surface, m
Sc	nombre de Schmidt
Sh	nombre de Sherwood
T	température, K
t	temps, s
u	composante tangentielle de la vitesse de couche limite, $m \cdot s^{-1}$
v	vitesse, $m \cdot s^{-1}$

Alphabet grec	–	*Variables physiques correspondantes*
α		angle (fibres, fils), $°$
β		inclinaison des fibres par rapport à une surface, $°$
δ		épaisseur de couche limite dynamique, m
δ_c		épaisseur de couche limite de concentration, m
$\Delta_f H$		enthalpie de formation, $J \cdot mol^{-1}$
$\Delta_f G°$		enthalpie libre de formation, $J \cdot mol^{-1}$
θ		orientation des plans de graphène, $°$
λ		conductivité thermique, $W \cdot m^{-1} \cdot K^{-1}$
$\tilde{\lambda}$		libre parcours moyen, m
ν		viscosité cinétique, $m^2 \cdot s^{-1}$
ρ		masse volumique, $kg \cdot m^{-3}$
τ		temps caractéristique, s
υ		volume molaire, $m^3 \cdot mol^{-1}$

Indices et exposants	–	*Relatif à (au)*
a		ablation
c		composite ou carbone
eff		grandeur effective
exp		donnée expérimentale
f		fibre
i		indice
m		matrice
p		pore
s		en indice : solide, en exposant : stationnaire
t		total
wp		weak phase (phase faible)
y		yarn (fil)
0		initial, référence

Formalisme	–	*Signification*
$\partial A / \partial t, \; ou A_t$		dérivée partielle de A par rapport à t
x, y, z		coordonnées cartésiennes
r, θ, z		coordonnées cylindriques
$\mathbf{A}$		vecteur A
$\underline{\underline{A}}$		tenseur A d'ordre 2
$\overline{\nabla} A$		gradient de A
$\overline{A}$		valeur moyenne de A
$\tilde{A}$		grandeur adimensionnée

Constantes	–	*Valeurs*
$\mathcal{R}$		$8.3145107 \; J \cdot mole^{-1} \cdot K^{-1}$: constante des gaz parfaits
$\mathcal{M}_c$		$12 \; g \cdot mol^{-1}$: masse molaire du carbone

1 Introduction

1.1 Cadre de la thèse

1.1.1 Contexte historique

Dans les applications à température modérée, la suprématie des métaux a été remplacée par celle des thermoplastiques et des thermodurcissables, appelés communément *plastiques*. Parallèlement, les matériaux céramiques s'imposent de plus en plus pour les hautes températures. Parmi ceux-ci ont été élaborés les matériaux composites thermostructuraux, qui, comme leur nom l'indique, sont par ailleurs suffisamment résistants pour constituer la structure d'une application. Ironie de l'histoire, une des familles de matériaux thermostucturaux la plus utilisée, et qui remplace avantageusement les alliages métalliques ou le tungstène dans de nombreux cas, est celle des composites en carbone, dont le constituant majoritaire est le carbone sous une forme proche du graphite, c'est-à-dire un charbon de bois amélioré. L'avènement de ces matériaux a constitué un véritable changement de paradigme nécessitant par la même une recherche approfondie et spécifique pour le perfectionnement de leur élaboration et l'étude de leur comportement dans une situation donnée [75]. Le Laboratoire des Composites Thermostructuraux (LCTS), au sein duquel cette thèse a été réalisée, a été crée en 1988 pour répondre à ce besoin. Il s'agit d'une unité mixte de recherche (UMR 5801) regroupant deux partenaires académiques : le Centre National de la Recherche Scientifique (CNRS) et l'Université Bordeaux 1, et deux partenaires industriels : le groupe SAFRAN et le Commissariat à l'Energie Atomique (CEA).

1.1.2 Contexte industriel de l'ablation

Les composites carbone/carbone (C/C), dont les propriétés mécaniques sont conservées jusqu'à 2000°C, sont fréquemment employés comme matériaux thermostructuraux [19]. On peut citer quatre exemples d'applications hautes températures nécessitant, en l'état actuel des connaissances, l'utilisation des composites en carbone :
- le freinage hautes performances (Avions, Formule 1) (SAFRAN) [46] ;
- le projet ITER (International Thermonuclear Experimental Reactor), porté en partie par le CEA, dont l'objectif est la production d'énergie par fusion nucléaire par confinement magnétique [45, 103] ;
- les cols de tuyères utilisées pour la propulsion des fusées (SAFRAN) [11] ;
- les boucliers thermiques pour la rentrée atmosphérique des engins spatiaux (CEA) [31].

Cependant, le graphite n'est pas une forme inerte du carbone dans les conditions de ces applications [15] ; il présente principalement le défaut de s'oxyder significativement sous air à partir de températures avoisinant les 500°C (échauffement des freins, boucliers thermiques) [22], de s'oxyder fortement à 2000°C en présence des produits de combustion (H_2O, CO_2) du

15

propergol solide (cols de tuyères) [11], et de se sublimer vers 3000˚C (ITER, boucliers thermique) [27]. De plus, dans tous les cas, le matériau est susceptible de s'éroder sous l'effet de contraintes thermomécaniques générées soit par la friction (freinage) [46], soit par le bombardement du plasma (Tokamak (ITER) [45]) ou de particules d'alumine fondue (cols de tuyère [11]), soit enfin par l'écoulement d'air hypersonique (corps de rentrée [31]). En dehors de la sollicitation de friction qui appartient au domaine de la tribologie, l'ensemble de ces phénomènes est regroupé sous le terme générique d'ablation. Ils se traduisent par un recul de paroi et une modification de l'état de surface (apparition de rugosité) du matériau, provoqués sans contact mécanique solide. En présence d'oxygène, les réactions sont exothermiques, ce qui peut accroître sensiblement la température de surface et donc l'ablation. En revanche, endothermiques dans le cas des oxydations par H_2O et CO_2 et de la sublimation, les phénomènes de gazéification permettent de limiter le flux thermique traversant le matériau, et jouent paradoxalement un rôle important dans la protection de la structure. Ces processus de dégradation de la *surface* peuvent intégrer une couche plus ou moins profonde de la structure du matériau. Pour fixer les idées, en général, l'ablation se concentre dans les premiers millimètres.

1.1.3   Contexte scientifique

Le perfectionnement de l'élaboration des matériaux comme leur utilisation dans des applications thermostructurales nécessite une compréhension aussi précise que possible de leur comportement, dans le premier cas pour améliorer en priorité leur points faibles, dans le second, pour permettre un dimensionnement judicieux, limitant en particulier au strict minimum l'épaisseur des structures dans les applications aéronautiques et spatiales. Les tendances phénoménologiques générales sont bien comprises et simulées du point de vue du fluide pour la propulsion [11] et la rentrée atmosphérique [31] ; la composition et le comportement du plasma en confinement magnétique dans les Tokamaks (ITER) sont également bien connus [45, 103]. Cependant, le comportement complexe des composites en carbone n'est pas complètement maîtrisé et n'est pris en compte que de façon partielle dans les modèles. Les progrès continus des logiciels de simulation numérique et de la puissance des calculateurs permettent d'enrichir progressivement ces modèles, incitant à approfondir au fur et à mesure les points faibles. Ces dernières années, la demande d'une description précise du comportement ablatif du matériau, voire d'une modélisation, s'est faite de plus en plus pressante, en particulier en ce qui concerne l'évolution de l'état de surface ou *rugosité*. En effet, l'ablation des composites en carbone est connue pour conduire, entre autres, à une rugosité typique qui influence les autres phénomènes :

 – D'abord, l'apparition de la rugosité est potentiellement à l'origine d'une augmentation des transferts de masse et de chaleur à l'interface [43].
 – Ensuite, la rugosité conduit à un comportement composite complexe : la réactivité effective du composite n'est pas donnée par une moyenne arithmétique de celles de ses composants [68].
 – Par ailleurs, dans les cas ou l'advection est conséquente (propulsion, rentée atmosphérique), la rugosité favorise l'érosion thermomécanique.
 – Enfin, dans le cas de la rentrée atmosphérique, la participation majeure de la rugosité à la transition laminaire-turbulent dans la couche limite dynamique [16] entourant le bouclier thermique est expérimentalement observée [31].

En conséquence, pour toutes ces applications, la compréhension de l'interaction matériau/environnement est primordiale pour le dimensionnement. Pour l'instant, de nombreux essais permettant de caractériser le comportement des matériaux dans des conditions ciblées et fournissent les données d'entrée des modèles macroscopiques. Cette méthode est très fiable, sauf lorsqu'une extrapolation des modèles s'avère nécessaire. Pour améliorer l'extrapolation, des modèles thermomécaniques d'ablation ont été élaborés en vue d'analyser l'apparition de rugosité et le comportement des composites en carbone [26, 79]. De façon complémentaire, cette thèse se concentre principalement sur l'ablation physico-chimique, *i.e.* générée par des processus de gazéification (oxydation, sublimation). Dans les expériences réalisées dans le cadre de ce travail, l'érosion thermomécanique est un phénomène de second ordre qui n'apparaît que couplé aux phénomènes de gazéification dans les écoulements rapides. Cependant, l'érosion ne sera pas ignorée, mais au contraire analysée, voire modélisée, lorsque observée, c'est-à-dire sporadiquement.

1.2   Objectif de la thèse

Le travail présenté dans ce mémoire a pour but l'analyse et la modélisation du comportement complexe des composites en carbone lors de l'ablation physico-chimique, l'étude étant abordée d'un point de vue matériau. Une attention particulière sera apportée à la rugosité dont le rôle est majeur dans l'ablation.

1.3   Plan du mémoire

Le corps du mémoire étant écrit en anglais sous une forme de compilation d'articles, on propose dans une première partie (chapitre 2) une synthèse en français dont l'objectif est de faire apparaître la démarche de travail et les principaux résultats obtenus.

Les cinq chapitres suivants, qui peuvent être lus indépendamment, sont regroupés en une série d'articles intitulée *Physico-chemical ablation of carbon-carbon composites* :

I- Multi-scale analysis of surface roughness (chapitre 3),

II- Experimental evaluation of intrinsic reactivities (chapitre 4),

III- Multi-scale analytical modeling in steady state (chapitre 5),

IV- 3D numerical modeling of actual architectures in steady state (chapitre 6),

V- Analytical and 3D numerical modeling in transient regime (chapitre 7).

Le premier article présente l'analyse du comportement ablatif de deux composites en carbone (un 3D C/C et un 2D C/R), l'accent étant mis sur la classification de la rugosité multiéchelle. Une stratégie de modélisation est proposée à partir de cette analyse.

Le deuxième aborde la mesure des réactivités des composites et de leurs constituants. Une forte interaction entre expérimentation et modélisation permet d'obtenir les valeurs de réactivités géométriques intrinsèques nécessaires à l'alimentation et à la validation des modèles d'ablation.

Le troisième propose une modélisation analytique de la rugosité et du comportement du matériau en régime stationnaire. Des hypothèses simplificatrices sont faites sur la structure du matériau. Les résultats analytiques sont exploités et se montrent en bon accord avec les données expérimentales.

L'utilisation d'un code de simulation numérique, développé spécifiquement pour cette étude, permet d'aborder les géométries réelles dans le quatrième article. Les hypothèses du chapitre précédent sont validées, et de nouveaux résultats sont discutés.

Enfin, dans le cinquième article, une modélisation couplant simulation numérique et résolution analytique permet de prévoir en régime transitoire le comportement des matériaux : évolution de la rugosité, évolution de la réactivité effective et prédiction de la perte de masse.

L'ensemble des modèles est validé par comparaison à des essais en four d'oxydation. Les modèles sont ensuite appliqués à l'interpretation d'essais jet plasma.

Une conclusion en français synthétise la démarche de l'étude et les principaux résultats ; des lignes directrices pour l'exploitation et la poursuite de ce travail à court, moyen et long terme y sont suggérées.

2 Synthèse en français

Dans cette partie, dont le but est d'illustrer la démarche de travail et de synthétiser en français les principaux résultats obtenus, on se concentre pour plus de clarté et de concision sur la description et l'étude d'un seul composite : un 3D C/C. Les comportements d'un composite 2D carbone/résine phénolique pyrolysé (2D C/R) et d'un graphite polycristallin, étudiés en parallèle, seront évoqués lorsque les résultats obtenus pour ceux-ci sont spécifiques.

La démarche de modélisation suivie s'appuie fortement sur l'architecture multiéchelle des matériaux, qui joue un rôle primordial dans leur comportement ablatif. Pour plus de clarté, la nature et l'architecture des matériaux est d'abord brièvement présentée. Puis, partant de l'analyse d'observations préliminaires de composites ablatés et de résultats de la bibliographie, on montre l'intérêt d'orienter l'étude, au moins dans un premier temps, vers l'analyse et la modélisation du comportement d'échantillons issus d'un procédé modèle d'ablation, pour lequel les conditions expérimentales seraient parfaitement connues et maîtrisées. Un procédé modèle, répondant à un cahier des charges élaboré à partir des observations préliminaires, a été conçu, mis en place et utilisé au cours de la thèse. Ce dispositif a permis l'étude quantitative du comportement ablatif des composites et de leurs composants pris séparément. La stratégie de modélisation multiéchelle synthétisée ensuite est l'aboutissement de cette démarche analytique. Afin de résoudre les modèles proposés dans la stratégie de modélisation, le développement et la validation d'un outil de simulation numérique spécifique a paru indispensable. Cette étape clef du projet est brièvement décrite. Enfin, les résultats de modélisation, issus de résolutions analytiques et/ou numériques, sont présentés en partant des petites échelles et en allant vers les grandes. Connaissant les propriétés microscopiques (composants des composites), et après plusieurs changements d'échelle par homogénéisation, on aboutit à une prédiction du comportement macroscopique du composite. L'accent est mis ici sur les étapes d'homogénéisation successives et sur la comparaison aux résultats expérimentaux. En conclusion, l'apport des modèles est synthétisé.

2.1 Description succincte des matériaux

2.1.1 Le carbone turbostratique

Dans le cadre de l'approximation orbitalaire avec effet d'écran, la configuration électronique de l'atome de carbone, qui possède un cortège de six électrons, est de type $\{[1s^2];[2s^2,2p^2]\}$ [44,83]. La théorie de l'orbitale moléculaire, associée à la théorie semi-empirique de la liaison de valence (ou hybridation) et à la théorie de Hückel, permet d'expliquer en partie l'origine de la grande variété des formes du carbone solide [24]. Les matériaux étudiés étant principalement constitués de carbone, on se focalisera sur la liaison carbone-carbone (voir tableau 2.1).

Types de liaisons	Hybridation	Nombre de coordinations	Longueurs de liaison (Å)	Énergie ($kJ.mol^{-1}$)	Phases solides
Simple	$sp^3 - sp^3$	4	1.54	344	3d, tétraédrique (diamant)
Aromatique	$aro - aro$	3	1.40	575	2d, lamellaire (graphite)
Double	$sp^2 - sp^2$	3	1.33	615	2d, trigonal
Triple	$sp^1 - sp^1$	2	1.21	812	1d

TAB. 2.1 – Caractéristiques des principales liaisons chimiques entre atomes de carbone dans un solide [83].

Le graphite est la forme cristalline stable du carbone dans les conditions usuelles de température et de pression. Il possède une structure lamellaire, on parle de plans de graphène [24]. Les feuillets sont liés entre eux par les forces d'interaction de Van der Waals. L'ensemble est assimilable à un cristal de structure hexagonale (plus rarement rhomboédrique). Le caractère lamellaire de la structure graphitique engendre une forte anisotropie de ses caractéristiques (électrons π délocalisés sur les plans de graphène / liaisons de Van der Waals perpendiculairement à ces plans).
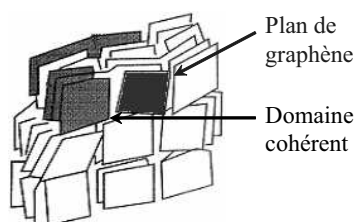
FIG. 2.1 – Schéma de la structure d'une cristallite dans un carbone turbostratique [12].

Le carbone constitutif des composites C/C est de type turbostratique [102]. Par rapport à la structure graphitique, la structure turbostratique se caractérise par un arrangement moins ordonné des plans de graphène à l'intérieur des pseudo-grains cristallins, appelés *cristallites*. Dans les cristallites, des domaines, dits *cohérents*, présentent un empilement parallèle des plans de graphène (voir figure 2.1) [12]. Cependant, l'ordre cristallin tridimensionnel n'étant plus strictement respecté, la distance moyenne qui sépare les feuillets est supérieure à celle du graphite. Par ailleurs, l'orientation relative des divers cristallites peut conduire à des textures plus ou moins isotropes. Les propriétés physico-chimiques du carbone turbostratique varient fortement en fonction de sa structure et de sa texture [84].

2.1.2 Architecture du composite 3D C/C

Le composite 3D C/C de cette étude est un matériau hétérogène multiéchelle, composé d'une préforme tridimensionelle (3D) de fibres ex-PAN (PolyAcryloNitrile) et d'une matrice ex-brai [33]. Plusieurs milliers de fibres sont associées en un fil unidirectionel, puis les fils sont arrangés orthogonalement en un motif élémentaire (voir figure 2.2) répété par translation sur un réseau cubique. Cette macrostructure conduit à un réseau de macropores, appelés

octets après densification de la préforme par imprégnation de brai, puis carbonisation et graphitisation. A l'interface entre deux éléments, se forme une interphase de matrice peu organisée et très réactive.

a) Avant densification
(diamètre des fibres non réaliste)

b) Après densification

Fil parallèle
Octet de matrice
Interphase
Fil perpendiculaire
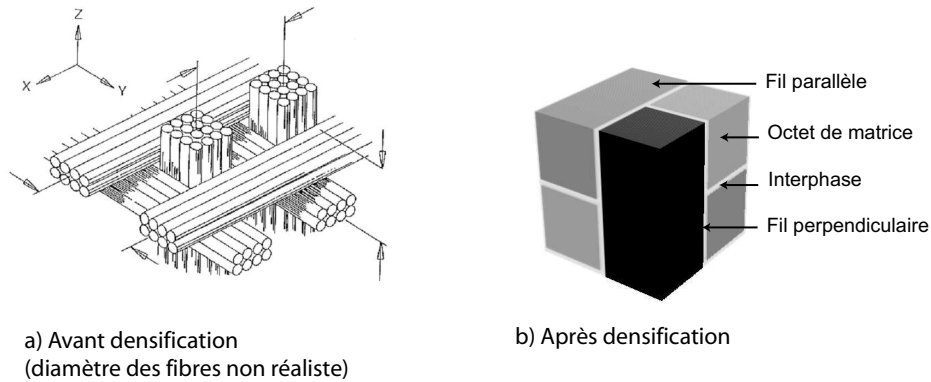
FIG. 2.2 – Motif élémentaire du 3D C/C.

Les composants élémentaires des composites C/C (fibre, matrice, interphase), constitués de carbones turbostratiques d'origines diverses, donc de structures et textures différentes [33, 84, 94], ont des propriétés différentes. Lors de l'ablation physico-chimique, la réactivité intrinsèque des composants influe directement sur la vitesse de récession locale de la paroi [40]. Le comportement global du composite est conditionné par l'hétérogénéité de son architecture qui peut conduire à l'apparition de rugosité et à des couplages complexes.

2.2 Etude expérimentale et stratégie de modélisation

Les résultats présentés dans cette section sont principalement extraits de la partie 3.

2.2.1 Choix d'un procédé modèle d'ablation

Les conditions réelles de fonctionnement des tuyères, objets balistiques et Tokamaks ne sont pas optimales pour l'étude du comportement des matériaux ablatifs du fait des problèmes de mise en œuvre, de mesure *in-situ* et de reproductibilité. Les jets plasmas sont utilisés pour la caractérisation des matériaux constitutifs des boucliers thermiques [31] (l'état de surface est visible sur la micrographie 2.3-a) et des Tokamaks [79] (voir micrographie 2.3-c). Les matériaux de tuyère sont testés en point d'arrêt derrière une tuyère [11] (voir micrographie 2.3-b). Pour les trois applications citées, l'étude complète de l'évolution de la rugosité nécessite la prise en compte de nombreux couplages, parfois forts, entre écoulement global, transferts de masse dans la couche limite de concentration, transferts thermiques dans la couche limite thermique, état de surface du matériau et réactions d'ablation à la paroi. Il n'est pas envisageable de résoudre un modèle complet : de nombreuses hypothèses simplificatrices sont nécessaires. Par ailleurs, les conditions expérimentales locales, sur le matériau, sont difficilement accessibles. Afin de commencer par un modèle simple et dans des conditions d'alimentation et de validation optimales, des essais modèles en four isotherme ont été réalisés (voir micrographie 2.3-d). Les micrographies de la figure 2.3 montrent une grande similitude malgré la différence des conditions d'essai et des matériaux. Le même phénomène local est à l'origine des morphologies

observées : les fibres, plus résistantes à l'oxydation et/ou à la sublimation que la matrice intrafil (ou d'une partie de celle-ci), se trouvent partiellement dénudées et s'affinent. En anglais, on parle de *needle clusters* [17, 48, 67], terme traduit en français par *bouquets d'aiguilles* [66]. On n'observe pas d'érosion sur ces micrographies. La comparaison présentée se concentre sur l'échelle des fibres, cependant, des similitudes sont observées à toutes les échelles.

a- *Rentrée atmosphérique*

b- *Tuyère*

c- *Réacteur de fusion* [79]

d- *Procédé modèle : Four d'oxydation*
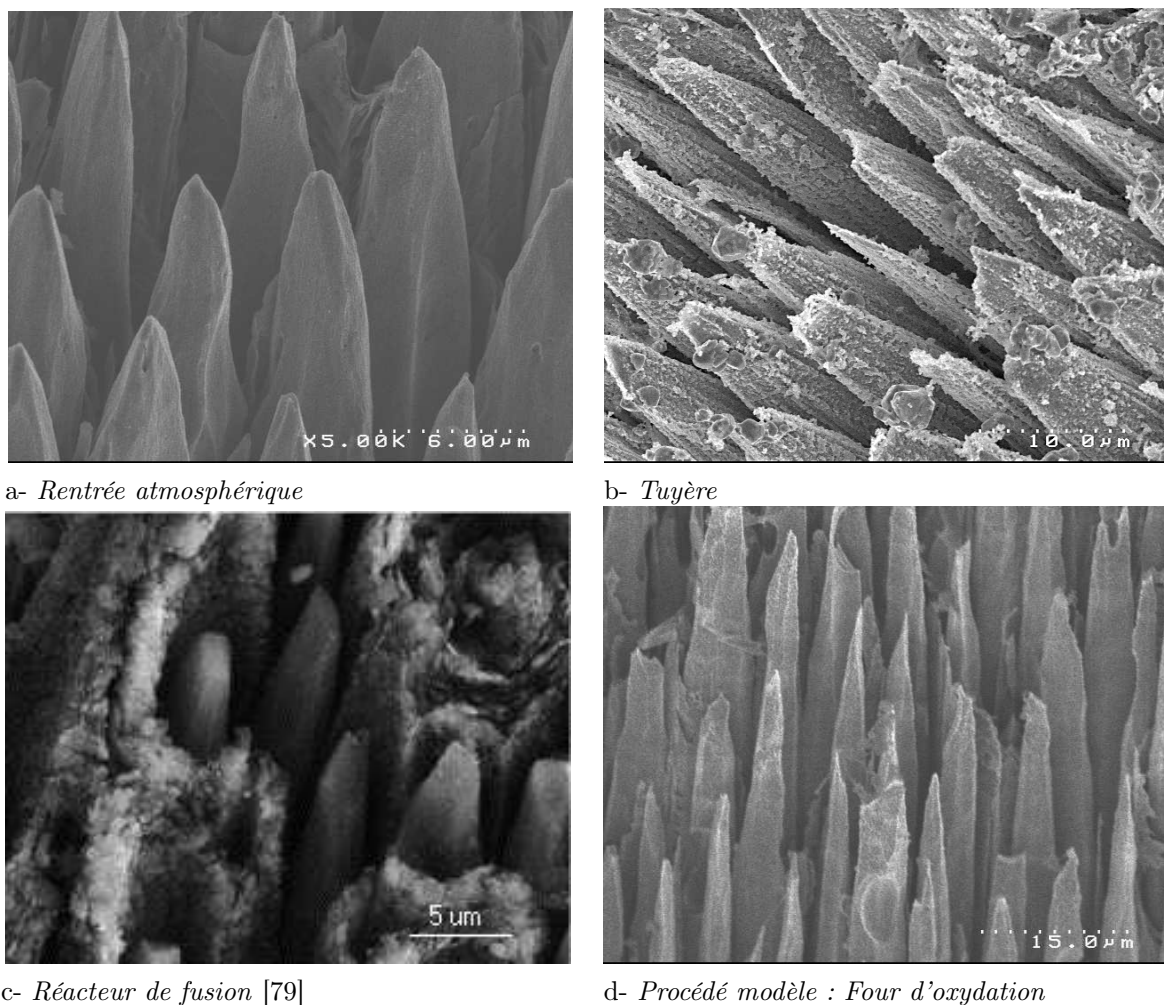
FIG. 2.3 – Micrographies de fils de composites C/C ablatés : bouquets d'aiguilles [66].

2.2.2   Analyse de la rugosité multiéchelle

Le composite 3D C/C a été soumis à un test d'ablation sous air sec à pression atmosphérique dans un réacteur d'oxydation à $625°C$. Après une ablation correspondant à 30% de perte de masse d'un échantillon de $1\,cm^3$, l'état de surface de l'échantillon a été analysé qualitativement par microscopie électronique à balayage (MEB) au LCTS et quantitativement par microtomographie à haute résolution en contraste de phase à l'ESRF (European Synchrotron Radiation Facility, Grenoble). L'ablation exhibe l'architecture du composite, générant une rugosité multiéchelle :
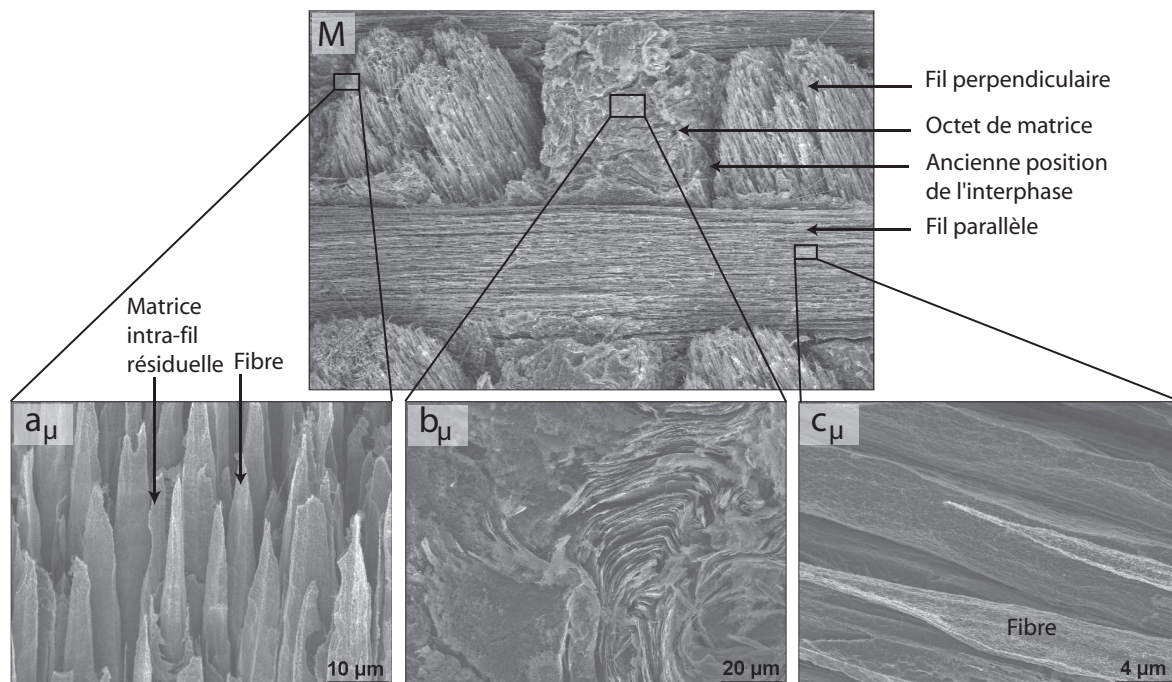
FIG. 2.4 – Micrographies MEB de la surface du composite 3D C/C après ablation par oxydation (air sec, 625°C, pression atmosphérique).

– Une rugosité, dite épi*macro*structurale, se développe sur la macrostructure du composite (voir figures 2.4-M et 2.5-a). L'interphase inter-fils est fortement ablatée et les fils perpendiculaires prennent une forme pyramidale. Les fils parallèles et les octets de matrice restent à la hauteur des fils perpendiculaires.

– Une rugosité épi*méso*structurale se développe à la surface des fils perpendiculaires, et ressemble à des bouquets d'aiguilles (voir figures 2.3, 2.4-a_μ). Dans le cas du 3D C/C, les fibres et la matrice intra-fil ont des réactivités équivalentes. Cependant, une fine interphase de matrice, comprise entre les fibres et une matrice mieux organisée, est plus réactive. La récession de l'interphase est alors plus rapide, dénudant la fibre et la matrice, qui prennent des formes acérées. Dans le cas des fils parallèles, le même phénomène est observé, si ce n'est que les composants pointus sont plus effilés (voir figures 2.4-c_μ, 2.5-c et 2.5-e). Ces morphologies sont représentées sur les schémas 2.5-b et c (la matrice n'est pas représentée). A cette échelle, la rugosité des octets de matrice peut être négligée (voir figure 2.4-b_μ).

– Une rugosité épi*micro*structurale se développe également. On note principalement deux types d'irrégularités : (i) sur les fibres, des facettes (voir figures 2.4-a_μ et 2.5-d), (ii) sur la matrice, l'ablation fait apparaître une structure lamellaire (figure 2.4-b_μ). Ces rugosités microscopiques sont en partie à relier à la texture des matériaux.

Les idées directrices pour la modélisation du comportement du matériau émergent de l'analyse de la rugosité :

– la rugosité suit la structure du matériau : les modèles doivent inclure cette dernière ;
– la rugosité est multiéchelle : la modélisation doit l'être également.
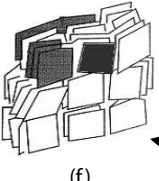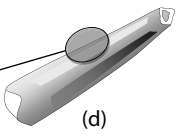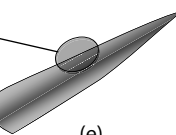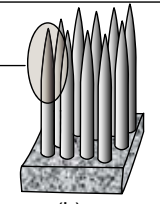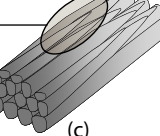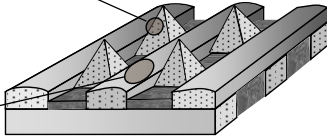
Materiau	carbone turbostr.	fibre	fil	composite
Rugosité	epi**nano**structurale	epi**micro**structurale	epi**meso**structurale	epi**macro**structurale
3D C/C				
Echelle	nanoscopique 100 nm	microscopique 1 µm	mesoscopique 0.1 mm	macroscopique 10 mm
Modélisation	**qualitative**	**quantitative**	**quantitative**	**quantitative**

Fig. 2.5 – Tableau de synthèse de la rugosité multiéchelle stationnaire sur un composite 3D C/C.

2.2.3   Stratégie de modélisation

On présente la stratégie de modélisation dans le cas de l'oxydation. Le cas de de la sublimation est mathématiquement équivalent sous les hypothèses de Knudsen-Langmuir (voir section 5.5.3). La stratégie de modélisation se focalise sur le comportement du matériau, particulièrement sur la récession différentielle de sa surface hétérogène qui conduit à l'établissement de la rugosité. Le point de départ retenu pour la modélisation est l'équation d'Hamilton-Jacobi pour la récession d'une surface définie par la relation $S(x, y, z, t) = 0$ [53] :

$$\frac{\partial S}{\partial t} + \mathbf{v} \cdot \nabla S = 0 \tag{2.1}$$

où l'expression de vitesse de récession de la surface $\mathbf{v}$ [53] est :

$$\mathbf{v} = -v_s \, J \, \mathbf{n} \tag{2.2}$$

où v_s est le volume molaire du solide, $\mathbf{n} = \nabla S / \|\nabla S\|$ la normale sortante. J est la densité de flux molaire d'oxydation donnée par la relation [32] :

$$J = k(T) \, C^n \tag{2.3}$$

où C est la concentration en oxydant à la paroi et n l'ordre de la réaction. $k(T)$ est la réactivité, dont les variations d'un constituant à l'autre, ou d'une zone chaude à une zone plus froide, sont à l'origine de la rugosité. La description de l'évolution de la surface nécessite la connaissance de $\mathbf{v}$ en tout point de l'interface, et par conséquent celle de C, n, T, et du constituant considéré. Dans cette étude, les conditions choisies permettent de considérer le matériau isotherme et l'ordre de la réaction unitaire. Le champ de concentration C résulte

d'un équilibre entre la consommation à la paroi et le transport de masse en phase fluide. Dans les conditions expérimentales des essais modèles d'oxydation, on a montré que l'effet de la convection était négligeable. La conservation de la concentration en oxydant dans la phase fluide s'écrit :

$$\frac{\partial C}{\partial t} + \nabla \cdot (-D\nabla C) = 0 \qquad (2.4)$$

où D est le coefficient de diffusion de l'oxygène dans l'air. La condition limite sur la paroi réactive d'un composant c est donnée par :

$$J_c = (-D\nabla C) \cdot \mathbf{n} = -k_c C \qquad (2.5)$$

Ce modèle de récession de surface est ensuite appliqué à chaque échelle. La stratégie de modélisation retenue consiste à partir des petites échelles pour "remonter" vers les grandes, en utilisant des changements d'échelle. Le point de départ est le plan de graphène, le point d'arrivée le composite homogénéisé (voir figure 2.5).
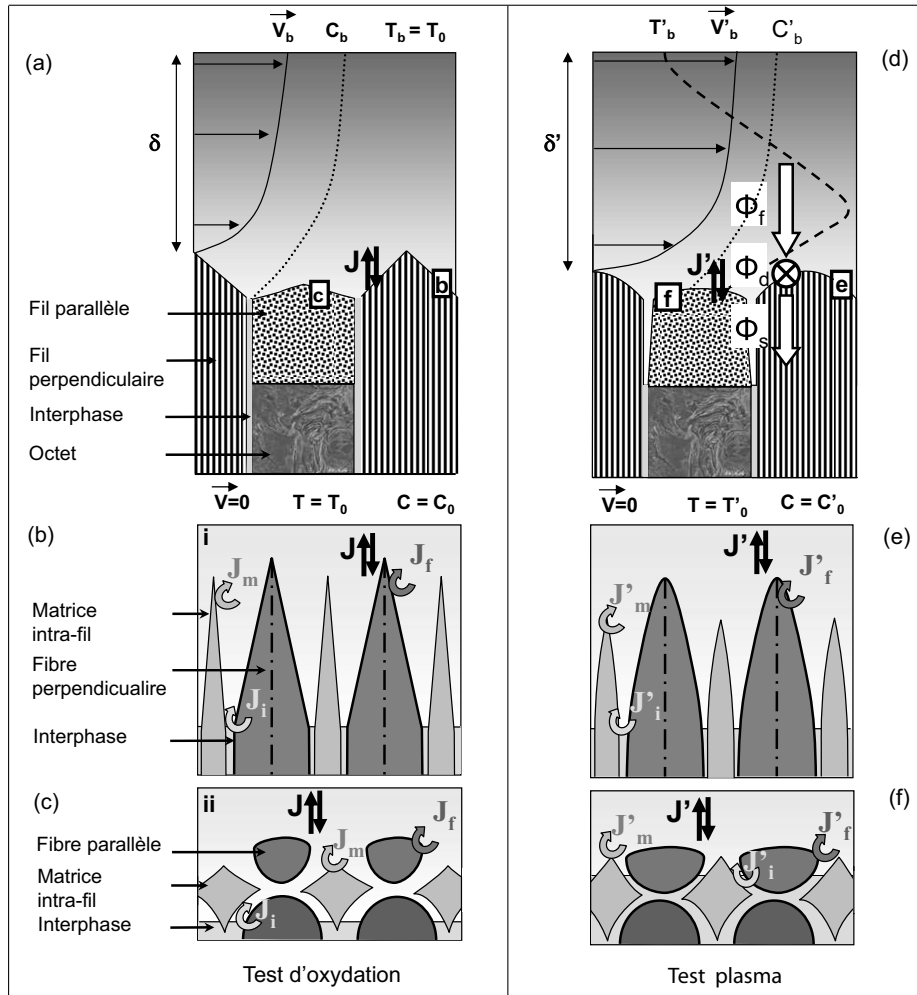
FIG. 2.6 – Stratégie de modélisation : schématisation des phénomènes couplés sur un 3D C/C.

Le passage de l'échelle nanoscopique à l'échelle microscopique requiert la prise en compte dans les modèles de l'anisotropie du plan de graphène et de la texture du carbone. On se

propose de chercher à relier cette structure anisotrope tridimensionnelle au comportement microscopique du carbone.

Du point de vue de l'étude du comportement effectif du composite, la plus petite échelle à laquelle des données expérimentales quantitatives sont accessibles est celle des fibres. Deux changements d'échelle sont utiles pour remonter aux propriétés du composite (voir figure 2.6) :

1. échelle microscopique (fibres, matrice, interphase) vers échelle mésoscopique (fil),

2. échelle mésoscopique (fils, matrice, interphase) vers échelle macroscopique (composite).

2.3   Développement d'un outil de simulation numérique : AMA

Pour résoudre les problèmes présentés ci-dessus, un code de simulation numérique permettant le suivi de front (interface fluide/solide) est indispensable, au moins dans un premier temps, comme moyen d'expérience numérique, pour guider la modélisation analytique. Partant des bases d'un code écrit par G. Vignoles [97] pour simuler l'infiltration et le dépôt en phase vapeur [99], AMA (Ablation Marches Aléatoires) a été développé et validé. La description détaillée de l'algorithme d'AMA et sa validation, dont on présente ci-dessous les grandes lignes, sont exposées à la section 6.2.

2.3.1   Présentation

AMA est écrit en C ANSI. Le déroulement de la simulation est divisé en cinq étapes principales (voir figure 2.7) :
- Une image 3D contenant plusieurs phases (fluide/solides) est discrétisée en voxels (pixels 3D) cubiques [97] ;
- La position de l'interface fluide/solide (mobile) est approximée par un Marching Cube simplifié [97] ;
- Le transfert de masse est simulé par une marche aléatoire basée sur le principe du mouvement Brownien [36, 67, 82] ; cette méthode, codée au cours de la thèse, est particulièrement efficace pour simuler la diffusion en régime continu.
- La réaction hétérogène du premier ordre est simulée par une probabilité de collage adaptée à la nouvelle marche aléatoire utilisée [67, 82] ;
- Une condition limite de Dirichlet a été ajoutée ; elle est simulée à l'aide d'une zone tampon dans laquelle la concentration est maintenue constante.

2.3.2   Validation

AMA a été validé par comparaison à un modèle analytique 1D dans tous les régimes et à un modèle analytique 3D en limitation réactive. La figure 2.8 présente, pour la validation 3D, la cellule de départ, le résultat du calcul analytique et le résultat du calcul numérique. Un excellent accord qualitatif est obtenu. Quantitativement, l'erreur est inférieure à 2.5%. Grace à la méthode simplifiée de description de la surface et à la marche aléatoire basée sur le principe du mouvement Brownien, les calculs sont rapides. La méthode d'intégration utilisée n'est aucunement limitante ; elle pourrait être appliquée à des cellules dont la discrétisation serait extrêmement fine. Cependant, une limitation est apportée par la mémoire vive (RAM) de la station de calcul qui doit pouvoir charger l'image 3D. Dans le cas des calculs présentés dans la suite (images d'environ 10^6 voxels), le régime stationnaire (fin du calcul) est atteint pour un temps de simulation de l'ordre de 48 heures sur un microprocesseur Xeon de $3.2\,GHz$.

a) Schéma de l'algorithme

b) Schéma de principe
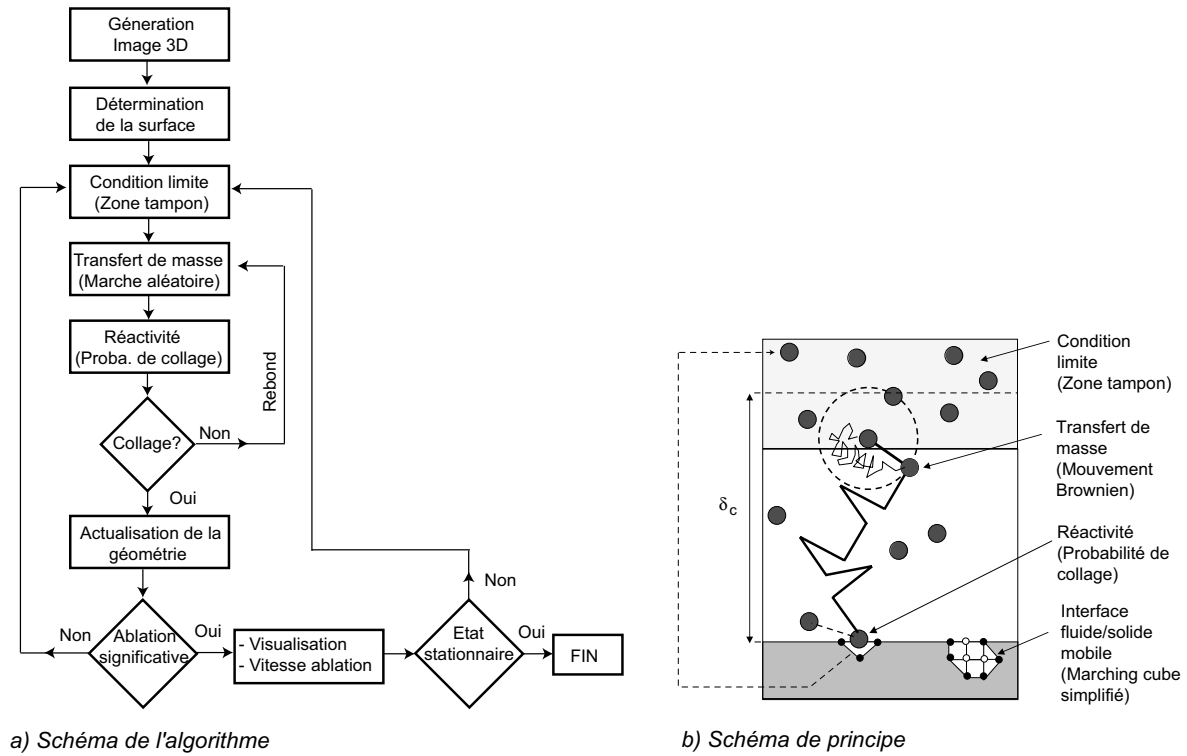
Fig. 2.7 – Description schématique du code de simulation numérique AMA.

a) Cellule élémentaire 3D : instant initial

b) Résultat analytique : régime établi

c) Simulation AMA : régime établi
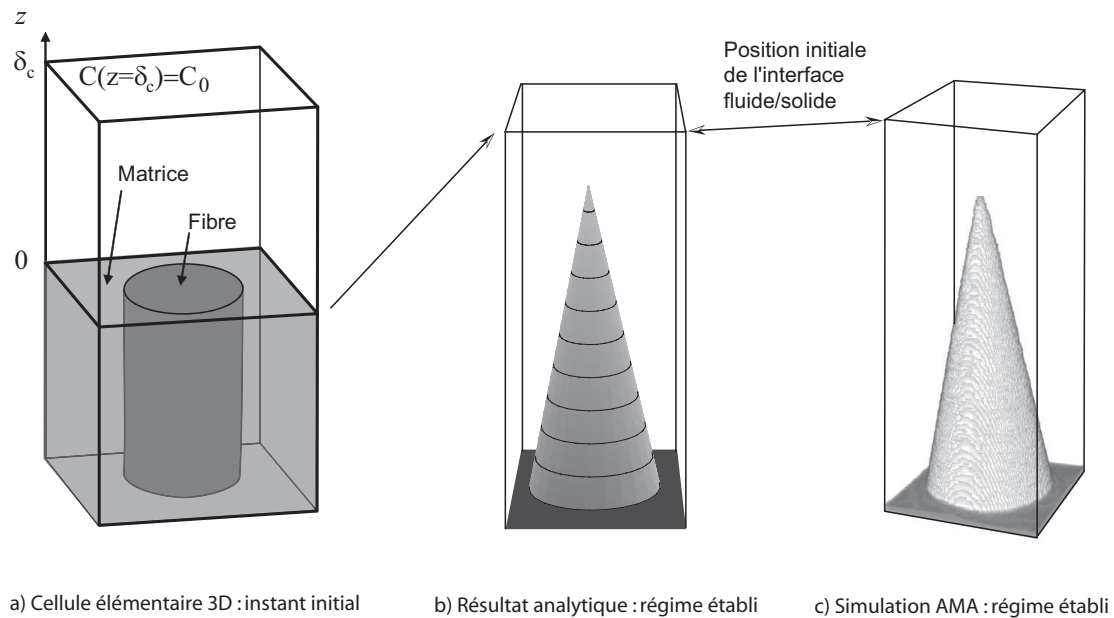
Fig. 2.8 – Validation 3D du code AMA par comparaison à un modèle analytique.

2.4   Principaux résultats de modélisation

Cette section présente une synthèse illustrée des résultats obtenus de l'échelle nanoscopique
à l'échelle macroscopique (voir figure 2.5).

2.4.1   Echelle nanoscopique

Cette étude est développée en annexe A, section A.4.2.

Le point de départ de la modélisation est le plan de graphène, dont la courbure est négligée.
La probabilité de collage (acte élémentaire à l'origine de la réactivité) des bords de plans de
graphène $(P_\parallel)$ est grande devant celle de la direction perpendiculaire $(P_\perp)$ (voir figure 2.9).
D'après G. H. Hennig [49], on a $P_\parallel \simeq 100\,P_\perp$. On propose de modéliser cette propriété par
une probabilité de collage orthotrope :

$$\underline{\underline{P}} = \left(\begin{array}{ccc} P_\parallel & 0 & 0 \\ 0 & P_\parallel & 0 \\ 0 & 0 & P_\perp \end{array} \right)_{(\mathbf{i},\mathbf{j},\mathbf{k})}$$
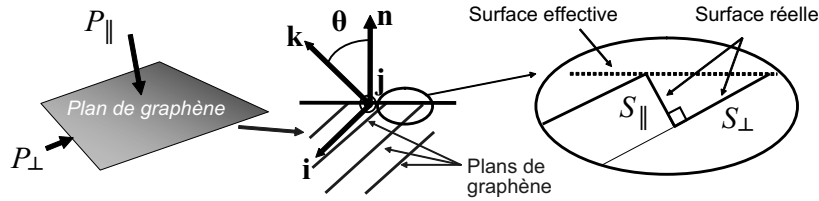
FIG. 2.9 – Interprétation de la réactivité des plans de graphène : schémas et notations [60].

La probabilité de collage $\tilde{P}_\theta$ associée à une surface effective par rapport à laquelle les plans
de graphène sont inclinés d'un angle θ, peut être interprétée comme la projection de $\underline{\underline{P}}$ sur
cette surface, et s'écrit :

$$\tilde{P}_\theta = \frac{P_\parallel |\sin\theta| + P_\perp |\cos\theta|}{|\sin\theta| + |\cos\theta|} \tag{2.6}$$

Cette forme de probabilité de collage a été intégrée dans AMA. A chaque voxel est associée une
orientation (celle des plans de graphène). La probabilité de collage associée à une facette de
l'interface dépend alors de son orientation par rapport à celle du voxel auquel elle appartient.

A partir de cette interprétation, on modélise le comportement d'un matériau modèle :
un graphite polycristallin (EDM3, Poco), formé de grains de graphite d'environ $4\,\mu m$ de
diamètre orientés aléatoirement (voir figure 2.10). Ses domaines cohérents sont de très grande
extension, et correspondent aux grains qui sont des cristallites idéaux. La texture du matériau
est donnée par l'orientation aléatoire des grains. Ce matériau est assez facilement modélisable
moyennant quelques hypothèses. On s'appuie sur deux changements d'échelles numériques
pour remonter à son comportement macroscopique : (i) plan de graphène vers empilement
de plans (domaine cohérent), (ii) empilement de plans vers matériau homogénéisé. Lors du
premier changement d'échelle, la croissance de figures d'attaque typiques, appelées *pitting*,
expérimentalement observée [88] et simulées en 2D dans des études antérieures [47,87], ont
été obtenues ici à partir du modèle 3D (voir figure 2.11). La simulation du comportement
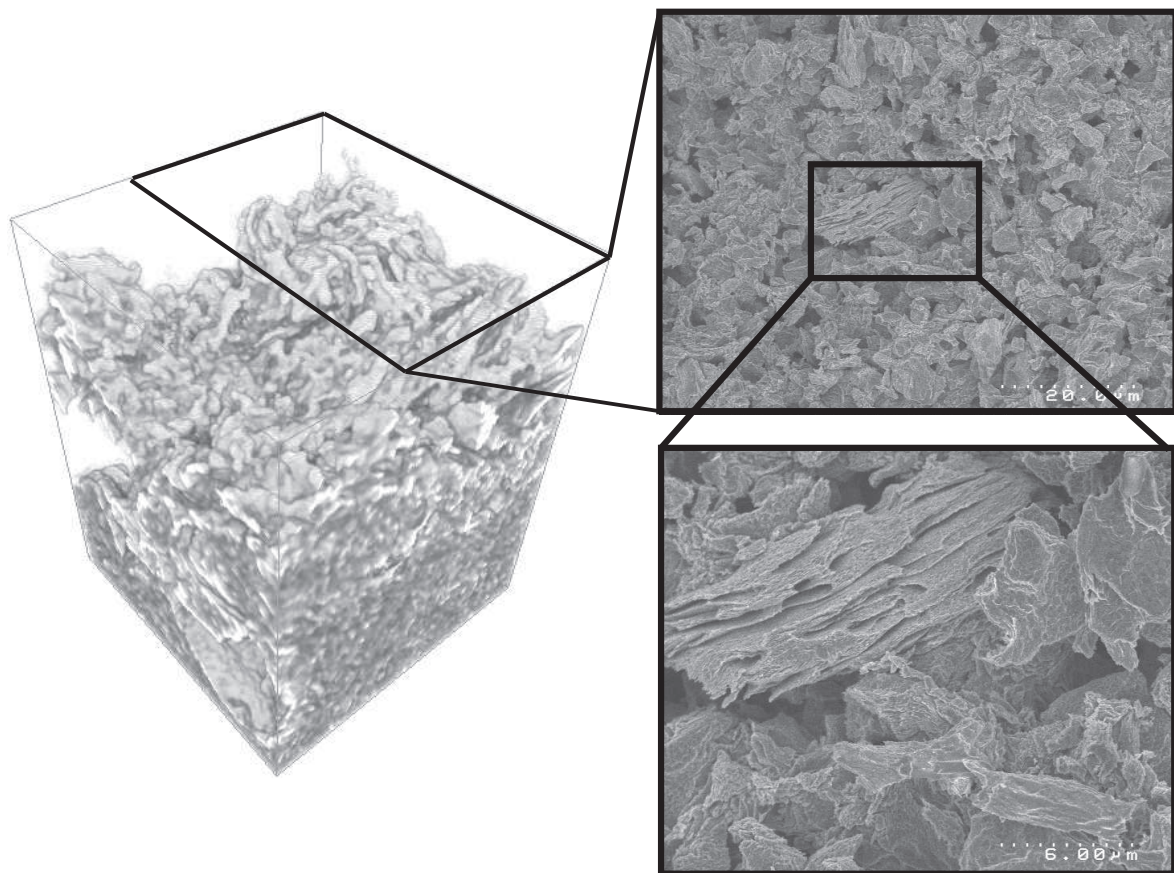
FIG. 2.10 – Microtomographie (gauche) et micrographie MEB (droite) de la surface d'un graphite EDM3 après ablation [60].
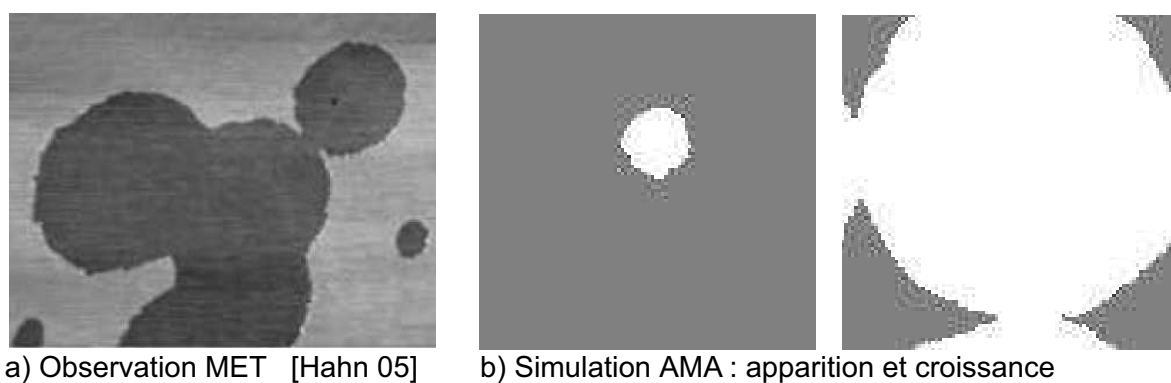
a) Observation MET   [Hahn 05]   b) Simulation AMA : apparition et croissance

FIG. 2.11 – Attaque (*Pitting*) d'un empilement de plans pour $\theta = 0$

d'un graphite polycristallin idéal (sans joint de grains) est présenté sur la figure 2.12 en régime réactif.

Un accord qualitatif est obtenu avec les observations expérimentales de graphite ablaté
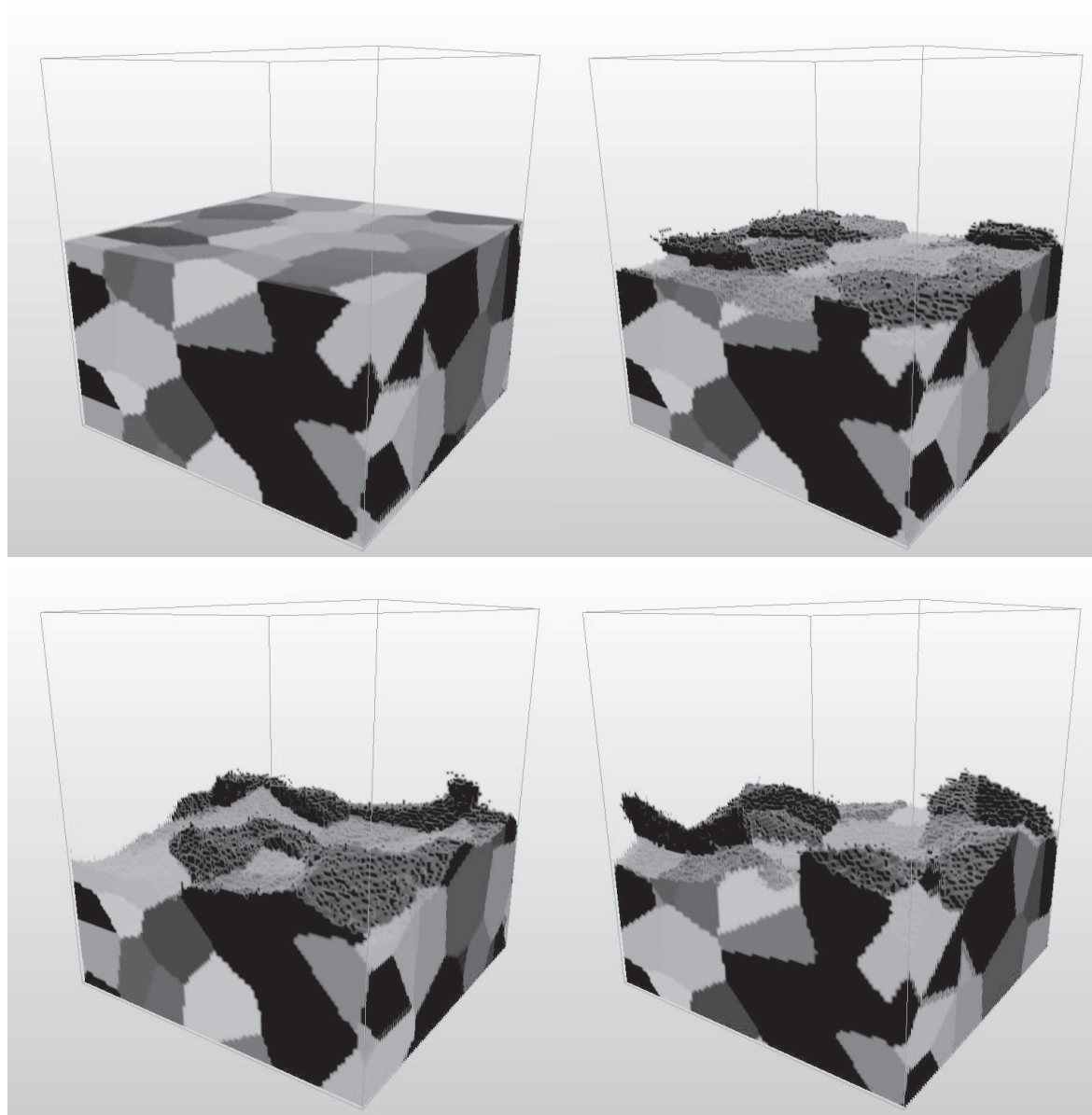
FIG. 2.12 – Simulation de l'évolution de la surface d'un graphite polycristallin idéal durant l'ablation [60].

dans le four d'oxydation (voir figure 2.10). La dimension caractéristique de la rugosité pseudo-stationnaire obtenue est approximativement égale à celle des grains. Ce modèle permet d'expliquer l'apparition de rugosité sur les graphites polycristallins durant l'ablation. Le même phénomène, mais à une échelle inférieure, est à l'origine des petites facettes ou irrégularités observées sur les fibres ablatées (voir figure 2.3).

2.4.2   Echelle microscopique

Les résultats présentés dans cette sous-section sont principalement issus du chapitre 4.

Les modèles anisotropes de l'échelle précédente peuvent expliquer les petites irrégularités observées sur la surface des fibres. Les facettes qui s'étendent sur toute la longueur des fibres (voir figure 2.13-c) ont très probablement une autre origine, car la taille des domaines cohérents pour les fibres observées est seulement de l'ordre de la centaine de micromètres. Lorsque l'on résout le modèle 3D utilisé pour la validation du code AMA (voir figure 2.8) sur une section initiale de fibre irrégulière (voir figure 2.13-a et b), on obtient la morphologie représentée sur la figure 2.13-d. Ce résultat suggère que les grandes facettes sont simplement issues des irrégularités de la section des fibres.

a) Sections de fibres :
observation (MEB)

b) Section de fibre :
modèle (AMA)

c) Régime établi (MEB)

d) Régime établi (AMA)
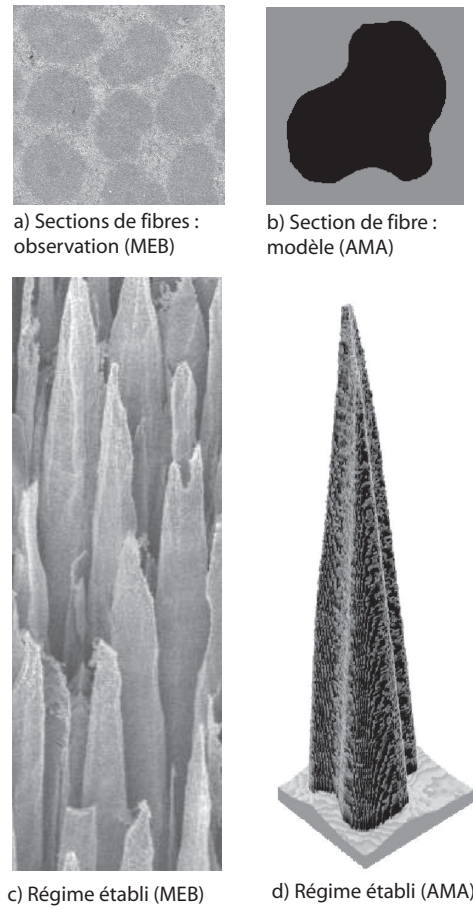
Fig. 2.13 – Fibres facettées : comparaison des observations expérimentales avec un modèle de fibres à section irrégulière (figure issue de la section 6.3).

A cette échelle, il est souhaitable de définir une surface élémentaire représentative pour laquelle les constantes de réactions hétérogènes, évoquées précédemment en terme de probabilités de collage, sont isotropes homogènes. Du point de vue des phénomènes étudiés, les fibres et matrices de cette étude peuvent être considérées homogènes isotropes pour une surface représentative de l'ordre du micromètre carré, grande devant la taille des domaines cohérents (inférieure à $100\,nm$, mesure par microscopie électronique en transmission). Cette surface est
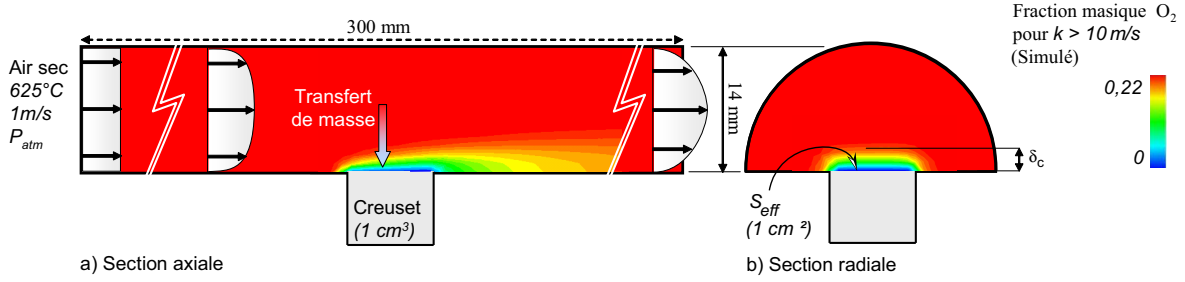
FIG. 2.14 – Champ de concentration en réactif dans la partie utile du four d'oxydation (air sec, $T = 625°C$, $P = 1atm$).
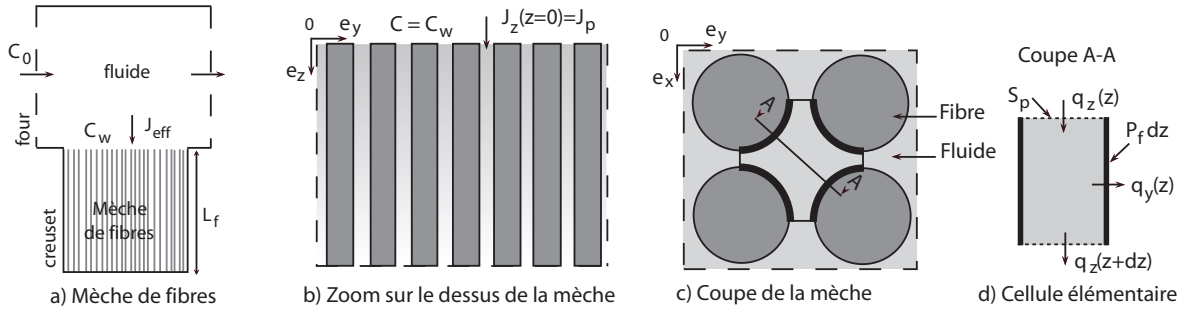
FIG. 2.15 – Schéma d'un empilement unidirectionnel de fibres placé dans un creuset cubique.

élémentaire pour les phénomènes physico-chimiques considérés ; en particulier, elle est suffisamment petite pour que le temps caractéristique de diffusion associé soit négligeable. Les données d'alimentation quantitatives des modèles isotropes (échelles mésoscopique et macroscopique) sont obtenues à cette échelle. De nombreuses définitions de la réactivité ont été proposées pour le carbone [9] ; pour la modélisation de l'évolution de géométrie de l'état de surface, la réactivité intrinsèque géométrique doit être mesurée. A une réactivité est associée une surface ; ici, il s'agit de la surface moyennée à l'échelle micronique ; elle peut être vue comme une enveloppe lissant la rugosité nanoscopique, les effets des rugosités nanoscopiques étant directement intégrés dans la valeur mesurée.

Les mesures des taux d'oxydation, desquels les réactivités géométriques intrinsèques peuvent être extraites, ont été réalisées dans le four d'oxydation utilisé pour étudier le comportement ablatif des composites. Pour ce type de mesures, les dispositifs à analyse thermogravimétrique (ATG) sont habituellement employés [9, 25, 34, 58, 68, 70, 100] ; cependant, à la température cible retenue ($625°C$) une limitation diffusive est atteinte dans ces dispositifs, *i.e* le transfert en oxygène est insuffisant pour alimenter la réaction. Le four d'oxydation a été conçu pour remédier à ce problème. Néanmoins, les effets diffusifs, même s'ils n'y sont plus limitants, sont toujours présents. Afin de garantir la pertinence des valeurs mesurées, le four d'oxydation a été modélisé en 3D : réaction hétérogène, convection et diffusion sont pris en compte. Cela permet de déterminer le champ de concentration en oxydant dans le dispositif (voir figure 2.14) et de prévoir une éventuelle limitation diffusive (concentration nulle sur l'échantillon). Lorsque la limitation diffusive n'est pas totalement atteinte, le modèle est utilisé pour extraire des données expérimentales la réactivité intrinsèque d'un échantillon en soustrayant les
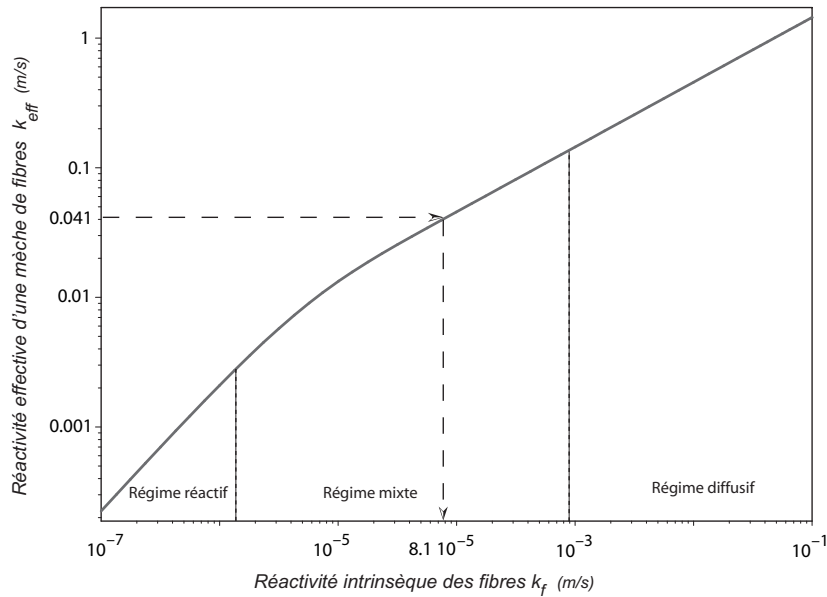
FIG. 2.16 – Courbe reliant la réactivité effective de l'empilement de fibres k_{eff} à la réactivité géométrique intrinsèque des fibres k_f : illustration pour des fibres ex-PAN (flèches).

effets diffusifs. Cette méthode permet d'obtenir la réactivité effective d'un échantillon dense donné (composites, matrices). Dans le cas des fibres, une étape supplémentaire est nécessaire. Elles sont arrangées en un empilement unidirectionnel dans un creuset cubique (voir figure 2.15), qui constitue un échantillon dont la réactivité effective est déterminée par la méthode présentée ci-dessus. Ensuite, un modèle prenant en compte la diffusion et la réaction dans ce milieu poreux permet d'exprimer la réactivité géométrique intrinsèque des fibres k_f (en m/s) en fonction de la réactivité effective de l'empilement k_{eff} (voir figure 2.16). Ces mesures ont montré que les réactivités intrinsèques des composites étaient supérieures à celles des fibres de plus d'un ordre de grandeur, s'approchant de celles des matrices. On en déduit que la réactivité des composites n'est pas une propriété additive ; un principe de maillon faible est observé. Une explication de ce phénomène est attendue des études aux échelles mésoscopique et macroscopique.

2.4.3   Echelle mésoscopique

Dans les sous-sections suivantes, afin de mettre en avant la démarche de modélisation et d'illustrer les résultats obtenus échelle par échelle, il a été choisi de combiner des résultats analytiques et numériques complémentaires des chapitres 5, 6 et 7. Pour faciliter le jeu de piste au lecteur qui souhaitera plus d'explications, l'origine de chaque figure est précisée.

a) Simulation AMA d'un fil de 3D C/C ablaté et incliné de 15°   b) Observation MEB d'un fil de 3D C/C ablaté et incliné de 15°
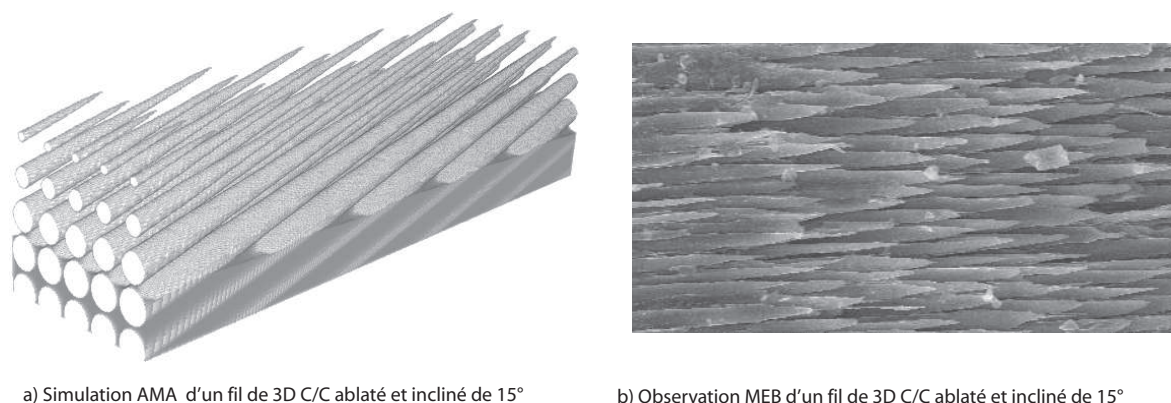
FIG. 2.17 – Comparaison qualitative entre les résultats de simulation numérique et les observations expérimentales : surface d'un fil incliné d'environ 15° (figure issue de la section 6.4.2).

α_y	90°	75°	60°	45°	30°	15°
Géométrie des fibres Régime établi et réactif						

FIG. 2.18 – Morphologies des fibres en fonction de leur inclinaison par rapport à la surface moyenne (*cf.* section 6.4.2).

L'échelle mésoscopique est celle des fils et des matrices inter-fils. La matrice est supposée homogène à cette échelle. On se concentre sur l'étude des fils, constitués de fibres, de matrice intra-fil et éventuellement d'une interphase entre fibre et matrice (cas du 3D C/C). L'interphase étant très réactive, elle joue le rôle de la phase faible, tandis que la présence de la matrice à coeur devient négligeable. Dans le cas du 2D C/R cette interphase n'existe pas,
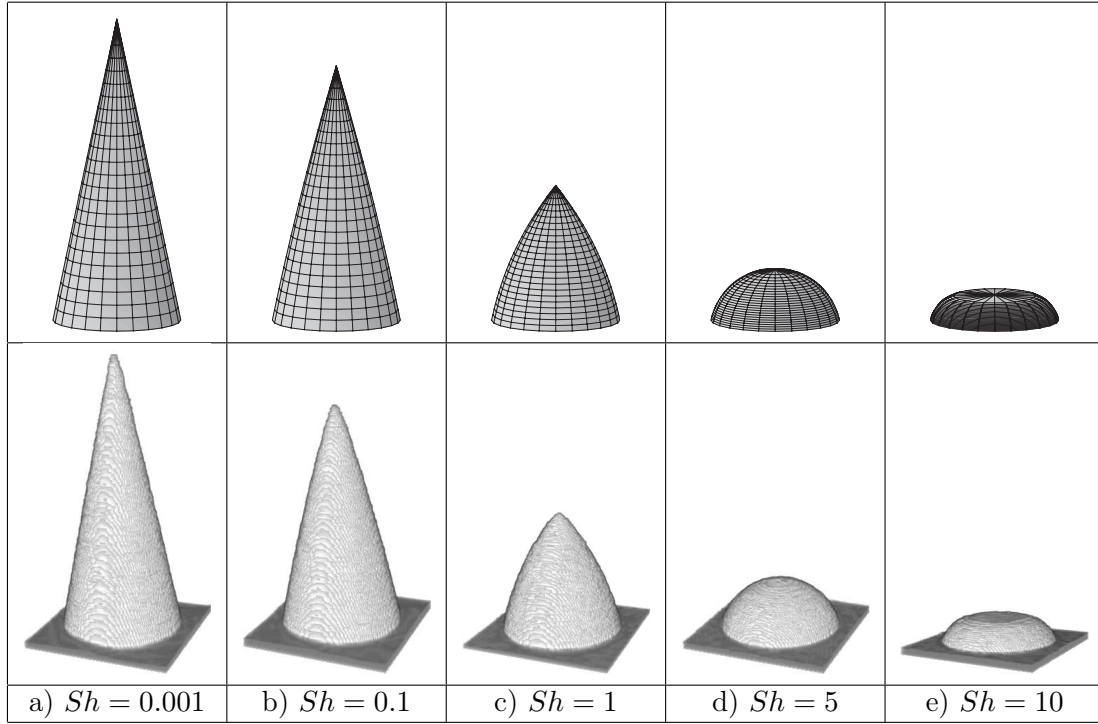
FIG. 2.19 – Morphologie des fibres en régime stationnaire en fonction de Sh (avec $A = 5$) : comparaison entre solution analytique (haut) et simulation numérique (bas) (*cf.* section 6.4).

la phase faible est la matrice. Pour traiter simultanément le cas des deux composites de cette étude, on considère une cellule élémentaire constituée d'une fibre entourée d'une phase faible (voir figure 2.8-a), qui peut être répétée suivant le motif voulu pour former un fil. Le modèle présenté en section 2.2.3 est résolu pour la cellule représentée, la concentration en oxygène au sommet des fibres étant déduite du calcul 3D dans le four (voir figure 2.14). Sur la figure 2.8-a, la surface moyenne est perpendiculaire à la direction des fibres, mais ce n'est pas nécessairement le cas dans la réalité. Les autres orientations ont été étudiées en 3D (voir figure 2.17) ; les coupes correspondant à une étude paramétrique réalisée en régime stationnaire sont présentées en figure 2.18. La simulation numérique a montré que la réactivité effective des fils ne dépendait pas de leur orientation avec la surface ; or, pour les fils perpendiculaires à la surface, le modèle peut être résolu analytiquement. Les résultats obtenus, qui sont strictement équivalents à ceux de la simulation numérique (voir figure 2.19) mais beaucoup plus explicites, sont présentés dans un premier temps pour le régime stationnaire ; puis, le régime transitoire est abordé.

La solution analytique conduit aux résultats suivants :
– Du fait de la récession plus rapide de la phase faible, les fibres sont partiellement dénudées, s'affinent et acquièrent une forme pointue (voir figure 2.20) ;
– Seulement deux paramètres sont nécessaires pour décrire cette rugosité en régime stationnaire : un contraste de réactivité A et un nombre de Sherwood Sh.

Le contraste de réactivité entre la fibre et la phase faible A est donné par la relation :

$$A = \frac{k_{wp}\,v_{wp}}{k_f\,v_f} \tag{2.7}$$

La concentration Co en oxygène au sommet des fibres est imposée par les conditions expérimentales. La matrice étant plus réactive que la fibre, l'oxygène doit diffuser vers le bas de la cellule pour alimenter la réaction, conduisant, en fonction du rapport vitesse de consommation sur vitesse de diffusion, appelé nombre de Sherwood (*Sh*), à trois type de régimes représentés ci-dessous.
Code de couleurs pour le champ de concentration: Rouge : C=Co, blanc : C=0
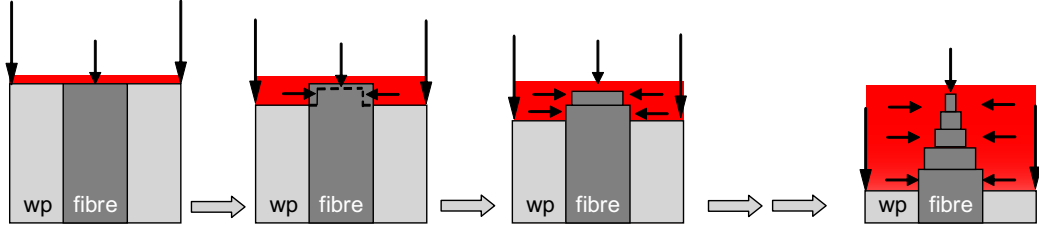
a) Pas d'effets diffusifs (limitation réactive : *Sh<<1*) : la vitesse de recul local de paroi dépend unique--ment de la phase considérée, conduisant à des géométries coniques. La vitesse de recul est imposée par la matrice par principe de maillon faible.
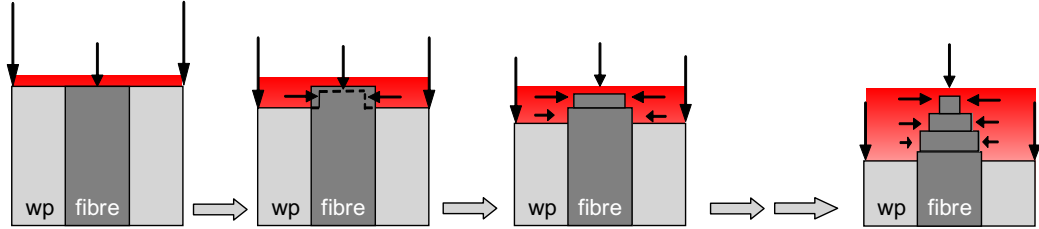
b) Avec effets diffusifs modérés (régime mixte : *Sh~1*) : les effets diffusifs ralentissent la vitesse de recul à la base de la fibre par appauvrissement en oxygène, conduisant à des géométries ogivales. La vitesse de recul est une fonction complexe des réactivités des fibres et de la phase faible.
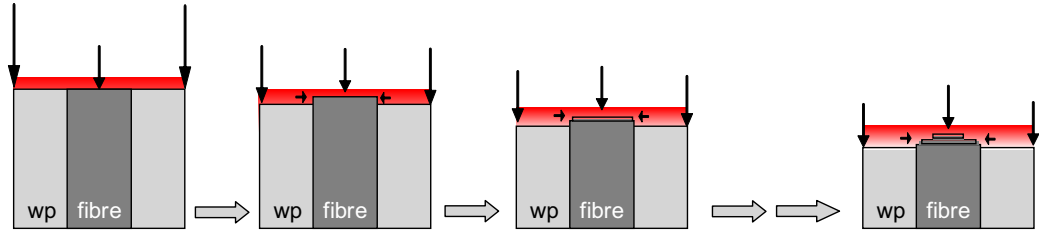
c) Avec effets diffusifs prépondérants (limitation diffusive : *Sh >>1*) : les effets diffusifs ralentissent con--sidérablement la vitesse de recul à la base de la fibre par appauvrissement en oxygène, conduisant à une protection totale de la phase faible par la fibre. La vitesse de recul est imposée par la fibre.

Fig. 2.20 – Schématisation intuitive de l'apparition de rugosité à l'échelle mésoscopique : vue en coupe de fibres entourées d'une phase faible et ablatées par la face supérieure.

où les indices wp et f sont respectivement associés à la phase faible et aux fibres, k et v étant leurs coefficients de réaction et leurs volumes molaires respectifs. Dans le cas des matériaux de cette étude, on a : $A > 1$. La géométrie en régime stationnaire est fortement corrélée à ce contraste ; la partie dénudée des fibres h_f^s augmente avec A. Le nombre de Sherwood Sh retenu s'écrit :

$$Sh = \frac{k_{wp} R_f}{D} \tag{2.8}$$

où R_f est le rayon des fibres. Sh est un indicateur des trois régimes de transfert qui peuvent apparaître sur cette surface hétérogène réactive : régime de limitation diffusive ($Sh >> 1$),

régime mixte ($Sh \sim 1$) et régime limité par la réaction ($Sh << 1$). Pour des valeur de Sh faibles, la géométrie des fibres est conique et dépend seulement de A, avec $\widetilde{h}^s_f = h^s_f/R_f = \sqrt{A^2 - 1}$ (voir figures 2.19-a, 2.20-a et 2.21). Quand Sh augmente, mais reste inférieur à $\sqrt{A^2 - 1}$, les effets diffusifs tendent à diminuer h^s_f et la pointe de la fibre devient ogivale (voir figures 2.19-b-c-d, 2.20-b et 2.21). Pour de plus grandes valeurs de Sh, le bout des fibres présente un plateau et $\widetilde{h}^s_f = (A-1)/Sh$; donc, en régime limité par la diffusion, la rugosité est pratiquement inexistante (voir figures 2.19-e, 2.20-c et 2.21). A titre d'exemple, dans le cas des micrographies b et d de la figure 2.3, Sh est très faible, ce qui explique les formes très pointues observées. Pour la micrographie a, le nombre de Sherwood est proche de l'unité, ce qui justifie la forme ogivale observée. Dans le cas de la micrographie c, les conditions expérimentales ne sont pas connues avec suffisamment de précision pour déterminer Sh, mais la géométrie ogivale de la fibre suggère un nombre de Sherwood unitaire (on note que l'interphase très réactive a été ablatée, mais que la matrice de coeur est plus résistante). Dans le cas du composite 3D C/C, le modèle a permis de déterminer la réactivité de l'interphase, qui ne peut pas être obtenue indépendamment, par analyse de la rugosité (mesure de $\widetilde{h}$). D'après le modèle, l'interphase est trente fois plus réactive que les fibres.
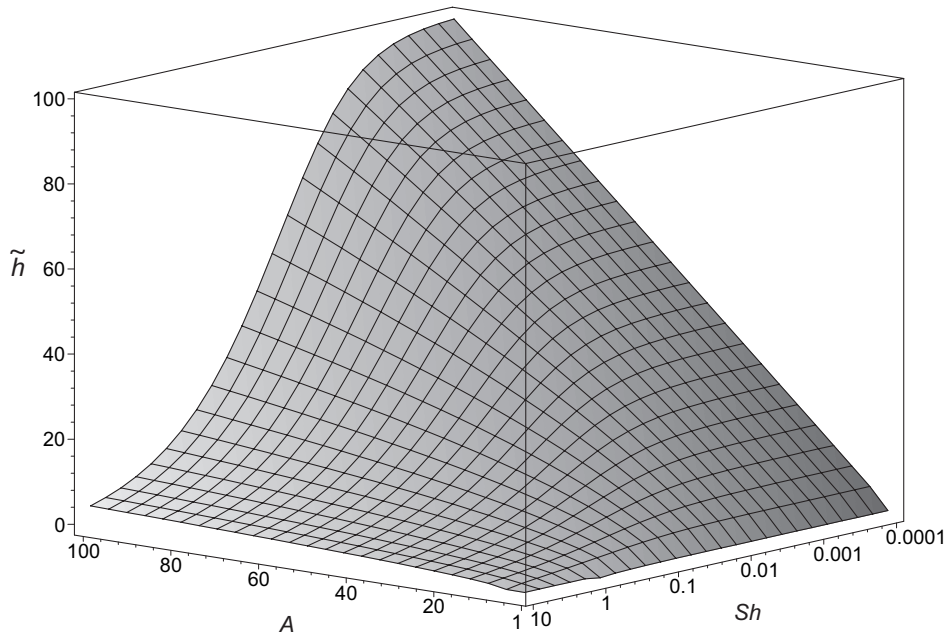
FIG. 2.21 – Courbe 3D de la hauteur de fibre réduite $\widetilde{h} = \widetilde{h}^s_f$ en fonction de A et Sh (*cf.* section 5.3.5).

En régime transitoire, moyennant quelques hypothèses validées par simulation numérique, une solution analytique a également été obtenue (voir figure 2.22). Dans le repère mobile lié à la position de la phase faible, tout se passe comme si la géométrie de la rugosité se développait dans une enveloppe correspondant à sa géométrie en état stationnaire (pointillés). La vitesse de croissance de la fibre dépend fortement du régime de réaction considéré, comme représenté sur la figure 2.23. En régime réactif, la vitesse de croissance est constante en fonction du temps ; les effets diffusifs tendent à diminuer cette vitesse. D'autre part, comme les effets diffusifs sont d'autant plus importants que la hauteur augmente, la vitesse de croissance diminue au
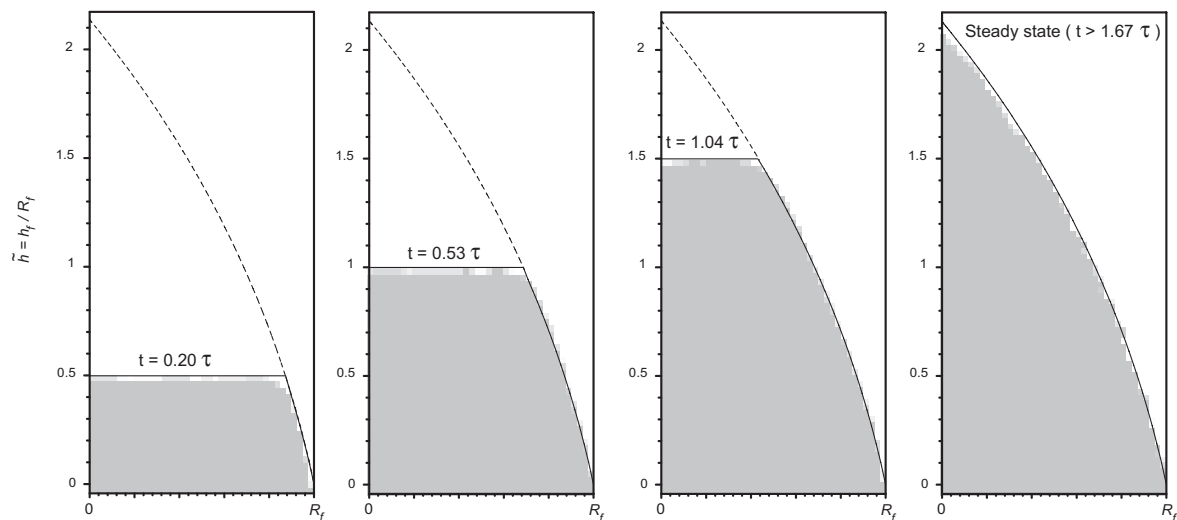
FIG. 2.22 – Morphologie de la section d'une fibre en fonction du temps pour $A = 5$ et $Sh = 1$: comparaison entre solution analytique (ligne continue) et simulation numérique (pixels gris) (*cf.* section 7.3).
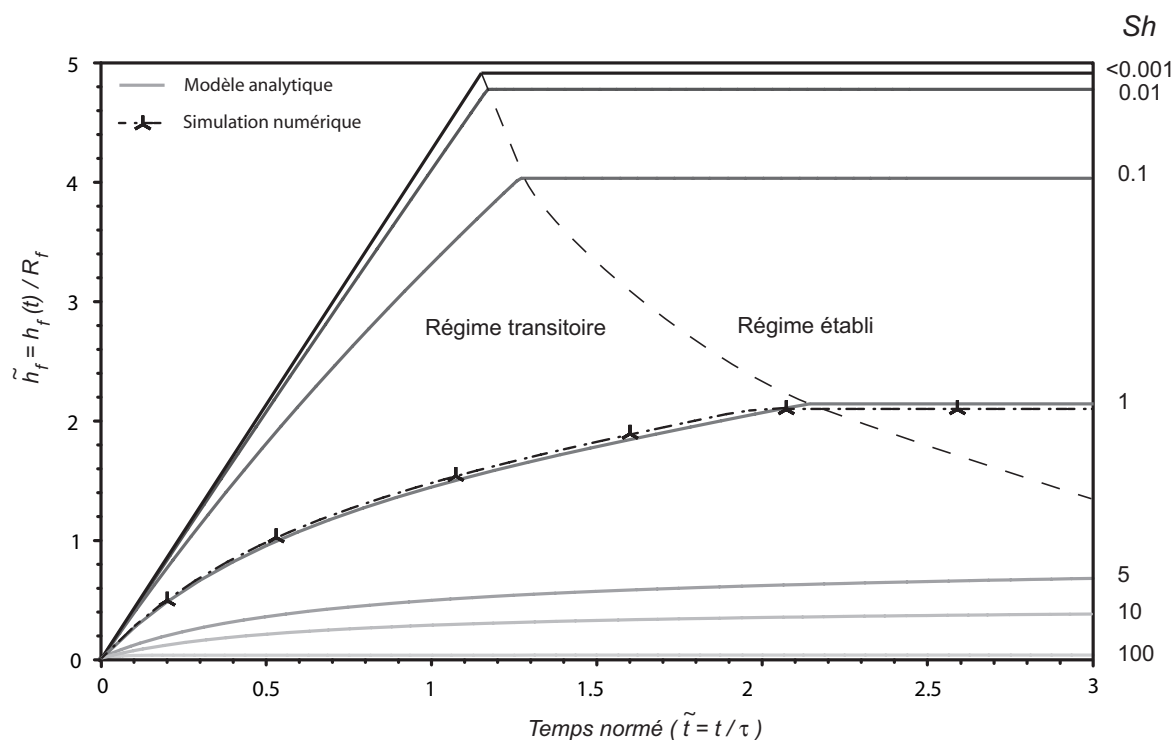
FIG. 2.23 – Hauteur de fibre en fonction du temps adimensionné pour différentes valeurs de Sh avec $A = 5$. $\tau = R_f/(C_0 k_f \upsilon_f)$ est un temps caractéristique donné par les paramètres expérimentaux (*cf.* section 7.3).
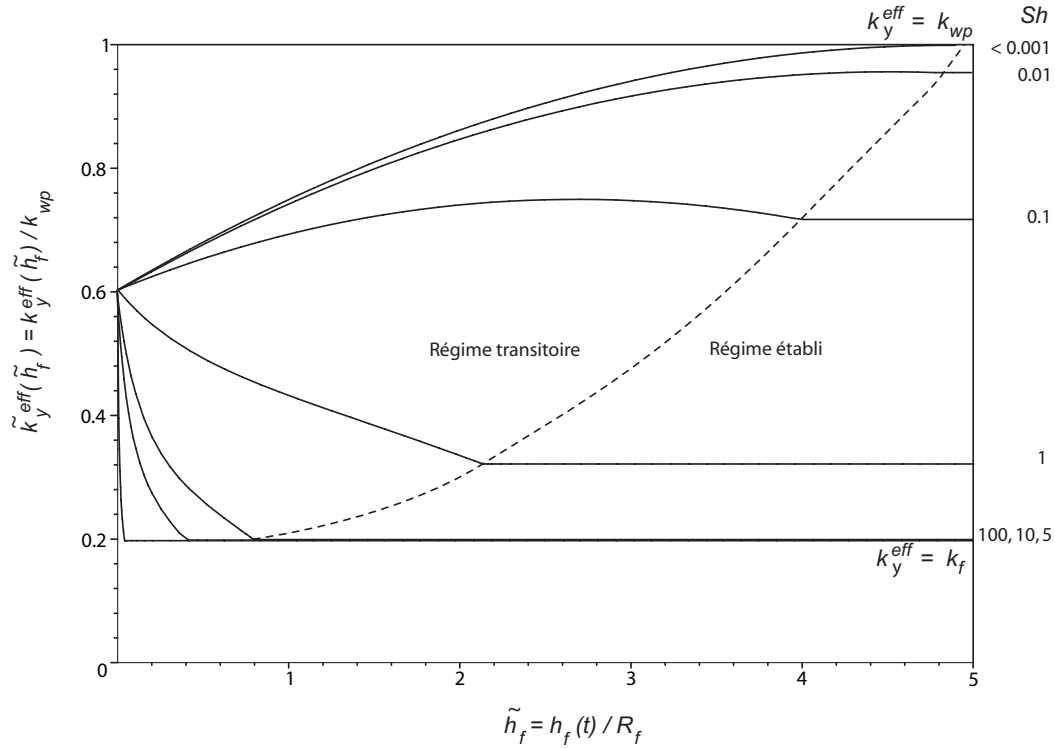
FIG. 2.24 – Réactivité effective normalisée représentée en fonction de la hauteur de fibre ($A = 5$) (*cf.* section 7.3).

cours du temps en régimes mixte et diffusif ($Sh > 0.001$). La réactivité effective du fil évolue également au cours du temps. L'évolution de la réactivité effective normée par la réactivité de la phase faible est présentée en figure 2.24. Au départ (pas de rugosité), cette réactivité est la même pour toutes les conditions. Lorsque la rugosité apparaît, le comportement du composite est modifié. En limitation réactive, on observe un processus de maillon faible : la réactivité évolue vers sa valeur en régime stationnaire, celle de la matrice. En limitation diffusive, l'effet inverse est observé : la fibre protège peu à peu la matrice, jusqu'à ce que la réactivité du fil soit imposée par la fibre. Le comportement du composite dépend fortement des conditions expérimentales auxquelles il est soumis. La prévision théorique de la rugosité est comparée aux observations expérimentales pour un 3D C/C à la figure 2.25. Un bon accord est obtenu sur la modélisation de l'état de surface. La validation de la prédiction de la réactivité effective ne sera possible qu'après le changement d'échelle à l'échelle macroscopique par comparaison à la valeur mesurée expérimentalement sur le composite. Notons cependant qu'une validation à cette échelle serait envisageable à condition de disposer d'un composite unidirectionnel.

| 0.05 | 0.3 | 0.7 | 1 |
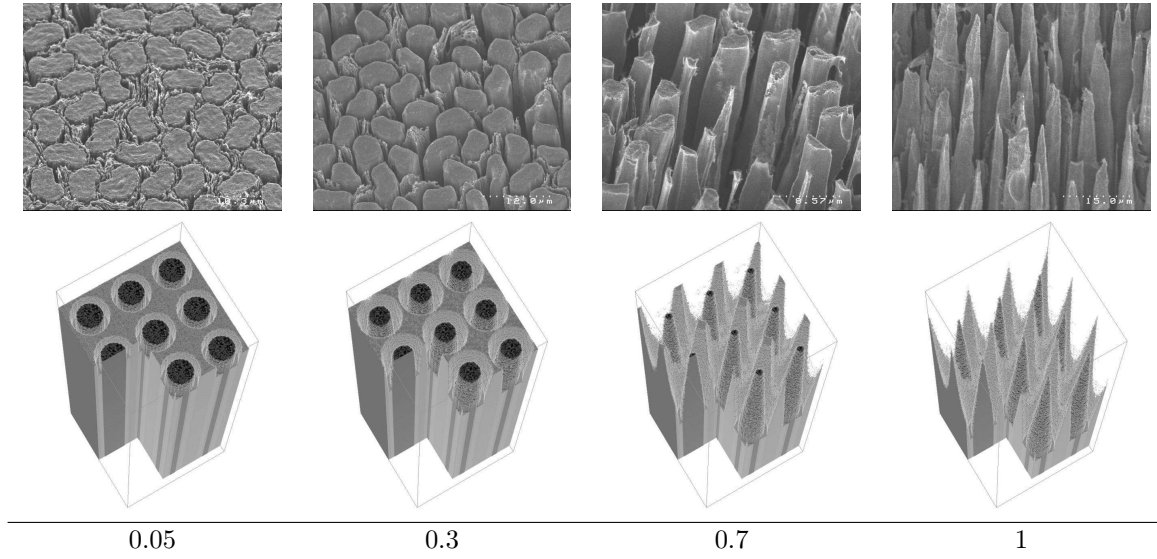
Fig. 2.25 – Comparaison entre observations expérimentales et résultats de simulation numérique en fonction du temps nécessaire pour atteindre le régime permanent ($A = 30$, $Sh < 0.001$) (*cf.* section 7.5).

2.4.4   Echelle macroscopique

L'échelle macroscopique est celle du composite. Il est constitué de fils et de matrice interfil. Le modèle résolu à l'échelle mésoscopique peut être réutilisé, si ce n'est que la section des fils est rectangulaire (carrée pour le 3D C/C). En remplaçant le diamètre des fibres par le côté des fils (l), on a montré que le cas de l'échelle macroscopique était strictement équivalent. Comme représenté sur la figure 2.26, des pyramides sont obtenues à la place des cônes. Les nouveaux nombres adimensionnés A_y (contraste entre phase faible inter-fil (wp-y) et fil) et $Sh_y = lk_{wp-y}/D$ sont cependant différents à cette échelle. En effet, dans le cas général $Sh_y >> Sh$ et $A \neq A_y$; les comportements aux échelles macroscopiques et mésoscopique peuvent donc être différents. En particulier, le régime peut être réactif à l'échelle mésoscopique, mais mixte, voire diffusif, à l'échelle macroscopique. La nature de l'interphase inter-fil (voire figure 2.6-a) ne peut pas être mesurée expérimentalement de façon directe car elle n'est pas disponible indépendamment. Application intéressante du modèle développé, l'analyse de la géométrie de la rugosité permet de monter que A_y vaut environ 8. Les prévisions d'évolution de la rugosité du modèle sont représentées à la figure 2.27. Un bon accord est obtenu avec les observations expérimentales. Le plateau observé sur les fils est dû au fait que le régime permanent n'est pas encore atteint. En effet, d'après le modèle, le régime permanent aurait dû être atteint pour une durée d'essai de 26 heures environ (oxydation, air sec, 625˚C), or l'expérience n'a duré que 17 heures.

En utilisant le modèle, il est possible de prévoir la perte de masse du composite au cours du temps en fonction des réactivités de ses constituants élémentaires. Le cheminement est représenté figure 2.28. Partant de la réactivité des fibres (mesurée expérimentalement), la réactivité de l'interphase intra-fil est déterminée à partir de la géométrie de l'état de surface du fil ($A = 32$), ensuite la réactivité du fil est déduite théoriquement. La réactivité du fil,
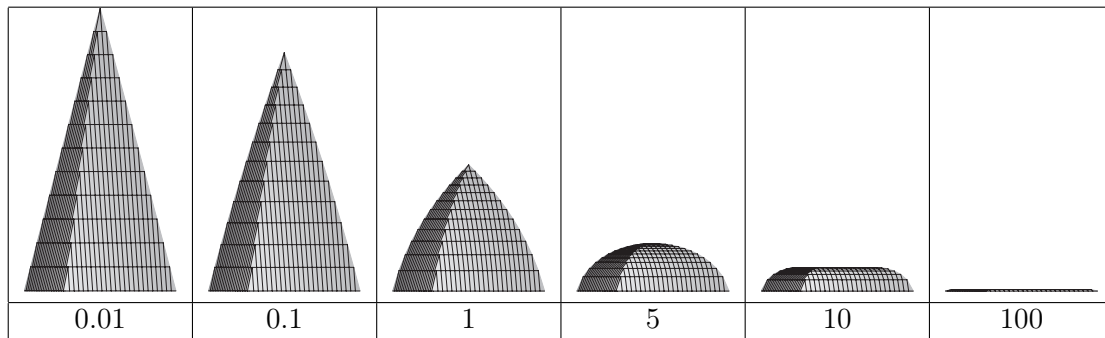
FIG. 2.26 – Morphologie de fils à section carrée en régime stationnaire en fonction de Sh_y (avec $A_y = 5$) (*cf.* section 5.4).

a) Instant initial (MEB)   b) Fin de l'essai (MEB) : régime transitoire   c) Zoom sur un fil (MEB)

Fil parallèle

Octet de matrice

Interphase

Fil perpendiculaire

d) Instant initial : Cellule numérique (AMA)

e) Régime transitoire : Simulation (AMA)

f) Régime transitoire : Modèle analytique
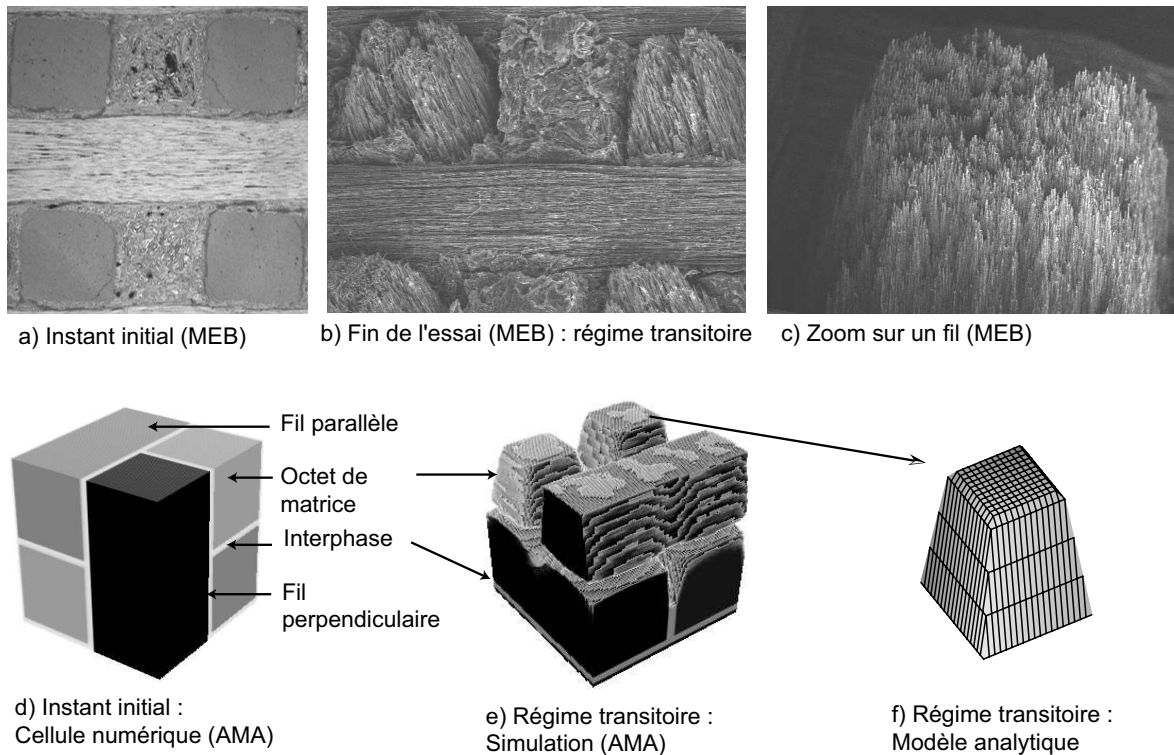
FIG. 2.27 – Comparaison des observations expérimentales et des résultats de simulation numérique à l'échelle macroscopique (*cf.* section 7.5).

associée à l'analyse de la rugosité macroscopique, permet de déterminer la réactivité effective de la phase faible du composite, puis du composite lui-même. La réactivité du composite et sa perte de masse instantanée évoluent au cours du temps. La perte de masse instantanée est intégrée pour obtenir à un instant donné la perte de masse totale d'un échantillon depuis l'instant initial. Le résultat de la prédiction théorique est en excellent accord avec les relevés expérimentaux de perte de masse (voir figure 2.29). L'expérience a été arrêtée au bout de 17 heures car le régime permanent semblait atteint (perte de masse quasi constante) ; le modèle
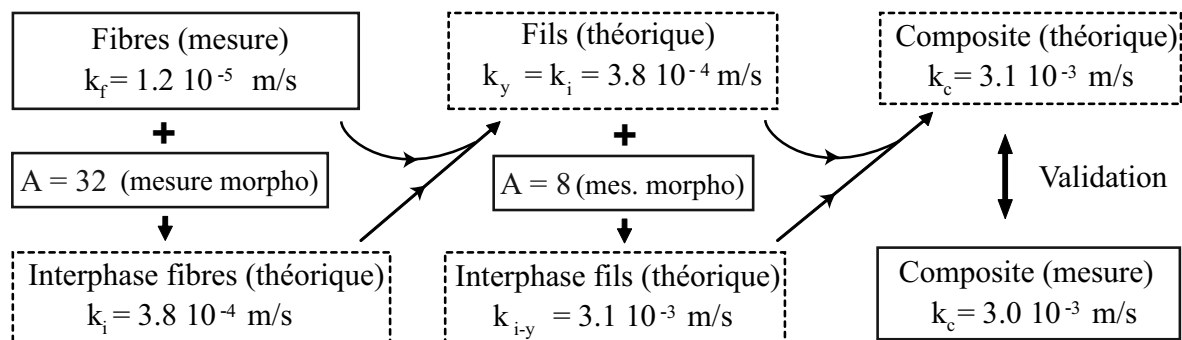
FIG. 2.28 – Schéma de validation multiéchelle (3DCC, air sec, 898 K).
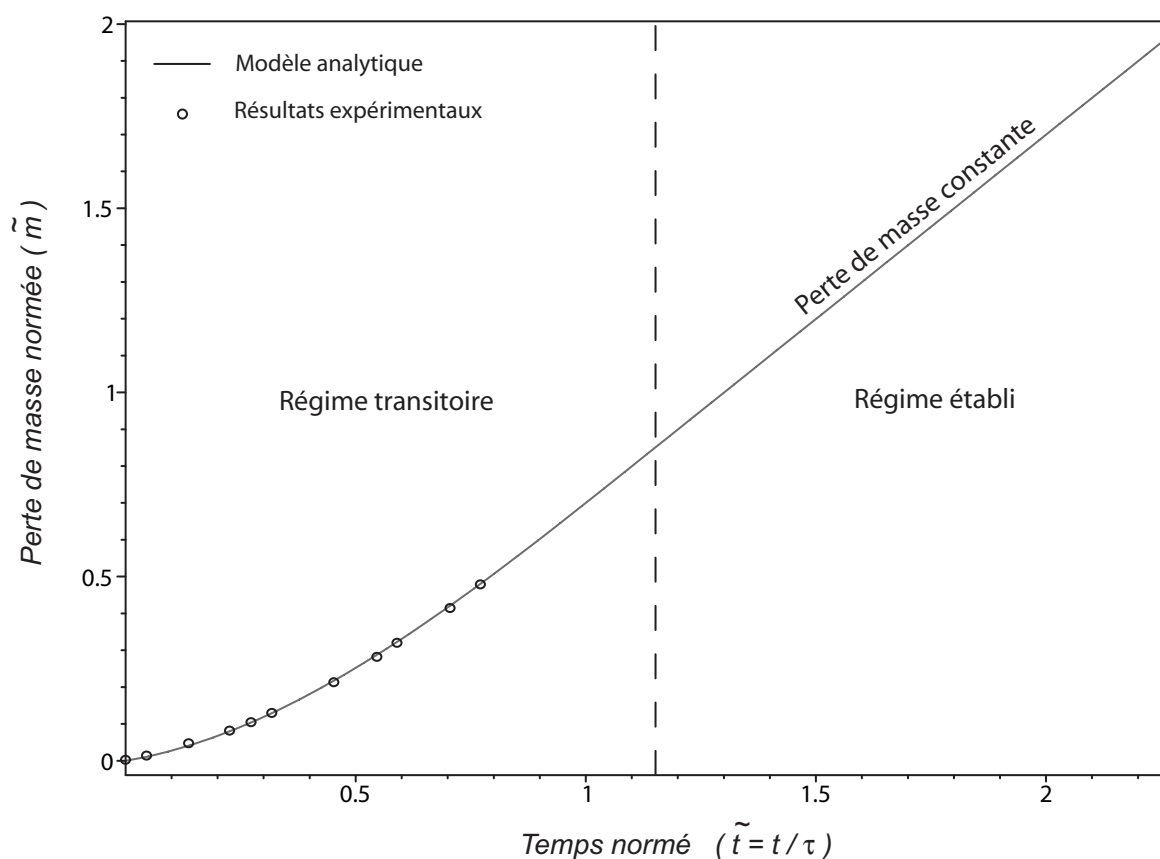
FIG. 2.29 – Comparaison des pertes de masses expérimentales et théoriques (3DCC, air sec, 898 K) (*cf.* section 7.5).

montre bien, en effet, qu'à la fin du régime transitoire la perte de masse est presque constante. Le modèle permet d'extrapoler la réactivité effective du composite et de prévoir sa valeur en régime premanent : elle est de 10% supérieure à la valeur mesurée à la fin de l'expérience.

Le modèle, validé dans le cas de l'ablation par oxydation pour le 3D C/C (synthétisé ici) et le 2D C/R (présenté au chapitre 5), a été appliqué aux essais plasmas. Pour les essais

plasmas, à l'échelle mésoscopique, les résultats obtenus sont cohérents avec les données expérimentales disponibles (*cf.* section 5.5.3) ; à l'échelle macroscopique, le modèle montre que l'érosion thermomécanique intervient de façon couplée aux phénomènes de gazéification (*cf.* section 6.5).

2.5 Bilan de l'approche multiéchelle

Les résultats obtenus sont notamment :
– la compréhension du comportement du matériau en régimes transitoire et établi ;
– la prédiction de l'état de surface à toutes les échelles en fonction des paramètres expérimentaux ;
– la possibilité de retrouver par analyse inverse les propriétés des constituants des composites à partir de l'analyse de la rugosité ;
– la prédiction de la perte de masse d'un matériau dans des conditions données à partir des réactivités géométriques intrinsèques de ses constituants.

Les modèles ont été validés par comparaison à des résultats d'essais d'oxydation et ont été appliqués avec succès à l'analyse d'essais plasmas.

Trois axes de valorisation des modèles sont envisagés :
– amélioration des critères de conception, notamment lorsqu'une extrapolation s'avère nécessaire, par l'utilisation de modèles phénoménologiques du comportement des matériaux ;
– choix optimal des matériaux pour une application donnée en fonction de leur comportement attendu ;
– idées directrices pour l'amélioration des composites en fonction du domaine d'utilisation, via le renforcement du constituant faible (les interphases en régime réactif, c'est-à-dire à température modéré ; les fibres en régime diffusif, soit à haute température).

N.B. : La conclusion générale et les perspectives de ce travail sont présentées en français à la page 153.

3 Multi-scale analysis of surface roughness

Préambule

Ce chapitre constitue un projet de publication soumis à la revue *Carbon*.

Titre : Physico-chemical ablation of carbon-carbon composites : I-Multi-scale analysis of surface roughness.

Auteurs : J. Lachaud[1], G. L. Vignoles[1], J.-M. Goyhénèche[2] et J.-F. Epherre[1,2]

Affiliations :

[1]Laboratoire des Composites ThermoStructuraux (LCTS)

UMR 5801 : CNRS-SAFRAN-CEA-UB1

Domaine Universitaire de Bordeaux – 3, Allée de La Boétie, 33600 Pessac, France

[2]CEA-CESTA, 33114 Le Barp, France

Résumé

Ce travail est la première partie d'une série de cinq articles dont l'objectif est d'expliquer et de modéliser le comportement des composites carbone-carbone (C/C) durant l'ablation. Des bases expérimentales et une stratégie pour la modélisation du comportement ablatif de deux composites C/C (un 3D C/C et un 2D C/résine phénolique pyrolysé) y sont proposées. Deux tests d'ablation sont utilisés : un jet plasma et un réacteur d'oxydation. La morphologie de l'état de surface (rugosité), qui est utilisée comme guide pour la modélisation, est observée, analysée et classée. Cette analyse montre que ces matériaux ont des comportement similaires et fortement corrélés à leur architecture. Une statégie de modélisation qui prend en compte ces observations et les interactions matériau/environnement est proposée. Elle repose sur deux changements d'échelle :(i) échelle microscopique (fibre, matrice intra-fil) vers échelle mésoscopique (fil) et (ii) échelle mésoscopique (fil, matrice inter-fil) vers échelle macroscopique (composite homogénéisé). Les données d'entrée des modèles sont les propriétés des composants élémentaires du composite et la géométrie de la rugosité. Les résultats attendus sont des prédictions : (i) de l'évolution de la rugosité, (ii) du comportement multiéchelle des composites C/C en fonction des conditions expérimentales et des propriétés du matériau.

Abstract

This work is the first part of a paper series which aims to explain and model the complex behavior of carbon-carbon (C/C) composites during ablation. It settles some experimental bases and a strategy for the modeling. Two C/C composites (a 3-D C/C and a pyrolyzed 2-D C/phenolic resin), ablated using two different ablation tests (plasma-jet test, oxidation reactor), are studied. The surface roughness morphology, which is used as a guide for the modeling of the material behavior, is observed, analyzed and classified. The study of surface roughness shows that these materials display similar multi-scale behaviors closely linked to their architectures. A modeling strategy, taking into account these observations and the material/environment interaction, is proposed. It features two changes of scale : (i) microscopic

scale (fiber, intra-bundle matrix) to mesoscopic scale (yarn) and (ii) mesoscopic scale (yarn, inter-yarn matrix) to macroscopic scale (composite). The inputs of the models are the properties of the composites components, and their 3-D multi-scale architectures. The expected outputs of the models are : (i) the evolution of the surface roughness, (ii) the complex multi-scale behavior of the C/C composites as a function of experimental conditions and material properties.

3.1 Introduction

Carbon/Carbon (C/C) composites, which keep excellent mechanical properties at high temperatures [38], are used as thermostructural protections in various applications such as atmospheric re-entry (vehicle thermal protection systems) [22, 31, 32], propulsion (rocket nozzle) [10, 11, 57], and experimental Tokamak reactors for nuclear fusion (divertor and first wall armor) [13, 79, 103]. In these applications, the C/C composites are progressively destroyed by oxidation (re-entry and propulsion), sublimation (re-entry and Tokamaks), and, up to a certain extent, plasma etching (Tokamaks), and thermo-mechanical erosion (all the cases). These degradation processes, resulting in a high interfacial mass transfer, induce a non negligible recession of the wall. They are collected in the generic term of *ablation*. Nevertheless, ablation, which is usually globally endothermic, is partially beneficial as it reduces the wall temperature and the heat flux that penetrates the internal structure.

An efficient design of a thermostructural protection relies on an accurate evaluation of the wall recession caused by ablation. General phenomenological tendencies are now well explained and simulated in the bulk fluid phase for re-entry [55] and propulsion [11], and in the plasma for Tokamaks [106]. However, the complex behavior of C/C composites is not fully understood, and consequently not taken accurately into account in the models. Due to the progress of the computational hardware and software, which enables to handle richer models, the demand of an accurate description and modeling of the material behavior has increased, especially as far as surface roughness is concerned [22, 31]. Indeed, ablation of C/C composites is known to lead, among others, to a typical surface roughness. The surface roughening, which is inseparable from material behavior, influences strongly other phenomena. First, it increases the active surface of the wall ; this induces an enhancement of heat and mass transfer at the interface [43, 51]. Second, the onset of the surface roughness leads to a complex composite behavior : the effective ablation rate of the composite can not be modeled using a simple arithmetic average of the ablation rates of its components [68]. Third, for re-entry and propulsion, it can trigger mechanical erosion, since a high speed flow surrounds the protection. Fourth, in the case of re-entry, it contributes to the laminar-to-turbulent transition in the dynamic boundary layer. PANT (Passive Nosetip Technology) program results show that the heat flux may be multiplied by a factor of up to three in turbulent regime [104].

Therefore, the understanding of the interaction between the material and its close environment has to be improved for all of these applications. The lack of knowledge is balanced by many data from plasma-jet experiments, which provide the composite behavior in the tested conditions. Experimental results are then used as input data for the global scale simulations [22, 31]. Using this method, extrapolation is of poor reliability.

To improve the extrapolation, some interpretations of the onset of surface roughness caused by a thermo-mechanical ablation, and an accurate modeling of the behavior of the materials, have been recently proposed [26, 79]. In a complementary way, this work focuses chiefly on

physico-chemical ablation, *i. e.* induced by gasification processes (oxidation, sublimation). Due to the efficient architecture of the composites, in the experiments carried out for this study, the thermo-mechanical erosion is shown to be a second-order phenomenon. It appears only in a high speed flow, when the shear stress of the flow is large enough to root out fibers or matrix pieces, which have been partially lain bare by a gasification process. Nevertheless, mechanical erosion is not ignored, but commented when observed, that is, sporadically.

Hence, this work aims to analyze and model the complex behavior of carbon-carbon composites during physico-chemical ablation, the focus being definitely set on the material, and especially on the typical surface roughness that develops on the wall. It is presented in a series titled *Physico-chemical ablation of carbon-carbon composites* and features five parts :

I- Multi-scale analysis of surface roughness,

II- Experimental evaluation of intrinsic reactivities [62],

III- Multi-scale analytical modeling in steady state [63],

IV- 3D numerical modeling of actual architectures in steady state [64],

V- Analytical and 3D numerical modeling in transient regime [65].

The first part of this work aims to setup the experimental bases and a modeling strategy. Let us introduce this part.

The surface roughness of C/C composites has been first studied in the sixties to address the laminar-to-turbulent transition induced by surface roughness on the nosetip of re-entry vehicles. The data available on surface roughness in these works are statistical values which are mainly of interest for a transition criterion [6]. The transition is determined using a criterion based on PANT experiments, while the actual surface roughness is ignored [31]. By the way, it should be noticed that the knowledge of the evolution of surface roughness as a function of ablation duration could help improving the transition criterion. Since the nineties, many works [3, 17, 18, 38, 48, 52, 58, 72, 77–79, 90] have reported observations of surface morphology of various carbon-based materials under several ablation conditions. Most of them have directly focused on the micrometer-scale morphologies. Among them, it is important to notice the work of D. Cho et al. [17] who qualitatively described SEM micrographs of micro-metric roughness features of fiber/phenolic composite ablated by an oxyacetylene torch. Carbon fibers are shown to change into icicle or needle shapes during ablation. This phenomenon, illustrated on several micrographs published in the literature, will be addressed, discussed, and compared to the experimental results of this study. Nevertheless, surface roughness also appears at larger and smaller scales, which are not clearly addressed in the former studies. They are analyzed in this work to enable multi-scale modeling.

This article is divided in four sections. First, the architecture and the structure of the two C/C composites of the study are presented in regard to their ablative properties. Second, the two ablation tests of the study are presented : (i) a traditional plasma-jet test, for which modeling difficulties are pointed out ; (ii) an original ablation test, especially designed for this study, which provides favorable experimental conditions for an accurate modeling. Third, the morphologies of the roughness features of both C/C composites submitted to both tests are analyzed and compared. A common multi-scale classification of those features is proposed. Finally, a multi-scale strategy for the modeling of material behavior is proposed.

3.2   Materials description

The two materials of this study are a 3D C/C composite and a pyrolyzed 2D carbon/phenolic resin (C/R) composite. First, their fabrication processes and their architectures are described. Then, the ablative properties of these two carbon-based materials are discussed.

3.2.1   Architecture and elaboration of the studied C/C composites

The two studied materials are representative of the two most common classes of carbon-based composites used for ablative applications :

1. A 3D C/C composite, made from a 3-D preform of ex-PAN carbon fibers and a matrix of pitch-based carbon. It is a heterogeneous multi-scale material. Several thousands of fibers are linked together with a pitch-based matrix into a unidirectional yarn, often named bundle of fibers. Then, fiber bundles are orthogonally fit together into a unit pattern repeated by translation on a cubic lattice. This macrostructure leads to a network of parallelepipedic macropores (located near each node of the lattice), which are partially filled with pitch-based matrix. These macro-pores are named octets. The composite has then been graphitized. This class of C/C is used in tokamak divertors [13], in re-entry vehicles as thermal shield [31], and in the throat of rocket nozzles [11].

2. A carbon/phenolic resin composite (C/R) made from ex-cellulose carbon fibers grouped in yarns, which are themselves woven in satin plies ; the plies are then stacked together and impregnated with phenolic resin. Under typical ablation conditions, the phenolic resin is not any more present as such, but has suffered pyrolysis and is transformed into a highly porous carbon with an approximate density of $0.7\,g.cm^{-3}$. The C/R composite is then converted into a C/C composite before ablation occurs [23]. Its physico-chemical properties are lower than for the 3D C/C. For spatial applications, the main interests of this ablative material are a strong outgassing of pyrolysis gases which cools down the surface, a poor thermal conductivity and its low density [23]. Its ease of use is also a critical criterion in its choice for the manufacture of thermal protection systems [31] and divergent of rocket thrusters [11].

The architectures of these two composites can be divided into three scales : (i) microstructure (fibers), (ii) mesostructure (yarns : bundles of fibers which are linked together with an intra-yarn matrix), and (iii) macrostructure (composite pattern : yarns linked together with an inter-yarn matrix). In the following, fibers which are parallel (resp. perpendicular) to the average surface are simply named parallel (resp. perpendicular) fibers.

3.2.2   Carbon structure of C/C composites and their ablative properties

The components of ablative carbon-based materials are made of various kinds of turbostratic carbons [102], which differ from graphite by a less organized and extended crystalline structure [12]. At atomic scale, this difference arises from a lack of pure sp^2 carbon atoms, as compared to graphite ; this fact might be explained by the presence of sp^3-like defects [95] and 5 or 7 membered rings [99]. Such defects tend to disorientate graphene planes inside graphene layers, which can be slightly curved [95] or exhibit an inter-plane average length up to ten percent larger than for graphite [84]. The change of inter-plane average distance (X-ray diffraction measurement of d_{002}) reduces the local density. d_{002} generally decreases with graphitization degree [76]. The extension of graphene planes and the size of graphene

stacks increase with graphitization degree [12, 76]. Consequently, the local density increases with graphitization degree [84]. The way the graphene stacks are connected together has also a strong effect on density, as it can lead to a more or less optimized space occupation. Then, the size of the representative elementary volume for the global density evaluation is at least ten times the size of individual graphene stacks.

The gasification rates (oxidation or sublimation) of the graphene planes increase with plane perimeter to plane surface ratio [28]. Indeed, the reactivity of the edges, whose atomic conformations constitute active sites [50], is three orders of magnitude higher than the reactivity of the plane surface [49], which contains few defects and then few active sites. Thus, the gasification resistance of turbostratic carbons is strengthened with the graphitization rate [38], as graphitization tends to expand the graphene planes. Consequently, the gasification rate of turbostratic carbons generally decreases as local density increases [24]. An interpretation of the graphene plane reactivity followed by a multi-scale modeling of poly-crystalline graphite has produced results in qualitative agreement with the experimental observations [60].

Switching to composite scale, the local recession velocity of the surface depends on the local gasification rate discussed above. It leads to the onset of surface roughness on composite materials, which are heterogeneous materials made of several kinds of turbostratic carbons, since fibers and matrices have different origins and structures. This phenomenon can be balanced by a mass transfer limitation in the fluid phase [51]. The competition between mass transfer and heterogeneous reactions explains a large part of the roughness features observed on the material surface. These phenomena constitute the basis of the models exposed in the modeling strategy (section 3.5).

3.3 Actual ablation environments versus laboratory tests

Both composites have been ablated using two complementary tests : a traditional plasma-jet test, and an original oxidation test. Materials ablated with the plasma jet test (resp. oxidation reactor test) are referred to as C/C-plasma and C/R-plasma (resp. C/C-oxi and C/R-oxi). To clearly establish the context and the scope of the study, the actual ablation environments are briefly described first, then the two tests are presented.

3.3.1 Examples of actual ablation environments

In the case of propulsion, ablation is chiefly caused by oxidation of the composite by the products of solid propergol combustion (H_2O, CO_2) at approximatively $2000\,K$ [11]. A non negligible amount of alumina particles are also projected among these products, but it has been proved that they do not erode the material [11].

For Tokamak reactors, ablation mainly occurs by sublimation during the plasma disruptions which generate sudden high fluxes of fast electrons on the material ; its temperature abruptly switches from about $1200\,K$ to more than $3000\,K$ [13]. Ionic etching [105] and thermo-mechanical erosion [79, 106] can also occur ; these latter causes of ablation, which have already been analyzed and modeled [79, 105, 106], are not addressed in this work.

During re-entry (on earth), the vehicle speed reaches many km/s in the dense atmosphere ; the resulting flow close to the nosetip is then hypersonic. In this case a thin bow shock surrounds an inviscid flow (eulerian flow), while a dynamic boundary layer develops in the vicinity of the wall [22]. It has been shown [22, 32] that temperature of the flow may reach

$7000\,K$ and it may lead to a maximal wall temperature of $4500\,K$ for pressures higher than $100\,bar$.

3.3.2   Plasma-jet and related tests

Plasma-jet tests are commonly used to qualify the materials of the three applications described above. The plasma properties are then adapted to the requirements of the involved application. Micrographs of samples submitted to tests simulating propulsion [3,11], Tokamaks [13,79], and re-entry [31,32] environments are available in the literature ; they will be referred to in section 3.4. Note that in the case of propulsion, the ablative materials are often tested behind a nozzle, the conditions are then close to the real ones [11]. The plasma test of this study reproduces conditions close to atmospheric re-entry [22].

The 3D C/C has been tested in stagnation point configuration under a high thermal flux of air-plasma ($50\,MW.m^{-2}$) at $Mach\,4$. It approximatively leads to a wall temperature of $4000\,K$ and a pressure at the stagnation point of $5\,MPa$. Under these conditions, the composite is mainly ablated by sublimation, but oxidation also occurs [31]. Mechanical erosion sporadically occurs, but it is shown to be negligible [31]. The recession velocity of the material surface is about $1\,mm/s$.

The C/R is tested in plane flow configuration, and pyrolyzed *in situ*. It leads to a blowing of pyrolysis gases which tends to cool down the sample surface [23]. The mass loss caused by pyrolysis is around 18% of the initial mass. The exhaust flow of pyrolysis gases is then about 22% of the total mass flow lost by ablation. In these conditions, the wall temperature reaches $3000\,K$. The recession velocity of the material surface is around $0.5\,mm/s$.

3.3.3   Oxidation reactor

An unconventional ablation test has been designed to blend five main requirements for the first steps into the modeling of surface roughness evolution : (i) isothermal conditions on the sample, (ii) laminar flow on the sample, (iii) negligible advection close to the wall (no mechanical erosion), (iv) sample size much larger than composite unit pattern size, (v) test leading to typical roughness features obtained by ablation.

The reactor, which is fully described elsewhere [62], is cylindrical and heated by electrical resistances. Samples of both materials are reduced to a $1\,cm^2$ square surface incorporated in the reactor. It should be noticed that for this ablation test, the C/R is fully pyrolyzed at $1473\,K$ under vacuum before the experiment. First, this enables the study of its C/C form which is of interest for ablation ; also, it prevents outgassing effects that can thus be decoupled from pure ablation [31,93].

Experiments are carried out at a controlled temperature of $898\,K$ under dry air at atmospheric pressure. For lower temperatures, the experiments would last weeks before the steady state could be reached. For temperatures higher than $973\,K$, Boudouard equilibrium would introduce a homogeneous reaction [8], which would increase the complexity of the modeling to no purpose. The retained conditions induce a heterogeneous oxidation process [15] ($C_{(s)} + O_2 \rightleftharpoons CO_2$) that leads to a significant ablation velocity.

At this temperature, oxidation is exothermal ; its reaction enthalpy is $-394\,kJ.mol^{-1}$ [15]. The molar impinging flux of oxygen per surface unit J is lower than $0.1\,mol.m^{-2}.s^{-1}$ for the C/C composites of this study. The induced thermal flux is then of $55\,kW.m^{-2}$. Knowing a lower limit of the thermal conductivity of the composite at this temperature ($\geq 40\,W.m^{-1}.K^{-1}$ [38,

84]), Fourier's law gives a thermal gradient lower than $1\,K/mm$, which is then negligible [66]. Moreover, convection on the sample and radiation are also factors for thermal homogenization in the reactor and sample cooling. Consequently, the sample can be considered isothermal. Experimental measurements of the temperature in the reactor and on the sample have been carried using thermocouples ; they are in agreement with this evaluation.

The fluid velocity is $1\,m.s^{-1}$. This value is a compromise chosen to ensure both laminar flow conditions and a high enough oxygen injection flow.

Concerning the three last points of the reactor requirements, they are also well respected as shown in the following section. As a conclusion, the oxidation reactor satisfies well the required conditions.

3.4 Analysis and multi-scale classification of surface roughness features

Surface roughness is analyzed using four complementary techniques : binocular magnifier (BM), optical microscope (OM), scanning electron microscopy (SEM), and Synchrotron X-ray computed micro-tomography (SXMT). Three scales of surface roughness have been identified : macroscale, mesoscale, and microscale. They are strongly linked to the material architecture described in section 3.2. Indeed, at each scale of the composite architecture, a typical surface roughness develops.

In the references of the photographs of the figures presented in this work, the following notations or subscripts are used : M : macro, m : meso, and μ : micro. Let a nomenclature, useful for the description of roughness features, be introduced. At each scale, roughness features will be referred to as epi-*scale*-structural, *i.e.* situated on (*epi* is Greek for on) the structural element whose scale is *scale*.

To set the emphasis on several strong similarities, it has been chosen to sketch and describe simultaneously the surface roughness of 3D C/C and pyrolyzed 2D C/R samples, from the macroscopic to the microscopic scale. A synthesis tabular including sketches of multi-scale surface roughness situated on the preform is presented on figure 3.1. It is commented in this section.

3.4.1 Macroscopic scale : epi-macro-structural roughness features

3.4.1.1 3D C/C composite

As expected, the two ablated samples (C/C-plasma and C/C-oxi) show comparable surface states. The description is given for C/C-plasma. Then the slight differences of C/C-oxi are pointed out.

Basically, ablation reveals the architecture of the composite. Epi-macro-structural surface roughness seems to result from the difference of reactivity between parallel bundles, perpendicular bundles and inter-bundle matrix (cited by increasing order of reactivity). The recession of the most reactive phase is the fastest until a steady situation settles. As represented on the micrograph M_1 of figure 3.2, octets are more reactive, hence they recess faster, creating crenelation features. The section of emerging bundles (parallel or perpendicular) is slightly undulating. Indeed, if edges of initially square section of bundles are emerging, they are smoothed out to a wavy form by ablation. On the C/C-plasma slice (OM) of figure 3.2-M_2, this phenomenon is obvious. From left to right : the tip of a perpendicular bundle is concave ;

Material	fiber	yarn	architecture
Roughness	epi**micro**structural	epi**meso**structural	epi**macro**structural
3D C/C	(f) (g)	(d)	(a)
2D C/R	(h) (i)	(e)	(b) (c)
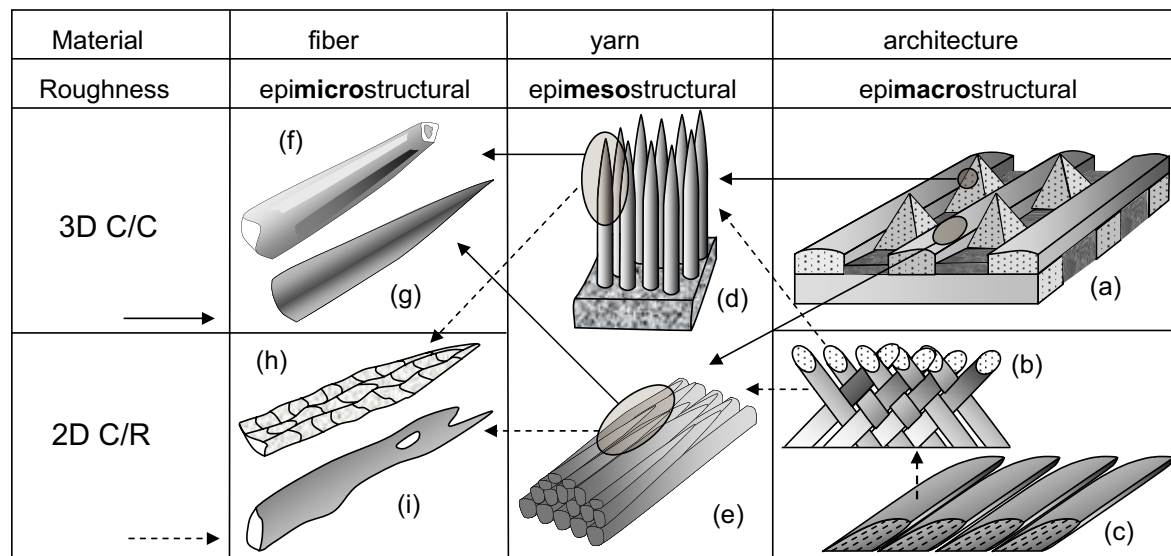
FIG. 3.1 – 3D multi-scale roughness on ablated composite materials : synthesis tabular.

next, the parallel bundle section is convex ; then appears another concave tip of a perpendicular bundle. Between the bundles, a deep crack results from the preferential ablation of the inter-bundle matrix. It is difficult to exonerate thermo-mechanical erosion to explain these cracks. The surface looks inclined on the slice, mainly because the sample is conical. Under the parallel bundle, a pitch-based matrix octet features the edge of a residual macro-pore. This kind of macro-pores lies in the middle of all the octets and is roughly spherical. Mechanical erosion sporadically occurs through the detachment of a matrix octet or of some fibers emerging from parallel bundles.

In the oxidation reactor, mechanical erosion can not occur. Ablation is then only driven by the gasification process. The most reactive phases progressively uncover the least reactive phases, which increase their exposed surface area [67]. In these conditions, as shown on micrograph M of figure 3.3, the perpendicular bundles look like truncated pyramids : their tips display a plateau. The height of the truncated pyramids is approximatively equal to the square section edge size.

3.4.1.2   2D C/R composite

The C/R sample orientations were different in the two tests. For the C/R-oxi sample, the tissue ply and the weaving inside the ply have been placed perpendicular to the surface to facilitate ablation analysis and modeling (see figure 3.5-M). In the C/R-plasma sample, the tissue ply are inclined of 30 degrees to withstand the shear stress of the high speed flow with a minimal mechanical erosion. Yarn weaving inside the tissue is inclined by 45° with the surface of the sample. This configuration is sketched in figures 3.1 b and c.

3.4.1.2.1   C/R-plasma

The photograph M_1 of figure 3.4 shows a surface characteristic of this material. The surface features look like saw-teeth spaced out by one ply thickness (see also figure 3.1-c). This morphology is caused by the preferential ablation of the thin layer of inter-ply matrix.
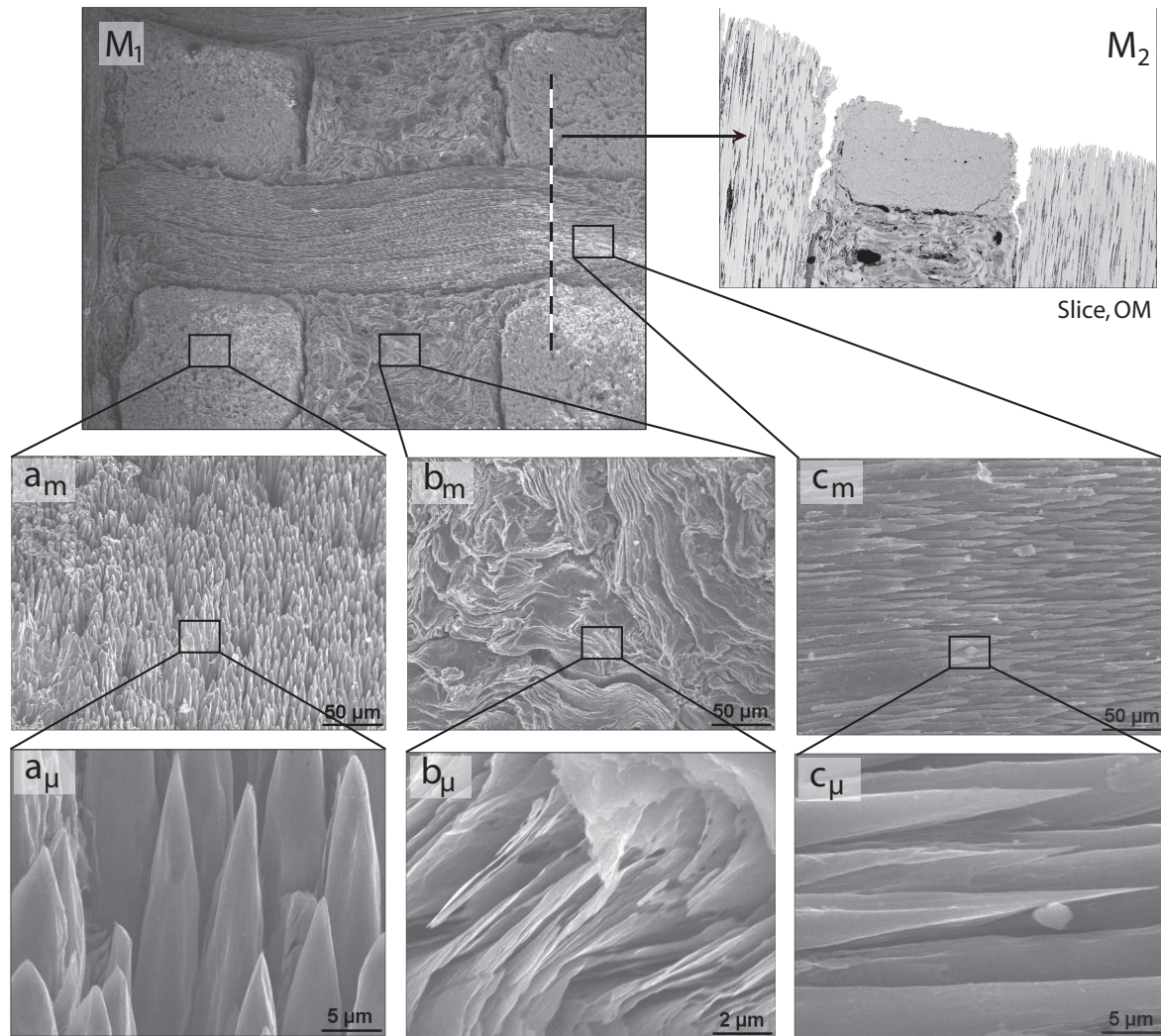
FIG. 3.2 – SEM micrographs of 3D C/C surface after plasma jet ablation

Nevertheless, in some places, the inter-yarn matrix (inside the plies) appears protected by the yarns (zone b) of figure 3.4. Ablation uncovers the yarns, which emerge slanted with respect to the surface (see micrograph M_2 of figure 3.4). The smoothing, induced by advection and/or diffusion limitation, creates a wavy surface state (see figures 3.1 b and c). The amplitude of the waves is close to the inter-ply matrix thickness, while their wave length is equal to yarns section. Some chain yarns sporadically emerge, perpendicularly to the wavy surface (see zone c of figure 3.4).

3.4.1.2.2   C/R-oxi

At this scale, the surface roughness of the sample is quite different from C/R-plasma. Perpendicular yarns, which seem less reactive than parallel yarns, emerge by about $400\,\mu m$ from the surface level of parallel yarns (see micrograph M of figure 3.5). Inter-ply and inter-yarn matrices have been deeply ablated.

As a conclusion, at macroscopic scale, ablation phenomenon uncovers the material struc-
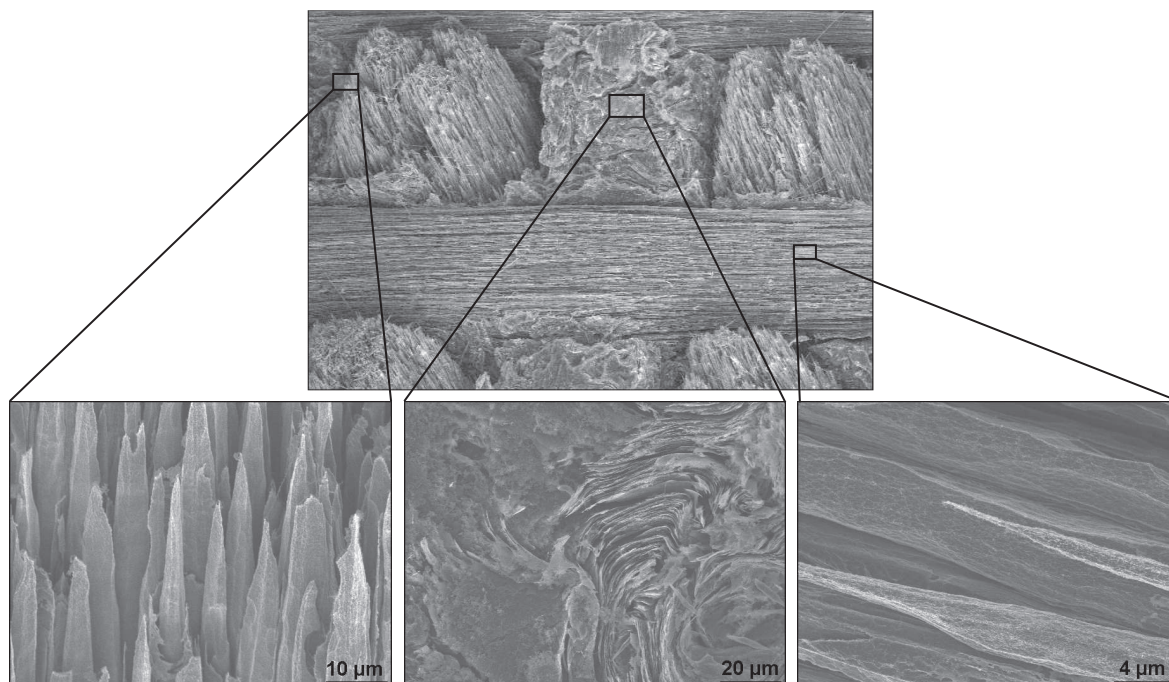
FIG. 3.3 – SEM micrographs of 3D C/C surface after oxidation in a reactor

ture through the onset of surface roughness. Geometrical features follow the material structure. Then, let it be called structural surface roughness to make a difference with a purely physical roughness which is observed at micro-scale (see subsection 3.4.3).

3.4.2 Mesoscopic scale : epimesostructural roughness features

At mesoscopic scale, a structural surface roughness also takes place on the material. For all the samples, three characteristic common features are observed on three supports : (i) perpendicular yarns, (ii) parallel yarns, (iii) inter-yarn matrix.

3.4.2.1 Perpendicular yarns : "needle clusters"

The typical surface roughness taking place on perpendicular fibers is quoted in a large number of past studies. A wide variety of samples are observed in these works : several C/R and C/C composites have been ablated by different ground tests leading either to oxidation [3, 17, 34, 52, 58, 72, 90] or both to oxidation and sublimation [18, 48, 71, 77–79]. In such a diversity, the similarities are remarkable. Thus, this subsection aims to analyze and compare the roughness features of the four samples of this work under the light of previous literature descriptions.

3.4.2.1.1 Previous observations reported in the literature

Inside a yarn, made of compacted parallel fibers linked together by matrix, one phase is always found to be less resistant to ablation than others. Three cases of weak phases have been reported in the literature : the intra-yarn matrix for C/R composites [17, 18, 77, 78], the
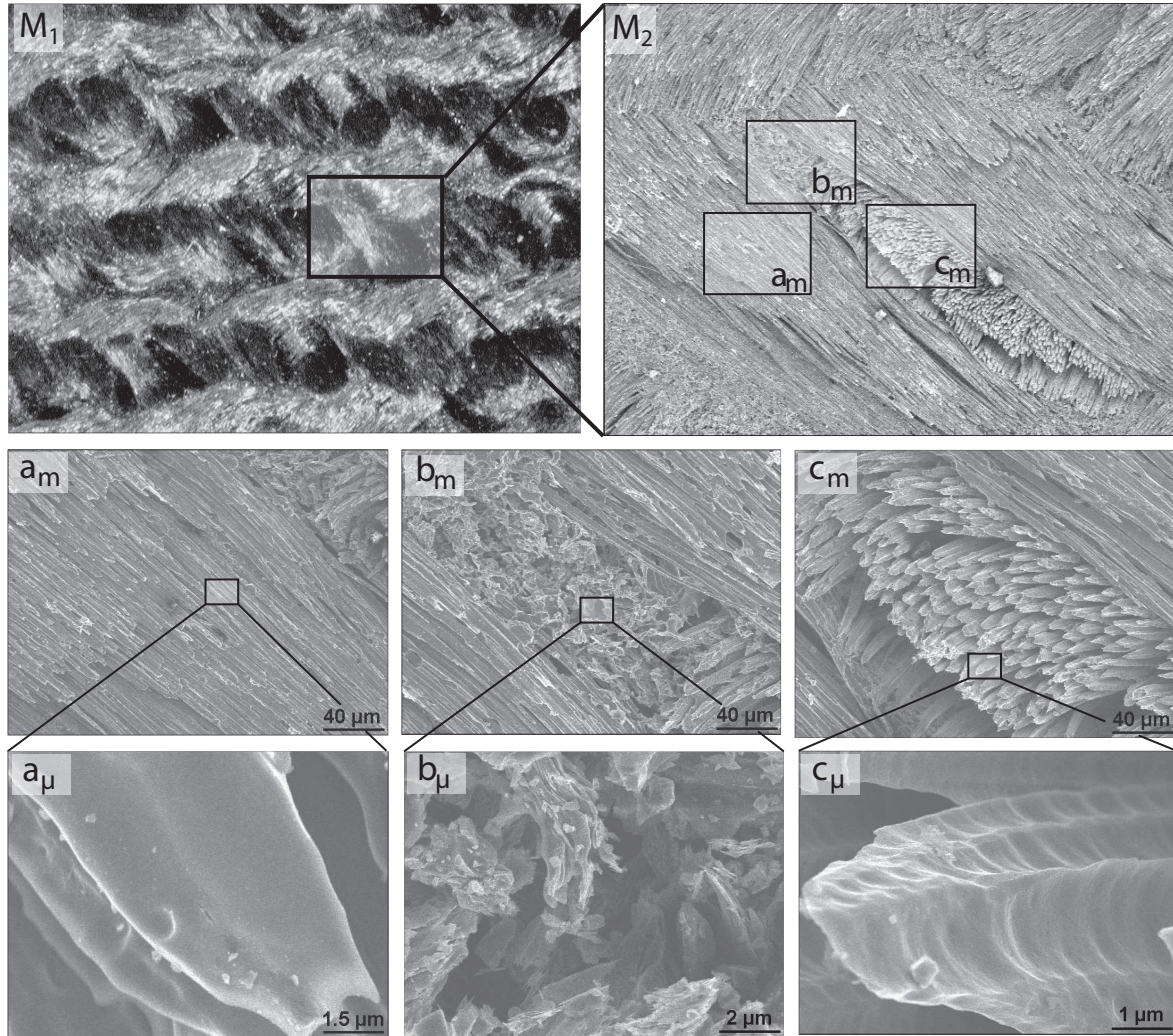
FIG. 3.4 – Micrographs of 2D C/R surface after plasma jet ablation (Top left photograph : BM, others : SEM)

interphase lying between the fibers and the matrix [3, 34, 52, 58, 79, 90] or the fibers surface itself [48, 71] for C/C composites. Due to an important recession of this weak phase, the fibers (or fiber cores), which are more resistant, are partially stripped, become thinner, and acquire a needle shape. This illustrates well the close link existing between composites behavior and the onset of surface roughness. The resulting morphology in steady state is sketched in the case of a weak matrix on figure 3.1 d and e, and in the case of a weak interphase on the schemes b and e of figure 3.9.

3.4.2.1.2 Qualitative analysis of the samples

This phenomenon is well observed on the four samples of this work. The respective behaviors of C/R and C/C composites are also in agreement with previous observations. On figures 3.2-a_m and 3.3-a_μ, the micrographs show clusters of emerging sharp fiber tips. For 3D C/C, the results of short oxidation tests supports the idea that the weakest phase is an
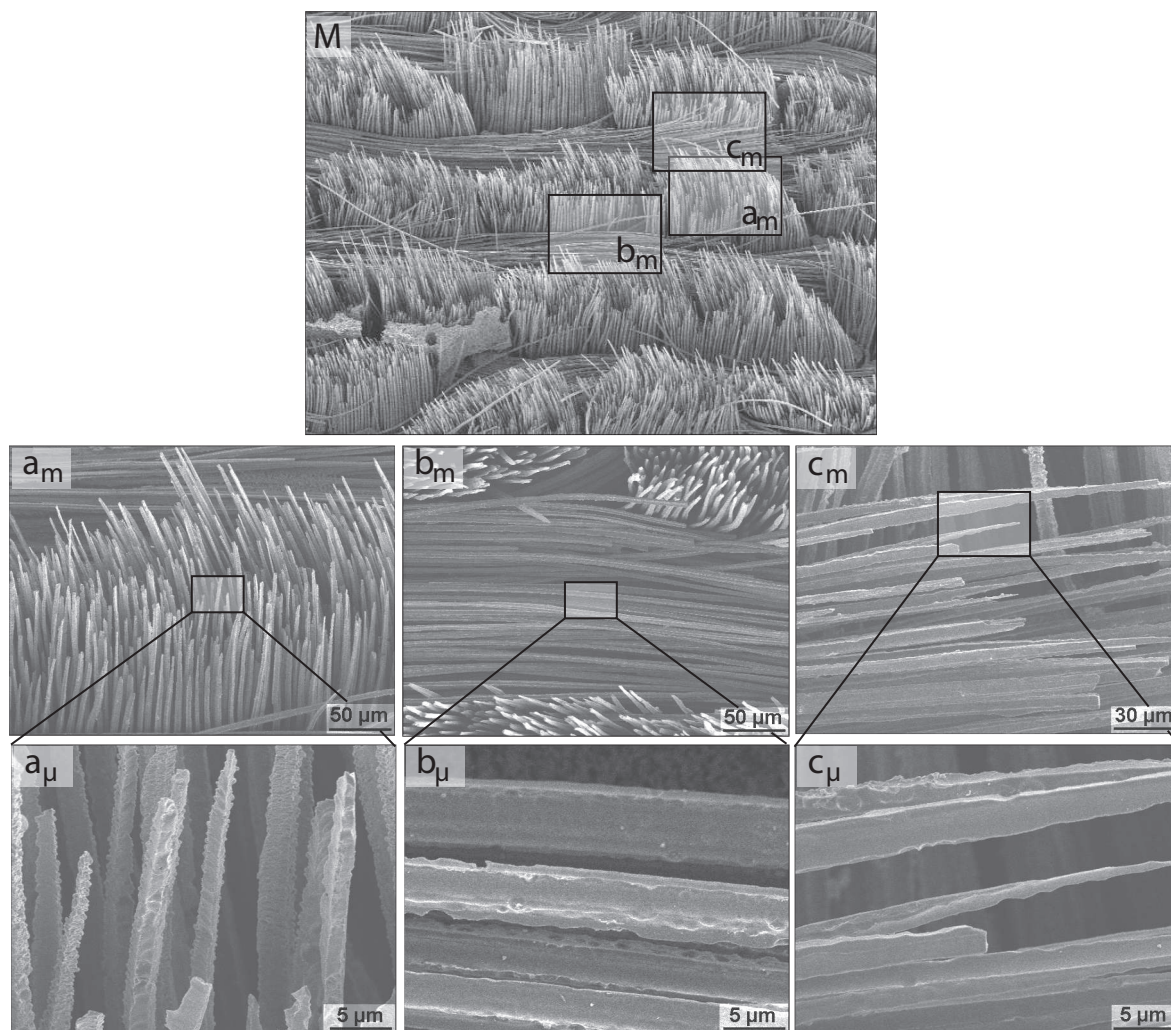
Fig. 3.5 – SEM micrographs of 2D C/R surface after oxidation in a reactor

interphase lying between the fiber and the matrix (see figure 3.6-a). The interphase, which is about $0.5\,\mu m$ thick, is obviously ablated first. Its cohesion to carbon fibers has been shown to be excellent by TEM analysis both for pitch-based matrices [33] and pyrolytic matrices [58]. As the fiber surface is rough, the graphene stacks cannot grow and stretch close to the surface as well as in the bulk matrix phase. It leads to the formation of a less organized turbostratic carbon near the fibers [33, 58], which, considering the remarks of subsection 3.2.2, is less resistant to ablation. To improve the interphase strength to oxidation it has been put forward that porous fibers may be used [81].

For 3D C/C, at steady state, due to the higher recession rate of interphase, only fibers and residual intra-bundle matrix are found at the surface. On figure 3.3-a_μ, the features which are not needle-like are matrix-based. They appear nearly as high as fiber tips. On figure 3.8-a, a matrix gangue surrounds the base of the denuded fibers, but its highest point lies $50\,\mu m$ under the fiber top.

On figures 3.4-c_m and 3.5-a_m, the micrographs of 2D C/R also feature clusters of stripped

and needle-like fibers perpendicular to the material surface. As expected, the ablation tests have confirmed that the weakest phase was the matrix. The pyrolyzed phenolic resin, which has a low density (0.7) and a poor organization, is ablated first. Moreover, in the case of plasma-jet experiments, the outgassing may trigger thermo-mechanical erosion of this porous matrix. The tip of the fibers are sharp but irregular. The causes of the irregularities are to be searched at micro-scale (see subsection 3.4.3).

3.4.2.1.3   Quantitative analysis of the samples

Several characteristics are necessary to quantify such a surface roughness : (i) the fiber radius (r_f), (ii) the volume fraction of fibers (characteristic of mean spacing between fibers, noted V_f), (iii) the traditional peak-to-valley distance (*i.e.* height of the stripped and pointed fibers, noted h_f), and (iv) when significant, the angle of fiber tips (α_f). From an analysis of the SEM and OM micrographs, it is possible to evaluate these characteristics. Nevertheless, at this scale, the quantification is profitably completed by a micro-tomography analysis. A Synchrotron X-ray computed microtomography (SXMT) campaign has been carried out at European Radiation Synchrotron Facility (ID19, Grenoble, France) on a 3D C/C composite after a short oxidation test (figure 3.6 b and c), and on the samples C/C-plasma and C/C-oxi (figure 3.7). The set-up is fully described elsewhere [21]. Due to the low X-ray absorption rate of light materials such as carbon, a poor image is obtained using basic absorption tomography. Fortunately, phase contrast imaging is readily feasible using the coherence properties of modern synchrotron beams like that of ESRF [21,98]. In the present campaign the resolution (size of a pixel) is $0.3\,\mu m$. After 3D reconstruction and an appropriate segmentation [98], the agreement between tomographs and SEM micrographs is correct, as shown on figure 3.6. However, the resolution of the SEM micrographs is still higher than for the tomographs ; that is why SEM micrograph representations were preferred in this work. Nevertheless, as illustrated on figure 3.6 through the numerical extraction of a fiber, the non-destructive CMT characterization enables 3D quantitative measurement and analysis of the material structure. In the scope of this study, the tomographs were mainly used to measure the characteristics of surface roughness on sections of the 3D images (figure 3.7). In the future, the tomographs may also be used to carry out direct numerical simulations of ablation on actual geometries.

a) Surface (SEM)   b) Surface (CMT)   c) Fiber (CMT)
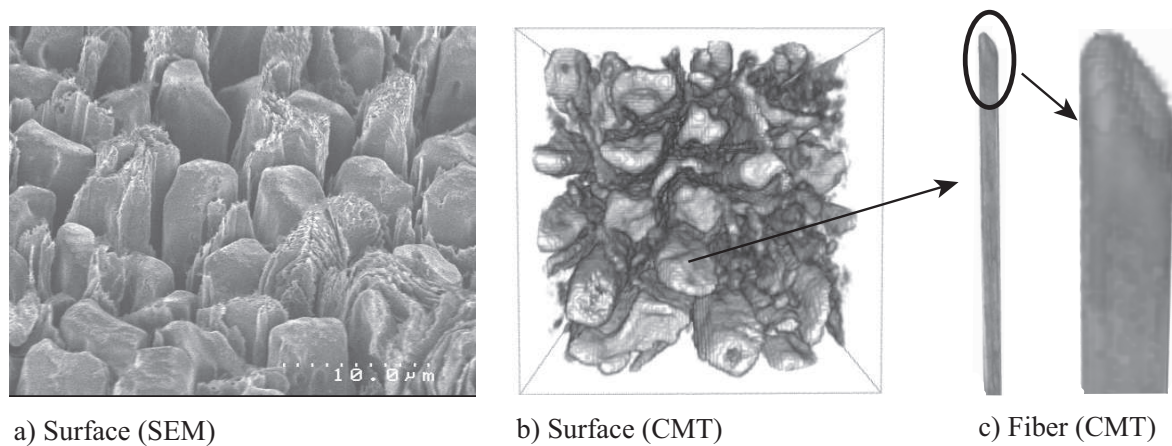
FIG. 3.6 – Comparison of SEM and tomography observations of a C/C surface after a short ablation test.

The characteristic length and angles of needle clusters have been reported in table 3.1. For the C/C samples, the reported values are measurements on CMT slices. The agreement between measurements on CMT images and SEM micrographs is correct, even if the analysis of CMT images is easier and more reliable. For the C/C samples, the reported values are measured on CMT images. The indicated error is the standard deviation on ten measurements in a representative zone. For measurements on SEM micrographs (C/R samples), no mean deviation is given because the evaluation is less accurate : the uncertainty is about 20%. Note that the SEM micrographs at micro-scale (μ) have been taken with a tilt of $\theta = 45$°; then the real angle of fiber tip α_f is given by the relation : $\alpha_f = \alpha_\theta.cos(\theta)$, where α_θ is the apparent angle.

a) 3D C/C-plasma   b) 3D C/C-oxi
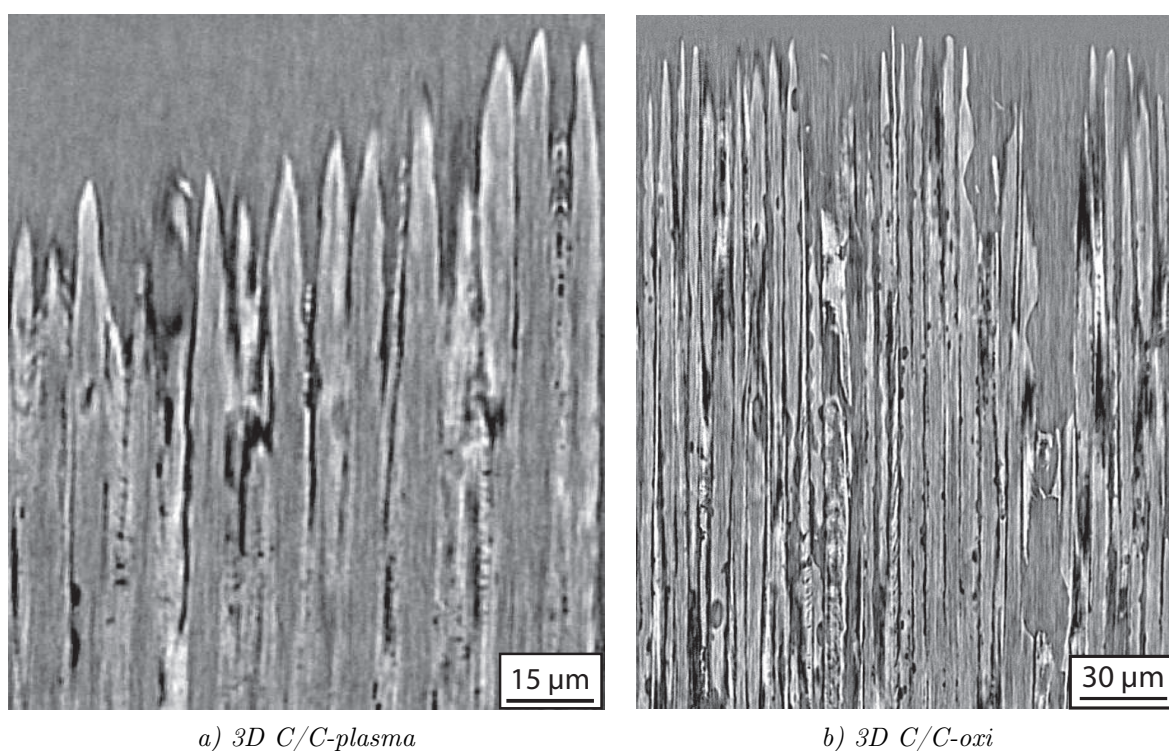
FIG. 3.7 – Sections of micro-tomographs

Sample	V_f	$r_f\,(\mu m)$	$h_f\,(\mu m)$	$\alpha_f\,(deg.)$
C/C-jet	0.61±0.04	3.5	37±2	20.5±2
C/C-oxi	0.61±0.04	3.5	111±6	7±1
C/R-plasma	0.46±0.03	4	∼ 50	irregular
C/R-oxi	0.46±0.03	4	> 400	< 4

TAB. 3.1 – Characteristics of needle clusters (perpendicular yarns).

3.4.2.2   Parallel yarns : "needle layers"

Parallel yarn ablation differs from perpendicular one by the fact that the fibers are stripped layer by layer, often on many levels. Reactants and products migrate by diffusion in this porous medium. For the four samples, this results in a characteristic shape of needle layers represented on figure 3.1-e. When the fibers are slightly inclined with respect to the surface, they display a sharp tip (see micrographs 3.2-c_m, 3.3-c_μ, 3.4-a_m, and 3.5-b_m). In this case, the ablation mechanism is comparable to the one described for needle clusters, but adapted to slanted fibers : α_f is lower and h_f is higher. For each sample, the weak phase is unchanged. On all samples but C/C-plasma, the parallel fibers are denuded on nearly their whole length and on many fiber layers as represented on figures 3.5 b and c. There is a slight difference in the case of C/C-plasma : the fibers which are strictly parallel to the surface are stripped on a single fiber layer in depth. Two causes may explain this tendency : (i) because of the high ablation velocity the matrix is protected by a diffusional limitation, (ii) the high speed flow may favor the mechanical detachment of denuded fibers.

The sharpness of the fiber tips is linked to their inclination angle β with respect to the surface : the more parallel to surface they are, the lower the tip angle α is. The sensitivity of α to β is high when β is close to zero. For the C/C samples, on the micrographs c_μ of figures 3.2 and 3.3, α is respectively about 8° and 6° for values of β lying around 5°. For C/R-plasma, the satin architecture leads to a very disturbed orientation of the fibers ; nevertheless, as a whole, β is given by the plies orientation, which is about 30° ; α is around 9°. Concerning C/R-oxi, parallel fibers are globally strictly parallel to surface, as represented on zone b of figure 3.5. However, some fibers are slightly inclined (zone c : $\beta \simeq 5°$), leading to very sharp fibers tips ($\alpha \simeq 2°$).

3.4.2.3   Inter-yarn matrix

Inter-yarn matrix surface roughness is not represented on figure 3.1 as (i) for C/R samples it is not observed on the surface (or sporadically a very porous matrix is observed, see figure 3.4-b_m) and (ii) for C/C samples it is flat at this scale (see figures 3.2-b_m and 3.3-b_μ).

3.4.3   Microscopic scale : epimicrostructural roughness features

At microscopic scale, some structural and physical surface roughness features take place on the fibers and on the matrices. For the fibers, four geometries of surface roughness have been observed. They have been sketched in figure 3.1 f-g-h-i. From top to bottom, one has :
– Figure 3.1-f : Faceted fibers (see micrographs 3.2-a_μ and 3.3-a_μ), with a hole on the top (see micrograph 3.8-a) ;
– Figure 3.1-g : Very thin and sharp fiber tips with slight wavy irregularities (see micrographs 3.2-c_μ, 3.3-c_μ, and 3.5-c_μ) ;
– Figure 3.1-h : Scalloped fibers, with conchoidal roughness features displaying a curvature radius of $2\,\mu m$ (see micrograph 3.4-c_μ).
– Figure 3.1-i : Icicle-like fibers, named that way by Han [48] to illustrate their particular shape (see micrographs 3.4-a_μ and 3.5-a_μ). On the sample of this study, these fibers often contain holes (see micrographs 3.8-b).

The few matrix pieces remaining on 2D C/R samples are very porous (see micrograph 3.4-b_μ). Ablation reveals the layered structure of pitch-based carbon matrix of 3D C/C samples, leading to deep and narrow notches as represented on micrograph 3.2-b_μ.

a - C/C fiber tips b - C/R fiber body
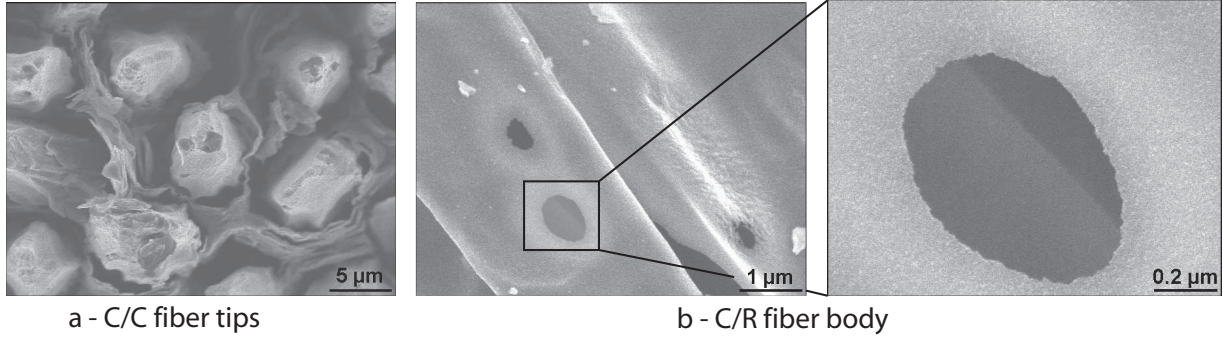
FIG. 3.8 – Presence of holes on several ablated carbon fibers.

These features may have many origins, addressed in section 3.5. The most probable causes are : (i) physical phenomena (flow disturbances, competition between reaction and diffusion [32]) (ii) structural heterogeneities [60], (iii) initial geometrical irregularities conserved or amplified by ablation, (iv) catalysis effects, which could be attributed to a residual presence of alkaline or alkaline-earth metals [34, 38].

3.4.4 Synthesis on surface roughness

Three guiding ideas for the modeling of the material behavior emerge from the analysis of surface roughness :

1. Ablation-related geometrical features of the rough surface mainly follow the material structure. Accordingly, it is called structural surface roughness to make a difference with a purely physical roughness [32] which is sporadically observed on homogeneous materials at micro-scale. Regarding structural roughness, physical phenomena are also of importance : reactivity differences between the different phases and possibly perturbations of local mass transfer. As a result, models including structure and physics have to be taken in consideration.

2. The geometrical features of the different samples are quite similar. The same models should explain their origin.

3. The multi-scale surface roughness underlines the multi-scale behavior of the material. Each scale has to be studied apart first, and then fit together with the other ones using change-of-scale procedures.

3.5 Multi-scale strategy for the modeling of material behavior

The modeling strategy focusses on the material behavior, namely on the differential recession of its heterogeneous surface that leads to the onset of surface roughness. The starting point for such a model may be the Hamilton-Jacobi equation for the recession of a surface [67] defined by the relation $S(x, y, z, t) = 0$ [53] :

$$\frac{\partial S}{\partial t} + \mathbf{v} \cdot \nabla S = 0 \qquad (3.1)$$

where the expression for surface recession velocity $\mathbf{v}$ [53] is :

$$\mathbf{v} = -v_s \, J \, \mathbf{n} \tag{3.2}$$

Here, v_s is the solid molar volume, $\mathbf{n} = \nabla S / \|\nabla S\|$ the normal pointing outwards of the surface, and J is the molar rate of ablation, which is itself expressed as a function of temperature and reactant gas concentration [32] :

$$J \,=\, k(T) \, f(C, T) \tag{3.3}$$

In the case of oxidation, the reactant gas is the oxidative species and one has $f(C) = C^m$ (m is a reaction order) and in the case of sublimation, the considered gas is gaseous carbon and one has $f(C, T) = (C_s(T) - C)$, where C_s is the partial concentration at thermodynamical equilibrium [31, 63]. $k(T)$ is the gasification rate, whose variation from one constituent to another will be responsible for structural roughness. The description of roughness acquisition involves the evaluation of $\mathbf{v}$ at any point of the interface, and this requires knowledge of the temperature T and concentration C fields, *i.e.* it is a non-local model. This latter requirement implies the resolution of balance equations for at least these two variables, where terms describing convection, diffusion, and consumption/creation may be included. The main point is that bulk transport and heterogeneous consumption are possibly in concurrence, and it is anticipated that this competition may have strong effects on the surface geometry. Various levels of modeling may be produced, depending on the choice of simplifications in the description of heat and mass balances. Very rich models have been produced for the description of the gas phase in ablation systems [11, 22, 55, 106], but none have included the coupling with a Hamilton-Jacobi recession equation.

The first step in this direction has to be done for conditions as simple as possible. There are three reasons : (i) modeling can be made without assumption, (ii) an accurate understanding of the elementary causes of ablation is made possible, and (iii) the validation of the models can be done rigorously. This should be possible in the case of the oxidation reactor test. The second step should consist in extrapolating the elementary models to more complex conditions, like those of plasma-jet tests. This may be addressed via two approaches. First, predictably enough, adding to the models the specific phenomena of plasma-jet ablation (advection, thermal gradients, out-flow...). Second, using physical evaluations to make assumptions on the experimental conditions, without change in the models. For instance, the surface roughness of plasma-jet experiments may be analyzed under the light of the results of the elementary models, as soon as the added phenomena, like advection and thermal gradients, are shown to be negligible.

The modeling strategy is based on the guiding ideas arising from the samples analysis. The retained strategy is to study ablation from the smallest scale of structural surface roughness (microscopic) to the largest one (macroscopic), using suitable up-scalings. The input values are then the intrinsic properties of fibers and matrices. The onset of surface roughness is modeled using two changes of scale : (i) microscopic scale (fiber, intra-bundle matrix) to mesoscopic scale (yarn) and (ii) mesoscopic scale (yarn, inter-yarn matrix) to macroscopic (composite) scale. At each scale, the models have to be validated by comparison to experiments. Let the modeling strategy be illustrated using the 3D C/C as a model material ; indeed, its architecture is regular and hopefully simple enough to be model (see figure 3.9).

3.5.1   First step : oxidation reactor conditions

For the oxidation test, the temperature gradients are negligible in the fluid phase as well as in the material, and advection effects are negligible.

3.5.1.1   Microscopic scale

The microscopic scale is that of the constitutive elements of the carbon-based composites of this study : the carbon fibers and the carbon matrices. Independent measurements of the oxidation rates of fibers and matrices have then to be carried out to feed the models. Since a geometrical description of surface roughness is the expected output of the models, a geometrical reactivity [9] has to be measured.

It should be noticed that the effects of epimicrostructural surface roughness are already taken into account in the geometrical reactivity. Nevertheless, trying to understand the causes of surface roughness can be constructive. Addressing the items of the micro-scale (subsection 3.4.3), one can give the following interpretations. Concerning the first two : the facets (figure 3.1-f) and the wavy irregularities (figure 3.1-g), they are thought to be epiphenomena of mesoscale surface roughness : the ablation of fibers with an irregular cross-section could lead to the formation of facets during ablation [64]. An interpretation of conchoidal surface roughness (figure 3.1-h) has already been proposed and modeled [32] : this physical roughness is assumed unrelated to the material structure. The cause seems to be a dynamical effect based on the concurrence between mass transfer and chemical reactions. The other items are probably linked to the material structure and locally catalyzed oxidation due to alkaline elements. Unfortunately, the knowledge of these catalysts (accurate description, repartition) is not sufficient to model their impact on the onset of the epimicrostructural surface roughness. It could be the purpose of future works. Indeed, some promising progresses have been done in the modeling of the gasification of anisotropic structures, using poly-crystalline graphite as a model material [60].

3.5.1.2   Mesoscopic scale (first change of scale)

The material/environment interaction at mesoscopic scale is represented for a 3D C/C on figures 3.9-b-c. Note that, although the scales are not necessarily respected, the fibers, the bulk matrix, and the interphase have been purposely represented more or less as described in section 3.4. Indeed, the models at this scale should explain the general geometries as well as the slight differences between figures 3.9-b-c and 3.9-e-f. The phenomena to take into account for the modeling of ablation in the oxidation reactor are :
  – Surface recession, under a heterogeneous oxidation process in isothermal conditions. The recession velocity of an elementary surface is then only a function of the considered composite component and of the local concentration in reactant.
  – The local reactant concentration is attained by solving a mass balance equation featuring consumption by the surface, and transport in the bulk of the gas phase. An exact evaluation of convection effects on mass transport will be useful. However, the mass Péclet number is expected low close to the wall [51, 62]. In this case, gas transport, resulting in a globally vertical molar flux J, is restricted to pure diffusion.

The input values are : the yarn architecture (fiber, interphase, matrix repartition), k_f, k_i, k_m, C_W, and D (diffusion coefficient of O_2 in the air). The resolution of this model should
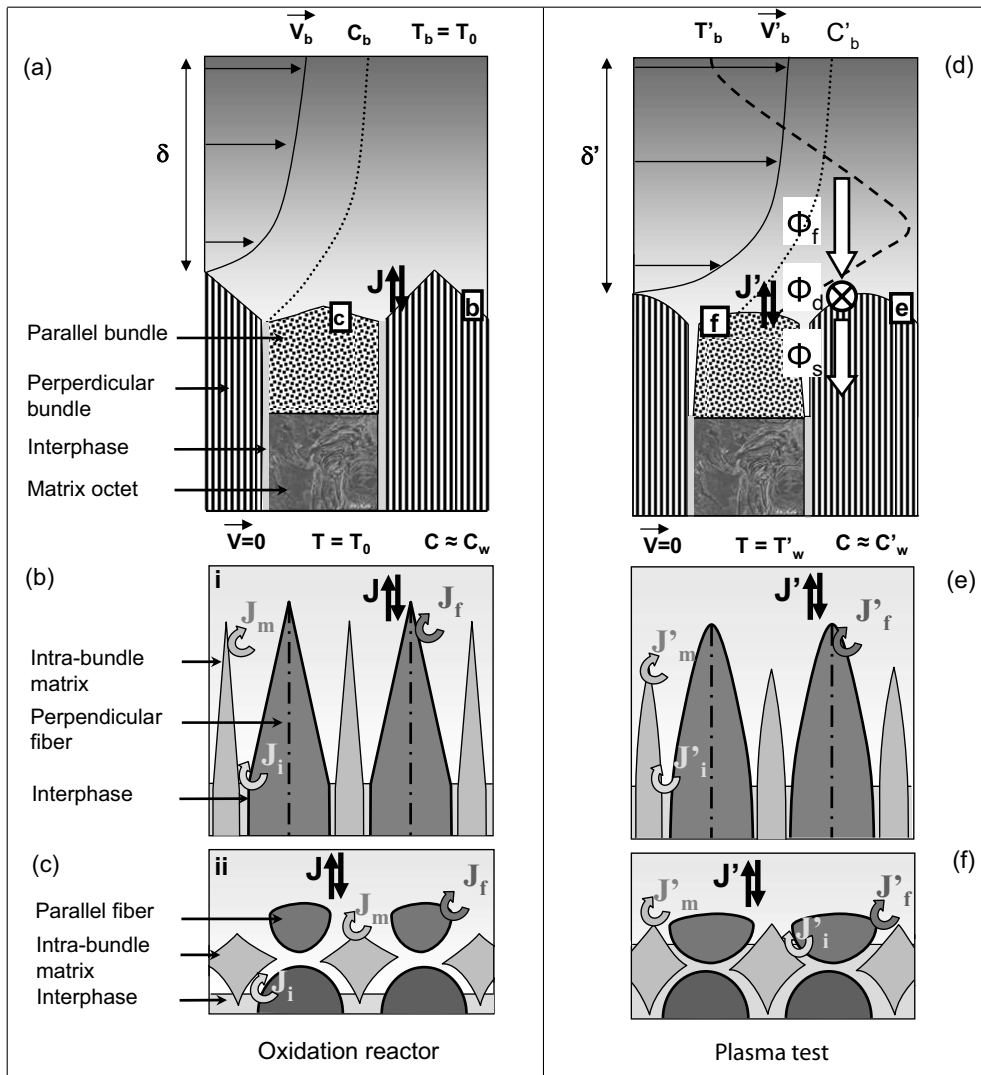
FIG. 3.9 – Modeling strategy : sketch of the coupled phenomena on a 3D C/C

give : (i) the evolution of surface roughness, (ii) the effective oxidation rate of the yarns (first up-scaling).

3.5.1.3 Macroscopic scale (second change of scale)

The concentration gradient of reactant C_b in the dynamic boundary layer results from a competition between an injection by advection, globally parallel to the surface, and a consumption, globally perpendicular to the surface (see figure 3.9-a). Close enough to the wall, the mass Péclet number is also expected low at this scale. Accordingly, the phenomena to take into account are the same as for the mesoscopic scale. The constitutive phases are now : perpendicular bundles, parallel bundles, matrix octets, and inter-yarn interphase. At this scale, the phases may be considered homogeneous. The input values of gasification rate could be obtained either by the first change of scale (at mesoscopic scale : homogenized properties of yarns) or by direct experimental evaluation at microscopic scale (matrix octet properties). The

output of the model should be : (i) the evolution of the epimacrostructural surface roughness, (ii) the complex multi-scale behavior of the C/C composites as a function of experimental conditions and material properties (second up-scaling).

The overall model, which is based on two changes of scales, is validated if, using the microscopic data as input data, the global scale behavior of the composite is well reproduced.

3.5.2 Second step : plasma tests

The gasification processes are chiefly oxidation and sublimation [54]. At high temperatures ($> 3000\,K$) ablation by oxidation can be neglected with respect to ablation by sublimation [31]. The general model of surface recession can then be applied to these tests. However, the experimental conditions are more complex than for the oxidation reactor. Indeed, temperature gradients as well as advection effects may not be negligible. The maximal thermal gradients are evaluated to lie around $0.4\,K.\mu m^{-1}$ in the material under a pure heat conduction hypothesis. Then, for a surface roughness feature length of $100\,\mu m$, it leads to a maximal relative temperature difference of $1\,\%$ between top and bottom, that can be neglected. Moreover, this difference is further decreased by radiative heat transfer. Hence, as a first approximation, $k(T)$ can be assumed constant. Advection effects have to be discussed separately for mesoscopic and macroscopic scales.

3.5.2.1 Microscopic scale

Gasification rates in plasma tests cannot be practically measured on fibers or matrices separately, since the high speed flow would favor erosion rather than gasification of the samples. Thus, model validation is not possible. Conversely, whenever the model were validated for oxidation tests, an outlook could be to evaluate the properties of the composite components in plasma-test conditions by inverse analysis.

3.5.2.2 Mesoscopic scale

At mesoscopic scale, advection should be negligible because of the no-slip condition [51]. The overall dynamic boundary layer is known to be turbulent [22], nevertheless, a thin laminar layer develops close to the wall [16]. Turbulence effects could then be neglected in mass transfer. The model presented for the oxidation reactor should be valuable at this scale, except that the gasification process is now sublimation. Provided that the oxidation process is first order and Knudsen-Langmuir hypotheses are retained to describe sublimation, these two cases are mathematically equivalent considering either reactant diffusion to the wall or vaporized carbon diffusion from the wall [32]. The exploitation of this model for plasma tests should give : (i) an approximation of the properties of the components of the yarns (fibers, matrix, interphase) by an inverse analysis, (ii) the evolution of surface roughness, (iii) the effective sublimation rate of the yarn.

3.5.2.3 Macroscopic scale

The model is represented on figure 3.9-d. T_b, V_b, C_b are the respective evolution tendencies of temperature, velocity, and ablative gas concentration inside the dynamic (viscous) boundary layer of height δ evaluated over a smooth surface [1]. However, computations of the impact of a plasma flow on the actual rough surface would be necessary to evaluate the exact effect of

advection. Unfortunately, this has not yet been achieved [3,31,51]. One may neglect in a first approach advection and turbulence effects. The macroscopic model of the first step may be then exploited, at least as a first approximation. Despite these strong hypotheses, the model may help to understand ablation. The outputs of the model might be some interpretations of : (i) the components properties, (ii) the evolution of the epimacrostructural surface roughness and material behavior.

3.6 Conclusion

This first part of the series *Physico-chemical ablation of carbon-carbon composites* sums up the experimental bases and the strategy for the modeling of surface roughness and of behavior of C/C composites during ablation.

First, the architectures of the materials of this study (a 3D C/C composite and a pyrolyzed 2D C/R composite) are presented, and their turbostratic carbon structure is analyzed to explain their physico-chemical ablative behavior. Second, results of two ablation tests are presented : the first one is the well-known plasma-jet test, the other one is an original oxidation test that provides favorable conditions for the modeling and the understanding of the basic phenomena leading to surface roughening. The latter has been designed on purpose for this study. Third, the surface roughness of the materials ablated during these tests is analyzed, classified, compared to the previous description of the literature and related to the reactivity properties of their constitutive phases. It is shown that a multi-scale surface roughness (SR) develops on the architecture of these composite materials :
  – on the microstructure (fibers and matrix) : epi-micro-structural SR,
  – on the mesostructure (yarns, bundles, inter-bundle matrix) : epi-meso-structural SR,
  – on the macrostructure (composite pattern) : epi-macro-structural SR.
Fourth, this multi-scale behavior, related to the experimental conditions, has led to the set-up of a multi-scale modeling strategy. It is shown that ablation has to be modeled from the microscopic scale up to the macroscopic one, using two suitable changes of scale : (i) microscopic scale (fiber, intra-bundle matrix) to mesoscopic scale (yarn) and (ii) mesoscopic scale (yarn, inter-yarn matrix) to macroscopic scale (composite). The input values are the intrinsic properties of fibers and matrices . The outputs of the models are : (i) the evolution of the surface roughness, (ii) the complex multi-scale behavior of the C/C composites as a function of experimental conditions and material properties. A first step in ablation modeling of C/C composites has to be done for conditions as simple as possible. The oxidation reactor has been designed in this idea. A second step, featuring more complex fluid behavior (like in plasma-jet test), is introduced in this work.

4 Experimental evaluation of intrinsic reactivities

Préambule

Ce chapitre constitue un projet de publication soumis à la revue Carbon.

Auteurs : J. Lachaud, N. Bertrand, G. L. Vignoles, G. Bourget, F. Rebillat et P. Weisbecker
Affiliation :
Laboratoire des Composites ThermoStructuraux (LCTS)
UMR 5801 : CNRS-SAFRAN-CEA-UB1
Domaine Universitaire de Bordeaux – 3, Allée de La Boétie, 33600 Pessac, France

Résumé

Les réactivités géométriques intrinsèques des matériaux sont indispensables à l'alimentation et à la validation des modèles d'ablation. Les cinétiques d'oxydation de deux composites C/C et de leur composants disponibles séparément (fibres, matrices) sont déterminées par mesure de pertes de masse dans un dispositif d'oxydation sous air sec et à la pression atmosphérique. Afin d'identifier le régime réactionnel, et de développer une méthode rigoureuse pour l'identification des réactivité hétérogènes intrinsèques, des modèles ont été développés. Le transport des gaz oxydants vers la surface de l'échantillon est modélisé dans le dispositif (modélisation à l'échelle globale) : convection, diffusion, et réaction hétérogène sont pris en compte. De plus, les fibres ont été rangées selon un empilement unidirectionnel dans lequel diffusion et réaction sont également modélisées (modélisation à l'échelle locale). Lorsque la cinétique de réaction est suffisamment lente, les effets diffusifs peuvent être négligés ; dans le cas contraire, l'utilisation des modèles permet de soustraire les effets diffusifs des données expérimentales et d'obtenir les réactivités intrinsèques.

Abstract

The intrinsic geometrical reactivities of the materials are useful to feed and validate ablation models. The oxidation kinetics of two carbon-carbon composites and of their available components (fibers, bulk matrices) are determined by measurement of mass loss rate in a cylindrical oxidation reactor under dry air and at atmospheric pressure. In order to identify reactional and diffusional regimes, and to provide a safe method for the identification of the intrinsic heterogeneous reaction rates, a modeling approach has been developed. Diffusion of the oxidant is considered throughout the reactor for all the samples (global-scale modeling) in combination with convection and reactions. Moreover, the fibers have been arranged in unidirectional bundles in which diffusion is also considered (local-scale modeling). The importance of the reaction rate relatively to global-scale and local-scale diffusion has been evaluated.

When reaction is slow enough, diffusion effects can be neglected; in the converse case, corrected values of the intrinsic reaction rates are extracted from the experimental data using the models.

4.1   Introduction

This work is the second part of an article series which aims to improve the understanding of the behavior of carbon-carbon (C/C) composites during ablation by oxidation or sublimation, and to model it [61, 63–65]. In this work, the study is restricted to oxidation. During ablation, C/C composites develop multi-scale surface roughness features [61], which may display a strong coupling with the surrounding environment [31, 104]. The surface roughness chiefly arises from the heterogeneity of the composites, whose fibers and matrices are made of distinct forms of carbon. Experimental works have already shown that the effective reactivity of the composite is not an additive property of its components reactivities [41, 68, 74]. To efficiently address the global study of ablation and to provide a theoretical interpretation for these observations, an accurate knowledge of both the composite reactivity and the intrinsic reactivities of the composite components are necessary [61, 63]. However, measurements of the oxidation rate of a carbon material under apparently similar experimental conditions may differ by a factor ten [4, 25, 34, 86]; the causes of the discrepancy are well known [9, 38] : catalytic effects, different thermal treatments of a same material, experimental conditions (gas velocity, quality of the air, configuration of the reactor, diffusion effects...). Consequently, in the frame of this ablation study, it appears that reactivity measurements have to be done on the materials of the study themselves paying special attention to the material history, and that the experimental conditions should be perfectly mastered, or even modeled.

Thermogravimetric analysis (TGA) reactors are the most convenient ones to study oxidation rates because they enable a continuous *in situ* measurement of mass loss [9, 25, 34, 58, 68, 70, 100]. Nevertheless, using TGA, some Arrhenius plots of the experimental oxidation rates versus temperature show a slope change around $900\,K$ [58, 70, 74]. This is attributed to a mass transfer limitation [9]. Indeed, considering heterogeneous reactions, on the one hand, mass transfer of reactant from the bulk of the fluid phase to the material wall is conducted by diffusion, which arises from molecular agitation, and from a driving potential : the concentration gradient of reactant species [51]. This gradient exists in a given boundary layer, the size of which depends on the competition between various transfer phenomena. It is strongly linked to the dynamic boundary layer thickness, which is imposed by the reactor geometry and the air flow properties (velocity, viscosity, density). On the other hand, the reactants that reach the wall are consumed at a rate which is dictated by the material reactivity. At low enough temperatures, though the reaction of oxygen with carbon is thermodynamically favored [15], the reaction is controlled by kinetics : the reactivity tends towards zero, and the concentration gradient also tends towards zero. This is the well-known reaction-limited regime [9]. For higher temperatures the reactivity strongly increases according to an Arrhenius law. At a high enough temperature, the apparent oxidation rate becomes limited by diffusional mass transfer. Between these regimes lies an intermediate regime, or mixed-regime, where the effective oxidation rate results from both intrinsic oxidation and gas diffusion. At $898\,K$, which is a reasonable temperature to carry out the ablation study [61], the diffusion-limited regime is attained in TGA for the materials of this study, and then the intrinsic reactivities of the materials cannot be determined. Consequently, in this work, the oxidation rates of the

composite and of its components are measured using another setup : an oxidation reactor, which has been designed on purpose. Naturally, diffusional limitations may appear as well in the oxidation reactor, and have to be taken into account. However, a more appropriate geometry and a larger possible gas flow rate favor a thin dynamic boundary layer above the sample, that is, a thin concentration boundary layer. This increases the mass transfer to the wall and the transition temperature, so that useful measurements may be conducted at the target temperature of $898\,K$. In addition to this, its geometry has been designed to enable a detailed computational fluid dynamics (CFD) modeling which helps in providing a truly intrinsic oxidation rate. By the way, a third non-negligible advantage is that composites and their components can be oxidized in rigorously similar physico-chemical conditions.

This document is divided in four sections. The first section addresses the experimental conditions and data : the materials of the study and their pre-treatments are described, the oxidation reactor and the experimental protocol are presented. The second section describes the 3D CFD modeling of the reactor. The results of the CFD model are analyzed and proved to be consistent with a 1D analytical approximation. Using the results of the CFD model, an effective reactivity, free of diffusional effects, is determined for each material from the raw reactivity. In a third section, the critical issue of fibers reactivity measurement is addressed : a safe original method in proposed to assess their intrinsic reaction rate, even when diffusive effects are not negligible. Finally, the results are discussed.

4.2 Experiments

4.2.1 Materials

Two C/C composites are studied : (i) a 3D carbon/carbon composite (3D C/C), graphitized at high temperature, made from a 3-D preform of ex-PAN carbon fibers, named $F1$, and a matrix of pitch-based carbon, named $M1$, and (ii) a 2D carbon/phenolic resin composite (2D C/R), pyrolyzed for an hour at $1673\,K$, made from ex-cellulose carbon fibers, $F2$, and a pyrolyzed phenolic resin, $M2$. Most of the composite components are available separately, and are representative of the composite history. Concerning the fibers, $F1$ and $F2$ are available separately with an equivalent thermal treatment. $F2$ is also available under its untreated form, named $F2-R$ in the following. To furnish a larger data set, and to permit comparison of the values of the oxidation rates with those of well-known commercial fibers, other fibers from other precursors have been oxidized. Two forms of $P100$ ex-pitch fibers are tested : (i) raw $(F3-R)$ (ii) treated at $1673\,K$ for an hour $(F3-T)$. Three forms of T300 ex-PAN fibers are tested : (i) raw $(F4-R)$, (ii) treated at $1673\,K$ for an hour $(F4-T)$, (iii) $F4-G$: treated at high temperature $(2300°C)$. Concerning the matrices, $M2$ is easy to obtain by pyrolysis of a phenolic resin. Due to the high pressures and temperatures required to fabricate the 3D C/C, a matrix representative of $M1$ can only be obtained using the 3D C/C process. Bits of 3D C/C matrix have been isolated from the crust of the coarse material at different processing stages : (i) carbonized $(M1-C)$, (ii) graphitized $(M1-G)$.

The samples are treated for one hour under vacuum at $1673\,K$, which is a sufficient temperature to vaporize sodium and calcium impurities that are known to strongly catalyze the oxidation reaction at low temperatures [34]. In order to quantify this effect, the oxidation rates of some untreated fibers have also been evaluated.
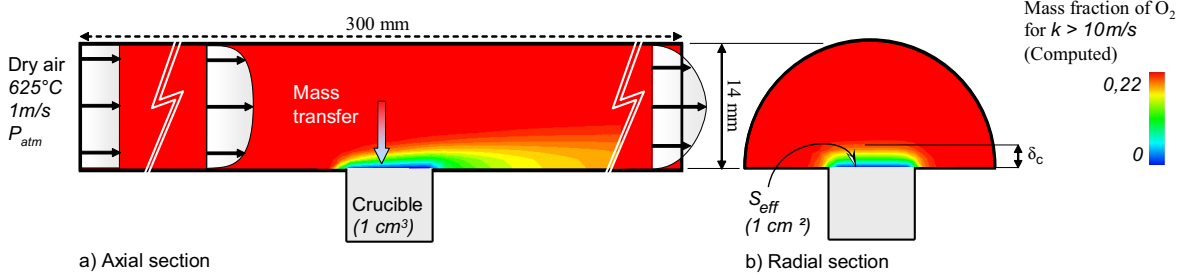
Fig. 4.1 – Oxidation reactor geometry and experimental conditions (dry air, $T = 898\,K$, $P = 1atm$).

4.2.2 Oxidation reactor and experimental protocol

The oxidation reactor is a cylindrical tube, heated resistively ; the lower half of the tube is occupied by a semi-cylindrical refractory block. The sample is placed in a $1\,cm^3$ cubic crucible, incorporated in the center of the lower wall of the inner part of reactor (see figure 4.1). The effective reactive surface of the sample is reduced to a $1\,cm^2$ square surface. The cubic crucible, made of quartz, doesn't display any catalytic effect on oxidation reaction. The composites and the pitch-based matrix are dense materials which are machined at the crucible size and inserted in the crucible. The pyrolyzed phenolic resin, which is very porous, is ground and its powder is placed in the crucible. As represented at figure 4.2-a, the fibers are arranged in dense bundles in the crucible. The resulting unidirectional porous medium, whose effective reactivity is experimentally measured, is modeled in section 4.3.2, the intrinsic reactivity of the fibers being then assessed using the model.

The main drawback of this reactor is that continuous measurements of mass loss are not possible *in situ*. Nevertheless, the access to the sample is easy : the crucible containing the sample is regularly extracted from the reactor and weighted to follow mass loss. Experimental investigations have shown that this operation does not disturb the oxidation process. The inner temperature of the reactor is not modified during this operation ; the required temperature ($898\,K$) is imposed using micro-controllers linked to thermocouple K. The required hot dry air flow velocity ($1\,m/s$) is conveniently mastered in standard conditions using a ball flowmeter, and extrapolated using the perfect gas law. The corresponding air flow is around 400 slh (standard liters per hour). Cold air is injected in the first part of the reactor (not represented on figure 4.1) where it is pre-heated and homogenized by using a gas diffuser.

4.2.3 Experimental results

The experimental results are given in table 4.1 for each sample. The intrinsic density (ρ_i) is obtained by helium pycnometry. The initial mass of the samples (m_0) gives an evaluation of the actual density of the material placed in the crucible. To feed the ablation models, the apparent geometrical oxidation rate j_g [9, 72, 74, 86] is useful. It enables to analyze and model the geometrical evolutions of the surface roughness of the composites, which is strongly linked to their behavior. That is why, to simplify the study, it has been chosen to protect five out
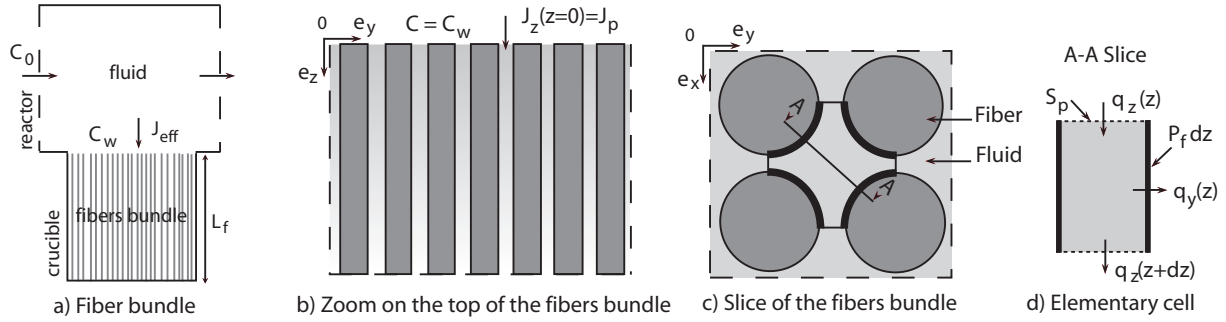
FIG. 4.2 – Sketch of a unidirectional bundle of cylindrical fibers placed in a crucible

of six faces of the samples by including them in a crucible. The samples are then oxidized through the $1\,cm^2$ square upper surface, noted S_{eff} (see figure 4.1). Hence, j_g is defined as the mass loss per unit of geometrical surface and time, given by the following equation [72] :

$$j_g = -\frac{1}{S_{eff}}\left(\frac{dm}{dt}\right) \tag{4.1}$$

where dm/dt is obtained as sketched on figure 4.3. The steady state value of j_g, noted j_{exp}, is assessed for 30% burn off. Indeed, for all the samples, a steady oxidation rate is reached at most after 30% burn off. To illustrate this tendency, the mass loss of the 3D C/C sample is plotted as a function of time on figure 4.3. For this sample, a steady oxidation rate is approximatively reached after ten hours, that is, 15% burn off. For the fibers bundles the steady oxidation rate is reached in a few minutes. Nevertheless, even if j_{exp} is directly representative of the overall recession of the composite surface in steady state, diffusional effects have to be subtracted to this raw experimental value. For the matrices, this method applies as well. For the fibers, the geometrical oxidation rate has to be assessed considering cylindrical fibers. The radial oxidation rate of the fibers may be determined by microscopic analyses ; for example, diameter evolution can be measured accurately by scanning electron microscopy [58]. This method, applied to independent fibers, would pile up three drawbacks : (i) a statistical value should be obtained by measuring the recession on a collection of fibers, (ii) the handling of a sample only constituted of raw fibers is difficult in a SEM, not to say impossible, and (iii) to follow mass loss as a function of time, the sample stacking has not to be modified during measurement. A global method applied to a representative sample of approximatively one million fibers, which requires a simple mass loss measurement interpreted using a simple model, is presented in section 4.3.2.

To clearly situate this work in the general context of the studies on carbon-carbon composites behavior, the interest of other oxidation rates should be discussed. The overall oxidation rate r $(g\,g^{-1}\,s^{-1})$ is often obtained by the following equation [9] :

$$r = -\frac{1}{m_j}\left(\frac{dm}{dt}\right) \tag{4.2}$$

where m_j is the mass of the sample either at initial time (m_0) or after a given burn-off level at time t (m). Both definitions of r are strongly correlated to the samples geometry and porosity [74] ; hence, they are convenient for the comparison of similar samples in different

experimental conditions (oxidation temperature [42, 72], gas composition or pressure [42]) or with specific treatments (antioxidation treatments [42, 72, 74], thermal treatments [58]). For a specific analysis of a material, two oxidation rates in $g\,m^{-2}\,s^{-1}$ may be determined from r : the specific rate j_s and the intrinsic rate j_i, respectively given by the following equations : $j_s = r/TSA$, $j_i = r/ASA$ [9, 35, 68, 85, 100]. TSA (in m^2/g) is the total surface area per mass unit determined for example by Krypton adsorption at $77\,K$ (BET method) [100]. As far as composite behavior is concerned, j_s is biased in general as the the TSA measured by BET is definitely a total surface area, that is, including the whole surface accessible to krypton, while during oxidation, because of mass transfer limitation, oxygen cannot reach the whole accessible surface in the general case [101]. The studies have then to be restricted to reaction-limited regime in the pores. Interestingly, in this regime, it has been shown that the specific reactivity of a 3D C/C composite was not an additive property with respect to that of its components [68]. ASA (in m^2/g) is the active surface area, a macroscopic value introduced to link the local notion of active site to the overall reactivity of carbon surfaces [69, 89]. Active sites are loci where chemisorption can occur [50], that is, where the pseudo-graphitic planes of the turbostratic carbon [102] structure present some defects. The ASA measurement may rely, among others, on oxygen sorption and CO, CO_2 thermodesorption at low temperatures [100]. Thus, as for j_s, j_i is only valuable to study the reaction limited-regime. It is an intrinsic oxidation rate related to the active sites activity of the total surface accessible to O_2. It depends on the nature of the carbon material and on the oxidizing environment, but interestingly it is nearly constant for burn-off values ranging between 0 and 12% [100]. Moreover, the intrinsic reactivity of a C/C composite made of ex-PAN fibers and pitch-based matrix has been shown to be an additive property of the reactivities of its components [100]. Unfortunately, these intrinsic reactivities cannot be directly correlated to the overall behavior of the material (recession rate, surface roughness onset), namely in diffusional regime inside the pores.

In the following, the geometrical oxidation rates will be called intrinsic oxidation rates, by opposition to oxidation rates distorted by extrinsic phenomena like diffusion effects.

4.3   Identification of Intrinsic reactivities

The measured rate j_{exp} is marred by diffusion effects : it is more or less lowered by mass transfer limitation as compared to the intrinsic (or geometric) oxidation rate. The purpose of the CFD modeling is to uncorrelate reactivity and diffusion effects in order to assess the intrinsic reactivity. For the global scale modeling, the effective reactivity k_{eff} of a sample of $1\,cm^3$ placed in the crucible may be considered as the reactivity of a flat effective surface S_{eff} placed on the top of the crucible and leading to the same mass loss rate :

$$\frac{dm}{dt} = -j_{exp}S_{eff} = -k_{eff}\mathcal{M}_c S_{eff} C^n \tag{4.3}$$

where C is the oxidative species concentration and n is a reaction order. $\mathcal{M}_c$ is the molar mass of carbon. This analogy is correct since the samples fit well the crucible size. The wall recession of the materials is low enough to be neglected. The intrinsic reactivities of the composites and matrices are then equal to the effective reactivity. In the case of the fiber bundles, the intrinsic (geometric) reactivity k_f is a complex function of the fibers arrangement, the mass transfer in that porous media, and k_{eff} ; this is treated in section 4.3.2. Anyway, for all the samples, the evaluation of the k_{eff} is the first step for the determination of the intrinsic reactivity. It is the aim of ths following subsection.

Sample Reference	ρ_i $(kg.m^{-3})$	m_0 (mg)	j_{exp} $(g.m^{-2}.s^{-1})$	k_{eff} $(m.s^{-1})$	R_f (μm)	$\overline{d}_p$ (μm)	k_f $(m.s^{-1})$	Regime Da	Φ
3D C/C	2.08	1504	0.095	$\mathbf{3.0\,10^{-3}}$	-	-	-	0.039	-
2D C/R	1.94	1038	1.31	$\mathbf{8.5\,10^{-2}}$	-	-	-	1.1	-
M1-C	1.92	974	0.25	$\mathbf{8.7\,10^{-3}}$	-	-	-	1.1	-
M1-G	2.12	940	0.080	$\mathbf{2.5\,10^{-3}}$	-	-	-	0.032	-
M2	1.97	714	0.64	$\mathbf{2.6\,10^{-2}}$	-	-	-	0.34	-
F1	1.85	463	0.30	$1.0\,10^{-2}$	3.5	28	$\mathbf{1.2\,10^{-5}}$	0.13	1.1
F2	1.60	312	0.96	$4.8\,10^{-2}$	3.5	37	$\mathbf{2.1\,10^{-4}}$	0.62	4.1
F2-R	1.60	472	2.16	0.46	3.5	23	$\mathbf{1.4\,10^{-2}}$	6.0	43
F3-R	2.16	522	0.41	$1.5\,10^{-2}$	5.5	45	$\mathbf{3.3\,10^{-5}}$	0.19	1.5
F3-T	2.16	341	0.27	$9.5\,10^{-3}$	5.5	74	$\mathbf{2.6\,10^{-5}}$	0.12	1.0
F4-R	1.79	844	0.95	$4.7\,10^{-2}$	3.5	12	$\mathbf{1.1\,10^{-4}}$	0.61	5.2
F4-T	1.79	579	0.44	$1.6\,10^{-2}$	3.5	20	$\mathbf{1.8\,10^{-5}}$	0.21	1.6
F4-G	1.96	368	0.097	$2.7\,10^{-3}$	3.5	35	$\mathbf{3.0\,10^{-6}}$	0.03	0.51

TAB. 4.1 – Experimental results and theoretical exploitation (dry air, $T = 898\,K$, $P = 1atm$).
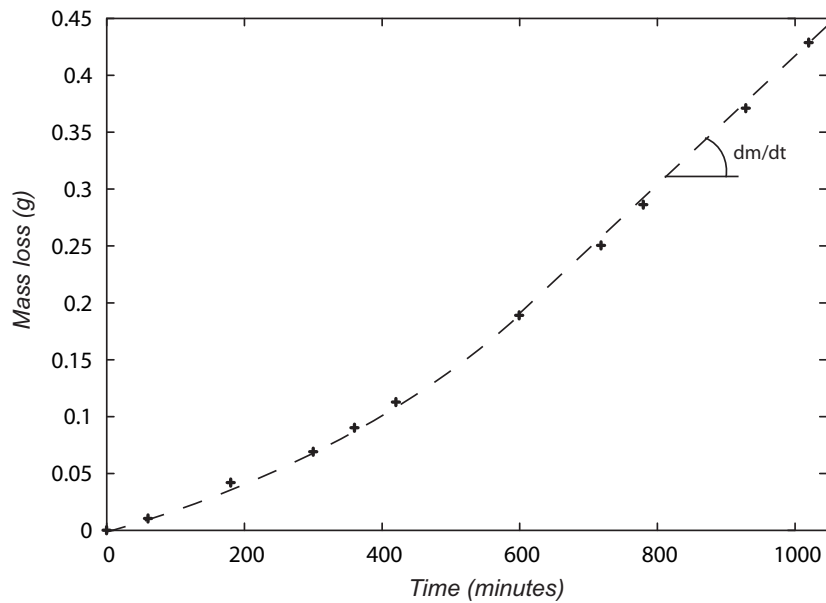
FIG. 4.3 – Mass loss versus time for the 3DCC sample (dry air, $T = 898\,K$, $P = 1atm$).

4.3.1   Modeling of the oxidation reactor

The hypotheses of the global model are as follows :

– According to thermochemical data, at $898\,K$, under dry air and at atmospheric pressure, the chemical balance of the oxidation process writes [15] :

$$C_{(s)} + O_2 \rightleftharpoons CO_2 \tag{4.4}$$

In the conditions described above, this reaction is thermodynamically promoted since $\Delta_f G°(CO_2) = -395 kJ/mol$. Moreover, the equilibrium of the partial pressures of reactants and products is attained for : $P_{CO_2} = 10^{23}.P_{O_2}$ [15]. This implies that : (i) only the kinetic aspect of the reaction has to be taken into account, (ii) the reaction may be limited by a low partial pressure of O_2. Studies on active site reactivity have shown that the reaction order n depends on many parameters like temperature, pressure or carbon crystallinity [34]. The proposed values of n lie between 0.5 and 1 [86]. Considering the ablation modeling as a whole, the chosen value is not an issue as long as it is maintained consistently in the further modeling developments [63–65]. In the following, a first-order oxidation process is considered. Thus, equation 4.3 rewrites : $r_{exp} = \mathcal{M}_c k_{eff} C_{O_2}$ $(g.m^{-2}.s^{-1})$, with k_{eff} $(m.s^{-1})$ and C_{O_2} $(mol.m^{-3})$ the oxygen concentration at the surface.

– CO_2 formation is exothermal ($\Delta_f H = -394\,kJ.mol^{-1}$, at $898\,K$) [15]. However, the sample is cooled down by conduction, convection, and radiation ; analytical evaluations and experimental measurements have shown that it could be considered isothermal [61].

– The surface recession, which is slow as compared to mass transfer, and low at any time, is neglected.

– The inner part of the reactor is accurately modeled in 3D, its geometry is represented on figures 4.1 and 4.4.

– The flow is supposed laminar. Indeed, the Reynolds number evaluated assuming a flow in a circular tube is found to lie around 300, while the onset of turbulence appears for values around 2300 [51].

– The hot ($898\,K$) laminar dry air flow is modeled using Navier-Stokes equations.

– Incompressible flow ($v < Mach\,0.2$) [16].

– Multi-component mass transfer is taken into account, the species being oxygen, nitrogen, and carbon dioxide.

The boundary conditions are :

– Inlet : $T = T_0 = 898\,K$, mass fraction of oxygen in dry air : 0.222, dry air velocity : $1\,m/s$ with a flat profile ;

– Outlet : $P = P_{atm}$;

– Walls : $T = T_0$, heterogeneous reaction on S_{eff}, non sliding condition.

The numerical simulations of gas flow and reactant species distribution in the experimental setup have been performed with a commercial software package, *Fluent6*. Steady-state solution was attained by a first resolution of the single Navier-Stokes equations, then followed by a coupled resolution of the Navier-Stokes and species balance equation including the heterogeneous reaction. Figure 4.4-b shows the geometry of the mesh, which has been optimized to favor a quick convergence : it features $122,200$ hexahedral cells and $124,313$ nodes. The quality of all elementary cell is acceptable (low distortion).

The first non-trivial result arising from this modeling is that the effect of mass transfer on the dynamic flow is not significant, even in diffusion-limited regime. On figure 4.4-a, the

velocity profile of the air flow is represented on an axial section and on three radial sections (inlet, crucible position, outlet). On figure 4.5, the velocity profiles are plotted for $y = 0$, along $\mathbf{z}$, for abscissa from inlet to outlet. As expected, the non sliding condition being respected, the viscous effects lead first to a hydrodynamic entrance region, in which a dynamic boundary layer develops from the wall to the inviscid flow region, the corresponding velocity profile displays then two parts : a parabolic part (viscous effects), and a flat part (inviscid flow). The dynamic boundary layer, of thickness δ, is the region delimited by an axial velocity lower than 99% of the inviscid flow region velocity [51]. As represented on figure 4.5, the flat part progressively disappears, leading to the establishment of a fully parabolic velocity profile ; the corresponding region is called fully developed. Clearly, the sample is placed in the hydrodynamic entrance region. As far as mass transfer is concerned, this is beneficial since the dynamic boundary layer size is then lower in this region. Indeed, for a species i, it is reasonable to deduce the mass concentration boundary layer thickness over an infinite sample, $\delta_c(i)$, from δ by the following relation :

$$\frac{\delta}{\delta_c(i)} \approx Sc^{\frac{1}{3}} \tag{4.5}$$

where $Sc = \nu/D_{iM}$ is the Schmidt number (with ν and D_{iM} (in $m^2.s^{-1}$) resp. kinematic viscosity and binary mass diffusion coefficient of species i in the gas mixture M), close to unity in gases [51]. Hence, one has $\delta_c(O_2) \simeq \delta$ for an infinite sample. Then, according to the considerations of the introduction, a low value of δ_c favors mass transfer : that is why the diameter of the inner part of the reactor has been chosen small and the velocity high. Note that the diameter and the velocity have to be chosen low enough to ensure a laminar flow, since the Reynolds number increases proportionally with the diameter and the mean fluid velocity. The retained geometry is then the result of an optimization between experimental requirements (accessibility, sample size, dry air supplying) and mass transfer. The radial section over the crucible shows that the velocity profile on the sample along the $\mathbf{y}$ axis is nearly constant in the first half of the section ($0 < z < 7\,mm$). The analysis of the axial section leads to the same conclusion along $\mathbf{z}$. The fact that the sample has finite size leads to unavoidable edge effects and naturally advection brings a higher oxygen flow on the sample edge at abscissa $x = -0.005$. Anyway, it may safely be assumed that once the velocity profile is established, the mass transfer should be mainly unidirectional along the direction $-\mathbf{z}$.

The results of the 3D numerical simulation for the mass concentration of oxygen in the fluid phase are sketched on figure 4.1. The concentration profiles represented on contour maps are similar in all the regimes, except for the fact that the reactive wall concentration strongly depends on the effective oxidation rate, as represented on figure 4.4-c. The maps of figure 4.1 show that the concentration boundary layer over the sample has a size of approximatively $2\,mm$. This is lower than the standard evaluation using Schmidt number ($\delta \sim 7\,mm$). The discrepancy is basically to be attributed to the oxygen flow carried by convection, since equation 4.5 assumes an infinite sample. Figure 4.4-c shows that the oxygen concentration on the reacting surface (S_{eff}) is nearly constant in all the regimes. At low reaction rates (figure 4.4-c1), a very small oxygen concentration gradient is observed. At high reaction rates (figure 4.4-c2), the gradients of oxygen concentration become important (diffusion-limited regime). In the latter case, the tangential gradients are mainly developed close to the edges, while the main part of the sample is submitted to a constant oxygen concentration. This fact enables to assume that the concentration on the samples is homogeneous in all regimes. The average molar concentration of oxygen on the reactive surface is estimated after surface integration of
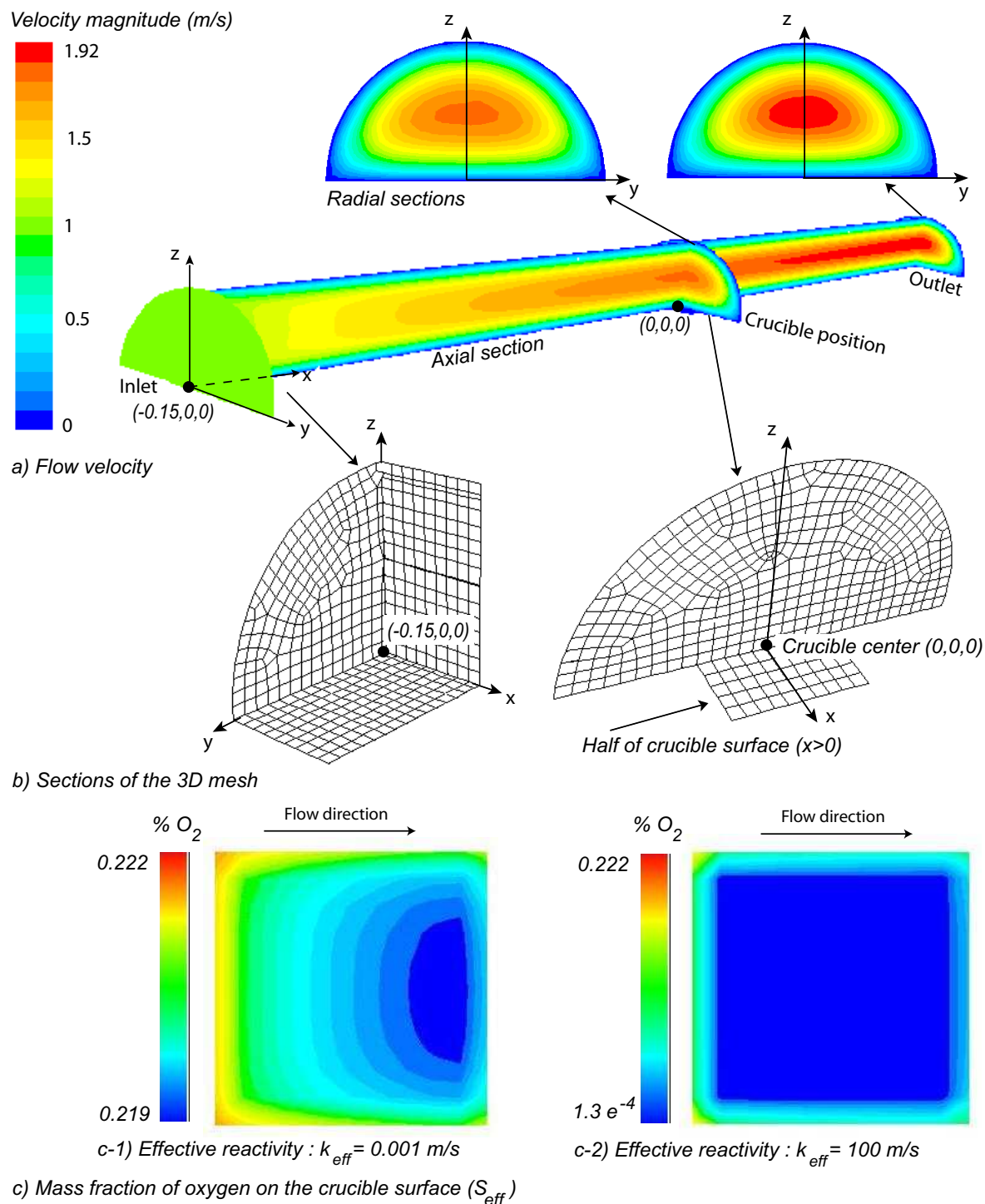
FIG. 4.4 – 3D numerical simulation results

oxygen molar fraction. The effective mass flow consumption of carbon per surface unit and time, noted j_C (in $g/m^2/s$), is then calculated versus the effective oxidation rate. The result of this numerical approach is plotted on figure 4.6. On a 3.2 GHz Xeon CPU the duration of
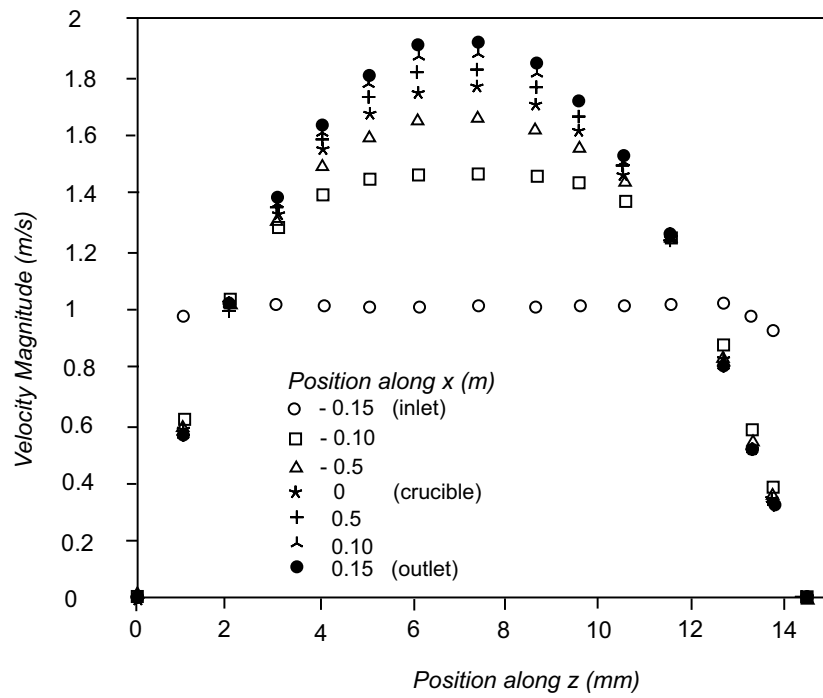
FIG. 4.5 – Velocity profile of the air flow in the oxidation reactor
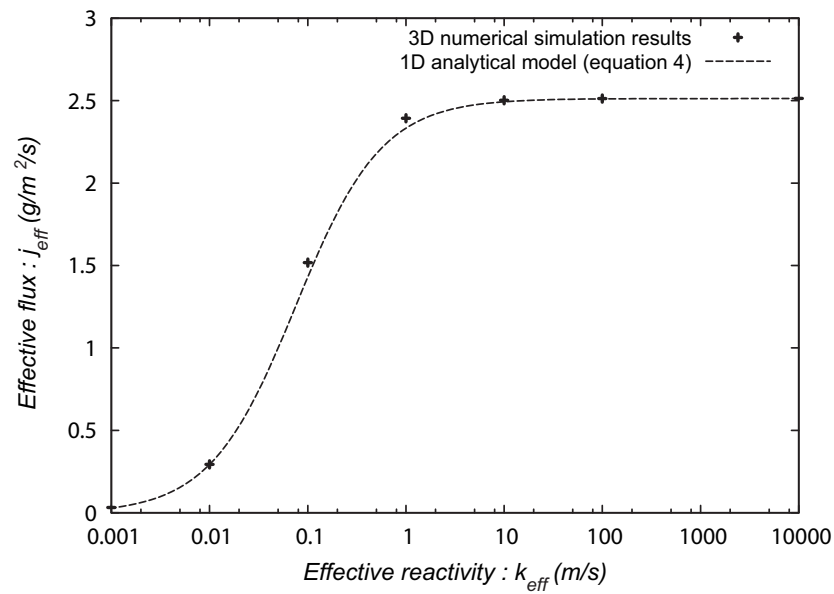
FIG. 4.6 – Mass loss as a function of effective oxidation rate : comparison of 1D analytical and 3D numerical results.

one numerical simulation run is approximatively 24 hours.

Since the concentration gradients study has shown that the mass transfer was mainly vertical, it may be of interest to compare the results of a 1D analytical approach to that

of the numerical simulation. Considering the diffusion of oxygen in air at $898\,K$ in 1D, the effective mass flow is proved to be of the form [67] :

$$j_C = j_0 \frac{1}{1 + \frac{D}{\delta_c\, k_{eff}}} \tag{4.6}$$

where $j_0 = DC_0\mathcal{M}_c/\delta_c$ is the maximal mass loss obtained in diffusion-limited regime. D is the diffusion coefficient of oxygen in air at $898\,K$; it is about $1.34\,10^{-4}\,m^2/s$. C_0 is the oxygen concentration at inlet position, its value is $2.713\,mol/m^3$. According to the numerical points represented on figure 4.6, one has $j_0 = 2.515\,g/m^2/s$. Hence, one deduces that $\delta_c = 1.73\,mm$, which is in agreement with all numerical simulations (see figure 4.1-b). The 1D approximation of j_C fits well the numerical results (see figure 4.6). In diffusion-limited regime and in reaction-limited regime, the approximation to the numerical solution is excellent. In intermediate regime, the error is lower than 6%. This approximation is preferable to any linear interpolation between the numerical points. Equation 4.6 is used to derive the effective reactivity k_{eff} from the experimental oxidation rate (j_{exp}) in table 4.1. Moreover, this study shows that close to the wall mass transport by convection is negligible when compared to mass transfer, that is, the mass Péclet number is low.
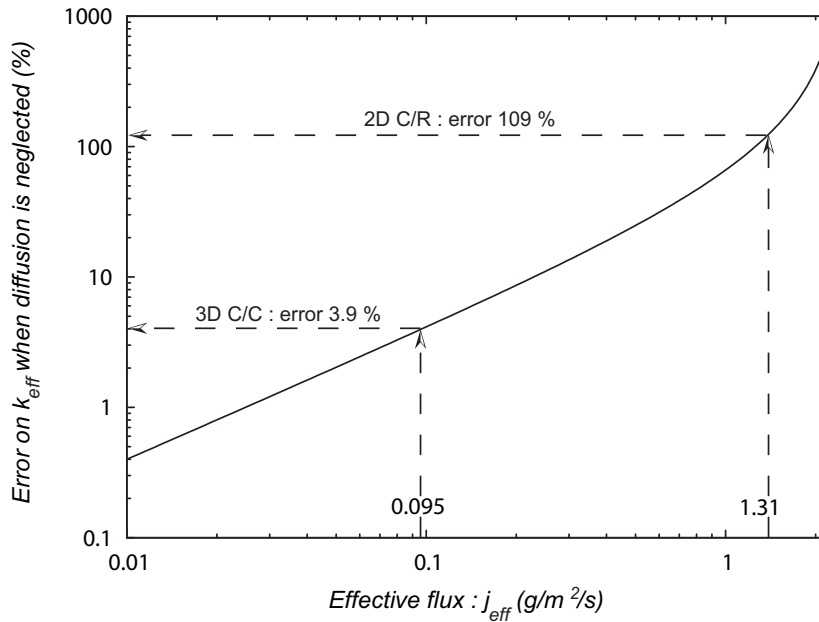
FIG. 4.7 – Relative error (%) made on k_{eff} evaluation when diffusive effects are neglected

To illustrate the importance of taking into account diffusion effects, the error made when diffusional effects are neglected is evaluated. If diffusion effects are neglected, the concentration on the reactive wall is considered to be C_0. Then the mass flow writes : $j_C = k_r C_0 \mathcal{M}_c$, where k_r is the oxidation rate obtained when diffusional effects are neglected. Note that k_r is lower than k_{eff}. The relative error is then : $(k_{eff} - k_r)/k_r$. This error is plotted in percent units on figure 4.7. As represented on this figure, the error that would be made for the 3D C/C sample is 3.9%. The error is low because the regime is close to the reaction-limited regime. However, for the 2D C/R sample, the error is considerable (108.9%). The oxidation reactor of this study

has been designed to prevent diffusional effects from limiting the reaction; nevertheless, they appear in a non-negligible way. The global scale modeling of the reactor gives the opportunity to extract effective reactivities from the experimental data.

4.3.2   Modeling of fibers bundle

The aim of this part is to derive k_f (in $m.s^{-1}$), the real oxidation rate of the fibers, from k_{eff}, the effective reaction rate of a fiber bundle, which is the accessible data at global scale. The approach is similar to the work of P. L. Walker [9, 101] developed for porous carbons, but with a more controlled pore morphology. Carbon fibers are assumed homogeneous and isotropic. The chemical reactions are restricted to the fiber surface. The oxidation process is as described in section 4.3.1. The local impinging molar flux density is given by $J_y(z) = k_f C(z)$, with C(z) (in $mol.m^{-3}$) the oxygen concentration at the position z (see figure 4.2).

The main difficulty to measure the intrinsic oxidation rate of the fibers is to find a suitable way to arrange the fibers. First, a sufficient mass of fibers has to be placed in the crucible to enable an accurate mass loss measurement. Secondly, the modeling of the fibers stack, which is a porous medium, must be feasible with a good accuracy. The retained solution is described below. A fibers bundle is included in the square crucible (see figure 4.2-a). The fibers bundle is made of approximatively 600,000 cylindrical fibers in a non-compact array. Indeed, it is practically impossible to arrange these fibers in a compact array. The local porosity of the bundle is homogeneous and the tortuosity is negligible along the $\mathbf{e_z}$ axis (see figure 4.2-b).

Mass loss is strongly coupled to mass transfer between the fluid phase and the wall. The diffusion regime inside the porous medium is given by the Knudsen number ($Kn = \overline{\lambda}/\overline{d_p}$, where $\overline{\lambda}$ is the mean free path and $\overline{d_p}$ is the mean pore length in the ($\mathbf{e_x}$, $\mathbf{e_y}$) planes). For a porous medium of total porosity ϵ and total internal surface area s ($m^2.m^{-3}$) the mean pore size writes [92] :

$$\overline{d_p} = \frac{4\epsilon}{s} \tag{4.7}$$

For this case, assuming cylindrical fibers, one derives :

$$\overline{d_p} = \frac{4\overline{S_p}}{\overline{P_f}} = \overline{d_f}(v_c\mu_f/m_f - 1) \tag{4.8}$$

where $\overline{d_f}$ (resp. $\overline{P_f}$) is the mean fiber diameter (resp. perimeter), $\overline{S_p}$ the mean horizontal section of the pores, v_c the crucible volume, μ_f the fiber mass volume, and m_f the fiber mass in the crucible. The value of $\overline{d_p}$ reported in table 4.1 takes into account the fibers radius reduction after 30% burn-off.

At $898\,K$ in dry air at atmospheric pressure, the mean free path value for oxygen is $\lambda \simeq 0.2\,\mu m$. For the bundles described above, $\overline{d_p}$ is larger than $12\,\mu m$ (table 4.1). Hence, the Knudsen number is low ($Kn \sim 0.01$); it characterizes bulk diffusion [92]. As the mass Péclet number is very low inside the fiber bundles, mass transfer inside this porous medium is restricted to ordinary diffusion of oxygen in air. The vertical diffusion flux per surface unit is given by Fick's first law :

$$J_z(z) = -D\nabla C(z) \tag{4.9}$$

The mass balance in the elementary cell represented on figures 4.2-c and 4.2-d writes :

$$q_z(z) - q_z(z + dz) = q_y(z) \tag{4.10}$$
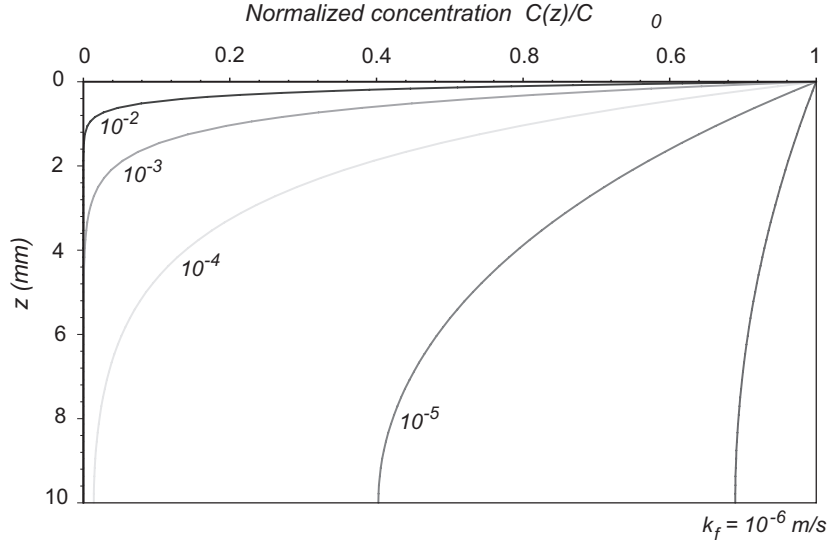
FIG. 4.8 – Normalized concentration gradient in a fibers bundle with $\overline{d_p} = 12\mu m$, $D = 1.34\,10^{-4}\,m^2/s$, $L_f = 10\,mm$, and for various values of k_f.

Neglecting transient effects, one has :

$$-D\nabla(C(z) - C(z + dz))S_p = k_f C(z)P_f dz \qquad (4.11)$$

Summing up, $C(z)$ is given by the following differential equation :

$$\frac{d^2 C(z)}{dz^2} - \frac{4k_f}{\overline{d_p}D}C(z) = 0 \qquad (4.12)$$

where the boundary conditions are $C(z = 0) = C_0$ and $\frac{dC}{dz}(z = L_f) = 0$.

After integration, the oxygen concentration inside the porous medium is found to be :

$$C(z) = C_0 \frac{\cosh\left(\Phi\left(z/L_f - 1\right)\right)}{\cosh\Phi} \qquad (4.13)$$

where $\Phi = L_f/L$ is the Thiele number, with $L = \sqrt{\frac{\overline{d_p}D}{4k_f}}$. The normalized concentration gradient $C(z)/C_0$ in the fibers bundle is plotted on figure 4.8 for $\overline{d_p} = 12\mu m$, $D = 1.34\,10^{-4}\,m^2/s$, $L_f = 10\,mm$, and various values of k_f. It can be shown straightforwardly that the mass loss on the top of the cylindrical fibers is negligible in front of that on the side of the fibers when the oxygen penetration in the bundle is higher than five times the fiber radius. The plot of figure 4.8 confirms *a posteriori* that this hypothesis is valid for the values obtained for k_f (table 4.1). According to this hypothesis, J_{eff} and the flux that penetrates in the porous media J_p (see figures 4.2-a and b) are linked by the relation :

$$J_p = J_{eff}\frac{S_{eff}}{\overline{S}_p} = J_{eff}\frac{1}{1 - m_f/(L_f\rho_f S_{eff})} \qquad (4.14)$$

At the position (z=0), the divergence of J_p is null. Then, Fick's first law gives :

$$J_p = D\left.\frac{dC}{dz}\right|_{z=0} = \frac{DC_0}{L}\tanh(\Phi) \qquad (4.15)$$
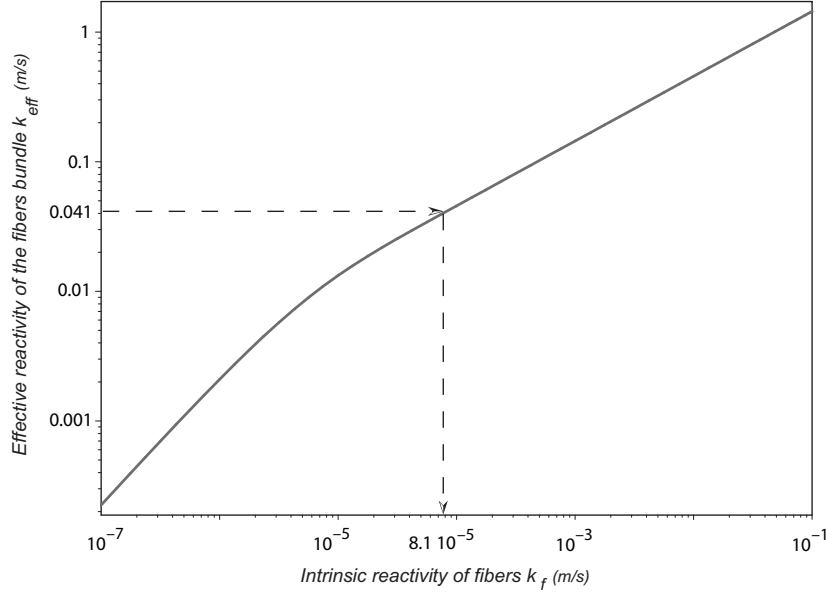
FIG. 4.9 – Plot of k_{eff} versus k_f for the fibers bundle $F4 - R$

Substituting the relation $J_{eff} = k_{eff}C_w$ in equation 4.14, and combining this latter with equation 4.15, one obtains k_f as an implicit function of k_{eff} :

$$k_{eff} = 2\sqrt{\frac{k_f D}{d_p}} \tanh\left(2L_f \sqrt{\frac{k_f}{d_p D}}\right) \left(1 - \frac{m_f}{L_f \rho_f S_{eff}}\right) \tag{4.16}$$

To illustrate this equation, k_{eff} is plotted versus k_f for the fibers bundle properties of sample $F4 - R$ on figure 4.9. The table 4.1 is then completed using equation 4.16. The values of k_f are discussed in the following part.

4.4 Discussion

First, it seems useful to compare the values obtained to previous results of the literature. It should be noticed that in most of the studies the oxidation rate values are not comparable to the one obtained in this study, though the units may appear consistent. Indeed, the oxidation rates are generally presented either under the form r, r_i, r_s, or, when raw mass loss rates are given, the geometrical surface of the sample is not given. I. W. Smith [86] summarized the intrinsic (geometrical) reactivities of a wide range of carbons between $580\,K$ and $2200\,K$. At $898\,K$, the reactivities, converted in the units of the present study, span between $7\,10^{-6}$ and $1.3\,10^{-2}\,m/s$. Hence, the order of magnitude of the intrinsic reactivities reported in table 1 are in agreement with this reference. A very reliable geometrical data is the radial recession velocity v of an ex-PAN fiber of a 3D C/C composite treated at high temperature $(2300^{\circ}C)$ which has been measured by SEM [58] in experimental conditions close to those of the present work, the temperature being only slightly lower $(873\,K)$. Its value is found to lie around $0.1\mu m/h$. According to the Arrhenius law proposed in [30], the reactivity of carbon fibers at

$898\,K$ is three times higher than at $873\,K$. Assuming that the regime was reaction-limited in that experiment, the resulting intrinsic oxidation rate k_f is then around $3\,10^{-6}m/s$ at $898\,K$, that is, it is equal to the oxidation rate of $F4-G$ which is also an ex-PAN fiber heat-treated at $2300°C$, and oxidized at $898\,K$. The geometrical gasification rate of a C/C composite made of ex-PAN fibers and pitch-based matrix has been reported by Mc Kee [74] in a wide range of temperatures in experimental conditions similar to that of the present study. At $898\,K$, a good agreement is obtained in the magnitude orders with the sample 3D C/C.

Comparing the oxidation rate of the fibers of this study, one notes that the oxidation resistance of the raw fibers are in the order : ex-pitch (F3-R), ex-PAN (F4-R), and ex-cellulose (F2-R). This should be expected from the knowledge of their degree of organization. As expected, the treatment at $1673\,K$ leads to an important diminution of the fibers reactivity, through a diminution of catalytic effects ($F1$, $F2$, $F3-T$, $F4-T$). High temperature treatments are known to graphitize ex-PAN fibers and then lower their reactivity. The fiber $F4-G$, which is an ex-PAN fiber treated at high temperature, is the most resistant.

Concerning the matrices, the pyrolyzed phenolic resin ($M2$), which is poorly organized, is about three times more reactive than the ex-pitch carbonized matrix ($M1-C$). The graphitized ex-pitch matrix ($M1-G$) is roughly 3.5 times more resistant than in carbonized state. It should be noticed that this matrix may be more representative of the matrix octets of the 3D C/C composites than of the matrix lying inside the composite components. Indeed, inter-bundle and intra-yarn matrices are submitted to different conditions in terms of temperature, pressure and space occupation during graphitization. Interestingly, the actual matrix is heterogeneous : a thin matrix interphase ($0.5\mu m$), which lies between the fibers and the bulk matrix, has a higher gasification rate than that of the bulk matrix. This is represented on figure 4.10-a for a short oxidation test. Scanning electron microscopy (SEM) micrographs have been taken on polished slices (diamond powder $1\mu m$) to analyze the material structure of raw composites (figure 4.10-b). The cohesion between the fiber and the matrix is excellent. However, close to the fiber, the matrix structure seems more disturbed. This is in accordance with the presence of a less organized and thus more reactive zone (interphase). Transmission electron microscopy (TEM) has also been carried out on a thin slice, obtained using first mechanical polishing then ion-milling. Ion-milling is known to generate a surface state (microfissures) susceptible to generate artifacts during TEM analysis [33]. This is observed on micrograph 4.10-c in bright field. An interesting fact is that artifacts are different at the interphase position. This strongly suggests the presence of a different structure at the interphase [33,58,76]. Anyway, as far as the composite behavior is concerned, the interphase exists, and plays a major role in oxidation process [58,59,81]. However, it is not possible to measure directly its oxidation rate since it is neither available separately nor practically extractable from the composite. A theoretical method is proposed elsewhere to assess its oxidation rate from the analysis of the steady-state surface roughness of the composite after oxidation [63].

It is interesting to note that 3D C/C oxidation rate is definitely higher than that of its constitutive fibers ($F1$). This may be attributed to a weakest-link process driven by the interphase reactivity [41]. As expected, 2D C/R is more reactive than 3D C/C. However, surprisingly, its reactivity is both higher than that of the fibers $F2$ and the matrix $M2$. This suggests that the behavior of this material is also complex.

a) SEM after a short oxidation test :
   interphase is deeply oxidized

b) SEM of a polished slice (diamond powder 1μm) :
   interphase seems more disturbed

c) TEM of a thin slice : different artifacts
   at the interphase (due to ion-milling)
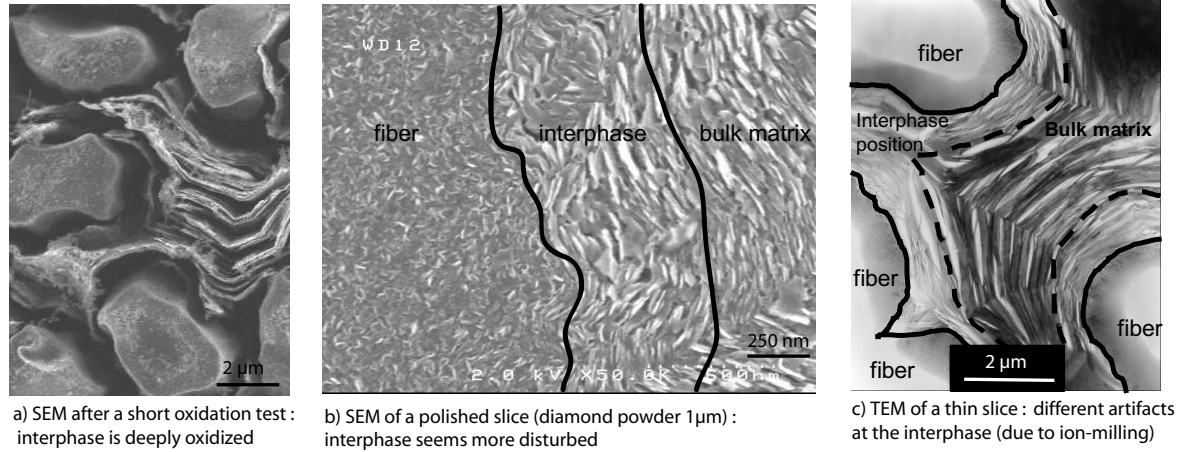
FIG. 4.10 – Observation of the interphase lying between fibers and inter-yarn matrix

4.5 Conclusion

The intrinsic geometrical oxidation rates of two carbon-based composites, of their available components, and of several carbon fibers have been measured at $898\,K$ under dry air and at atmospheric pressure. In these conditions, a diffusional limitation in the pores as well as in the bulk fluid phase was expected. In order to provide a safe method for the identification of the intrinsic reaction rates, a modeling approach associated to experimental measurements has been developed. All the samples have been inserted in a cubic crucible (the bulk materials being machined at the crucible size, the fibers being arranged in a unidirectional bundle) placed in a cylindrical oxidation reactor. The test configuration has been designed to favor a thin dynamic boundary layer above the sample, and consequently, a thin concentration boundary layer. This increases the mass transfer from the bulk fluid phase to the sample surface and lowers diffusional effects. The global scale CFD modeling of the reactor has been addressed in 3D : diffusion of the oxidant has been considered throughout the reactor in combination with convection and reaction on the sample surface. It has been shown that the overall mass transfer over the sample was unidirectional, and could be fitted by a simple analytical law in all regimes. This law has been used to extract the effective reactivity of the samples from the measured mass loss rates, which have been shown to be marred by diffusional effects. In the case of the bulk materials (composites, matrices), this effective reactivity is precisely their intrinsic geometrical reactivity. In the case of the fiber bundles, which are porous media, a second step has been useful to extract the fiber intrinsic reactivities. The bundles have been modeled considering diffusion of the oxidant throughout the pores in combination with reaction on the fibers surface. An analytical law has been obtained : it gives the intrinsic geometrical oxidation rate of the fibers as a function of the porous media properties and of the effective oxidation rate of the bundle. Then, the corrected values of the intrinsic geometrical reaction rates, extracted from the experimental data using the models, have been compared to those of previous studies. Correct orders of magnitude are obtained. Moreover, the method used to assess the fiber reactivity has been shown to be in correct

agreement with a very reliable direct measurement of the fiber section recession using SEM. Comparing the fiber reactivity, the well-known expected tendencies have been verified as far as the fiber precursors and the thermal treatments are concerned. Moreover, the study has confirmed that the composite geometric reactivity was not an additive property with respect to that of its components [68]. The behavior of the 3D C/C seems to be linked to a weakest-link process, due to the presence of a weak interphase lying between the fibers and the matrices.

5 Multi-scale analytical modeling in steady state

Préambule

Ce chapitre constitue un projet de publication soumis à la revue *International Journal of Heat and Mass Transfer.*

Titre : Physico-chemical ablation of carbon-carbon composites : III- Multi-scale analytical modeling in steady state.

Auteurs : J. Lachaud[1], Y.Aspa[1,2] et G. L. Vignoles[1]

Affiliations :

[1]Laboratoire des Composites ThermoStructuraux (LCTS)

UMR 5801 : CNRS-SAFRAN-CEA-UB1

Domaine Universitaire de Bordeaux – 3, Allée de La Boétie, 33600 Pessac, France

[2]Institut de Mécanique des Fluides de Toulouse (IMFT),

1, allée Prof. Camille Soula, 31000 Toulouse, France

Résumé

La modélisation du comportement ablatif des composites carbone-carbone (C/C) est abordée en régime permanent via deux changements d'échelle : (i) échelle microscopique (fibre, matrice intra-fil) vers échelle mésoscopique (fil) et (ii) échelle mésoscopique (fil, matrice inter-fil) vers échelle macroscopique (composite homogénéisé). Le point de départ est un modèle général pour les surfaces récessives, associé à un processus de gazéification couplé à un transfert de masse isotherme. Ce modèle est résolu analytiquement à chaque échelle en considérant une architecture composite simplifiée et un transfert de masse perpendiculaire à la surface globale de l'échantillon. A chaque échelle, seulement deux paramètres sont nécessaires à la description du comportement des composites : un contraste de réactivité entre la phase la plus faible et la plus résistante, et un nombre de Sherwood. Les principaux résultats des modèles sont les prédictions : (i) de la géométrie de la rugosité de surface en fonction des paramètres physico-chimiques, (ii) de la réactivité effective des composites en fonction de celles de leurs composants, (iii) de la réactivité des composants d'un composite connaissant la géométrie de sa rugosité après ablation. Les modèles sont validés par comparaison au comportement de deux composites C/C ayant subi une ablation par oxydation, puis appliqués à l'analyse de l'état de surface d'un échantillon soumis à un plasma d'arc.

Abstract

The modeling of the complex behavior of carbon-carbon composites during ablation is addressed in steady state using two suitable changes of scale : (i) microscopic scale (fiber, intra-bundle matrix) to mesoscopic scale (yarn) and (ii) mesoscopic scale (yarn, inter-yarn matrix) to macroscopic scale (composite). The starting point is a general model for receding surfaces under a first order gasification process coupled to isothermal mass transfer by diffusion. It

has been analytically solved at each scale considering a simplified composite architecture and a mass flux perpendicular to the overall surface. At each scale, only two parameters are necessary to describe the material behavior : the reactivity contrast between the weakest and strongest phases and a Sherwood number. The main outputs of the models are : (i) the multi-scale surface roughness geometry versus physico-chemical parameters, (ii) the effective reactivity of the composite as a function of those of its components, (iii) the composite's component reactivity deduced by surface roughness analysis. The models have been validated by comparison to the behavior of two C/C composites during oxidation, and applied to the analysis of a plasma-jet experiment.

5.1   Introduction

This work is the third part of an article series which aims to improve the understanding of the behavior of carbon-carbon (C/C) composites during ablation by oxidation or sublimation, and to model it [61, 63–65].

During ablation, C/C composites develop multi-scale surface roughness features, which may display a strong coupling with the surrounding environment [31, 104]. The surface roughness, which chiefly arises from the heterogeneity of the composites, has been characterized in the first part [61]. Two carbon-based composites (a 3D C/C and a pyrolyzed 2D C/R) have been ablated by two different ways (a plasma-jet test and an oxidation test). The actual surface roughness of the ablated samples has been analyzed by microscopy and micro-tomography. A common multi-scale classification of surface roughness features has been proposed from microscopic scale to macroscopic scale. Then, a multi-scale phenomenological analysis dealt with the onset of roughness features, that is, the behavior of the C/C composites. On these bases, a multi-scale modeling strategy has been proposed. It includes three scales and the following two changes of scales (see figure 5.1) : (i) microscopic scale (fiber, intra-bundle matrix) to mesoscopic scale (yarn) and (ii) mesoscopic scale (yarn, inter-bundle matrix) to macroscopic scale (composite). According to the modeling strategy, and in order to feed the models, independent measurements of the reactivities of the fibers and of the available intra-bundle matrix have been carried out in the second part [62]. The reactivity of the composites has also been evaluated for the validation of the model after the two changes of scale. Interestingly, this work has confirmed, for the material of this study, a previous observation [68] : the composites gasification rates cannot be trivially inferred from those of their components. Using the microscopic scale properties, the present part aims to predict the composite behavior in steady state. The main expected outputs of the models are : (i) the surface roughness at mesoscopic and macroscopic scales, (ii) the multi-scale behavior of the C/C composites, as a function of experimental conditions and material properties.

This paper is organized as follows. In the second section, a general receding surface model including heterogeneous reaction on the composite and diffusion in the bulk fluid phase is set up. In the third section, this model is applied to assess the mesoscopic scale properties from the microscopic ones. Using suitable hypotheses on the material architecture and on the mass transfer, an analytical solution is proposed and its consistency is tested and exploited using a parametrical study. The results are compared with a previous parameter variation study carried out at mesoscopic scale using an efficient 3-D simulation code [67]. Another numerical work in 2-D at mesoscopic scale [41] is also revisited under the light of this model. In the fourth section, the model equations are also solved at macroscopic scale. It includes
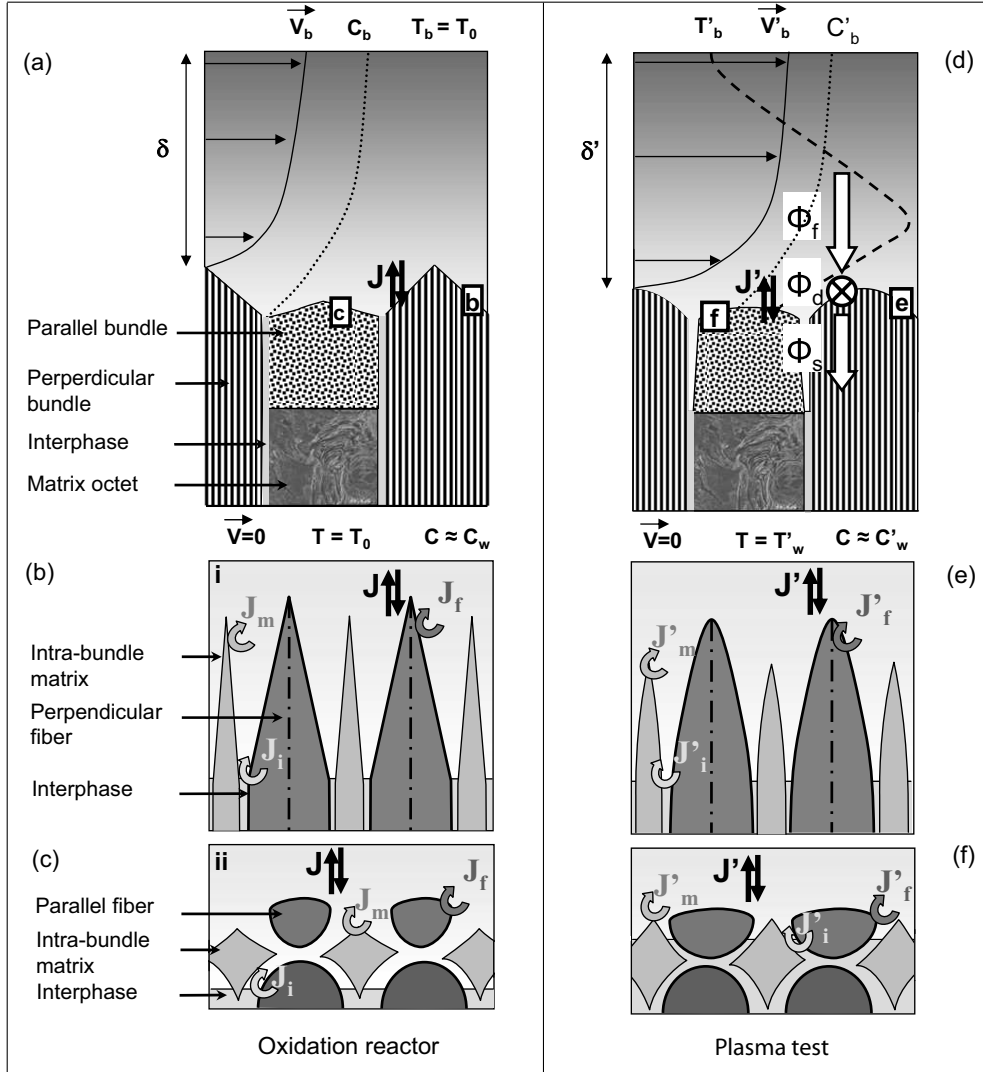
FIG. 5.1 – Modeling strategy : sketch of the coupled phenomena on a 3D C/C

the coupling of the two scales to infer the overall composite behavior. In the last section, a validation and an exploitation of the models is performed. First, the multi-scale model is validated by comparison to the experimental data obtained in oxidation conditions for the 3D C/C and the 2D C/R [62]. Incidentally, the reactivity of the interphase lying between the fibers and the bulk matrix [58] is evaluated by inverse analysis. Then, the model is applied for the analysis of the surface roughness of a 3D C/C ablated in a plasma jet test.

5.2 Model set-up

5.2.1 Scope of the model

The model presented in this section is a general model which applies to any physico-chemical ablation phenomena under the following hypotheses : (i) material in a dense flow,

(ii) negligible thermal gradients, (iii) negligible advection close to the wall, (iv) first-order gasification process leading to surface recession, (v) close to the wall, the mass Péclet number is low (mass transfer by diffusion). These hypotheses have been shown to be valid in the case of the oxidation test [61, 62]. The first step of this work is devoted to the modeling of the behavior of two C/C composites ablated using this latter test : a 3D C/C and a pyrolyzed 2D C/phenolic resin composite (2D C/R). Let the model be illustrated using the 3D C/C architecture. As represented on figure 5.1, the C/C composites are heterogeneous multi-scale materials. At microscopic scale, they are made of fibers (f), intra-yarn matrix (m_y) and sometimes interphase (i). At mesoscopic scale, they are made of yarns (y) – or bundles (b), inter-yarn matrix (m_c), and inter-yarn interphase. The oxidation experiments have been carried out under dry air at atmospheric pressure and a controlled temperature of $898\,K$ [62]. The chemical balance of the oxidation process writes [15] :

$$C_{(s)} \,+\, O_2 \,\rightleftharpoons\, CO_2 \tag{5.1}$$

In the conditions described above, this reaction is thermodynamically promoted : $\Delta_f G^\circ(CO_2) = -395\,kJ/mol$. Moreover, the equilibrium of the partial pressures of reactants and products is attained for : $P_{CO_2} = 10^{23}.P_{O_2}$ [15]. This implies that : (i) only the kinetic aspect of the reaction has to be taken into account, (ii) the reaction may be limited by a low partial pressure of O_2. Then, the diffusion of O_2 from the bulk of the fluid phase to the wall has to be modeled. Let J_e (in $mol.m^{-2}.s^{-1}$) be the molar impinging flux of oxygen per surface unit given by the first order kinetic law : $J_e = k_e.C_{O_2}$, with k_e (in $m.s^{-1}$) the intrinsic geometrical reactivity of the element e and C_{O_2} (in $mol.m^{-3}$) the reactant concentration on its surface [62].

5.2.2   Mathematical description

The following mathematical writing of the model may be applied to any first-order gasification process coupled to mass transfer by diffusion. Since the first step of the modeling strategy is to address the modeling of ablation by oxidation, let the mathematical formalism be presented using the oxidation notations.

Mass conservation of the reactant (of molar concentration $C = C_{O_2}$) in the fluid phase writes :

$$\frac{\partial C}{\partial t} + \nabla \cdot (-D\nabla C) \,=\, 0 \tag{5.2}$$

where D (in $m^2.s$) is the diffusion coefficient of O_2 in air.

Boundary conditions relative to the model domain are :
– On boundary layer top : a Dirichlet condition ($C = C_0$) ;
– At the fluid/solid interface the oxidation molar rate J_e above the solid element e writes :

$$J_e = (-D\nabla C) \cdot \mathbf{n} \,=\, -k_e C \tag{5.3}$$

where $\mathbf{n}$ is the normal to the surface ;
– On the lateral boundaries : symmetry or translation conditions.

The macroscopic motion of an interface between two media caused by the action of some process(es) can be interpreted as an advancing wavefront with a normal velocity equal to that of the interface. The interface is synonymously referred to as the surface S. Let a convenient mathematical description be introduced.
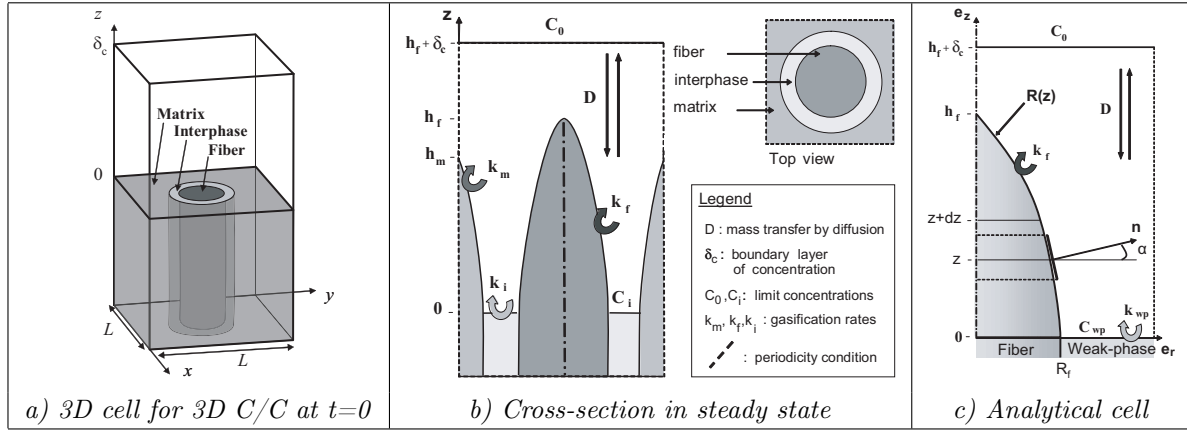
FIG. 5.2 – Scheme of the elementary pattern and of the proposed model

The interface position is commonly described in cartesian coordinates by the following scalar equation :

$$S(x, y, z, t) = 0 \tag{5.4}$$

such that the function S, which possesses almost everywhere first order partial derivatives, acquires nonzero values at all points not lying on the interface [53].

The function S satisfies the differential equation :

$$\frac{\partial S}{\partial t} + \mathbf{v_e} \cdot \nabla S = 0 \tag{5.5}$$

where $\mathbf{v_e} = v_e J_e \mathbf{n}$ is the surface local normal velocity , with v_e the solid molar volume of phase e [53]. Since in cartesian coordinates $\mathbf{n} = (S_x, S_y, S_z)/\sqrt{S_x^2 + S_y^2 + S_z^2}$, equation (5.5) can be rewritten into the convenient form :

$$S_t + v_e J_e \sqrt{S_x^2 + S_y^2 + S_z^2} = 0 \tag{5.6}$$

The interface position S is then given by the simultaneous resolution of equations (5.2) and (5.5) (or equation (5.6) in cartesian coordinates). For an analytical resolution, S can be rewritten under a more convenient explicit form like : $S = z - f(x, y, t)$. However, it requires the function $z = f(x, y, t)$ to be single-valued. For instance, the latter condition is not satisfied on vertical walls. Nevertheless, it is shown in section 5.3.4 that in some trivial cases the knowledge of the partial derivatives of f enable an extrapolation of S even if f is not single-valued.

Note that the above model may also be used for the description of ablation by sublimation (see subsection 5.5.3). Indeed, under Knudsen-Langmuir hypotheses, the sublimation problem is mathematically equivalent to the oxidation one considering vaporized carbon diffusion from the wall instead of reactant diffusion to the wall, and neglecting Stefan flux [32]. The effect of Stefan flux is presented and evaluated in subsection 5.5.3.

5.2.3 Concluding remarks on the modeling

The proposed model is sketched on figure 5.2-b for mesoscopic scale. On this scheme the stationary rough surface is represented ; at initial time, the fluid/solid interface is flat as

represented on figure 5.2-a. This profile has therefore to be obtained using a moving fluid/solid interface modeling (equation (5.5)). To rigorously cope with this latter point in 3-D and in transient regime on heterogeneous materials, one has to use efficient numerical simulation codes [2, 53, 67, 82]. However, even if simulation results are proved to be in agreement with the experimental observations and measurements, their exploitation is quite difficult and some conclusions arising from their analysis may be uncertain. Indeed, intuition is certainly of some help for the analysis of numerical results, but it can lead to some misinterpretations. The contribution of an analytical solution, despite some added hypotheses, is obvious. This work is motivated by this position.

This analytical part aims to model the multi-scale behavior of C/C composites of which yarn orientations are strictly perpendicular or parallel to the surface, as represented on figure 5.1. Following the modeling strategy, the problem is first addressed at mesoscopic scale (first change of scale) and then at macroscopic scale (second change of scale).

5.3   Mesoscopic scale analytical model

At mesoscopic scale, the 3D C/C composites are made of four components : inter-yarn matrix, inter-yarn interphase, parallel yarns (parallel to surface), and perpendicular yarns (perpendicular to surface). The gasification rate of the inter-yarn matrix is an input of the models. The behavior of the perpendicular yarns is quite difficult to cope with analytically at this scale because steady state cannot be strictly reached since they undergo layer-by-layer ablation, as represented on figure 5.1 [61]. Moreover they are shown to display no influence on the composite behavior in steady state (see subsection 5.4). Consequently, they are not modeled in this part. Nevertheless, their behavior and their effective gasification rates may be inferred numerically [64]. In this subsection, the behavior of the yarns that are perpendicular to surface is modeled in steady state. First, some added hypotheses, useful to solve analytically the model, are presented. Then, a complete resolution of the model is proposed. Finally, a parametrical study is followed by a discussion and a comparison to previous numerical studies.

5.3.1   Hypotheses

There are two kinds of added hypotheses : the first ones are on the material architecture, the second ones are on the physical phenomena. Concerning the first ones, inside the yarn, the fibers are assumed homogeneous, isotropic, perpendicular to surface, axi-symmetrical, and surrounded by an isotropic homogeneous weak phase, noted wp, which is either the interphase for 3D C/C or the matrix for 2D C/R. In the case of 3D C/C, as it is shown in the experimental part and represented on figure $5.2-b$, the height of the bulk matrix (h_m) is at any time lower than that of the fibers (h_f) – or at most equal. The hypotheses on the physical phenomena are : (i) the steady state is reached (numerical simulations in transient regime show that a steady state is always reached [67]), (ii) the weak-phase surface remains flat and perpendicular to the $\mathbf{z}$ axis (see figures 5.2-b and c). Some numerical simulations have shown that the roughness which develops on the weak-phase is negligible in front of the pointed fibers height (h_f) [67]. Moreover the numerical simulations also show that in steady state the gradient of reactant concentration is only vertical (along $\mathbf{z}$), that is, the mass transfer by diffusion is vertical [64]. This latter property has two main interests for the analytical modeling : first, the concentration profile at any point of the cell can be derived from a 1-D resolution of the model in steady state (see subsection below) ; second, it enables to address separately fiber and bulk matrix

recession in a 3D C/C (as mass transfer is then decoupled for these two phases). This second point, added to the fact that $h_m < h_f$, means that the intra-yarn matrix has no effect on the 3D C/C yarn behavior (see subsection 5.3.6). As its complex and irregular cross-section would make any analytical modeling of its behavior difficult, and since that it does not change the overall composite behavior, its modeling is not addressed is the present article. Nevertheless, the following model might be applied as well to the intra-yarn matrix.

5.3.2 Unidirectional Concentration gradient

Let the concentration gradient be determined. A simple approach is possible on a receding flat surface in steady state, solving the model presented above in that particular case. As justified above, the weak-phase surface is almost flat. Moreover, since it contains the lower part of the overall surface, the knowledge of the concentration above it provides the concentration in the whole fluid phase. The weak-phase surface S_{wp} can be described by : $S_{wp}(z,t) = h(t) - z = 0$. Let $V_a = \partial h / \partial t$ be the ablation velocity in steady state. Then, using the notations of figure $5.2-c$, equation (5.6) applied to S_{wp} gives :

$$V_a = -v_{wp} k_{wp} C_{wp} \tag{5.7}$$

where $C_{wp} = C(z = 0)$.

Assuming a vertical concentration gradient and steady state, equation (5.2) becomes : $\partial^2 C / \partial z^2 = 0$, with the following boundary conditions : $C(z = h_f + \delta_c) = C_0$ and $C_z(z = 0) = C_{wp} k_{wp} / D$. Hence, $C(z)$ at each point of the fluid phase is found to be :

$$C(z) = C_{wp} + \frac{C_0 - C_{wp}}{h_f + \delta_c} z \tag{5.8}$$

with $C_{wp} = C_0 / (1 + Da_{wp})$, where $Da_{wp} = k_{wp}(h_f + \delta_c)/D$ is a Damköhler number.

Equation (5.8) can be rewritten under the following non-dimensional form :

$$\widehat{C}(\widehat{z}) = \frac{1}{1 + Da_{wp}} \left(1 + Da_{wp} \, \widehat{z} \right) \tag{5.9}$$

with $\widehat{C} = C/C_0$ and $\widehat{z} = z/(h_f + \delta_c)$. $\widehat{C}$ is plotted on figure 5.3. Note that the normalized ablation velocity $\widehat{V_a} = V_a/(-v_{wp}k_{wp}C_0)$ is given by $\widehat{V_a} = \widehat{C}(\widehat{z} = 0)$ (see figure 5.4). The concentration gradient in the concentration boundary layer is a linear function of $\widehat{z}$ by definition (Fick's law). In reaction-limited regime ($Da_{wp} < 0.01$), the concentration is equal to C_0 in the whole fluid phase : the diffusion velocity is large compared to the gasification rate. In the converse case, the concentration close to the wall is null : the regime is diffusion-limited ($Da_{wp} > 100$). Between these two limits, the regime is called intermediate or mixed : the concentration value on the wall (as well as the normalized ablation velocity) stems from a competition between reaction and diffusion.

5.3.3 Differential equation of fibers surface

First, the equation of fiber surface is obtained by solving rigorously the mathematical model presented above in cylindrical coordinates. Two resolution methods are provided.
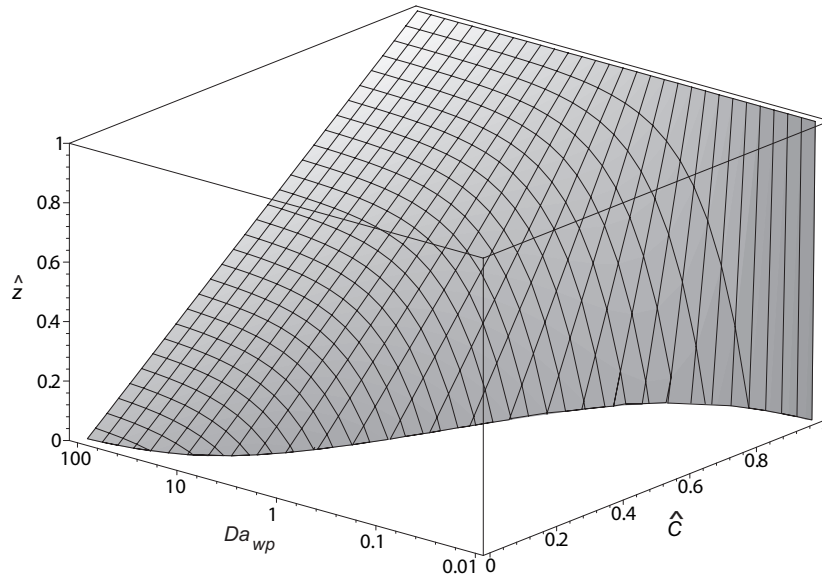
FIG. 5.3 – 3D plot of the normalized concentration $\widehat{C}$ versus Da_{wp} and $\widehat{z}$
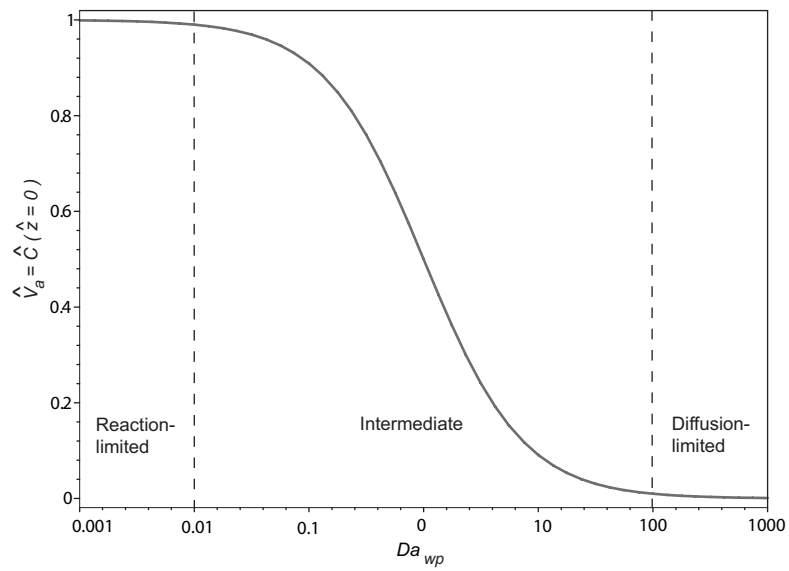
FIG. 5.4 – Plot of the normalized ablation velocity $\widehat{V_a}$ versus Da_{wp}. Identification of the different regimes.

5.3.3.1 First method

As represented on figure 5.2-c, the surface of an axi-symmetric fiber stripped by ablation can be described by the following equation in cylindrical coordinates : $S_f(r, \theta, z, t) = r - R(z, t)$. Substituting the derivatives in cylindrical coordinates of S_f in equation (5.5), one obtains :

$$-\frac{\partial R}{\partial t} + \upsilon_f J_f(z) \sqrt{\left(\frac{\partial R}{\partial z}\right)^2 + 1} = 0 \qquad (5.10)$$

where

$$\frac{\partial R}{\partial t} = \frac{\partial R}{\partial z} \frac{\partial z}{\partial t} = \frac{\partial R}{\partial z} V_a \qquad (5.11)$$

and where $J_f(z) = -k_f C(z)$.

Combining these results with the results of the unidirectional concentration gradient, $R(z)$ is found to be given in steady state by the following differential equation :

$$\frac{dR}{dz} = -\frac{1 + \frac{z}{La}}{\sqrt{A^2 - (1 + \frac{z}{La})^2}} \qquad (5.12)$$

where $A = (k_{wp}\upsilon_{wp})/(k_f \upsilon_f)$ and $La = D/k_{wp}$ are respectively a dimensionless number and a characteristic length of ablation. Equation (5.12) is defined only for $z \in [0, La(A - 1)[$. As sketched on figure 5.2-c, the boundary condition for integration is $R(z = 0) = R_f$.

Note that equation (5.12) features the first non trivial result : the value of C_0 and the size of the boundary layer δ_c have no influence on the material behavior in terms of surface roughness, whereas they are shown to strongly affect the ablation velocity (equations (5.7) and (5.8)). This result is also obtained by numerical simulation [3, 64, 67].

5.3.3.2 Second method

This second method provides a more concrete understanding of equation (5.12). Let the fiber tip surface be given by the function $R(z)$, represented on figure 5.2−c. In steady state, the weak phase recession along $\mathbf{e_z}$ is V_a at $z = 0$, while at this ordinate the fiber recession along $\mathbf{e_z}$ is necessarily null, since the fiber is protected by the weak phase. In other words, in a moving referential of velocity $V_a \mathbf{e_z}$ (note that $V_a < 0$), the weak-phase would seem static while the fiber would appear emerging from the weak-phase surface at a velocity $-V_a \mathbf{e_z}$. The steady state is made possible because the fiber is progressively ablated along $\mathbf{e_r}$ until it disappears ($R(z) = 0$ for some z). Then, as represented on figure 5.2−c, the value of $R(z + dz)$ is smaller than the value of $R(z)$, since it has been submitted to an ablation along $\mathbf{e_r}$ during an additional duration dt. In steady state, this duration is given by the vertical ablation velocity : $dt = dz/(-V_a)$. The horizontal ablation velocity $V_r(z)$ on the fibers is given by the projection on $\mathbf{e_r}$ of the normal ablation velocity $V_n = -\upsilon_f k_f C(z)\mathbf{n}$:

$$V_r = -\frac{\upsilon_f k_f C(z)}{cos(\alpha)} \qquad (5.13)$$

where $\alpha = (\mathbf{e_r}, \mathbf{n})$.

Then, in steady state, the increment of R between z and $z + dz$ writes :

$$R(z + dz) - R(z) = \frac{v_f k_f C(z)}{V_a cos(\alpha)} \, dz \tag{5.14}$$

Standard trigonometry gives :

$$\frac{1}{cos(\alpha)} = \sqrt{1 + \left(\frac{dR}{dz}\right)^2} \tag{5.15}$$

Summing up, one has :

$$\frac{R(z + dz) - R(z)}{dz} = \frac{dR}{dz} = \frac{v_f k_f C(z)}{V_a} \sqrt{1 + \left(\frac{dR}{dz}\right)^2} \tag{5.16}$$

Combining this result with equation 5.8, equation (5.12) is obtained again.

5.3.4   Solutions

First, the limiting cases are studied, then equation (5.12) is solved in the general case and interpreted in terms of physical fiber surface.

5.3.4.1   Reaction-limited regime

A reaction-limited regime is attained when the gasification rate is low compared to mass transfer. Hence, the concentration in the fluid phase is equal to C_0 everywhere (figure 5.3). In the present case, the mass transfer being restricted to pure diffusion, it means that La tends to infinite, or at least is large compared to any characteristic length of the problem. Then, with $La >> z$, equation (5.12) can be simplified :

$$\frac{dR}{dz} = -\frac{1}{\sqrt{A^2 - 1}} \tag{5.17}$$

The integration of equation (5.17) with the boundary condition $R(z = 0) = R_f$ gives the fiber geometry for a reaction-limited regime :

$$R(z) = R_f - \frac{z}{\sqrt{A^2 - 1}} \tag{5.18}$$

with $z \in [0, R_f\sqrt{A^2 - 1}]$.

The fiber is then a cone of height $h_f = R_f\sqrt{A^2 - 1}$ (see figure 5.5-a). Substituting $C_{wp} = C_0$ into equation (5.7), the ablation velocity is found to be driven only by the weak phase :

$$V_a = -v_{wp} k_{wp} C_0 \tag{5.19}$$

This result has a great physico-chemical implication. In the applications for which ablation is limited by the reaction (quite often), it is useless trying to improve the strong phases as far as a steady-state regime is attained. The weak-phase has definitely to be improved first. This result reinforces the following previous analysis : the oxidation of carbon/carbon composites is predominantly controlled by interphases [38, 62].

5.3.4.2   Diffusion-limited regime

In the converse case, when the gasification rate is low compared to mass transfer, a diffusion-limited regime establishes. La tends to zero. Since A is limited (for obvious physical reasons), the definition domain of equation (5.12) shrinks to an empty set. Indeed, the problem becomes 1-D : the wall remains flat, no surface roughness appears (see figure 5.5-f). Combining equations (5.7-5.8) for $h_f = 0$ and $L_a \to 0$, the recession velocity in diffusion-limited regime writes :

$$V_a = -\frac{v_{wp} C_0 D}{\delta_c} \tag{5.20}$$

Hence, this case is well described by the 1-D problem plotted on figures 5.3 and 5.4 for $Da_{wp} > 100$; the ablation velocity no longer depends on the oxidation rates, and the surface remains flat.

5.3.4.3   Trivial cases

When $A = (k_{wp} v_{wp})/(k_f v_f)$ tends to 1, or R_f tends to zero, the problem also turns out to be 1-D [67]. Then, in the following, it is assumed that $A > 1$ and $R_f > 0$.

5.3.4.4   General case

The integration of equation (5.12) gives the equation of the fiber surface $S_f(r, \theta, z) = r - R(z) = 0$ where :

$$R(z) = La \left(\sqrt{A^2 - \left(1 + \frac{z}{La} \right)^2} - \sqrt{A^2 - 1} \right) + R_f \tag{5.21}$$

with $z \in [0, La(A-1)[$ and $R(z) \geq 0$.

Note that if $R_f/La \geq \sqrt{A^2 - 1}$ then $R(La(A-1)) > 0$ and $\lim_{z \to La(A-1)}(\frac{dR}{dz}) = -\infty$, *i.e.* the slope at this point is horizontal. The surface S_f, which is no longer single-valued in this case, has to be extrapolated using this limit (see section 5.2.2). The value of the derivative tends to support the idea that the fiber tip exhibits a plateau and its height is limited, with $h_f = La(A-1)$. One has then to verify that the steady state is possible under this hypothesis. The equality between the recession velocity of the fiber on the plateau (V_z^f) and the weak-phase one (V_a) is to be obtained for a the fiber height $h_f = La(A-1)$. Combining equations (5.7) and (5.8), the recession rate on the plateau of the fiber is found to be :

$$V_z^f = v_f k_f C_0 \frac{1 + Da_{wp} h_f/(h_f + \delta_c)}{1 - Da_{wp}} \tag{5.22}$$

and it is shown to be equal to V_a for a unique value of h_f, which is the previously found value $h_f = La(A-1)$. The surface S_f has then to be extrapolated by a plateau (see figure 5.5-e).

Since R_f is supposed strictly positive, equation (5.21) can be rewritten for a parametrical study in the following convenient dimensionless form :

$$\widetilde{R}(\widetilde{z}) = Sh^{-1} \left(\sqrt{A^2 - (1 + Sh\,\widetilde{z})^2} - \sqrt{A^2 - 1} \right) + 1 \tag{5.23}$$

| a) Sh = 0.01 | b) Sh = 0.1 | c) Sh = 1 | d) Sh = 5 | e) Sh = 10 | f) Sh = 100 |
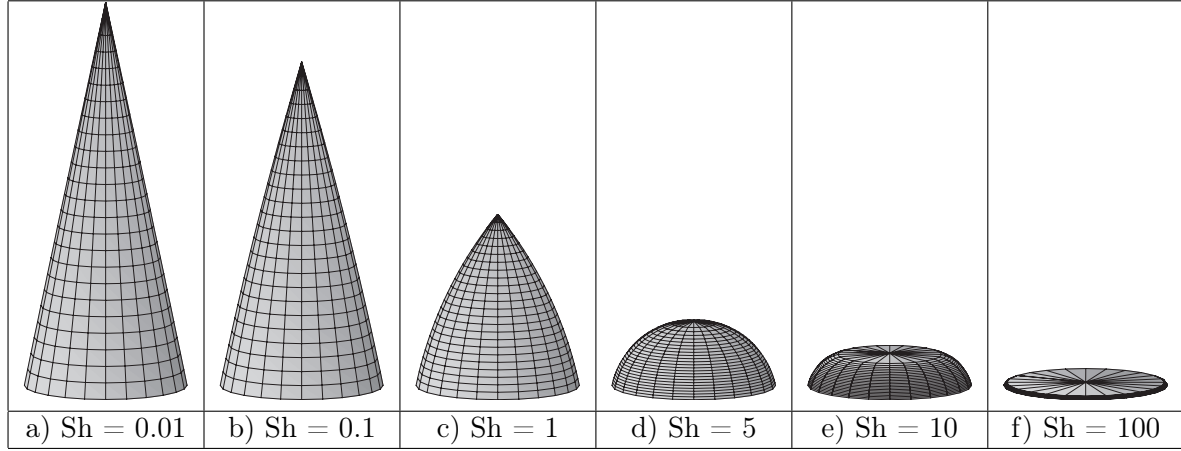
FIG. 5.5 – Fiber morphology at steady state as a function of Sh (with $A = 5$).

where, $\widetilde{R} = R/R_f$, $\widetilde{z} = z/R_f$, and $Sh = R_f/La = R_f\,k_{wp}/D$ is a Sherwood number, and with the condition $\widetilde{z} \in [0, (A-1)/Sh[$. This is the equation of a circle arc (sphere segment) with center at $(\widetilde{R} = 1 - \sqrt{A^2 - 1}/Sh\,;\widetilde{z} = -1/Sh)$ and radius A/Sh.

The reduced height $\widetilde{h} = h_f/R_f$ is an explicit function of A and Sh :

$$\widetilde{h} = \sqrt{Sh^{-2} + 2Sh^{-1}\sqrt{A^2 - 1} - 1} - Sh^{-1} \tag{5.24}$$

with $Sh < \sqrt{A^2 - 1}$, leading to an ogival fiber. In the converse case, as explained above, the fiber tip is a plateau and $\widetilde{h} = (A - 1)/Sh$.

In the experimental part, the angle at the tip of the fibers α_f has been evaluated for the pointed fibers in steady state. For $Sh < \sqrt{A^2 - 1}$ pointed fibers are theoretically obtained ; the expression of α_f in degrees is found to be :

$$\alpha_f = \frac{180}{\pi}\,2\,Arctan\left(-\frac{\partial\widetilde{R}}{\partial\widetilde{z}}(\widetilde{z} = \widetilde{h})\right) = \frac{360}{\pi}\,Arctan\left(\frac{1 + 2\widetilde{h}\,Sh}{\sqrt{A^2 - \left(1 + \widetilde{h}\,Sh\right)^2}}\right) \tag{5.25}$$

5.3.5   Parametrical study and analysis

The emerging fiber morphology, given by equation (5.23) and represented on figure 5.5 for $A = 5$, is a function of the Sherwood number $(Sh = R_f\,k_{wp}/D)$ and the contrast of the intrinsic oxidation rates $(A = (k_{wp}v_{wp})/(k_f v_f))$. The Sherwood number is an indicator of the regime : if it tends to infinite, the recession is controlled by diffusion and there is no roughness $(Sh > 100$ for $A = 5)$; if it tends to zero, reaction controls recession, and the surface roughness is maximal (conical fibers : $Sh < 0.01$ for $A = 5$) ; between these two limits the regime is intermediate (ogival fibers, possibly with a plateau : $0.01 < Sh < 100$). The number A is an indicator of the reactivity and density contrast between the fiber and the interphase. The higher it is, the higher $\widetilde{h}$ is, as soon as the mass diffusion process does not bring a limitation. In reaction-limited regime, when A is large, the increase of $\widetilde{h}$ is almost linear with A, as represented on figure 5.6 which has been plotted using equation (5.24). Indeed, for $A >> 1$, equation (5.18) gives $\widetilde{h} \sim A$. However, in diffusion-limited regime, A has no effect on the yarn
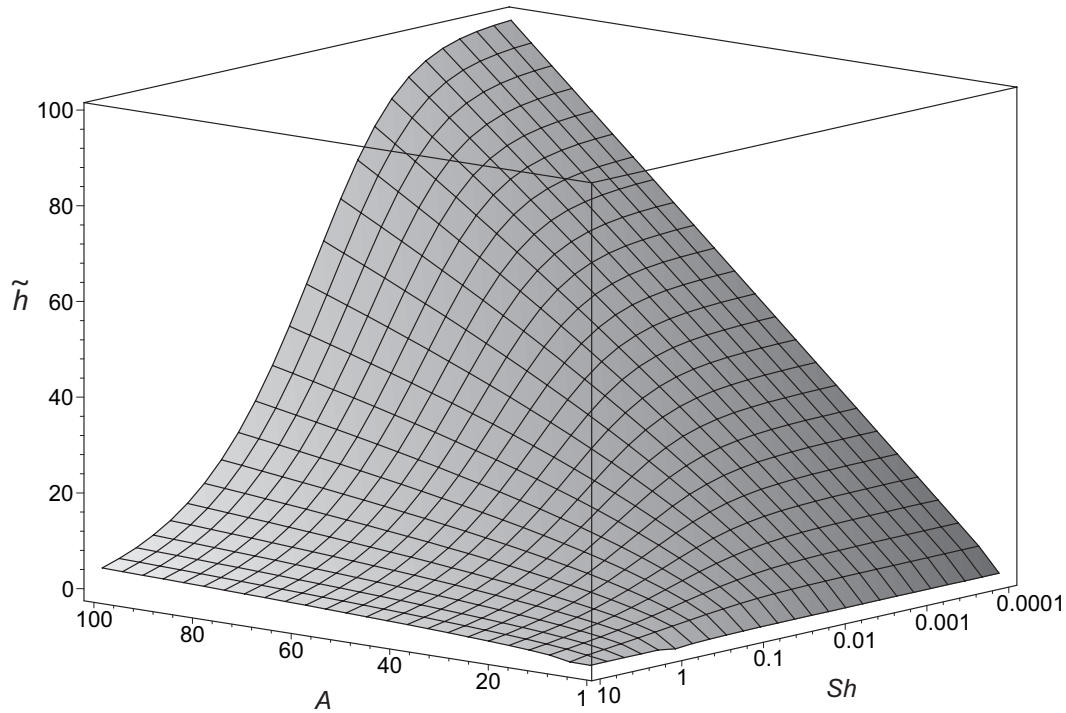
FIG. 5.6 – Plot of the reduced height $\widetilde{h}$ as a function of A and Sh.

behavior (see equation (5.20) and figure 5.6). In the intermediate regime, the evolution of $\widetilde{h}$ and of the fibers morphology versus A is no longer linear : the yarn behavior is a complex mixture law resulting from a competition between diffusion and reaction.

Figure 5.7 shows fiber geometries for various values of A for a constant ratio $A/Sh = 10$. In other words, it is a parametrical study on k_{wp}, whereas the other variables are taken constant. This figure tends to temper the widespread idea that the weak phase controls the oxidation when the composite seems to lie in reaction-limited regime. Indeed, as represented on this figure, the interphase seems to play a great role because it recedes first and because the fibers become sharp. The figure shows well that the increase of A (that is, of k_{wp}) has a great influence on the yarn behavior when A is low. However, when A becomes larger, its influence decreases until it disappears : for values of A higher than 500 the fiber morphology does not change any more (figure 5.7). This is due to a limitation by diffusion on the weak-phase, while the tip of the fiber is still in reaction-limited regime. Then, the weak-phase is fully protected by the fiber.

In the other intermediate cases, the weak phase is only partially protected by the matrix. According to the physico-chemical parameters, summed up in A and Sh, this phenomenon leads either to sharp (figure 5.5-a, b, c), rounded (figure 5.5-d), or button-shaped (figure 5.5-e, f) fiber tips. The analysis of the morphology of a fiber should enable to assess, by inverse analysis, the values of A and Sh. Indeed, the evaluation of the two geometrical parameters α_f and h_f are sufficient to determine A and Sh. It is easy to do such an inverse analysis on an analytical plot of the fiber geometry. However, the experimental part shows that the experimental evaluation of α_f is difficult, or even impossible in certain cases. Then, the effective gasification rate, which is experimentally easier to determine than α_f, may be used as a third
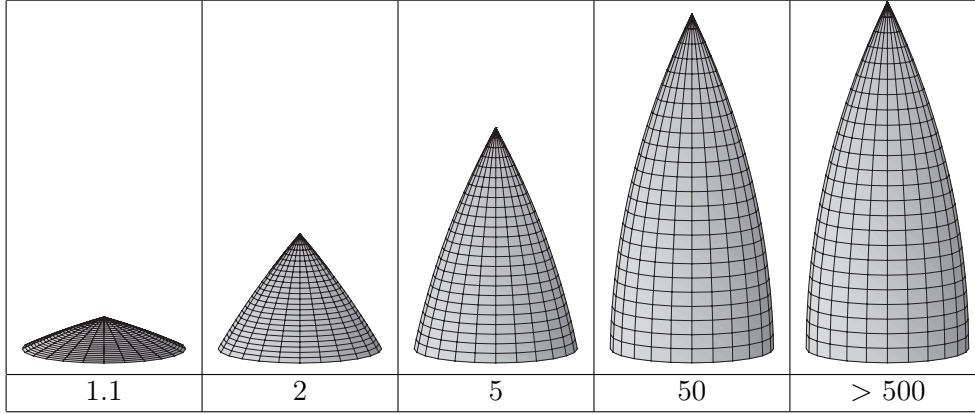
FIG. 5.7 – Fiber morphology at steady state as a function of A (with $A/Sh = 10$).

experimental parameter. This is addressed in the following.

5.3.6   Effective gasification rate

The effective gasification rate has to take into account the multi-scale behavior of the composite. Two up-scalings are then useful to determine its expression : (i) micro-scale (fiber) to meso-scale (yarn) and (ii) meso-scale (yarn) to macro-scale (composite). In the present section, the first change of scale is addressed.

The composite behavior in terms of surface roughness at mesoscopic scale has been shown not to depend on δ_c and C_0 ; then, the effective reactivity of the composite can be assessed using any value of δ_c. From the point of view of the flow passing over the material, the analytical model solved above is only correct if the mass Péclet number is low. In the oxidation reactor, this condition is verified [62]. In the case of plasma tests, it is in particular ensured by the no-slip condition on the rough surface. Actually, the rough surface is a volumic rough interface. It is not a trivial matter to determine in 3-D at which depth inside the rough interface the no-slip condition has to be applied. The knowledge on the subject is still limited for sharp roughness features. In view of the large density of pointed fibers, let the non sliding condition be applied at fiber tip. Then, in all the cases, it would be profitable to assess the effective reactivity at the height h_f ($\delta_c = 0$) using a formal concentration on the wall $C_w = C(z = h_f)$. Note that the concentration on the wall C_w may be determined at macro-scale (see subsection 5.4), just as C_{wp} is determined at meso-scale. The idea is then to replace the volumic cell of figure 5.2-c by an equivalent reactive and recessive surface placed horizontally at ordinate $z = h_f$. The aim of this up-scaling is to infer by homogenization a homogeneous material whose surface would have the chemical properties of the actual rough yarn. This would provide : (i) a law giving the effective properties of the yarn combining those of its components for a comprehensive analysis of the yarn behavior, (ii) input values for the model at macroscopic scale. The ablation velocity of a representative elementary surface (RES) of the yarn writes :

$$\begin{cases} V_{a,y} & = & -v_y k_y C_w \\ v_y & = & (\varepsilon_f/v_f + \varepsilon_{wp}/v_{wp} + (1 - \varepsilon_{wp} - \varepsilon_f)/v_m)^{-1} \end{cases} \qquad (5.26)$$

where k_y is the gasification rate of the yarn, and v_y the solid molar volume of the yarn, with ε_i the volume fraction of phase i. This change of scale is used for the sample analysis in
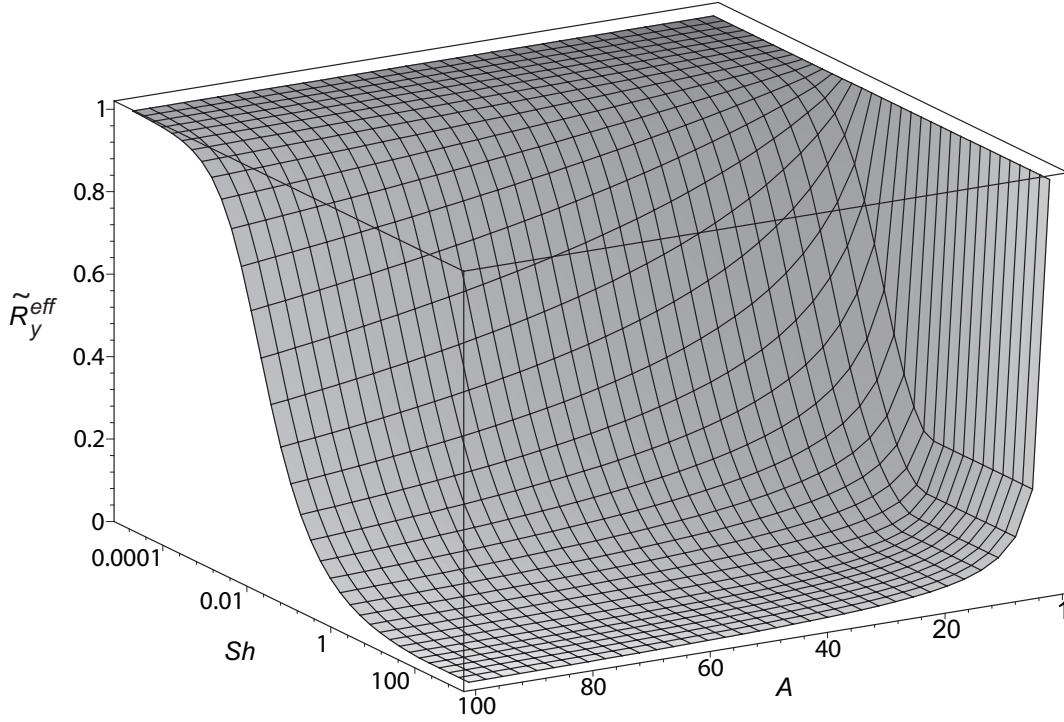
FIG. 5.8 – Normalized effective gasification rate of a yarn $\widetilde{R}_y^{eff}$ as a function of A and Sh.

section 5.5. Then, it has to take into account the actual architecture of the composite. That is why the notion of RES is introduced here, though the model is applicable to any fiber of the yarn. The RES must be large enough to be representative of the actual homogenized quantity : $v_y k_y$. Indeed, one notes a non negligible standard deviation in the measurement of the fiber bundles properties [61]. The value of v_y is directly connected to these local variations. The value of k_y is indirectly linked to these variations via the variations of k_{wp}, k_f, R_f. Then, the size of the RES has to be large in front of these local variations, which are of the order of a fiber diameter. The homogenized quantity $v_y k_y$ may then be associated to a representative surface of approximatively ten fiber diameters square. However, the yarn itself may be submitted to morphological variations (see section 5.4). Consequently, the RES must be elementary, that is, small with respect to the size of the phenomena that take place on the yarn. The section 5.4 shows that the size to take into account is the yarn section of width l. Hence, one has to verify $l < 100\,(2R_f)$. It is the case for the materials of this study.

The gasification ratio $\widetilde{R}_y^{eff} = (v_y k_y)/(v_{wp} k_{wp})$ is a convenient normalized form to express the effective gasification rate associated to a RES of the yarn. Combining equations (5.7), (5.8), (5.24) and (5.26), $\widetilde{R}_y^{eff}$ is obtained :

if $0 \leq Sh < \sqrt{A^2 - 1}$:

$$\widetilde{R}_y^{eff} = \frac{1}{\sqrt{1 + 2Sh\sqrt{A^2 - 1} - Sh^2}} \tag{5.27}$$

else if $Sh \geq \sqrt{A^2 - 1}$:

$$\widetilde{R}_y^{eff} = \frac{1}{A} \tag{5.28}$$

$\widetilde{R}_y^{eff}$ is plotted on figure 5.8 as a function of A and Sh, using, in the respective suitable domains, equations (5.27) and (5.28). Of course, the effective gasification rate of the yarn being lower or equal to that of the weakest phase, $\widetilde{R}_y^{eff}$ is lower than 1. For a given value of $v_{wp}k_{wp}$, the effective reactivity decreases with the increase of A and Sh. Indeed, A increases the strength of the fibers, which thus tend to protect the weak-phase provided the regime is not limited by reaction (as seen in the above subsection and on figure 5.8). When Sh is low, the ablation is limited by reaction (conical fibers), and then the effective reactivity is that of the weak-phase. When Sh becomes larger, after a transition to a mixed regime (ogival fibers), the ablation is limited by diffusion (no surface roughness), then the effective reactivity decreases. As a conclusion, this theoretical analysis reinforces the widespread idea, arising from experimental observations, that the effective ablation rate of the composite cannot be modeled using a simple arithmetic average of the ablation rates of its components [38,68].

5.3.7   Comparison of the results with two previous numerical works

The model has been solved recently in 3-D using a homemade simulation code based, among others, on random walks (diffusion) and an efficient surface description (moving reactive interface) [67,97]. A parametrical study has been carried out on the fibers morphologies in steady state [67]. The conclusions are in correct agreement with the analytical geometries presented above.

The model had been first numerically solved in 2-D in 1995 [41], using a finite difference scheme, with the following values : $k_f = 2.10^{-4}\,m/s$, $k_{wp} = 4.10^{-3}\,m/s$, $v_f = v_{wp}$, $R_f = 33\,\mu m$, and $D = 2.10^{-4}\,m^2/s$. Then, one has : $A = 20$, and $Sh = 6.6\,10^{-4}$. Hence the regime is very close to the reaction-limited regime (see figure 5.8) : oxidation is mainly driven by the weak-phase. Using equations (5.23) and (5.24), the fiber geometry can be assessed as conical with $\widetilde{h} \simeq 19.9$. The value for $\widetilde{h}$ numerically obtained in [41] is about 18. The error, around 10%, is likely to arise from some numerical approximations. In particular, the interface description, using a quadrangular approximation, may have introduced uncertainties in the resolution, as the orientation of the interface is shown to play a role in the onset of surface roughness [53] (see section 5.3.3). In the discussion of [41], it is underlined that the recession of the highly oxidizable layers slows down modestly with time, as the oxygen concentration at the bottom of the crevice is reduced. Indeed, according to equation (5.27), due to the protection of the weak phase by the fiber, the ablation velocity decreases by 1.3% in steady state. As a conclusion, the study presented in [41] is in good agreement with the present results.

5.4   Macroscopic scale analytical model

In this section, the second up-scaling is addressed. The steady state behavior of the composite is inferred from that of its mesoscopic components (intra-yarn matrix, perpendicular yarns, parallel yarns). First, the hypotheses of the problem are presented. Then, an analytical resolution of the problem is proposed, using the mathematical results of the mesoscopic scale. A parametrical study is carried out and discussed. The effective properties of the perpendicular yarn in steady state are then used to link the scales between themselves.

5.4.1   Hypotheses

Once more, some assumptions on the material structure and on the physico-chemical phenomena are to be added to that of the general model.

Concerning the first ones, at macroscopic scale, the perpendicular yarns can be assumed homogeneous, isotropic, strictly perpendicular to surface, and having a rectangular section surrounded by a weak phase, noted $wp - y$. Let the first two non-trivial hypotheses be discussed. As represented on figure 5.9-a, whose notations and associated model are depicted in the following subsection, in steady state the perpendicular yarn tips are somehow sharp, like the fibers [61]. Then, the local normal $\mathbf{n}$ to the elementary surface $dS(z)$ features an angle α_y with the horizontal. As represented on figure 5.9-b, and justified in subsection 5.3.6, the yarn surface is actually defined by the tips of the fibers. Moreover, according to equation (5.5), the local surface recession occurs along $-\mathbf{n}$. In consideration of the small size of the RES as compared to the yarn section, the local concentration on the wall $C_w(z)$ at ordinate z for a RES may be considered as constant. Then, the local 3-D cell can be represented by the scheme of figure 5.9-c. The associated model is the same as for the mesoscopic scale, except that the fibers are tilted of an angle $\pi/2 - \alpha_y$. This problem is solved for various angles in transient regime in [64]. The two main conclusions are : (i) steady state is always reached, (ii) the effective ablation velocity is not a function of α_y. In other words, the effective ablation rates obtained analytically for perpendicular fibers are usable for any orientation. Moreover, this result shows the accuracy of the assumption according to which the yarn could be considered as homogeneous and isotropic at macroscopic scale.

In the case of 3D C/C, the yarns section is square, and the weak phase associated to the perpendicular yarn is a pitch-based graphitized matrix, which constitutes an interphase between the perpendicular yarns and either the bulk inter-yarn matrix or the parallel yarns. The experimental part shows that both the bulk inter-yarn matrix and the parallel yarns appear lower than the perpendicular yarns, but higher than the weak phase. Concerning 2D C/R, in transient regime, the notches created by the recession of the inter-yarn matrix are progressively filled through a lateral extension of the parallel yarns. Then, in steady state, the weak phase is made of very porous parallel yarns. For both materials, at macroscopic scale, the weak phase is assumed homogeneous, isotropic, flat, and smooth. One should note that this hypothesis is equivalent the supposition that an up-scaling is possible to assess the effective ablation rate of the weak phase in steady state.

The hypotheses on the physical phenomena are : (i) the steady state is reached at all scales, (ii) vertical concentration gradient, (iii) the weak-phase surface associated to the yarns can be modeled by a flat surface perpendicular to the $\mathbf{z}$ axis, and (iv) the duration of the transient regime at mesoscopic scale is negligible compared to that at macroscopic scale. The 3-D numerical modeling of the experimental reactor has shown that the mass transfer is globally vertical on almost all the sample surface and restricted to diffusion [62]. Naturally, on the edges, the transfer is more complex. However, the sample is large : the edge effects on the overall composite behavior can be safely neglected. In any case, the middle part of the sample may be considered for the modeling.

5.4.2   Equation of perpendicular yarns surface

Under the above hypotheses, the macroscopic scale model is equivalent to that of the mesoscopic scale. This is represented on figure 5.9-a, where δ_{c-y}, C_{0-y} and h_y are the respective counterparts for the yarn of δ_c, C_0 and h_f for the fiber. However, this time, the surface of

a perpendicular yarn stripped by ablation features a rectangular cross-section of dimensions $l \times L$ (with $l < L$). Note that, in the case of 3D C/C yarn, one has $l = L$, $l/2$ being the homologue of R_f. Naturally, the geometry of a rectangular-section yarn is more efficiently described in cartesian coordinates : $S_y(x, y, z, t) = z - F(x, y, t) = 0$. The equation of the surface $z = F(x, y)$ in steady state can be derived using the method developed in subsection 5.3. One notices that in equation (5.5) the gradient along $\mathbf{e_r}$ in cylindrical coordinates is equivalent to both gradients along $\mathbf{x}$ and $\mathbf{y}$ in cartesian coordinates. Then, the results of the mesoscopic scales can be converted to macroscopic scale. Hence, using the suitable notations, $z = F(x, y)$ is inferred from equation (5.24). In cartesian coordinates, $z = F(x, y)$ writes :

$$z = min(f(x), f(y)) \quad \text{with} \quad (x, y) \in [-l/2, l/2] \times [-L/2, L/2] \quad \text{where} \tag{5.29}$$

if $l < 2\,La_y\,\sqrt{A_y^2 - 1}$

$$f(x) = La_y\left(\sqrt{A_y^2 - \left((|x| - l/2)/La_y + \sqrt{A_y^2 - 1}\right)^2} - 1\right) \tag{5.30}$$

if $L < 2\,La_y\,\sqrt{A_y^2 - 1}$

$$f(y) = La_y\left(\sqrt{A_y^2 - \left((|y| - L/2)/La_y + \sqrt{A_y^2 - 1}\right)^2} - 1\right) \tag{5.31}$$

else

$$f(x) = f(y) = La_y\,(A_y - 1) \tag{5.32}$$

where $La_y = D/k_{wp-y}$ is a length associated to the perpendicular yarn and $A_y = (k_{wp-y}\upsilon_{wp-y})/(k_y\upsilon_y)$ is the ratio between the ablation rates of the weak phase surrounding the yarn and the yarn itself.

5.4.3   Discussion

According to this model, the perpendicular yarns should emerge from the weak phase surface and adopt a pyramidal geometry if diffusion is not limiting. Let the Sherwood number associated to the yarns be : $Sh_y = l/(2La_y) = l\,k_{wp-y}/(2D)$. The morphology of a square-section yarn is represented as a function of Sherwood number for $A_y = 5$ on figure 5.10. Naturally, the evolution of the yarn morphology with the physico-chemical parameters is comparable to that of the fibers, since the model is the same. Nevertheless, note that in the general case $Sh_y >> Sh$ and $A_y \neq A$; then in a C/C composite, the behavior at macroscopic scale may be different from the behavior at mesoscopic scale. For instance, the regime may be reaction-limited at mesoscopic scale, while it could be intermediate at macroscopic scale (see subsection 5.4.4 and section 5.5). The same remarks apply for the rectangular-section yarn morphologies represented on figure 5.11 for $L/l = 5$. The width l drives the yarn height, since $f(x) < f(y)$ (equation (5.29)). Then, it also drives the perpendicular yarn behavior and the effective reactivity of the composite, since the parallel yarns appear lower.

a) Yarn section   b) Zoom on yarn section   c) Equivalent model
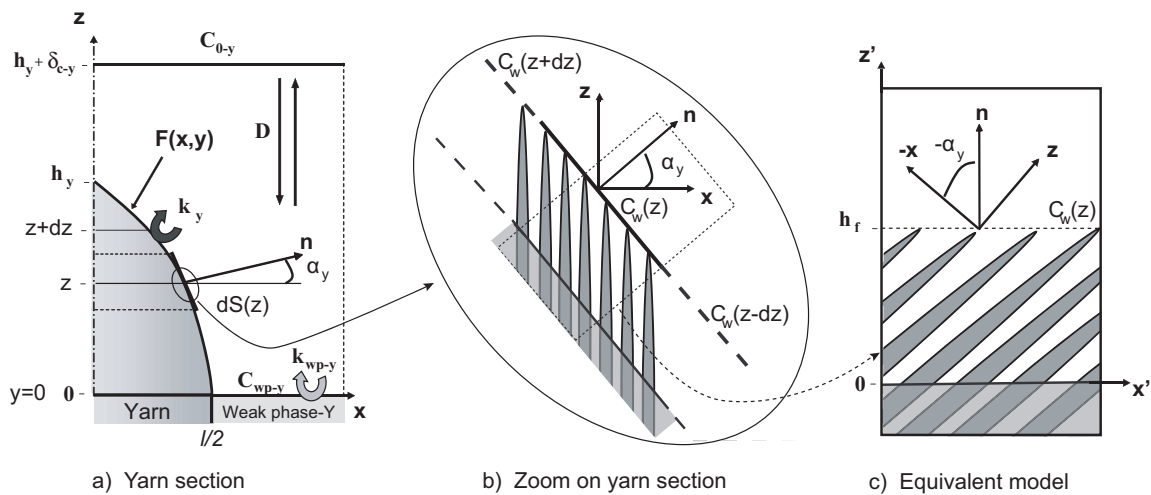
FIG. 5.9 – Scheme of the multi-scale surface roughness and of the associated multi-scale model for a C/C composite.

| 0.01 | 0.1 | 1 | 5 | 10 | 100 |
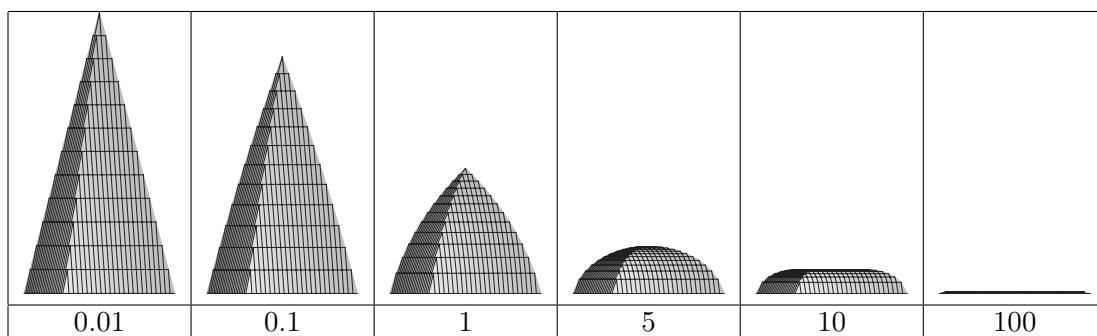
FIG. 5.10 – Square-sectioned yarn morphology at steady state as a function of Sh (with $A = 5$).

| 0.01 | 0.1 | 1 | 10 |
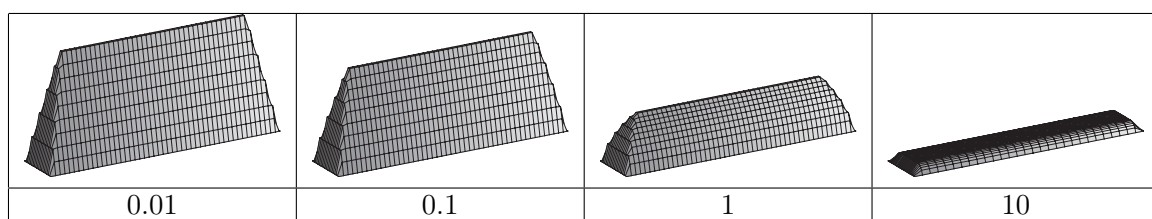
FIG. 5.11 – Rectangular-sectioned yarn morphology at steady state as a function of Sh (with $A = 5$).

5.4.4   Effective behavior of the composite in steady state

The effect of the surrounding flow on the composite behavior underlined at mesoscopic scale (subsection 5.3.6) is also critical at macroscopic scale. The composite behavior is still independent of δ_{c-y} and C_{0-y}, provided they have a physical meaning. As explained in the hypotheses of the macroscopic scale modeling, it is the case in the oxidation reactor. For the plasma tests, the comments of subsection 5.3.6 tend to support the idea that the model is no longer valid at macroscopic scale. This point is not addressed for such rough surfaces in the literature, and constitutes the second step of the proposed modeling strategy [61]. However, it is possible to deal with the problem from a material point of view. Under the light of the basic model, some circumspect analyses of rough features arising from plasma tests are presented in the last section : they give some information on advection effects.

The behavior of the composite at macroscopic scale in steady state is then derived using the method developed in subsection 5.3. The macroscopic scale behavior is directly obtained by properly rewriting equations (5.27) and (5.28). The normalized effective gasification rate of the composite $\widetilde{R}_c^{eff} = (\upsilon_c k_c)/(\upsilon_{wp-y} k_{wp-y})$ writes :

if $0 \leq Sh_y < \sqrt{A_y^2 - 1}$:

$$\widetilde{R}_c^{eff} = \frac{1}{\sqrt{1 + 2Sh_y\sqrt{A_y^2 - 1} - Sh_y^2}} \tag{5.33}$$

else if $Sh_y \geq \sqrt{A_y^2 - 1}$:

$$\widetilde{R}_c^{eff} = \frac{1}{A_y} \tag{5.34}$$

The plot of such a function is already represented on figure 5.8 and commented in subsection 5.3.6, except that the variables are now R_c^{eff}, Sh_y, and A_y instead of R_y^{eff}, Sh, and A.

5.5   Validation and exploitation

The model is first validated on a 3D C/C composite sample ablated by pure oxidation (referenced as C/C-oxi in [61]). Then it is exploited for the analysis of the behavior of two more complex samples : a pyrolyzed C/R composite ablated by pure oxidation (ref. C/R-oxi), and 3D C/C ablated by a high flux plasma test (ref. C/C-plasma).

5.5.1   Validation using C/C-oxi sample

Independent measurements of the intrinsic oxidation rates of the available composites components, that is, the ex-PAN fibers ($k_f \simeq 1.2\,10^{-5}\,m/s$) have been carried out in an oxidation reactor under the following experimental conditions : dry air, $898\,K$, atmospheric pressure [62]. Unfortunately, the interphases associated to the yarns and to the fibers are not available as such : their oxidation rates cannot be evaluated by independent measurements. In the following, they are evaluated using the model and the analysis of the surface roughness. Even though this evaluation is done using the model, the validation is possible because surface roughness may be considered as an additional independent input value, which stands in for the oxidation rates of the weak phases. The oxidation rate of the composite in steady state

lies around $k_c^{eff-exp} = 3\,10^{-3}\,m/s$ [62]. The procedure for the validation is firstly to assess the effective reactivity of the composite from the reactivity of the fibers, the physical parameters, the surface roughness, and using the two up-scalings. Secondly, the effective oxidation rate of the composite obtained using the model may be compared to the experimental value.

Let the effective reactivity of the yarn be evaluated from that of the fibers (first change of scale). The first step is to determine the Sherwood number associated to the fiber : $Sh = k_{wp}R_f/D$. The bulk diffusion coefficient of oxygen in dry air at atmospheric pressure and $898\,K$ has been obtained using the Chapman-Enskog relation : $D_b = 1.34\,10^{-4}\,m^2/s$ [80]. However, as represented on figure 5.2-b, the higher recession velocity of the interphase can lead to a ring-like groove which might have to be considered as a pore, where rarefied gas flow could occur. At $898\,K$ in dry air at atmospheric pressure, the mean free path value for oxygen is estimated from the kinetic theory of gases : $\overline{\lambda} \simeq 0,2\,\mu m$ [20]. The mean width of the groove mentioned above, $\overline{l_p}$, is around $0.5\,\mu m$ [62]. Hence, the Knudsen number, $Kn = \overline{\lambda}/\overline{l_p}$ lies around unity ; this characterizes mixed diffusion [92]. The effective diffusion coefficient in such a porous medium, noted D, is then related to both the bulk (D_b) and Knudsen (D_k) diffusivities [73, 92], and is given by Bosanquet relation :

$$D^{-1} = D_b^{-1} + D_k^{-1} \tag{5.35}$$

The Knudsen diffusion coefficient through cylindrical pores of radius r_p writes [73, 92] :

$$D_k = \frac{2\,r_p}{3}\,\sqrt{\frac{8\,R\,T}{\pi M}} \tag{5.36}$$

where M is the molecular weight of the diffusing species, T the temperature, and R the perfect gases constant. Considering a cylindrical pore of radius $r_p = 0.25\,\mu m$, expression (5.36) gives $D_k = 3.4\,10^{-4}\,m^2/s$, which is then a lower bound of the Knudsen diffusivity in the notch [73]. Hence, substituting the values of D_k and D_b in equation (5.35), one obtains a lower bound of the effective diffusion coefficient in the groove : $D_{min} \geq 0.98\,10^{-4}\,m^2/s$. Consequently, it is possible to determine an upper bound for the Sherwood number : $Sh = k_{wp}R_f/D < k_c^{eff-exp}R_f/D_{min} \simeq 10^{-4}$. According to the theoretical analysis, this clearly shows that the ablation regime is reaction-limited. This is also in accordance with the observation of sharp conical fibers on the C/C-oxi sample [61]. Moreover, the surface roughness analysis shows the fiber height, h_f, is $111 \pm 6\,\mu m$ for a mean fiber radius R_f around $3.5\mu m$, that is, $\widetilde{h} = h_f/R_f \simeq 32$. Then, the contrast in the oxidation rates, $A = (k_{wp}v_{wp})/(k_f v_f)$, is obtained from figure 5.6, or more accurately from equation (5.24). One notes that A is equal to $\widetilde{h}$ in reaction-limited regime ; then A also lies around 32. The effective ablation rate of the yarn is driven by the weak phase in reaction-limited regime (equation (5.19)). When $Sh << 1$, equation (5.27) becomes $\widetilde{R}_y^{eff} = (v_y k_y)/(v_{wp}k_{wp}) = 1$. The effective reactivity of the yarn is then $k_y = A\,k_f\,(v_f/v_y)$. In the case of the 3D C/C composite, one can assume that $v_f \simeq v_y$. Hence, one has $k_y \simeq 3.8\,10^{-4}\,m/s$. It is now possible to determine the oxidation rate of the interphase (i), which is the weak phase : $k_i = k_{wp} = A\,k_f\,(v_f/v_{wp}) \simeq 3.8\,10^{-4}\,m/s$.

Let us address the second up-scaling. In the case of the composite, the weak phase recession leads to a large notch [61]. Then, D is equal to D_b, since Kn is low in this case. The Sherwood number for the yarn, $Sh_y = lk_{wp-y}/(2D)$, lies around 10^{-3}. In the morphological study [61], $\widetilde{h}_y$ has been estimated to be about 5. Considering figure 5.6, one deduces that the regime is once more reaction-limited. At first sight, this doesn't seem in accordance with the observations : the yarns should globally feature sharp pyramidal shapes, like on figure 5.10-a.

However, the yarns look like truncated pyramids : their tips display a plateau. The fact that the Sherwood number is low excludes the possibility of a steady state plateau, like on figure 5.10 for $Sh = 10$, but rather supports the idea that the steady state is not fully reached as yet. This may appear surprising, as, experimentally, the overall oxidation rate was found to be approximatively constant at the end of the experiment (the observed sample has suffered 30% burn off). Actually, it is shown in [65] that (i) at the end of the transient regime, the ablation rate is nearly constant, and that, indeed, (ii) the transient regime at macroscopic scale is theoretically slightly longer than the duration of the experiment. Note that the transient regime at macroscopic scale is much longer than at mesoscopic scale, that is why the steady state at mesoscopic scale is independently well reached [65]. From the angle at the basis of the pyramid, it is possible to extrapolate the steady state reduced height, which is finally found to lie around 8. Then, one deduces $A_y = 8$ and $\widetilde{R}_c^{eff} = (v_c k_c)/(v_{wp-y} k_{wp-y}) = 1$ from equation (5.33). The effective reactivity of the composite assessed from the model is then $k_c^{eff-m} = A_y\, k_y\,(v_y/v_c)$. In the case of the 3D C/C composite, one can assume that $v_y \simeq v_c$. Hence, one has $k_c^{eff-m} \simeq 3.1\,10^{-3}\,m/s$. An unavoidable series of approximations, systematically underlined in the text, had to be done ; these approximations mainly concern the material properties. After the two up-scalings, the estimated cumulative relative error is about 30%. Nevertheless, even if this uncertainty may appear high, it should be noticed that two changes of scales have been operated, and that the properties of the weak phases have been obtained by morphological analyses on an irregular material. Moreover, the fact that more than two orders of magnitude separate the input data (fiber reactivity) from the output data (effective composite reactivity) dramatically enhances any uncertainty on the microscopic scale properties. Under these considerations, an uncertainty of 30% is already a sound result.

As a conclusion, using the model and only the fibers reactivity, the effective reactivity of the composite has been evaluated in steady state from the study of its surface roughness. Comparing experimental and theoretical values, the error in the prediction is found to be about 3%, that is, lower than the uncertainties. Moreover, the correct agreement, which is obtained in the modeling of surface roughness features (conical pointed fibers, pyramidal yarns), supports the validity of the model.

5.5.2   Exploitation and validation for C/R-oxi sample

The experimental oxidation rate of the composite is $k_c^{eff-exp} = 8.5\,10^{-2}\,m/s$. The oxidation rate of the ex-cellulose fibers is $2.1\,10^{-4}\,m/s$ for an apparent density of 1.6. The oxidation rate of a powder of a pyrolyzed phenolic resin has been measured. The intrinsic density of the powder is 1.29, while its apparent density lies around 0.7, the same as in the pyrolyzed composite. This very porous material, which is moreover poorly organized as attested by its low intrinsic density, has a very high effective oxidation rate : $k_m = 2.6\,10^{-2}\,m/s$. In the case of the pyrolyzed C/R composite, the weak phase is the whole pyrolyzed phenolic resin. The reactivity ratio is very high : $A = (k_{wp} v_{wp})/(k_f v_f) \simeq 284$. Moreover, since the weak phase is the pyrolyzed resin, the Knudsen number associated to the porous medium, delimited by the fibers, is low ; then Knudsen diffusion effects can be neglected. Thus the Sherwood number, given by : $Sh = k_m\, R_f/D_b$, is about $7\,10^{-4}$. As A is large, the regime is not reaction-limited, but close to it. Substituting the values of A and Sh in equation (5.24), the reduced height $\widetilde{h}$ is found to be around 260. Equation (5.27) shows that the matrix is protected by the fibers, the matrix recession velocity is thus only 85% of the raw value. The theoretical effective

reaction rate of the yarn in steady state is then $k_y = 0.85\, k_{wp}\, (v_{wp}/v_y)$; with $\rho_y \simeq 1.2$, one has $k_y = 3.8\,10^{-2}\, m/s$. This homogenized value is higher than the intrinsic oxidation rate of the pyrolyzed resin because it integrates the low density of the actual resin. This leads to a higher value of A, then a higher fiber length, and finally to a higher overall ablation rate. Consequently, a basic way to improve the composite resistance to low temperature oxidation might be to add high density carbon particles in the resin to artificially increase its density. However, the control of the penetration of such particles in the fiber bundles requires some expertise [7]. Switching to the surface roughness study, no contradiction is observed between the results of the model and experimental observations. Indeed, the fibers are thin and sharp, as expected. The theoretical angle at fiber tip is found to lie around 0.4°. The experimental value is somehow higher but difficult to estimate, because the fiber tips are very irregular. Some of the very thin tips are broken either by the experimentalist during the weighing (despite great care) or by thermo-mechanical stresses.
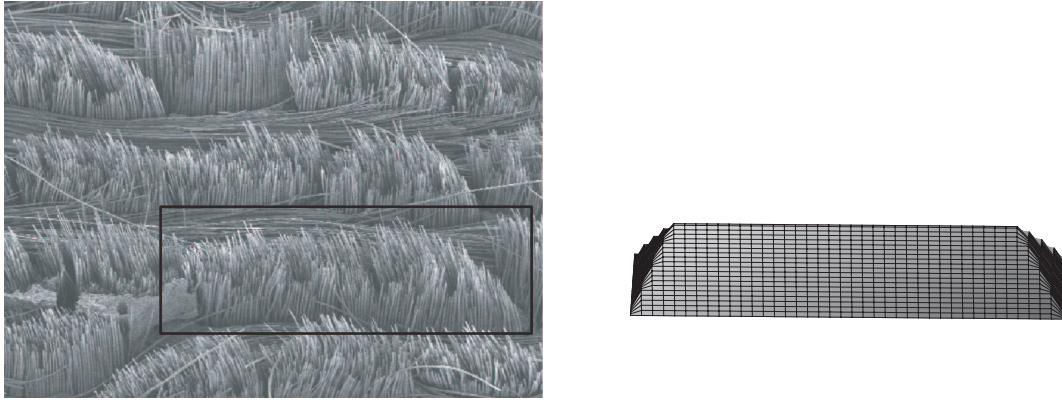
FIG. 5.12 – Comparison of a SEM micrograph of the epi-macro-structural surface roughness of the C/R-oxi sample with the prediction of the basic model, *tilt* : 45°.

Switching to macroscopic scale, $\widetilde{h}_y$ is about 2. One has then $A_y = 2.5$ for $Sh_y = 0.1$. Hence the effective intrinsic oxidation rate of the parallel yarns is $k_{wp-y} = A_y\, k_y = 9.5\,10^{-2}\, m/s$. The velocity decrease due to diffusion effects and parallel yarn protection by the perpendicular yarn is of 17% according to equation (5.33). The effective oxidation rate of the composite is : $k_c^{eff-m} = 0.83\, k_{wp-y} = 7.9\,10^{-2}\, m/s$. The agreement of the theoretical value with the experimental value is correct : the error is lower than 7 %. However, the accuracy of the prediction does not have to hide the perfectibility of the model. Indeed, one should note that at macroscopic scale, the SEM micrograph of figure 5.12 and the results of the model show that the emerging part of the perpendicular yarns are actually matrix-free fiber bundles, as matrix has been deeply ablated. Then, the up-scaling illustrated on figure 5.9 is no longer exact since for small values of α_y there is no matrix at the bottom of the cell represented on the right scheme. Then the exact effective reactivity of the bundle becomes that of a matrix-free porous medium. Considering a symmetrical bundle the diffusive flux is null on the plane of symmetry, that is, using the notations of figure 5.9-c, $J(z' = 0) = 0$ and $h_f = l/2$. In reaction-limited regime, the effective reactivity of this porous medium is found to be about $0.01\, m/s$. This value is lower than the one used in the macroscopic model ($k_y = 3.8\,10^{-2}\, m/s$). Then the angle at the basis of the bundles should be less pronounced than predicted by the model. Figure 5.12 tends to support this interpretation. As this effect is an issue only for

small values of α_y, the influence on the overall behavior is likely to be subtle, but this might explain the fact that the prediction of the oxidation rate was overestimated.

5.5.3   Illustration of the possibilities of extrapolation to C/C-plasma sample

The extrapolation to plasma tests is the second step of the modeling strategy, and is beyond the scope of this work, because some investigations and progresses have to be done in many fields before it can be properly treated [61]. In this subsection, the aim is no longer to validate the model, as, obviously, it is biased, especially at macroscopic scale. Nevertheless, an effort is done to illustrate the ability of such a model to give some invaluable information on the material behavior, even in complex conditions. The guiding idea is to encourage further research and improvement of the model in that way.

The properties of the components of the 3D C/C composite submitted to the plasma test of this study are not known in the test conditions. Indeed, the plasma-tests conditions are not reproducible on materials not susceptible to undergo high speed flows without being significantly eroded. These materials are then tested at lower temperatures using other tests, and their gasification rates are extrapolated [31]. Concerning the C/C-plasma sample, the order of magnitude of the overall recession velocity of the composite in steady state is $1\,mm/s$ [22]. The sample is chiefly ablated by sublimation in the test conditions ($T \simeq 4000\,K$, $P \simeq 5\,MPa$) [22]. Let us assume that sublimation is the only cause of gasification. The mass loss of carbon j is then given by the sum of Knudsen-Langmuir laws for each sublimed carbon species [22] :

$$j = \sum_i j_i = \sqrt{\mathcal{M}_c/2\pi\mathcal{R}T}\sum_i\left[\alpha_i\sqrt{i}(P_{s-i} - P_{w-i})\right] \tag{5.37}$$

where, the sublimed species are C_i, $i \in [1, N]$, of molar weight $i\mathcal{M}_c$, with $\mathcal{M}_c$ the molar weight of carbon. α_i is the sticking coefficient (kinetic parameter). $P_{s-i}(T)$ and P_{w-i} are respectively the thermodynamical equilibrium pressure at temperature T and the partial pressure on the wall of species C_i. Note that N may reach considerable values, but in the plasma-test conditions the most important species are $C_{i<6}$, and the major species is C_3 [15,27]. Theoretical and experimental studies for temperatures ranging from $3300\,K$ to $4600\,K$ have shown that α_i was only a function of the temperature, that is, among others, it is independent of i [5]. Nevertheless, in the general case, the expression (5.37) is not linearizable, because of the term $\sqrt{i}$. The maximal sublimation rate is obtained when P_{w-i} is null for each species. In that case, the mass loss is proportional to the sum of the P_{s-i} weighted by $\sqrt{i}$. At $4000\,K$, using the values of P_{s-i} of Ref. [15] for $i < 6$, C_3 is found to be responsible of $79\,\%$ of the total maximal mass loss. Then, for this first illustrative approach, the other species are neglected for temperatures around $4000\,K$. Consequently, under these hypotheses, equation (5.37) rewrites :

$$j = \alpha(T)\sqrt{\frac{3\,\mathcal{M}}{2\pi\mathcal{R}T}}(P_s(T) - P_w) \tag{5.38}$$

where P_s and P_w are related to C_3.

Combining the perfect gas law to equation (5.38), one obtains the molar flux J (in $mol.m^{-2}.s^{-1}$) under the following form :

$$J = \frac{\dot{m}}{3\mathcal{M}} = \alpha(T)\sqrt{\frac{\mathcal{R}T}{6\,\pi\mathcal{M}}}(C_s(T) - C_w) \tag{5.39}$$

where C_s and C_w are the concentrations (in $mol.m^{-3}$) associated to the pressures P_s and P_w.

The problem can be rewritten under the mathematical form of section 5.2.2 [32] :

$$J = \overline{k}\,\overline{C} \tag{5.40}$$

where $\overline{k} = \alpha(T)\sqrt{(\mathcal{R}T)/(6\,\pi\mathcal{M})}$ is analogous to a reaction rate, only function of the temperature, with $\overline{C} = C_s(T) - C$ the associated concentration. In the case of sublimation, the concentration C in C_3 at the boundary layer top is null, then $\overline{C_0} = \overline{C}(\widetilde{z} = \widetilde{h}) = C_s(T)$ (see figure 5.13).
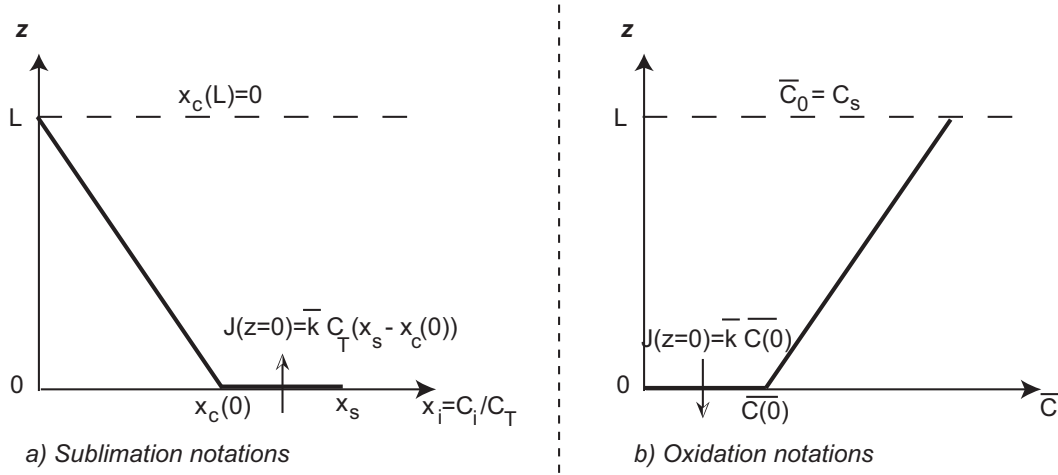
FIG. 5.13 – Analogy between sublimation and oxidation

In the model presented in section 5.2.2, it was tacitly supposed that in steady state : $\mathbf{J}(O_2) + \mathbf{J}(CO_2) = 0$, the only cause of mass transfer being the diffusion. However, in the case of sublimation, this assumption is no longer valuable, since the diffusion of C_3 in a static media M is not balanced by any species. Hence, one has : $\mathbf{J}(C_3) + \mathbf{J}(M) = \mathbf{J}(C_3) \neq 0$. Let C_T be the total concentration, x_c be the molar fraction of the sublimed species (C_3), x_s be the molar fraction associated to C_s, and D be the binary diffusion coefficient of C_3 in the media M. The molar flux $\mathbf{J}(C_3)$, noted $\mathbf{J}$ in the following, is then the sum of a diffusive flux given by Fick's law and an overall advection velocity of the species C_3 (caused by diffusion), which is called Stefan flux; this writes [51] :

$$\mathbf{J} = -C_T\,D\,\nabla x_c + x_c\,\mathbf{J} \tag{5.41}$$

The 1-D problem already presented in subsection 5.3.2 should be solved with this new expression of $\mathbf{J}$. Using the notations of figure 5.13−a, it is a trivial matter to show that $x_c(z = 0)$, noted $x_c(0)$ is solution of the following equation :

$$ln(1 - x_c(0)) = Da(x_c(0) - x_s) \tag{5.42}$$

where $Da = \overline{k}L/D$ is a Damköhler number associated to this 1-D model. The solution of equation (5.42) is a function of the principal branch of the LambertW function, which is real-valued on the considered set :

$$x_c(0) = 1 - \frac{LambertW(Da \, exp(Da(1 - x_s)))}{Da} \tag{5.43}$$

It is not possible to solve the analytical model using the LambertW function to describe the concentration gradient. Nevertheless, this gives the opportunity to evaluate Stefan flux effects. The parametrical plots of $\widehat{C}_{Stef}(z = 0) = \overline{C}_{Stef}(z = 0)/\overline{C}_0 = (x_s - x_c(0))/x_s$, versus Da for values of x_s ranging from 0 to 1, are difficult to differentiate from that of $\widehat{C}(z = 0)$ represented on figure 5.4. Indeed, for most of the values of Da and x_s the plots are superposed. Then, it is interesting to assess the relative error committed on the gasification rate, which is directly linked to the concentration on the wall by equation (5.40), when the Stefan flux is ignored. This error is plotted on figure 5.14 as a function of Da for values of thermodynamical equilibrium partial pressure of sublimed species, P_s/P (with P the total pressure), varying from 100% to 1%. First, one notes that when $P_s << P$ the effect of the Stefan flux is negligible. Logically, when P_s becomes high enough, the advection velocity caused by sublimed species diffusion is non negligible. Then, mass transfer is increased, and the formal concentration close to the wall, $\overline{C}_{Stef}(z = 0)$, increases. The Stefan flux is negligible for $Da < 1$, that is, when diffusional effects are low.
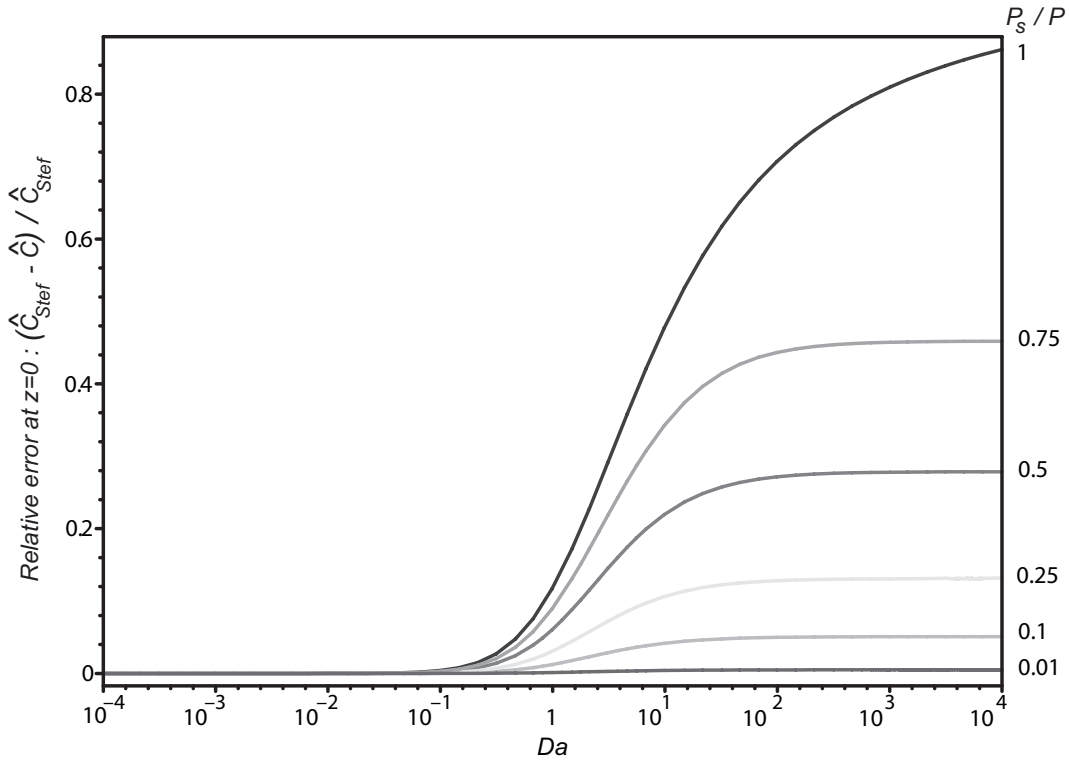
FIG. 5.14 – Plot of the relative error committed on wall concentration evaluation when Stefan flux is neglected versus Da and for various thermodynamical equilibrium partial pressures of sublimed species

| a) Fiber : front view | b) Fiber : tilt 45° | c) Bundle : reconstruction in accordance with SEM micrographs, tilt 45° |
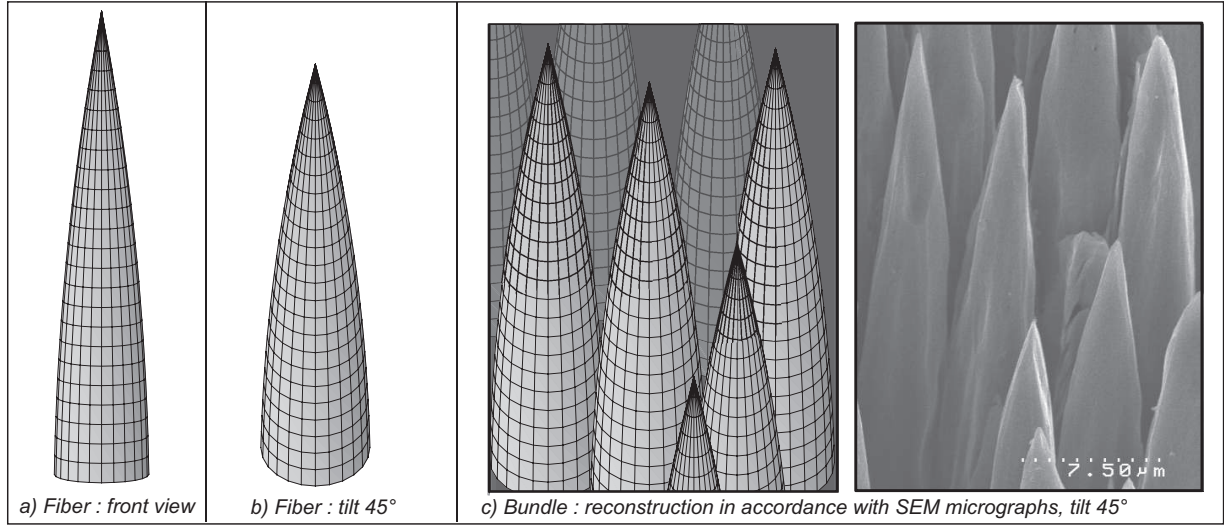
FIG. 5.15 – Reconstituting of a SEM micrograph for $Sh = 0.4$ and $A = 30$

Using these theoretical bases, let the material be analyzed. At mesoscopic scale, the surface roughness features typical sharp fiber tips surrounded by a ring-shaped matrix [61], the weak phase being the interphase, which is also about $0.5\mu m$ thick for sublimation. Note that the mean free path is equal to $5.10^{-8}m$ [20], so the Knudsen number is low, and Knudsen diffusion effects can be neglected. The reduced height of the fibers, $\widetilde{h}$, is about 10, and the angle of pointed fibers tip, α_f, is around 20° (see figure 5.15). Using the analytical model, one obtains $A = 30$ and $Sh = 0.4$. From the Sherwood number value and an estimation of the mass diffusivity for C_3 ($D = 2.10^{-5}\,m^2/s$, with $T = 4000K$, and $5MPa$ of N_2), one deduces : $k_{wp} = 2.3\,m/s$. In these conditions, Stefan flux is indeed negligible ($Da < 1$). The normalized effective reactivity, $\widetilde{R}_y^{eff}$, is found to be 0.2 (equation (5.27)). Hence, the fibers strongly protect the weak phase : the velocity decrease due to this protection being of 80% as compared to the weak phase reactivity. The effective reactivity of the yarn, $\overline{k_y} = 0.2\,\overline{k_{wp}}\,(v_{wp}/v_y)$, is approximatively $0.46\,m/s$. The recession velocity of $1\,mm/s$ leads to $j_c^{eff} = 56\,mol.m^{-2}.s^{-1}$ considering sublimation of C_3 and a density of 2. The micrographs of [61] show that the yarns feature a plateau (like on figure 5.10 for Sh=10). In that case, it is possible to assess the concentration on fiber tips knowing the effective molar ablation rate of the composite, and the yarn properties : $J_c^{eff} = \overline{k_y}\,\overline{C}$. One deduces $\overline{C} = 122mol.m^{-3}$. It leads to a partial pressure of C_3 of approximatively $4\,Mpa$. The corresponding temperature, which gives an equivalent partial pressure of carbon at thermodynamical equilibrium, is $4300\,K$ [5]. Note that the actual value of the surface temperature is not known, but estimated using extrapolations. The analysis of the surface roughness gives then a coherent approximation of the surface temperature, as well as of the intrinsic ablation rates of the components of the composite, since all the values are consistent.

At macroscopic scale, the validity of the assumptions of the model becomes dubious. Considering that the density of the yarn is equal to that of the inter-yarn interphase, one obtains : $Sh \simeq 7\,A_y$, for $D = 2.10^{-5}m^2.s^{-1}$. A_y is likely to be around 8, as determined for the $C/C - oxi$ sample. Anyway, because the regime is diffusion-limited, the yarns feature a large plateau (like on figure 5.10 for Sh=10) with $\widetilde{h}_y \simeq 0.1$, that is, the surface is nearly flat. This is

in good qualitative and quantitative agreement with the observations [61], but for one point : deep notches are experimentally observed close to the yarns, that is, the inter-yarn interphase is deeply ablated. The first interpretation that come to mind is an increase of mass transfer due to a high advection or even turbulent flow conditions. This would decrease the Sherwood number, and notches may be obtained, for $A_y = 8$ and $Sh = 10$ for example. However, since the notches are quite narrow, the high speed flow eddies are unlikely to reach their bottom. This analysis supports the occurrence of a thermomechanical erosion [26] of the inter-yarn interphase.

5.6   Conclusion

The behavior of C/C composites during physico-chemical ablation has been modeled in steady state from the microscopic scale up to the macroscopic one, using two suitable changes of scale : (i) microscopic scale (fiber, intra-bundle matrix) to mesoscopic scale (yarn) and (ii) mesoscopic scale (yarn, inter-yarn matrix) to macroscopic scale (composite). First, a general model for receding surfaces under a first order gasification process coupled to mass transfer by diffusion has been proposed. This model has been analytically solved at mesoscopic scale considering a simplified composite architecture and mass transfer perpendicular to the overall surface. Due to the higher recession rate of the matrix (or interphase), the fibers are partially stripped, become thinner, and acquire a needle shape. Only two parameters are necessary to describe the steady state surface roughness features of the yarn : the reactivity contrast between the weakest (matrix) and strongest (fiber) phases A and a Sherwood number Sh. The height of the stripped part of the fibers (peak-to-valley surface roughness) increases with A. The stripped part of the fibers is conical for low values of Sh (reaction-limited regime), ogival for Sh around unity (transition regime), and button shaped for high values of Sh (diffusion-limited regime). Whenever Sh is large with respect to A, no surface roughness is observed. The model has then been used to infer the effective reactivity of the yarn from that of its components. In reaction-limited regime, a weakest-link process occurs : the reactivity of the yarn is equal to that of the weakest phase. When diffusional effects appear, the matrix is somehow protected by the fibers and the effective reactivity progressively tends to that of the fiber, that is, its value in diffusion-limited regime. These results are consistent with previous numerical studies in 3D [41, 67]. At macroscopic scale, the mesoscopic model applies, considering square section yarns instead of cylindrical fibers, and inter-yarn matrix instead of intra-yarn matrix. It has been shown that the same set of equations was usable, except that the parameters had to be adapted to macroscopic scale (A_y, Sh_y). Consequently, the multi-scale behavior of the composite has been obtained. In a last section, the results of the model have been validated by comparison to the surface roughness and the oxidation rates of two C/C composites. During this validation, for 3D C/C, the intra-yarn and inter-yarn interphase reactivities, which cannot be independently measured, are deduced from a surface roughness analysis. Finally, the model has been applied to interpret the surface roughness of a 3D C/C ablated using a plasma-jet test. An evaluation of the reactivities of the composite components and of the test temperature are done using mesoscopic scale model. At macroscopic scale, thermomechanical erosion is believed to occur.

As a whole, the results of the steady state models may be useful for : (i) the prediction of the multi-scale surface roughness as a function of the physico-chemical parameters, (ii) the prediction of the effective reactivity of the composite from that of its components, (iii) the

research of an ideal theoretical material, (iv) the determination of the components properties from the analysis of surface roughness, and (v), in some way, the analysis of plasma tests.

The immediate outlook is to address actual composite architectures and transient regime. This is the subject of further articles [64, 65].

6 3D numerical modeling of actual architectures in steady state

Préambule

Ce chapitre constitue un projet de publication soumis à la revue *Journal of Computational Physics*.

Titre : Physico-chemical ablation of carbon-carbon composites : IV- 3D numerical modeling of actual architectures in steady state.

Auteurs : J. Lachaud et G. L. Vignoles

Affiliation :

Laboratoire des Composites ThermoStructuraux (LCTS)

UMR 5801 : CNRS-SAFRAN-CEA-UB1

Domaine Universitaire de Bordeaux – 3, Allée de La Boétie, 33600 Pessac, France

Résumé

Ce travail vise à expliquer et modéliser le comportement des composites carbone-carbone (C/C) durant l'ablation. Un code de simulation numérique a été développé sur un principe Monte-Carlo Marche Aléatoire afin de résoudre un modèle 3D pour les surfaces récessives intégrant transfert de masse et réaction hétérogène. Ce code est d'abord validé par comparaison à des modèles analytiques. Ensuite, il est utilisé pour la résolution du modèle sur des architectures composites réalistes à trois échelles. A l'échelle microscopique, on montre que les longues facettes observées expérimentalement sur les fibres pointues découlent de l'irrégularité de leur section initiale. A l'échelle mésoscopique, des simulations sur les fils sont comparées aux résultats analytiques obtenus précédemment, qui reposent sur des hypothèses supplémentaires. Un bon accord est obtenu et permet de valider ces hypothèses. De plus, il est montré que la réactivité effective d'un fil est indépendante de son orientation par rapport à la surface moyenne. Les géométries de rugosités prévues par le modèle sont en accord qualitatif avec les observations. A l'échelle macroscopique, des simulations numériques réalisées sur des architectures composites réalistes sont en accord avec les résultats d'expériences à température et vitesse d'écoulement modérées. Les réactivités de des composants d'un composite 3D C/C sont déduites par analyse inverse. Dans les conditions des essais plasma, les différences observées entre les prédictions du modèle et les résultats expérimentaux pourraient être expliquées par l'occurrence d'une érosion thermomécanique.

Abstract

This work aims to explain and model the behavior of carbon-carbon (C/C) composites during ablation. In order to solve a 3D model for receding surface including heterogeneous reaction and mass transfer, a homemade simulation code has been developed on a Monte-Carlo Random-Walk principle. The code is first validated by comparison to analytical models. Then,

it is applied to solve the 3D model on actual composite architectures at three scales. At microscopic scale, the large facets experimentally observed on sharp ablated fibers is shown to arise principally from their irregular initial section. At mesoscopic scale, some simulations on yarns are compared to previous analytical results, which relied on extra hypotheses. A correct agreement is obtained and tends to validate these hypotheses. Moreover, the effective reactivity of a yarn is shown to be independent of its orientation with respect to the overall surface. The resulting surface roughness features are in qualitative agreement with experimental observations. At macroscopic scale, the numerical simulations carried out on a 3D C/C are in agreement with experimental observations at moderate temperatures. The reactivities of its components are inferred by inverse analysis. In plasma test conditions, mechanical erosion may explain the discrepancy between model predictions and observations.

6.1   Introduction

This work is the fourth part of an article series which aims to improve the understanding of the behavior of carbon-carbon (C/C) composites during ablation either by oxidation or by sublimation, and to model it [61–63, 65].

During ablation, C/C composites develop multi-scale surface roughness features [61], which may display a strong coupling with the surrounding environment [31, 104]. The surface roughness chiefly arises from the heterogeneity of the composites, whose fibers and matrices are made of distinct forms of carbon [62]. However, neither the surface roughness onset [63], nor the composites effective reactivity can be trivially inferred from the reactivity of their components [68]. Following the multi-scale modeling strategy proposed before [61], the composite behavior has been analytically modeled in steady state [63]. The results are in agreement with the experimental measurements of surface roughness features dimensions [61] and of gasification rates [62]. Nevertheless, the modeling of the composite architecture has been simplified as much as possible to enable an analytical modeling. This paper aims to complete the analytical modeling using 3D numerical simulation. The actual architectures of C/C composites will be modeled with more accuracy and several physical assumptions removed. This should give the opportunity to validate the work hypotheses of the analytical model, to reproduce some particular features closely linked to the material structure, and to assess by inverse analysis [63] the reactivities of all the composite components.

The document includes four sections. In the first one, the ablation model [63] is summed up and a numerical solution is proposed through the presentation of a 3D numerical simulation code. In the three following sections of the document, this code is exploited for the multi-scale modeling of ablation. A section is devoted to each scale described in [61] : microscopic (fibers), mesoscopic (yarns), and macroscopic (composite) scales. In the second section (microscopic scale), it is shown how sharp faceted fibers are obtained when initial fiber sections not circular. In the third section (mesoscopic scale), the problem of a yarn inclined with respect to the surface is treated. In the last section, the macroscopic behavior of the actual architectures of a 3D C/C and of a 2D C/R are modeled. Simulation results are compared to experimental observations of surface roughness features. Also, an inverse method is applied to these actual architectures to determine the gasification rates of the composites components. This method relies on the comparison of surface roughness features shapes between experimental observations and numerical results [63].

6.2   Model and numerical simulation tool

The numerical simulation tool AMA has been designed to solve heterogeneous reaction/mass transfer problems with a receding surface. Physico-chemical ablation typically belongs to this kind of problems [61]. In a first subsection, a mathematical form of the problem, which has been shown to correctly describe physico-chemical ablation in the frame of this study [63], is presented. In a second subsection, an analytical solution for the ablation of carbon/carbon composite yarns, which is useful for software validation, is proposed. In a third subsection, AMA is presented and a numerical solution to this problem is developed. In the last subsection, AMA is validated by comparison to two complementary analytical models.

6.2.1   Ablation model

The ablation process leads to the recession of the material surface S under heterogeneous gasification processes, like oxidation or sublimation [61]. The macroscopic motion of this surface can be interpreted as an advancing wavefront. The surface position may be described in cartesian coordinates by the following scalar equation :

$$S(x, y, z, t) = 0 \tag{6.1}$$

such that the function S, which possesses first order partial derivatives almost everywhere, acquires nonzero values at all points not lying on the interface [53]. This equation may be derived with respect to time :

$$\frac{\partial S}{\partial t} + \mathbf{v_e} \cdot \nabla S = 0 \tag{6.2}$$

where $\mathbf{v_e} = \upsilon_e J_e \mathbf{n}$ is the surface local normal velocity , with υ_e the solid molar volume of e [53]. In the case of heterogeneous materials, e is also a function of space and time. J_e (in $mol.m^{-2}.s^{-1}$) is the molar rate of ablation. In this work, it is assumed to follow a first order kinetic law for oxidation and a Knudsen-Langmuir model for sublimation [63]. It is assumed that the Péclet mass number is low close to the wall [63]. Under these hypotheses, oxidation and sublimation are shown to be mathematically equivalent as far as gasification and mass transfer are concerned [32]. Using oxidation notations, the model writes :

$$J_e = -k_e.C(S = 0) = (-D\nabla C(S = 0)) \tag{6.3}$$

where k_e (in $m.s^{-1}$) is the gasification rate of the material e, D (in $m^2.s$) the diffusion coefficient of the reactant in the bulk fluid phase, and $C(S = 0)$ (in $mol.m^{-3}$) is the reactant gas concentration at the material surface. Mass conservation of the reactant in the fluid writes :

$$\frac{\partial C}{\partial t} + \nabla \cdot (-D\nabla C) = 0 \tag{6.4}$$

Boundary conditions for concentration relative to the model domain have to be specified (see for example figure 6.1-a). A Dirichlet condition ($C = C_0$) on the boundary layer top is shown to be suitable [62,63]. On lateral boundaries, a translation condition is retained. The interface position S as a function of space and time is then given by the simultaneous resolution of equations 6.2 and 6.4. For heterogeneous materials, this model cannot be solved analytically in the general case.

6.2.2   Example of analytical solution

Let us summarize some previous results useful for AMA validation and in the following of the study. The model of section 6.2.1 has been applied to the cell represented on figure 6.1-a. Translation conditions on lateral boundaries and the Dirichlet condition ($C = C_0$) on boundary layer top are respected. Under these boundary conditions, the cell represents a composite yarn, the lateral extension of which is infinite. It is ablated perpendicularly to its principal direction. Its components are supposed to be only carbon fibers and matrix which are gasified by a first-order reaction. The matrix is more reactive than the fibers. The concentration gradient of reactant in the fluid phase is assumed vertical, that is, along **z** (see figure 6.1-a). An analytical solution to this problem gives the following results [63] : i) Due to the higher recession rate of the matrix, the fibers are partially stripped, become thinner, and acquire a needle shape. ii) Only two parameters are necessary to describe the steady state surface roughness features of the yarn : a reactivity contrast A and a Sherwood number Sh. The reactivity contrast between the matrix and the fibers A is given by :

$$A = \frac{k_m \, v_m}{k_f v_f} \tag{6.5}$$

where the subscripts m and f are respectively related to fiber and matrix, and with $A > 1$. The geometry of the steady state is strongly linked to this contrast ; the higher it is, the higher the denuded fiber size h_f^s (from fiber tip to matrix level) is when steady state is reached. The Sherwood number Sh writes :

$$Sh = \frac{k_m \, R_f}{D} \tag{6.6}$$

where R_f is the fiber radius. Sh is an indicator of the three reaction regimes that can appear on this heterogeneous reactive surface : a diffusion-limited regime ($Sh >> 1$), a transition regime ($Sh \sim 1$), and a reaction-limited regime ($Sh << 1$). For small values of Sh, the fiber tip geometry is conical and only depends on A, with $h_f^s = R_f \sqrt{A^2 - 1}$ (see figure 6.1-b). When Sh increases but is lower than $\sqrt{A^2 - 1}$, diffusional effects tends to lower h_f^s and the fiber tips become ogival. For higher values of Sh, fibers tips display a plateau and $h_f^s = R_f(A-1)/Sh$. Hence, in diffusion-limited regime, h_f^s tends towards zero.

Even if it has been assumed that the concentration gradient was vertical in the general case, in reaction-limited regime, the concentration is constant in the bulk fluid phase. The analytical solution is then exact for the latter case. Hence, AMA can be validated by comparison to this case as far as equation 6.2 is concerned. Then, AMA validation could be completed by a comparison to a basic 1D analytical model in all regimes. The interest of AMA for the study of ablation is then obvious. First, the validity of the vertical concentration gradient hypothesis can be checked for all regimes. Second, more complex geometries may be addressed.

6.2.3   Numerical solution

AMA has been developed on a Monte-Carlo Random-Walk principle [37, 39, 56, 82, 91, 97]. AMA is the acronym for : *Ablation Marches Aléatoires* (Random Walk Ablation in French). A scheme of the general algorithm and a sketch of AMA main features are presented on figures 6.2-a and b. First, a 3D image containing several phases (fluid/solids) is generated. It is described in grey levels by the discrete cubic voxels (3D pixels) method. Then, the fluid/solid interface (equations 6.1) is determined by a simplified marching cube approach [97], which is a linear approximation of the actual surface in each voxel of the interface. The upper part

a) 3D elementary cell : initial time   b) Analytical result : steady state   c) AMA result : steady state
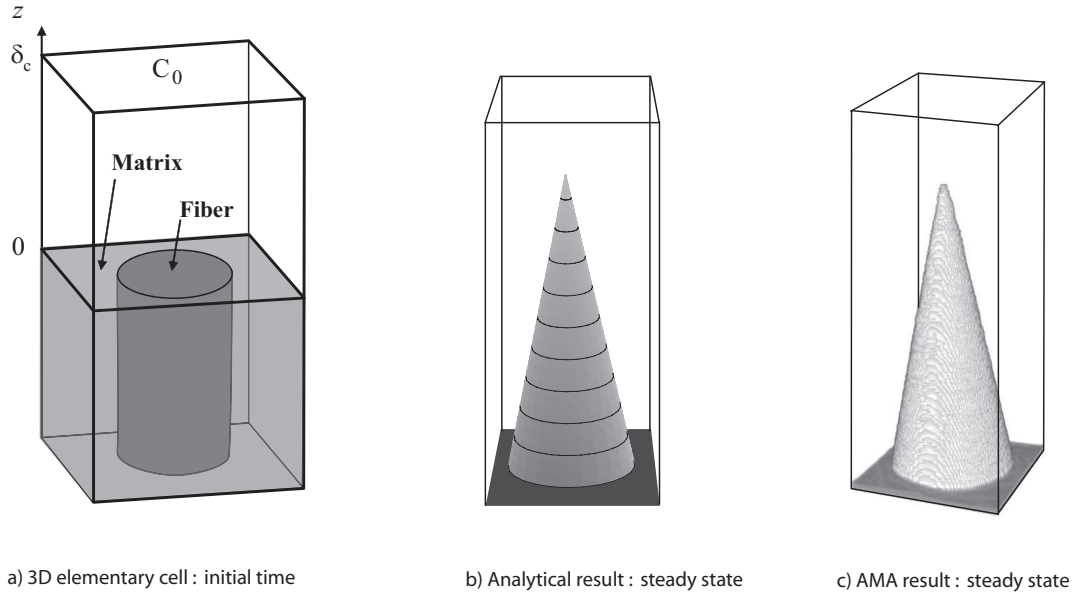
Fig. 6.1 – Validation of AMA by comparison to a 3D analytical model in reaction-limited regime ($A = 5$).

of the fluid phase is devoted to the buffer zone to apply the Dirichlet boundary condition. Since the numerical method is based on a random walk, the density of walkers has to be maintained constant in this zone. In practice, the simulation is operated with a constant number of walkers in the buffer zone, the total number of walkers in the fluid phase being automatically monitored by the diffusion/reaction process. Mass transfer from the buffer zone to the wall (equation 6.4) is simulated by a random walk. This walk is based on the Brownian motion simulation technique, which is a continuum (grid-free) and fast convergence method for diffusion in a continuous fluid [91]. As represented on figure 6.2-b, the path followed by a walker is no longer the physical one dictated by the molecular free path, but another one which requires less computational time. The space increment Δr is related to the time increment Δt by the following equation [91] :

$$\Delta t = \frac{\Delta r^2}{6D} \tag{6.7}$$

The size of the space increment has to be chosen small enough when compared to the characteristic size of the problem, but large enough to decrease the computational time. The trajectory of each walker is followed individually during a given elementary time Δt_e. Δt_e is evaluated to ensure a walk duration leading to a probability of about 50% to hit a wall. In general, Δt_e is much larger than Δt; the number of steps is thus large. At each step, the walk direction is randomly determined equiprobably in 3D space. The heterogeneous first order reaction on the wall (equation 6.3) is simulated using a sticking-event based method [82]. Let us assume that a walker hits the surface after a walk duration Δt_w ($0 < \Delta t_w < \Delta t_e$). A random number between 0 and 1 is generated. If that number is higher than a previously determined sticking event probability, the walker bounces back and its walk goes on until Δt_e is reached. In the converse case, the walker is assumed to stick, and another walker is released in the buffer zone (its walk starts again for a duration $\Delta t_e - \Delta t_w$). The amount of

a) Scheme of AMA alogorithm   b) Sketch of AMA principle
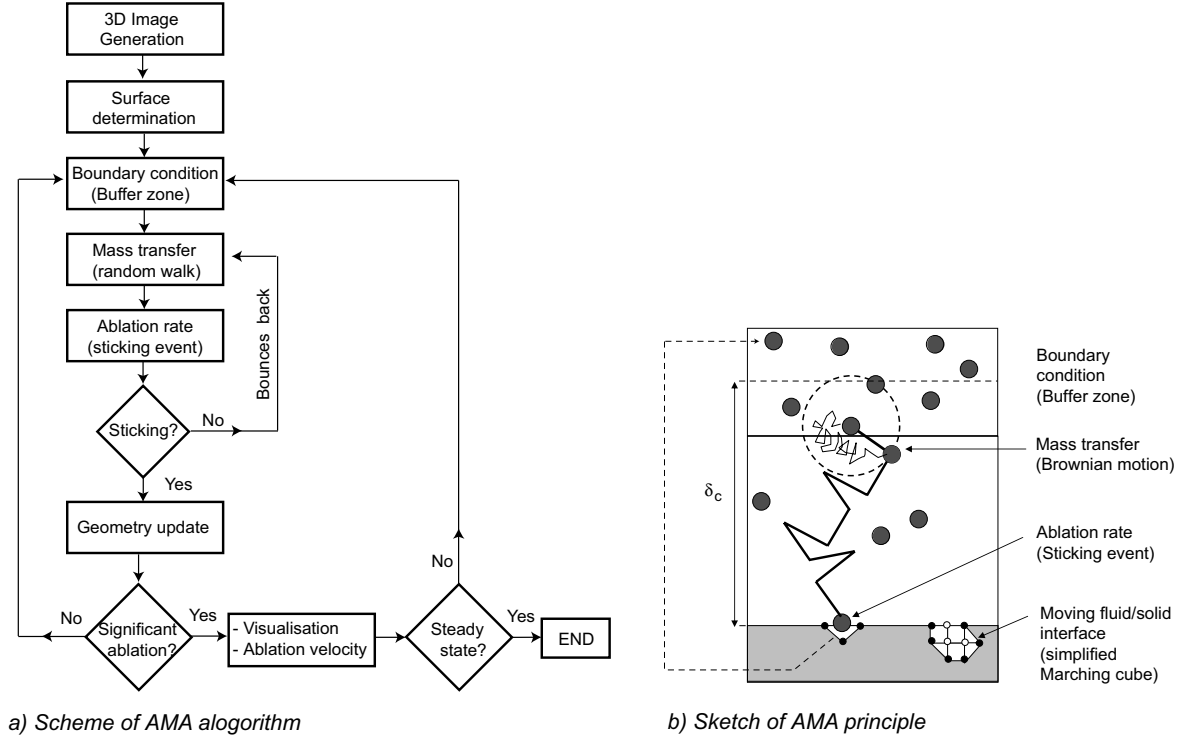
Fig. 6.2 – Schematic description of AMA

sticking events is recorded for every solid voxel of the fluid/solid interface. Whenever in a given solid voxel the cumulated number of sticking events reaches a given threshold, that is, when the required quantity of reactant to gasify that voxel is reached, it is converted into fluid. Then the surface is modified and has to be updated (equation 6.2). When a significant number of solid voxels is turned into fluid, an image is recorded. When an appreciable number of fluid voxels has been created (say, one horizontal slice of the image), the resolution domain is shifted downwards by the corresponding amount (one voxel height), in order to preserve a constant fluid volume throughout the simulation. The average ablation velocity is then deduced from the frequency of geometry shifts. The average ablation velocity and reactant flux are assessed since the last run. When the flux is constant from one run to another, this means the steady state is reached, and then the simulation ends. In the converse case, the simulation proceeds. In all the cases of this study, a steady state has been reached. The steady state may be visualized by 3D rendering and characterized by image analysis. Let some critical steps of the algorithm be further detailed.

To handle accurately the Dirichlet boundary condition, a parameter variation study has shown that the size of the buffer zone should be at least twice as large as the space increment Δr of the random walk. As sketched on figure 6.2-b, using a buffer zone, the boundary condition is applied in practice at a position Δr inside that zone, the size of the concentration boundary layer δ_c being then obtained by the sum of the fluid phase height (buffer excluded) and Δr.

The choice of the space increment size is critical as far as accuracy and computational time are concerned. In the bulk fluid phase, Δr has to be taken as large as possible, in order to lower

the computational time. Conversely, close to a wall, a parameter variation study has shown that Δr should be smaller than the characteristic size of the surface roughness (fiber radius for example). Indeed, in the converse case, some zones may be artificially shaded. Moreover, some conditions have to be respected for the bounce back. When a walker hits the wall, its last space increment Δr_w, which leads to collision, is smaller than Δr (or at most equal). In this algorithm, the walker bounces back according to a diffusive emission law with a space increment Δr_w. Using this bouncing rule, the average space increment size close to the wall decreases, leading to a more accurate simulation of surface recession.

Heterogeneous first-order reaction on the wall is simulated by a sticking probability P_s adapted to the Brownian motion simulation technique. Following some guidelines given in [82], P_s has been found to write [67] :

$$\tilde{P}_s = \frac{1}{1 + \dfrac{3\gamma D}{2k\Delta r_w}} \tag{6.8}$$

where γ is a coefficient depending upon the chosen bouncing rule. A parameter variation study has shown that γ lies around 0.8 in the case of the bouncing rule implemented in AMA.

In this study, the outputs are the surface recession and the global ablation velocity. However, surface evolution is slow compared to gas diffusion, since the molar volume of the material is low compared to the gas. In actual experiments, a huge number of reactant molecules may be necessary to gasify the volume of one elementary cube of solid. Using numerical simulation, it is impossible to have such a fine description, which fortunately is in no way necessary, especially in view of the discrete mode of geometry representation [82]. Then, the number of walkers can be restricted, using for each walker a representativeness of many reactant molecules estimated as follows. An elementary cube is assumed to be ablated when the corresponding number of sticking events reaches a given number N. N has to be chosen large enough so that statistical fluctuations are small, but is otherwise arbitrary. Theoretically, the statistical precision is roughly given by $N^{-1/2}$; a practical value for N is then higher than 100 [82]. The computational time being approximatively proportional to N, the interest of choosing N as low as possible is obvious. Tests on AMA have shown that a value of 10 was sufficient to predict with good accuracy the surface recession. If necessary, the local quality of the images can then be improved using a median filter.

6.2.4 AMA validation

AMA has been successfully compared to the 1-D steady state diffusion/reaction model reduced from the model proposed above [67]. The analytical reactant flux (J) at the interface writes [63] :

$$J = \frac{D}{\delta_c} C_0 \frac{1}{1 + \frac{1}{Da}} \tag{6.9}$$

where $Da = k\delta_c/D$ is a Damköhler number. Figure 6.3 illustrates the comparison between numerical simulation and equation (6.9) when k varies. The maximal relative error is lower than 2.5%, whatever the values chosen for δ_c, C_0 and D. This error is attributed to the uncertainties on sticking event probability evaluation, and on Dirichlet boundary condition monitoring. Nevertheless, this error is low enough to enable an accurate study of ablation phenomena.

Random walks have the particularity to converge on average at a rate proportional to the square root of the number of random drawings. The numerical method is then correct if
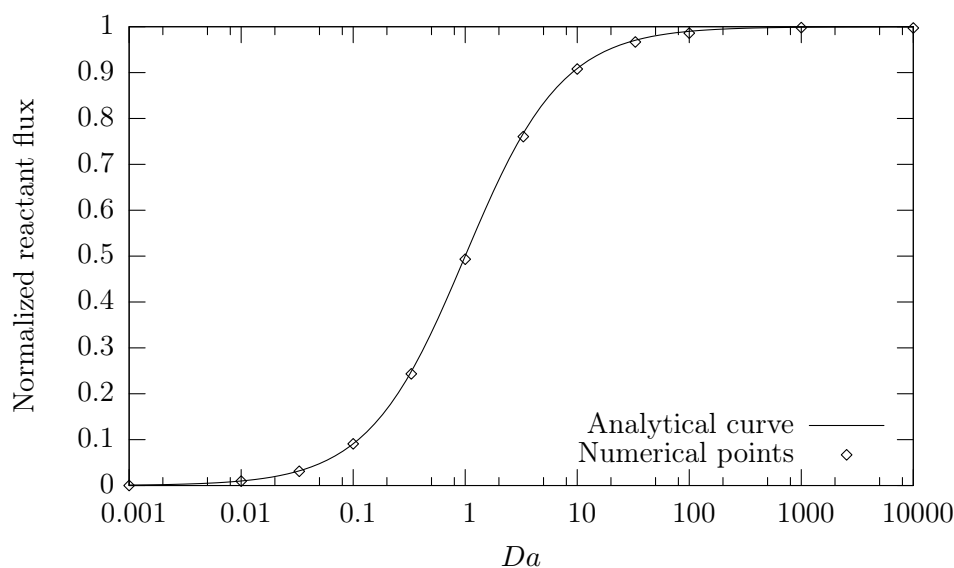
FIG. 6.3 – AMA validation by comparison to a 1-D model

$\Delta t_e >> \Delta t$ for diffusion and $N >> 1$ for reaction. In the simulations, these conditions are verified by the preprocessor. In the case represented on figure 6.4 ($Da = 1$), the evaluated flux quickly reaches correct values, but oscillates around the average flux value. Increasing the ratio between Δt_e and Δt, that is, decreasing Δr and increasing N, would lower the amplitude of the oscillations, but would dramatically enhance the computing time. Then it is preferable and valid to use the average flux as a reference value. Here, a quick convergence to a value with about 2% error is obtained.
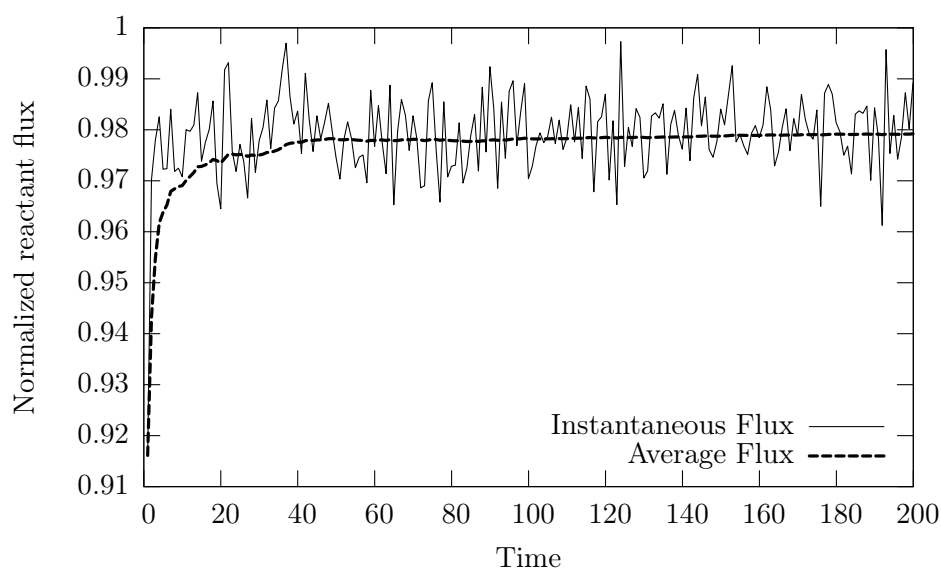
FIG. 6.4 – Convergence on average of random walks : Da=1
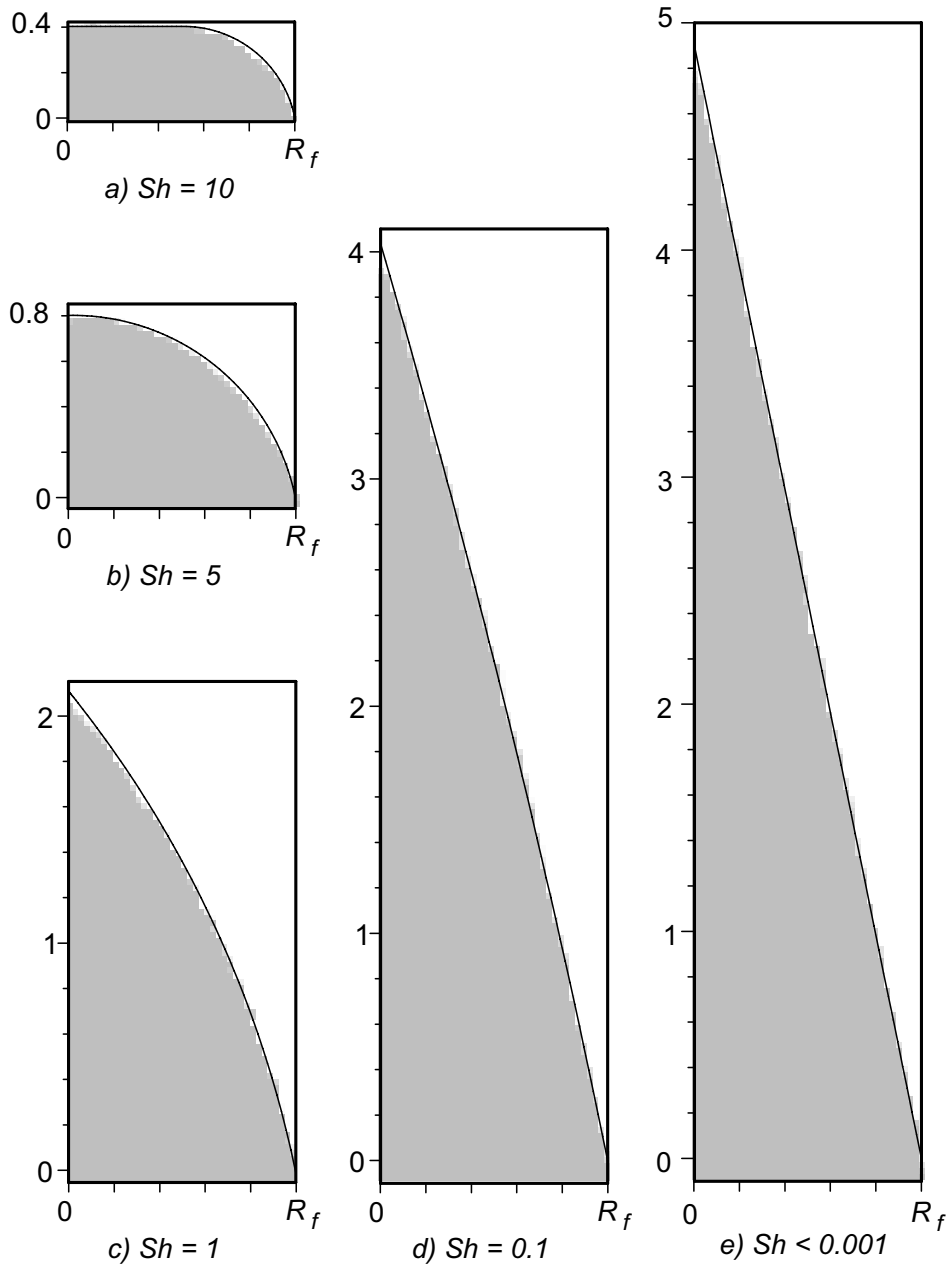
FIG. 6.5 – Comparison of analytical (black lines) and numerical (grey-filled parts) results.

The quality of the receding surface description has also to be checked for 3D images. The model of section 6.2.2 has been solved using AMA, in the case of the reaction-limited regime and for $A = 5$ (see figure 6.1-c). This result is in good agreement with the analytical result of figure 6.1-b. The fiber tip of figure 6.1-c seems smoothed because a median filter has been applied to the image to improve its regularity. A quantitative comparison of the analytical and numerical values of h_f^s has shown that, whatever the value retained for A, the numerical prediction is about 2% lower than the analytical one. On figure 6.5-e a section of the analytical (black line) and of the numerical solutions (grey-filled part) are compared. The

overall agreement between the two solutions is excellent : the error is not larger than one pixel width. Therefore, the receding surface description of AMA is correct.

As a conclusion, AMA is validated with an error lower than 2.5% in all situations. In the computed cases of the following sections, the steady state is reached after a computing time lower than 48 hours with a $3.2\,GHz$ Xeon CPU computer. The average horizontal section of the numerical cells is around a hundred square pixels. This is a correct compromise between computational time and the quality of the interface description.

6.3   Application to microscopic scale

At microscopic scale, some roughness features take place on the fibers. In particular, the ex-PAN fibers of the 3D C/C composites look faceted [48,61]. On figure 6.6-c, some fibers from a 3D C/C oxidized under dry air at atmospheric pressure show such facets. The oxidation process as well as the composite are fully described elsewhere [61]. The ablation regime is shown to be reaction-limited [63]. In this case, when steady state is reached, fibers with circular cross-section display a regular conical shape (see figures 6.1-b and c). A SEM (Scanning Electron Microscopy) analysis of the fibers cross-section clearly shows that it is indeed irregular (see figure 6.6-a). This may have an effect on the steady state geometry of the fibers. To verify this hypothesis, the irregularities of the fibers cross-section have been introduced in the model presented in section 6.2.2, as represented on figure 6.6-b. The result of the simulation is presented on figure 6.6-d. As a whole, the large facets which are experimentally observed on the fibers (from fiber tip to bottom) are qualitatively well reproduced. The numerical approach thus proves that they are originated from the irregularities of fibers sections. However, some facets, which are smaller, cannot be explained by this model. They are more probably linked to the fibers internal structure [60] or to a locally catalyzed oxidation [61].

6.4   Application to mesoscopic scale

The analytical model presented in subsection 6.2.2 addresses the case of yarns whose ablated surface is perpendicular to their main direction. This problem is fully treated elsewhere [63] under a vertical concentration gradient hypothesis. In a first subsection, the validity of this hypothesis is analyzed using AMA. Numerical simulation also enables to address other configurations which are commonly found in ablation of C/C composites. In a second subsection, the problem of a yarn inclined with respect to the surface is treated from a null angle to 90°. The case of yarns parallel to surface is singular and is addressed separately in a last subsection.

6.4.1   Perpendicular yarns : fibers perpendicular to surface

The model presented in subsection 6.2.2 is solved with no assumption on the concentration gradient using AMA. Moreover, in the analytical resolution, the matrix interface was supposed to stay flat and perpendicular to the **z** axis [63]. The numerical computation is also free of this hypothesis. A qualitative comparison of analytical and numerical results is proposed on figure 6.7 for $A = 5$ and for various values of Sh. All the reaction regimes are represented, except the diffusion-limited one ($Sh > 100$) which is trivial for both solutions (flat surface). The qualitative agreement between numerical and analytical results is correct. In particular, the plateau on fiber top ($Sh = 10$) is well obtained. This latter was extrapolated and shown

a) Fibers sections : observation (SEM)

b) Fiber section : model (AMA)

c) Steady state (SEM)

d) Steady state (AMA)
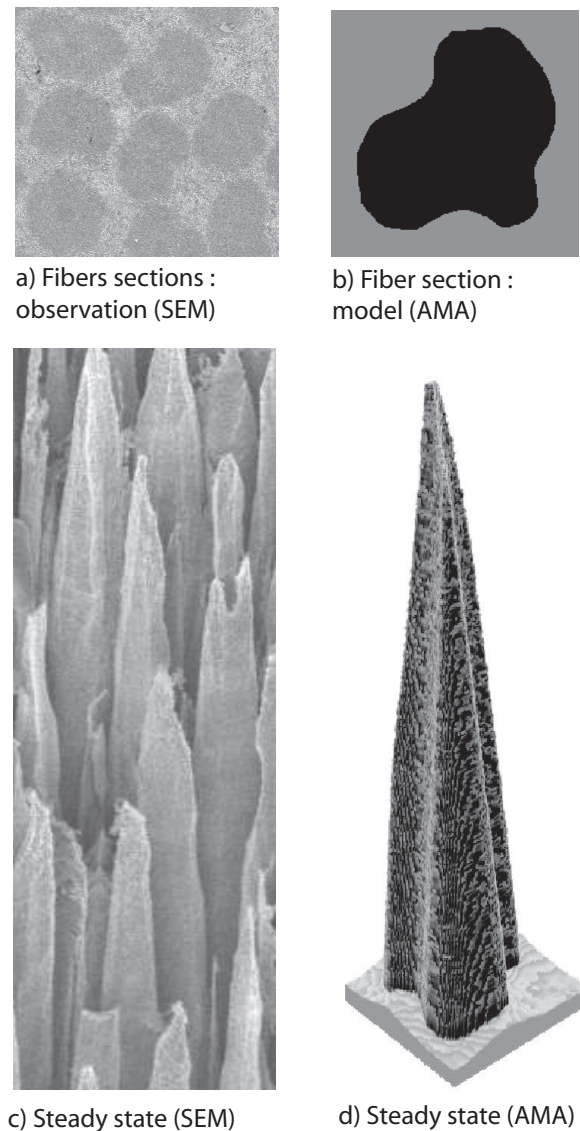
FIG. 6.6 – Faceted fibers : comparison of experimental observations with a model of irregular fiber section

to be possible in the analytical modeling [63]. Nevertheless, its existence was not certain, since no roughness feature observation is available in this regime. The hypothesis of a flat matrix is well verified : in all cases, the irregularities of the matrix surface are negligible. Using Brownian motion simulation technique with a large space increment enables one to address complex geometries with a reasonable computing time. One drawback is that the local concentration field is a piece of data which is difficult to obtain with accuracy because of the local variation of the concentration. However, the analytical model clearly shows that if the vertical gradient hypothesis were not taken, the resulting geometry would be quite different. Then, the validity of this hypothesis can be precisely studied by comparing analytical and numerical geometries in steady state. Such a comparison is presented on figure 6.5 :

some sections of the analytical (black lines) and numerical (grey-filled parts) are superposed. First, in all cases, the discrepancy on the steady state height prediction is lower than AMA uncertainties (2.5 %). Second, the agreement on the overall shape of the fibers is correct : the error is roughly equal to the voxel edge size. The error on the effective reactivity prediction is also lower than 2.5%. For fibers and matrix of equal density, the effective reactivity of the yarn k_y^{eff} in transient regime given by [63] :

$$k_y^{eff} = \begin{cases} k_m \left(1 + 2Sh\sqrt{A^2 - 1} - Sh^2\right)^{-1/2} & if \quad 0 \le Sh < \sqrt{A^2 - 1} \\ k_m/A & if \quad Sh \ge \sqrt{A^2 - 1} \end{cases} \qquad (6.10)$$

is then in agreement with numerical simulation results. As a conclusion, the vertical concentration gradient hypothesis is correct in steady state.
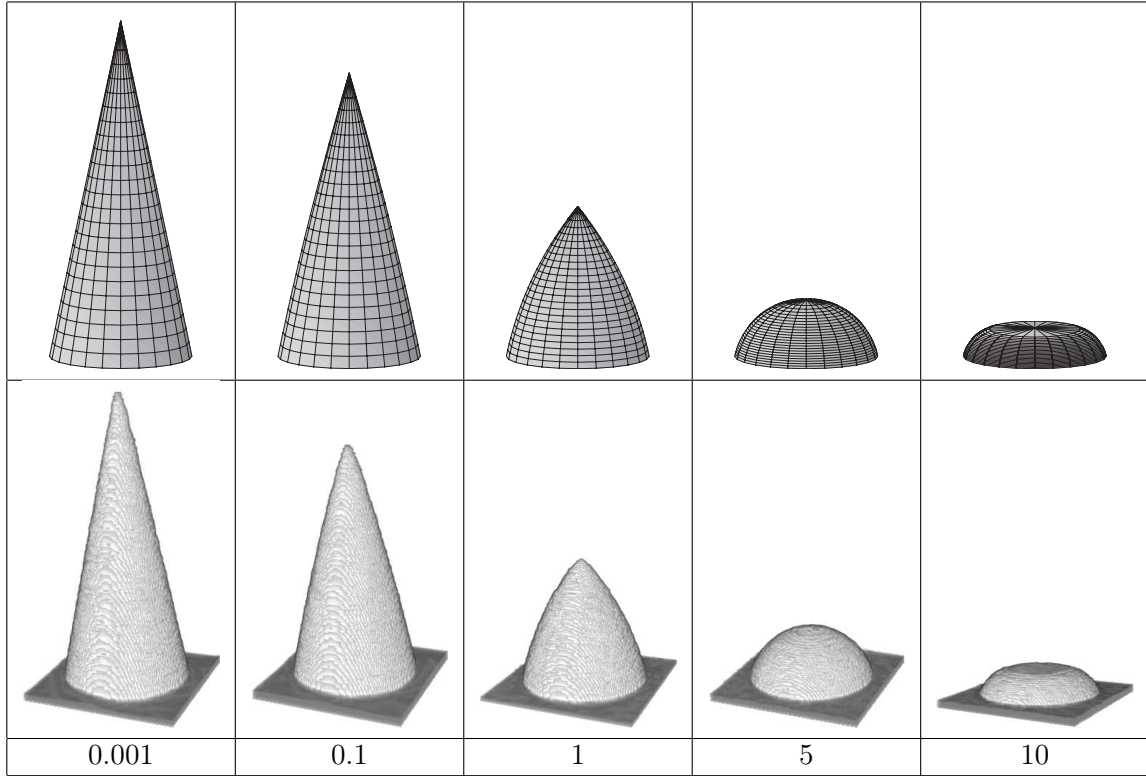
FIG. 6.7 – Fiber morphology at steady state as a function of Sh (with $A = 5$) : qualitative comparison of analytical solution (top) with AMA simulation (bottom).

6.4.2   Perpendicular yarns : inclined fibers

Let us consider the case of 3D C/C ablation. As represented on figure 6.8-a, when steady state is reached at macroscopic scale, the perpendicular yarns are sharpened more or less in the same way as individual fibers are. Then, the local normal $\mathbf{n}$ to the elementary surface features an angle α_y with the horizontal axis. As represented on figure 6.8-c, the yarn surface is actually defined by the tips of the sharpened fibers [63]. Moreover, the local surface recession is shown to occur along $-\mathbf{n}$.
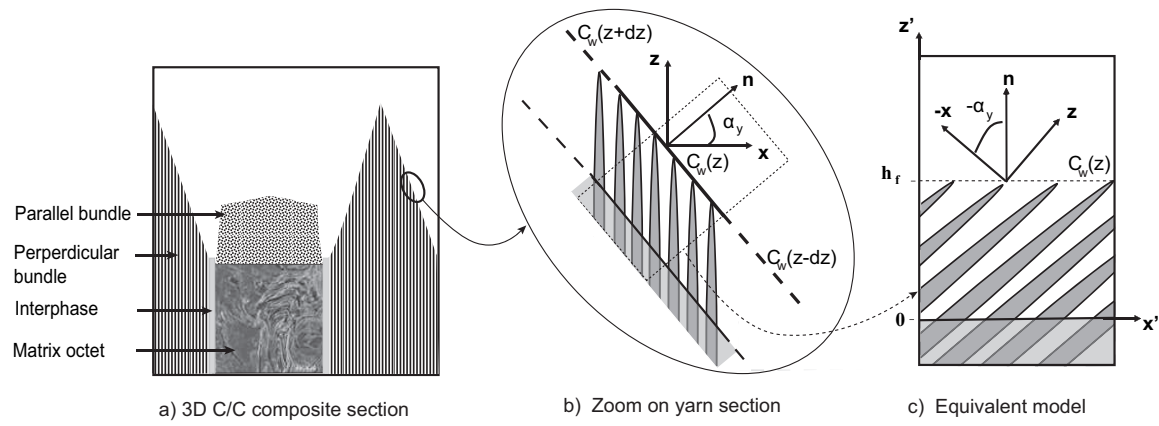
FIG. 6.8 – Scheme of the multi-scale surface roughness on a 3D C/C in steady state
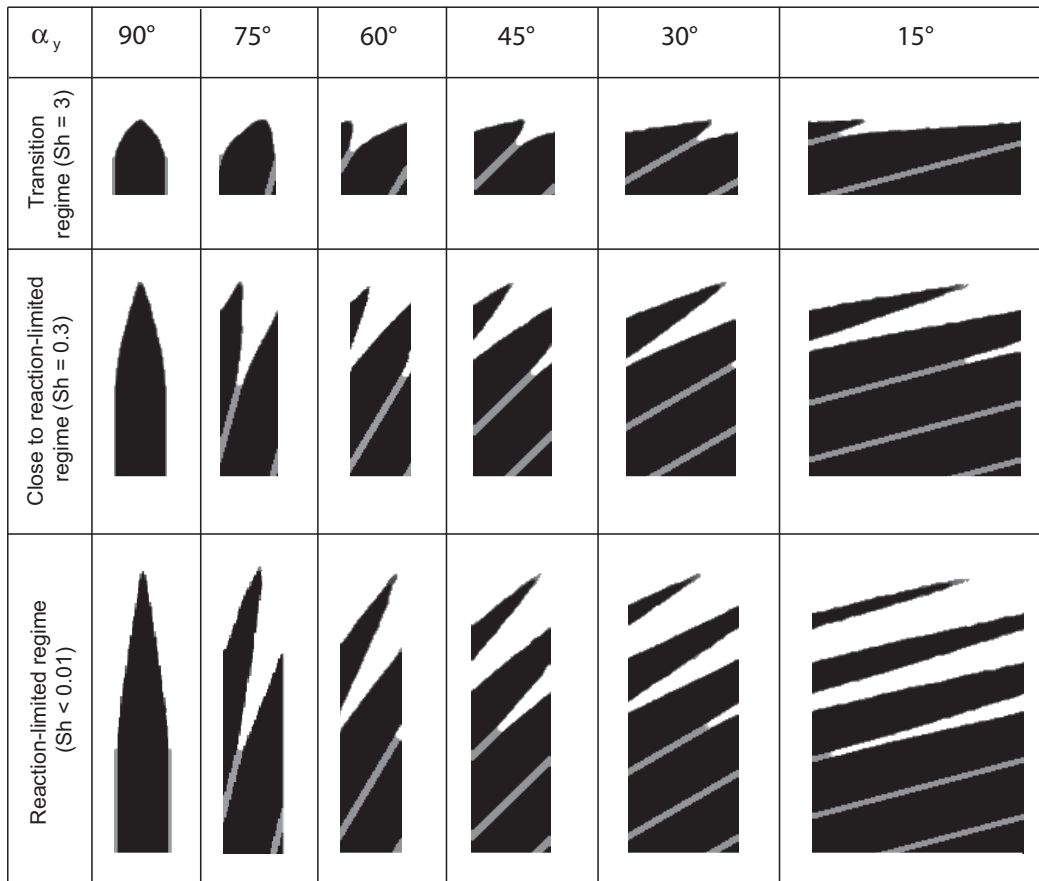
FIG. 6.9 – Comparison of the surface roughness features when α_y varies ($A = 10$).

In consideration of the small size of the fibers section compared to that of the yarn, the local concentration on the wall $C_w(z)$ at ordinate z may be considered as constant. Then, the
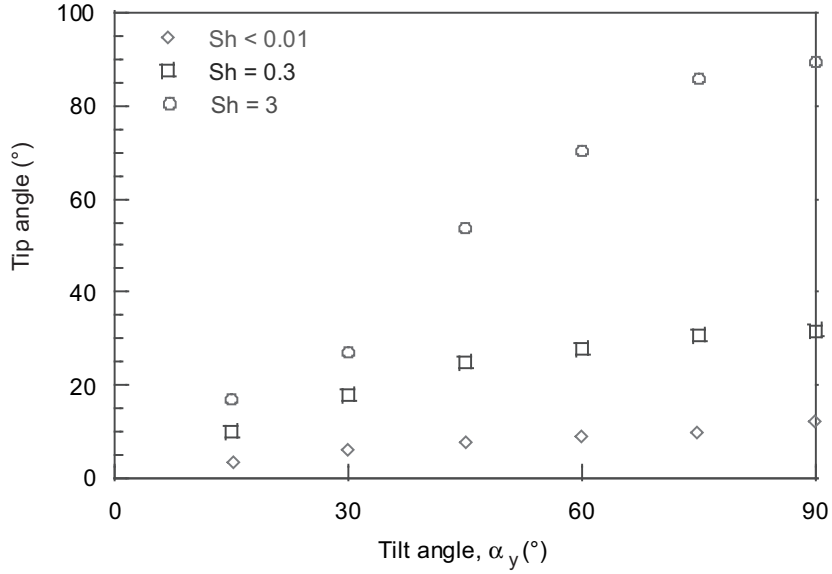
FIG. 6.10 – Fiber tip angle vs. tilt angle α_y

local 3-D cell can be represented by figure 6.8-c. The associated model is the same as the one presented in subsection 6.2.2, except that the fibers are tilted by an angle $\pi/2 - \alpha_y$ [63]. This problem has been solved in 3D for angles ranging from 90° to 15°, by steps of 15°. Sections of the resulting surface roughness features are presented on figure 6.9 for $A = 10$ and for various regimes. The respect of the translation boundary condition for the material leads to the fact that the lower α_y is, the larger the cells are. The diffusion-limited regime is not represented since it is trivial for all angles (flat surface). In reaction-limited regime ($Sh < 0.01$), the fiber height h_f^s, expressed as the vertical distance from matrix to fiber tip, does not depends on α_y. When diffusional effects appear, h_f^s seems to slightly increase with α_y. This could have been expected, since the fibers tend to protect a little more the matrix when they are inclined, by bringing some tortuosity to the diffusion stream lines. Due to this latter effect, the revolution symmetry is no longer obtained for the fiber geometry. Indeed, the part of the fiber tip which is oriented toward the bulk fluid phase undergoes a higher recession. This tends to lower the apparent fiber angle α_y. This phenomenon increases with Sh, that is, with diffusion effects. At the same time, the value of the fiber tip angle α_f decreases with the fiber angle α_y (see figure 6.10). This result is in qualitative agreement with experimental observations [61]. In all regimes, for a given value of Sh, the effective reactivity variations when α_y varies are lower than AMA uncertainties ($< 2.5\%$). Therefore, the effective reactivity is not a function of α_y, as soon as α_y is strictly positive. The effective reactivity of the inclined yarns is then given by equation (6.10). This result is of importance for the multi-scale modeling of C/C composites behavior, since the effective reactivity of the yarn can be assumed homogeneous when steady state is reached at mesoscopic scale. Moreover, the duration of the transient regime at mesoscopic scale (development of sharp fibers) is shown to be about five times lower than the duration of the transient regime at macroscopic scale (development of sharp yarns) for the 3D C/C of this study [65]. This is a sufficient condition to uncouple the two scales in steady state.

a) AMA simulation (A=10, Sh<0.01, α_y = 15°)   b) SEM observation of a 3D C/C yarn inclined by approximatively 15°
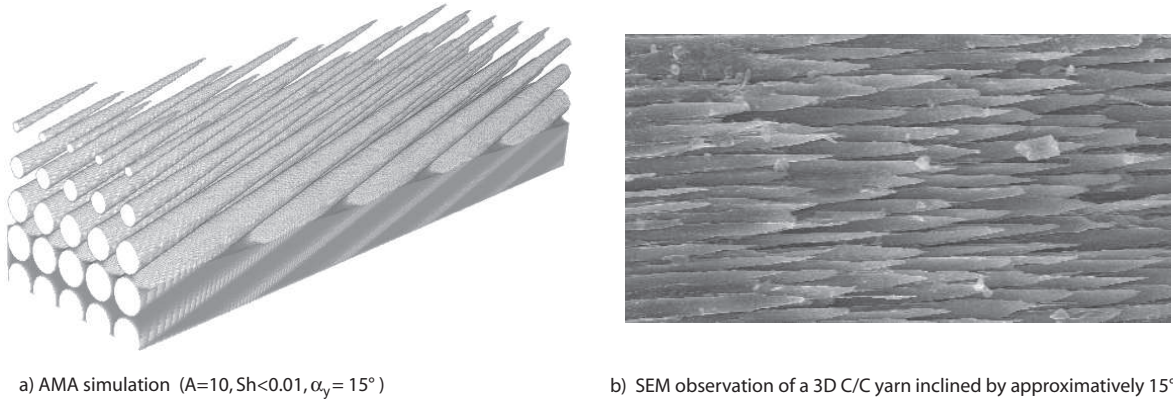
FIG. 6.11 – 3D visualization of a simulation result qualitatively compared to a SEM observation

6.4.3   Parallel yarns

In 3D C/C composites, some yarns are parallel to the overall surface (see figure 6.8-a). Their fibers are then also parallel to surface. They are tilted by 90° when compared to the situation sketched on figure 6.1-a. Steady state cannot be reached in such a configuration, since the fibers are ablated layer by layer [61]. Nevertheless, a steady periodic behavior may be expected. This section addresses this latter in various reaction regimes. Mechanical erosion is also discussed.

The actual architecture of 3D C/C yarns is as follows. Carbon fibers are surrounded by a weak phase of ex-pitch carbon matrix, called interphase. Its thickness is about $0.5\,\mu m$ [62]. The rest of the inter-fiber space is filled by a bulk pitch-based matrix whose reactivity is approximatively equal to that of the fibers. For this material in the tested ablation conditions (oxidation at $898\,K$, sublimation at $4000\,K$), the reactivity contrast between the interphase and the fibers is found to lie around 30 [63]. It is noted A in the following. As shown on figure 6.6-a which is representative of the whole yarn architecture, the fibers array is quite compact. Two adjacent fibers are then linked by interphase, whereas the bulk matrix is mainly found in the vacancies formed between fibers. This retained geometry is visible on the bottom of the numerical cell of figure 6.12-e. Translation conditions on the lateral boundaries are respected. A Dirichlet boundary condition is applied on boundary layer top, with $\delta_c = R_f$. In a first approach, mechanical erosion is neglected. The behavior of the yarn is represented on figure 6.12 from reaction-limited regime ($Sh << 1$) to diffusion-limited regime ($Sh >> 1$). The value of the normalized effective reactivity ($\widetilde{k} = k_{eff}/k_m$) decreases from a value around unity in reaction-limited regime to a value close to $1/A$ in reaction limited regime. These values are very close to those obtained using equation (6.10). The maximal discrepancy is obtained in diffusion limited regime ($\sim$ 17%). Nevertheless, as far as gasification rate is concerned, the error is lower since diffusional effects tends to smooth out the reactivity differences. Then, as a first approximation, the effective reactivity of parallel yarns can be assessed using the results of inclined yarns.

Of course, when mechanical erosion is not neglected, the apparent ablation rate may be found higher, since the fibers can be drawn out by the shear stress of the surrounding flow. The ablation rate can then be in a large part dictated by the flow velocity. The drawing

a) Sh = 0.014   b) Sh = 0.14   c) Sh = 1.4   d) Sh = 14   e) Sh = 140
   $\tilde{k} \sim 1$ $\tilde{k} \sim 0.375$ $\tilde{k} \sim 0.13$ $\tilde{k} \sim 0.05$ $\tilde{k} \sim 0.04$

FIG. 6.12 – Simulation of a parallel yarn behavior as a function of Sh for $A = 30$.

hypothesis may explain the fact that the parallel yarns seems slightly more reactive than the perpendicular ones in plasma-jet tests [61], whereas it has been shown that for a given set of conditions their effective gasification rates should be roughly equal. For the 3D C/C ablated at high thermal flux (plasma test), Sh has been estimated to lie around 0.4 from a surface roughness analysis of the perpendicular yarns [63]. Then, the resulting morphology without drawing should look like something between figures 6.12-b and 6.12-c. The parallel fibers should be stripped on approximatively three levels. The SEM analysis shows that no parallel stripped fiber lies on the surface [61]. This observation supports the idea that mechanical erosion occurs. Nevertheless, it is difficult to evaluate to which extent. However, most of the the parallel yarns are not strictly parallel to surface. Then, the configuration is in general more rigorously modeled by inclined fibers, with a low angle, as represented on figure 6.11. As a conclusion, mechanical erosion is likely to occur, but sporadically, and it might explain the slightly higher ablation rate of the parallel yarns. Some more experimental investigations would be useful to give a quantitative evaluation of mechanical erosion effects.

Concluding on parallel yarns, one may object that the description of the yarn architecture could have a significant influence on the ablation rate evaluation. Indeed, even if the presented description looks quite accurate and reliable for 3D C/C, a new study should be done for any new architecture. Moreover, the quality of the results strongly depends on the ease of the structure to be modeled. Hence, in the following section, another method, based on an inverse analysis, to assess the ablation rate of the perpendicular yarns as well as of any other mesoscopic component of the composite is proposed.

6.5 Application to macroscopic scale

The macroscopic scale behaviors of a 3D C/C and a 2D C/phenolic resin composite (2D C/R) have been analytically modeled using the model of subsection 6.2.2 [63], considering square-section yarns instead of cylindrical fibers. The model has been validated by comparison to experimental results [63]. In steady state, the composite behavior is shown to be only driven by the inter-yarn interphase and the perpendicular yarns (see figure 6.8-a). The composites architectures have been strongly simplified in the analytical model; among others, parallel yarn reactivities have been left apart. In this section, the purpose is to model actual architectures. Two materials are considered : a 3D C/C and a 2D C/R with ply orientation inclined by 30° with respect to the overall surface.

6.5.1 3D C/C

The 3D C/C actual architecture is represented on figure 6.13-a and modeled on figure 6.13-c. This material has been ablated using two ablation tests : a plasma test, and an oxidation test. In the case of the plasma test the Sherwood number at mesoscopic scale has been found to lie around 0.4 [63]. Hence, the Sherwood number associated to the macroscopic scale is higher than 100. Therefore, gasification processes cannot be the direct cause of surface roughness at this scale. The fact that the ablation rate of parallel yarns is slightly higher than for perpendicular yarns [61] is then to be attributed to mechanical erosion. Switching to the oxidation test, in the conditions of this study ($898\,K$, dry air), the reactivity contrast A_y between perpendicular yarns and interphase has been found to lie around 8 [63]. The Sherwood number is very low, that is, the regime is reaction-limited. All the mesoscopic components densities are close to $2\,g.cm^{-3}$, except for the porous matrix octets ($1.6\,g.cm^{-3}$). The unk-

nowns of the problem are then the reactivity contrasts between parallel and perpendicular yarns A_{pp}, and between matrix octets and perpendicular yarns A_{mop}. They are assessed by matching the surface roughness morphologies obtained by numerical simulation and by SEM analysis. According to the micrograph of figure 6.13-b, A_{pp} and A_{mop} seem to be equal and close to 1. The results of the numerical simulations using this value are presented on figures 6.13-d and e. The numerical simulation shows that the oxidation test was shorter than the transient regime duration. It is then more convenient to compare the transient regime morphologies. With $A_{pp} = 1$ a correct agreement between experimental and simulation results is obtained. Note that this value is in agreement with the results of the previous section, since parallel and perpendicular yarns are shown to display the same effective reactivity. To show the sensibility of the method, on figures 6.13-f and g, some simulations are presented with $A_{pp} = 2$. They are clearly less appropriate. Nevertheless, the sensibility of the method is closely linked to the accuracy of the experimental analyses. Tomographs at macroscopic scale would help to improve quantitatively the prediction, as this has been shown for mesoscopic scale [61, 63].

The predicted steady state morphology is represented on figure 6.13-c. The interphase, which is more reactive, has a higher recession rate. The parallel yarns and the matrix octets are then totally stripped after a duration that can be short in comparison to their characteristic ablation time. Therefore, erosion can occur through the detachment of these components. This phenomenon is experimentally observed for matrix octet when advection is high enough [61]. To illustrate this effect, erosion has been taken into account in the simulation of figure 6.13-c. The apparent ablation rates of the parallel yarns and of the matrix octets are then higher than expected. The resulting surface roughness is quite similar to that of figure 6.13-e. Hence, the apparent ablation rates are approximatively equal to that of the latter simulation case, that is, twice as high as expected.

6.5.2   2D C/R

The aim of this section is to model a 2D C/phenolic resin composite for which ply orientation is inclined by 30° with respect to the overall surface. As represented on figure 6.14-a, the ablation of these materials leads to a typical sawtoothed surface roughness [61] in plasma tests. The proposed modeling of the material is represented on figure 6.14-b. A_y has been found to lie around 3 for this material in another configuration (the ply orientation was perpendicular to surface) [63]. The simulation is performed in reaction-limited regime. As expected and shown on figure 6.14-b and c, the sawtoothed geometry may be explained by the physico-chemical model. This result applies to moderate temperatures, for which the regime is reaction-limited ($Sh << 1$). Unfortunately, no experimental observation is available for comparison in this regime. However, since the model has been validated for other orientations [63] on this material, and for 3D C/C, the represented feature is strongly expected to appear in steady state for reaction limited-regime. In plasma tests conditions (high temperature and high reactivity), the macroscopic Sherwood number is high. Then, like for 3D C/C, gasification is more likely to play a role in the triggering of other phenomena leading to surface roughness, like mechanical erosion.

As a conclusion of this macroscopic scale study, when advection is low, the physico-chemical model of ablation gives correct results. Moreover, the reactivities of the composite components can be inferred by inverse analysis. For plasma test conditions, the model is no longer applicable as such, since other phenomena like advection or turbulence have a strong

a) Initial time (SEM)

b) End of the oxidation test (SEM) : transient regime

Parallel yarn

Matrix octet

Interphase

Perpendicular yarn

c) Initial time : numerical cell (AMA)

d) Transient regime $(A_{wp} = 1)$

e) Steady state prediction $(A_{wp} = 1)$

f) Transient regime $(A_{wp} = 2)$

g) Transient regime $(A_{wp} = 2)$

h) Steady state prediction $(A_{wp} = 2)$
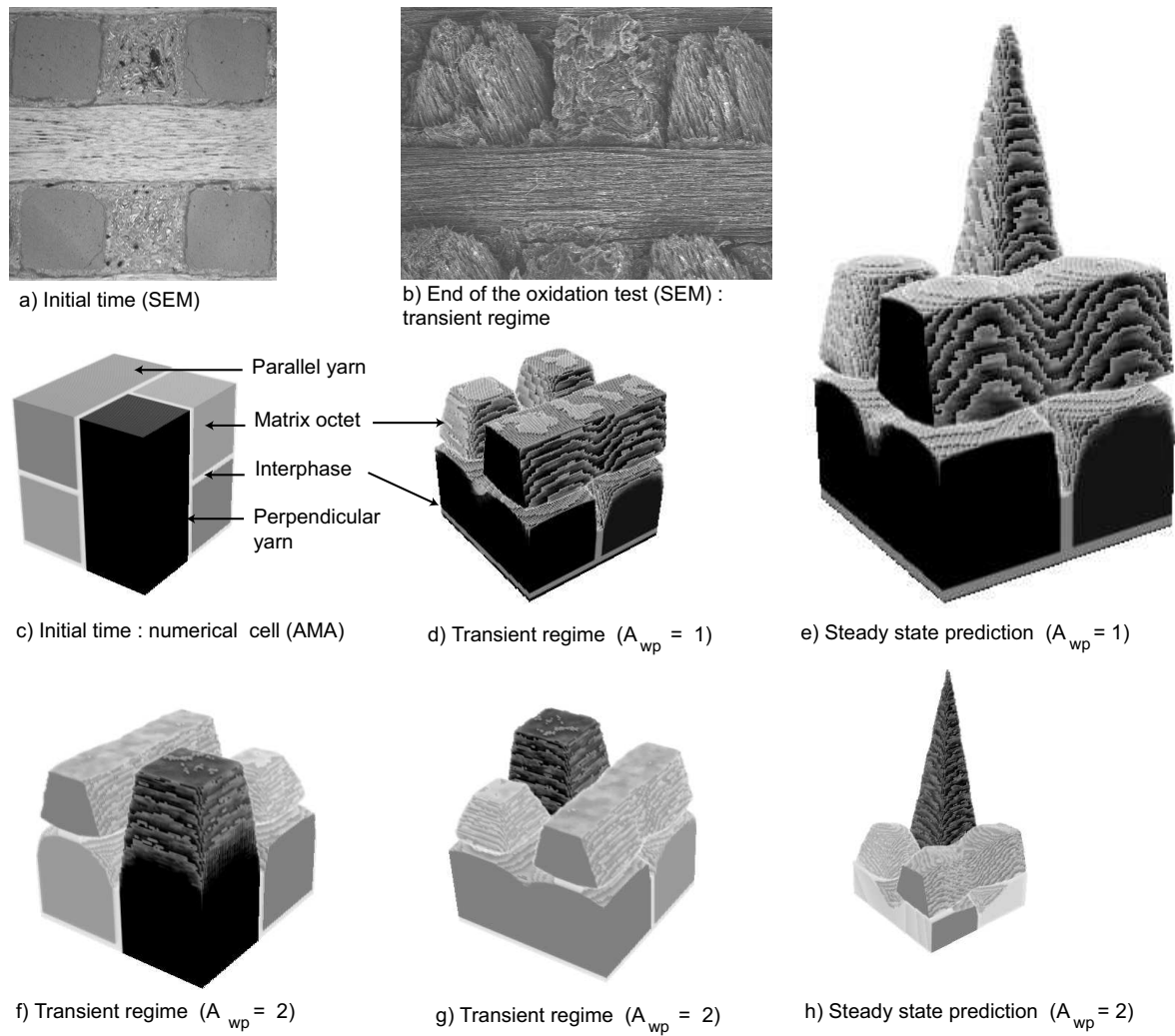
FIG. 6.13 – 3D C/C actual architecture and simulation of ablation (dry air, $898\,K$).

Ply

Matrix

a) SEM observation of surface roughness

b) Simulation result (section)

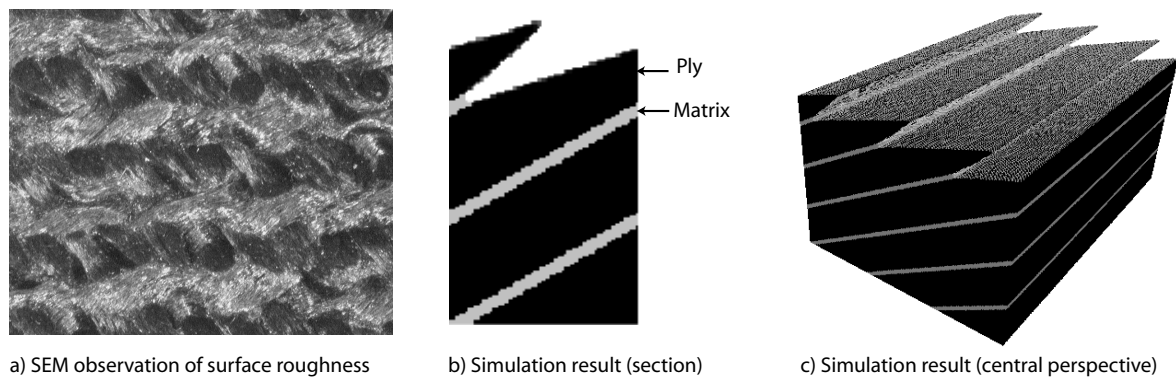c) Simulation result (central perspective)

FIG. 6.14 – 2D C/C actual architecture and simulation of ablation

effect on the material behavior. Nevertheless, the model shows that gasification processes cannot explain alone the observed morphologies, but tend to promote a mechanical erosion which seems to occur in parallel.

6.6   Conclusion

The modeling of physico-chemical ablation of C/C composites has been addressed in steady state on actual architectures. A general model for receding surfaces under a first-order gasification process, which has been shown to explain well the ablation phenomenon [63], has been presented. The results of an analytical solution, obtained for simple architectures and under some extra physical hypotheses, have been used as a reference, in order to validate the analytical model hypotheses and to address more complex architectures. To solve these problems, a 3D numerical simulation code, AMA, has been developed on a Monte-Carlo Random-Walk principle. AMA solves efficiently reaction/diffusion problems with a receding surface. It has been validated by comparison to two analytical models :(i) a 1D reaction/diffusion model in all regimes, (ii) a 3D model in reaction-limited regime. The multi-scale ablation of actual architectures has then been addressed using AMA. First, at microscopic scale (fibers), an interpretation of the origin of the large facets displayed by sharp ablated fibers has been proposed. The large facets basically seem to arise from the irregularities of fibers section which are intensified by ablation. Second, the mesoscopic scale (yarns) has been approached. The hypotheses of the analytical model, which had to be verified at this scale, have been shown to be correct. Then, the case of yarns inclined with respect to the overall surface has been analyzed. For the retained yarn structure, the inclination angle has been shown to display no influence on the effective reactivity. Nevertheless, in the case of yarns parallel to surface, mechanical erosion might occur in high velocity flow. Finally, the macroscopic architectures of a 3D C/C and a 2D C/R have been modeled. The results of the simulations are in correct agreement with experimental observations at low temperatures. Nevertheless, for plasma-jet tests, the surface roughness features cannot arise only from gasification processes. Mechanical erosion is likely to be coupled to them. In the future, particular care should be taken to mechanical erosion to improve the understanding of ablation in plasma-jet conditions at macroscopic scale.

7 Analytical and 3D numerical modeling in transient regime

Préambule

Ce chapitre constitue un projet de publication soumis à la revue *Journal of Applied Physics.*

<u>Titre</u> : Physico-chemical ablation of carbon-carbon composites : V- Analytical and 3D numerical modeling in transient regime.

<u>Auteurs</u> : J. Lachaud[1], Y.Aspa[1,2] et G. L. Vignoles[1]

<u>Affiliations</u> :

[1]Laboratoire des Composites ThermoStructuraux (LCTS)

UMR 5801 : CNRS-SAFRAN-CEA-UB1

Domaine Universitaire de Bordeaux – 3, Allée de La Boétie, 33600 Pessac, France

[2]Institut de Mécanique des Fluides de Toulouse (IMFT),

1, allée Prof. Camille Soula, 31000 Toulouse, France

Résumé

Le comportement ablatif d'un composite 3D C/C est abordé en régime transitoire. Un modèle de récession de surface est résolu analytiquement. Le composite étant un matériau multiéchelle, sa modélisation suit son architecture via deux changements d'échelle. D'abord, le comportement du composite à l'échelle mésoscopique (fil) est déduit des propriétés de ses composants microscopiques (fibres, matrice intra-fil). Ensuite, son comportement macroscopique est obtenu à partir de ceux des fils et des composants inter-fils. Un code de simulation numérique est utilisé pour valider les hypothèses du modèle analytique. Un bon accord est obtenu entre les résultats théoriques et expérimentaux. Les principales données de sortie du modèle sont la géométrie de la rugosité en fonction du temps, la durée du régime transitoire et la réactivité effective du composite en fonction du temps. Enfin, les résultats du modèle sont comparés à un essai d'oxydation réalisé sur un composite 3D C/C. Un bon accord est obtenu. De plus, les résultats théoriques s'avèrent très utiles pour l'analyse des données expérimentales.

Abstract

The behavior of a 3D C/C composite is addressed in transient regime. A surface recession model is solved analytically. Since the composite is a multi-scale material, its modeling follows its architecture through two changes of scales. First, the mesoscopic scale behavior of the composite (yarn) is inferred from the properties of the microscopic scale components (fiber, intra-yarn matrix). Second, the macroscopic scale behavior of the composite is obtained from that of the yarn and the inter-yarn components. A numerical simulation code is used to validate the hypotheses of the analytical model. The agreement between numerical and analytical

results is shown to be correct. The main outputs of the models are the description of surface roughness as a function of time, the prediction of the duration of the transient regime, and the determination of the effective reactivity of the composite versus time. Finally, the results of the model are compared to an ablation experiment carried out on a 3D C/C composite. A correct agreement is obtained. Moreover, the theoretical results are shown to be of invaluable help in the analysis of experimental data.

7.1   Introduction

Carbon/Carbon (C/C) composites, which keep excellent mechanical properties at high temperatures [38], are used as thermostructural protections in various applications such as atmospheric re-entry (thermal protection systems of vehicle) [22, 31, 32], propulsion (rocket nozzle) [10, 11, 57], and experimental Tokamaks reactors for nuclear fusion (divertor and first wall armor) [13, 79, 103]. In the applications cited above, the C/C composites are progressively destroyed by oxidation (re-entry and propulsion), sublimation (re-entry and Tokamaks), and, up to a certain extend, ionic etching (Tokamaks), and thermo-mechanical erosion (all cases). These degradation processes, coupled with a high interfacial mass transfer, induce a non negligible recession of the wall. They are collected in the generic term *ablation*. Nevertheless, ablation, which is usually globally endothermic, is partially beneficial as it reduces the wall temperature and the heat flux that penetrates the internal structure.

An efficient design of thermostructural protection relies on an accurate evaluation of the wall recession caused by ablation. Hence the coupled physical phenomena leading to carbon loss and resulting in a global surface recession have to be known. This work is the fifth part of an article series which aims to improve the understanding of the behavior of carbon-carbon (C/C) composites during physico-chemical ablation, and to model it [61–64].

The behavior of C/C composites is closely linked to the onset of a multi-scale surface roughness [61], which may display a strong coupling with the surrounding environment [31, 104]. The surface roughness chiefly arises from the heterogeneity of the composites which are multi-scale materials : (i) microscopic scale (fibers, intra-yarn matrix), (ii) mesoscopic scale (yarns, inter-yarn matrix), and (iii) macroscopic scale (composite architecture). Independent measurements of the reactivities of the composites and of their components are carried out in the second part [62]. This work shows that the composites oxidation rates cannot be trivially inferred from that of their components. In a third part, following the multi-scale modeling strategy proposed in the first part, the composite behavior is analytically modeled in steady state [63]. The results are in qualitative and quantitative agreements with the experimental observations of [61, 62]. Part IV [64] completes the analytical modeling of part III [63] using 3D numerical simulation : the actual architectures of C/C composites are modeled with more accuracy and some simplifying assumptions of the analytical model are removed. This gave the opportunity to validate the work hypotheses of the analytical model, to reproduce some particular features closely linked to material structure, and to assess by inverse analysis the reactivities of all the composite components. 3D numerical simulations also enable to treat accurately the transient regime. It is the purpose of the present contribution.

This paper is organized as follows. First, a general model for receding surfaces in transient regime is set up. Second, adding a hypothesis on the boundary conditions and using the bases of the previous steady state analytical model [63], an analytical solution for the transient regime is proposed and exploited at mesoscopic scale. The results at macroscopic scale are

shown to be mathematically equivalent, though the characteristic orders of magnitude are different. Third, after a brief presentation of the numerical simulation tool implemented for this study [64], the results of the numerical simulation in transient regime are compared to the analytical solution. The agreement between the two solutions is shown to be correct. Fourth, the analytical model, or the numerical results when the actual geometry is modeled, are then exploited and applied to the study of the behavior in transient regime of a 3D C/C composite, which has already been successfully modeled in steady state [63]. To enable the validation of the modeling in transient regime, the 3D C/C composite has been ablated in an oxidation reactor fully described in [62]. The material behavior is presented : it has been followed by SEM analysis and mass loss measurement as a function time. Experimental [61,62] and theoretical results are then compared and shown to be in correct agreement, qualitatively (morphology of surface roughness) as well as quantitatively (mass loss rate).

7.2 Model set-up

This section aims to present the scope of the model, to justify some physico-chemical assumptions, and to set up a mathematical description of the model. This presentation is synthetic ; more complete discussions are done elsewhere [61, 63].

7.2.1 Scope and assumptions of the model

This work focuses on physico-chemical ablation, that is, ablation either by oxidation or by sublimation, which can be considered as first-order gasification processes [63]. The retained model is a quite general model which applies to any physico-chemical ablation phenomena under the following hypotheses : (i) material in a dense flow, (ii) negligible thermal gradients, (iii) negligible advection close to the wall, (iv) first-order gasification process leading to surface recession, (v) close to the wall, the mass Péclet number is low (mass transfer by diffusion). In particular, those hypotheses are shown to be valid in the case of the oxidation test used for the study of C/C composite behavior during ablation [63]. The architecture of the 3D C/C composite and the ablation phenomena are sketched at figure 7.1 in transient regime. Since the C/C composite is a multi-scale material, the modeling of the overall behavior of the material has to be done using two changes of scale. First, the fiber bundles properties are inferred from that of their components (fibers, interphase, intra-yarn matrix) at mesoscopic scale (see figure 7.1-b). Second, the composite behavior is obtained from the bundles and inter-bundle matrix properties at macroscopic scale (see figure 7.1-a).

7.2.2 Mathematical description

The following mathematical writing of the model may be applied to any first order gasification process coupled to mass transfer by diffusion. Let the general mathematical formalism be presented using the oxidation notations.

Let J_e (in $mol.m^{-2}.s^{-1}$) be the molar impinging flux of reactant per surface unit given by a first order kinetic law : $J_e = k_e.C$, with k_e (in $m.s^{-1}$) the oxidation rate of the material e and C (in $mol.m^{-3}$) the reactant concentration at the material surface. Mass conservation of the reactant in the fluid phase writes :

$$\frac{\partial C}{\partial t} + \nabla \cdot (-D\nabla C) = 0 \tag{7.1}$$
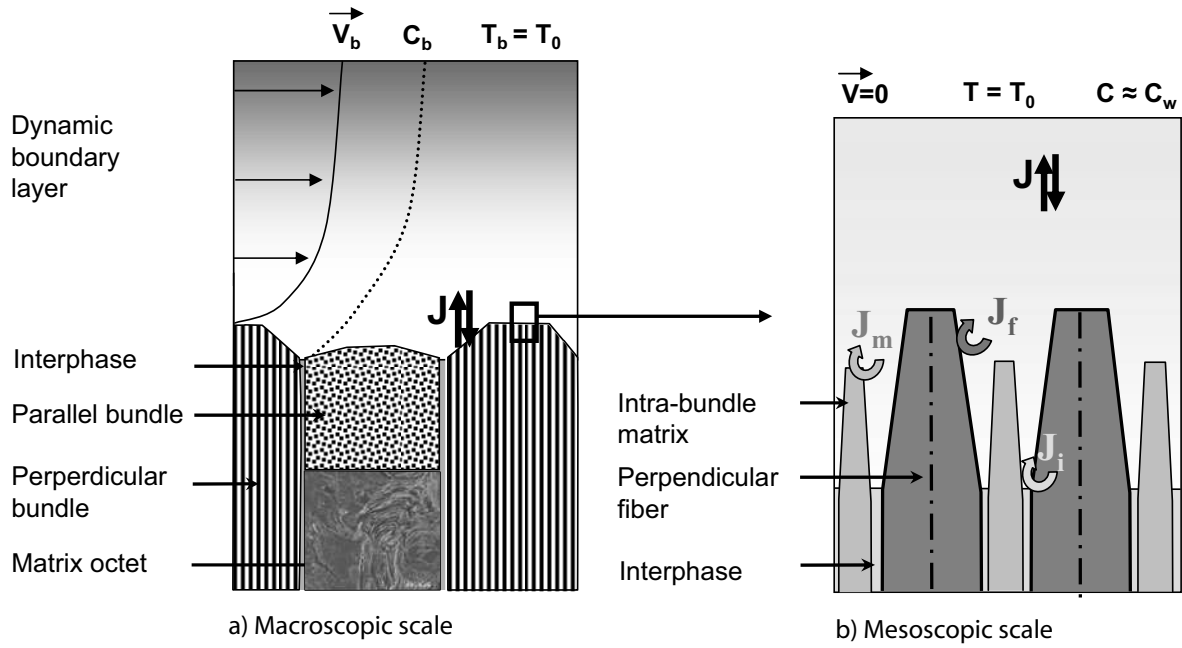
FIG. 7.1 – Modeling strategy : sketch of the ablation phenomena and of the surface roughness of a 3D C/C in transient regime

where D (in $m^2.s$) is the diffusion coefficient of the reactant in the bulk fluid phase.

Boundary conditions relative to the model domain are :

– On boundary layer top : $C = C_0$;

– At the fluid/solid interface the oxidation molar rate j_e above the solid element e writes :

$$J_e = (-D\nabla C) \cdot \mathbf{n} = -k_e C \qquad (7.2)$$

where $\mathbf{n}$ is the normal to the surface ;

– Periodicity on lateral boundaries.

Simultaneously, the gasification processes lead to the recession of the material surface S. The macroscopic motion of this surface can be interpreted as an advancing wavefront. The surface position is commonly described in cartesian coordinates by the following scalar equation :

$$S(x, y, z, t) = 0 \qquad (7.3)$$

such that the function S, which possesses almost everywhere first order partial derivatives, acquires nonzero values at all points not lying on the interface [53]. The function S satisfies the differential equation :

$$\frac{\partial S}{\partial t} + \mathbf{v_e} \cdot \nabla S = 0 \qquad (7.4)$$

where $\mathbf{v_e} = v_e j_e \mathbf{n}$ is the surface local normal velocity , with v_e the solid molar volume of e [53]. The interface position S is then given by the simultaneous resolution of equations (7.1-7.4). For an analytical resolution, S can be rewritten under a more convenient explicit form like : $S = z - f(x, y, t) = 0$ [63].

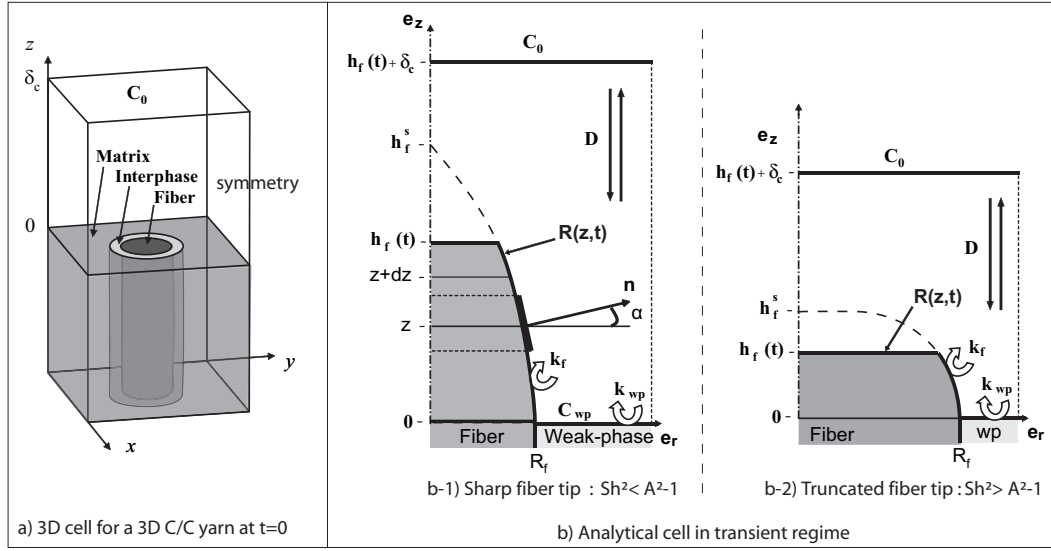FIG. 7.2 – Scheme of the elementary pattern and of the proposed model in transient regime

7.3 Analytical solution

This analytical part aims to model in transient regime the multi-scale behavior of C/C composites for which yarn orientations are strictly perpendicular or parallel to surface. The hypotheses of the steady state approach [63], which have been shown to be correct [64, 67], are : (i) the weak phase remains flat and perpendicular to the **z** axis (see figures 7.2 b and c), (ii) the gradient of reactant concentration is only vertical (along **z**). Let these hypotheses be also used for the analytical modeling of the transient regime. Their validity is evaluated in section 7.4 by comparison to numerical results.

7.3.1 Mesoscopic scale

For the first change of scale, the behavior of the yarns perpendicular to surface has to be modeled [63]. Inside the yarn, the fibers are assumed homogeneous, isotropic, perpendicular to surface, axi-symmetrical, and surrounded by an homogeneous weak phase (the interphase) as represented on figure 7.2-a. The height of the bulk matrix is at any time lower than that of the fibers (h_f) and higher than that of the weak-phase ($h = 0$), or at most equal [61, 63]. Then, under the vertical mass transfer hypothesis, the intra-yarn matrix displays no influence on the fibers and interphase behaviors. Moreover, the latter determines the overall yarn behavior [63]. The problem is then more conveniently treated in cylindrical coordinates, as represented on figure 7.2-b. The surface of the fiber can be described by the following equation : $S_f(r, \theta, z, t) = r - R(z, t) = 0$. Under the above hypotheses and in steady state ($R(z, t) = R(z)$), the dimensionless fiber surface $\widetilde{R}(\widetilde{z}) = R(\widetilde{z})/R_f$ is given by the positive part [63] of :

$$\widetilde{R}(\widetilde{z}) = Sh^{-1} \left(\sqrt{A^2 - (1 + Sh\,\widetilde{z})^2} - \sqrt{A^2 - 1} \right) + 1 \tag{7.5}$$

with $\widetilde{z} \in [0, (A-1)/Sh[$. R_f is the fiber radius, $\widetilde{z} = z/R_f$, $Sh = R_f\,k_{wp}/D$ is a Sherwood

number, and $A = (k_{wp}\upsilon_{wp})/(k_f\upsilon_f)$ the contrast in the reactivities weighted by the molar volumes between fibers (subscript f) and weak phase (subscript wp). This is the equation of a circle arc (sphere segment) with center at $(\widetilde{R} = 1 - \sqrt{A^2-1}/Sh\,;\ \widetilde{z} = -1/Sh)$ and radius A/Sh. If $Sh \geq \sqrt{A^2-1}$, the fiber tip is truncated, and its reduced steady-state height $\widetilde{h_f^s} = h_f^s/R_f$ is limited to $(A-1)/Sh$ (see figure 7.2-b-2) [63]. Else if $Sh < \sqrt{A^2-1}$ (figure 7.2-b-1), the fiber tip is sharp and $\widetilde{h_f^s}$ writes :

$$\widetilde{h_f^s} = \sqrt{Sh^{-2} + 2Sh^{-1}\sqrt{A^2-1} - 1} - Sh^{-1} \tag{7.6}$$

On figures 7.2-b-1 and 7.2-b-1, the steady state shape is represented in dashed lines. In transient regime, the fiber tip displays a plateau in both cases (grey-filled part surrounded by a continued line). At initial time, one has $h_f(t=0) = 0$ (see figure 7.2-a) ; when steady state is reached $h_f(t=t^s) = h_f^s$.

It has been shown that the values of C_0 and of δ_c, the size of the concentration boundary layer, have no influence on the steady state surface roughness [63]. However, they affect ablation velocity as well as transient regime duration. The concentration gradient in the concentration boundary layer is vertical by hypothesis in all regimes. The concentration on fiber plateau in transient regime is then given by [63] :

$$C_{eff}(t) = C_0\,\frac{1}{1 + \frac{k_y^{eff}(t)\,\delta_c}{D}} \tag{7.7}$$

where $k_y^{eff}(t)$ is the effective reactivity of the yarn (fiber and matrix) in transient regime at the position $h_f(t)$. Let $k_y^{eff}(t)$ be determined. The cylindrical fibers are supposed arranged in a square array in the yarn. In the actual material, this array is compact ; therefore, the bulk matrix volume fraction is low, since most of the inter-fiber space is occupied by the interphase. The analytical resolution domain is then the one represented on figure 7.2-b. According to the unidirectional gradient hypothesis, the concentration of the weak phase writes [63] :

$$C_{wp}(t) = C_{eff}(t)\,\frac{1}{1 + \frac{k_{wp}\,h_f(t)}{D}} \tag{7.8}$$

The molar flux by surface unit consumed by the weak phase is then :

$$J_{wp}(t) = k_{wp}\,C_{eff}(t)\,\frac{1}{1 + \frac{k_{wp}\,h_f(t)}{D}} \tag{7.9}$$

Considering the transient regime configuration, the part of the fiber between $\widetilde{R} = 1$ and $\widetilde{R}(\widetilde{h}(t))$ has the same recession velocity as the matrix, that is, its consumed molar flux by surface unit projected on matrix plane, J_{fs}, is equal to J_{wp}. The molar volumes of fiber and weak phase are supposed equal for 3DC/C. The molar flux by surface unit consumed by the fibers on the plateau is basically :

$$J_f(t) = k_f\,C_{eff}(t) \tag{7.10}$$

Combining equations (7.7-7.10), one obtains the normalized effective reactivity of the yarn as a function of $\widetilde{h_f}(t)$:

$$\widetilde{k}_y^{eff}(\widetilde{h_f}) = \frac{\widetilde{R}^2(\widetilde{h_f})}{A\widetilde{S}_t} + \left(1 - \frac{\widetilde{R}^2(\widetilde{h_f})}{\widetilde{S}_t}\right)\frac{1}{1 + Sh\,\widetilde{h_f}} \tag{7.11}$$
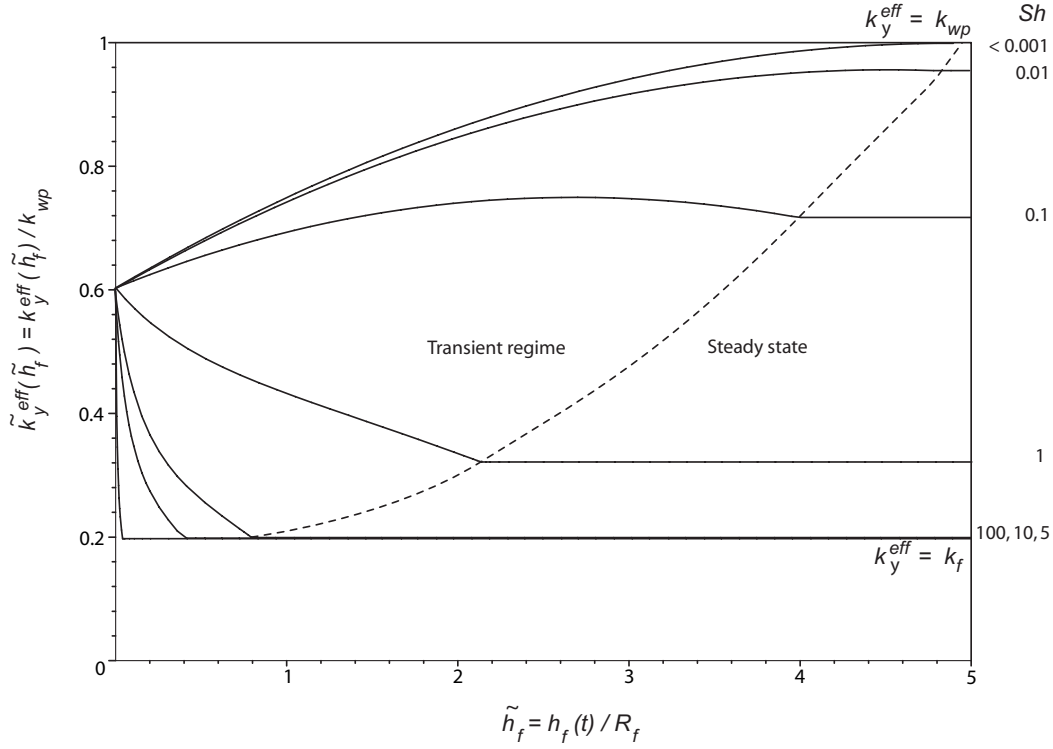
FIG. 7.3 – Normalized effective reactivity versus fibers height ($A = 5$, $\widetilde{S}_t = 2$).

with $\widetilde{k}_y^{eff} = k_y^{eff}/k_{wp}$, $\widetilde{S}_t = S_t/(\pi R_f^2)$ (where S_t is the total surface of the cell), $\widetilde{R} = R/R_f$, and $\widetilde{h_f} = h_f(t)/R_f$. $\widetilde{k}_y^{eff}$ is represented on figure 7.3 for values of Sh ranging from reaction-limited to diffusion-limited regime for $A = 5$ and $\widetilde{S}_t = 2$. For the whole sample, the initial effective reactivity is the arithmetic average of the fiber and the matrix reactivities, since their related surfaces are equal. In reaction-limited regime, the weak phase progressively uncovers the fiber, which increases its exposed area. The concentration in the whole fluid phase being constant and equal to C_0, the effective reactivity of the yarn progressively tends to that of the weak phase. The steady state is reached when $k_y^{eff} = k_{wp}$. When diffusional effects become non negligible, the weak phase is partly protected by the fiber. In diffusion limited-regime inside the yarn ($Sh > \sqrt{A^2 - 1}$), this protection increases until it is total : in steady state the effective reactivity is equal to that of the weak phase. Between these limiting cases, it is interesting to note that the reactivity may increase due to the reaction-limited effect, and then decrease due to diffusive limitation (see the $Sh = 0.1$ curve on figure 7.3). In all the cases, the effective reactivity in steady state is in agreement with the previously found value [63].

The value of h_f as a function of time can be inferred from k_y^{eff}. The growth of h_f as a function of time is given by the difference between the vertical recession velocities of fibers (v_f) and weak phase (v_{wp}) :

$$\frac{dh_f}{dt}(t) = v_{wp} - v_f = C_{wp}k_{wp}v_{wp} - C_{eff}k_f v_f \qquad (7.12)$$

Substituting equations (7.7-7.8) in equation (7.12) and rewriting the latter in dimensionless form, one obtains the following differential equation for $\widetilde{h_f}(t)$:
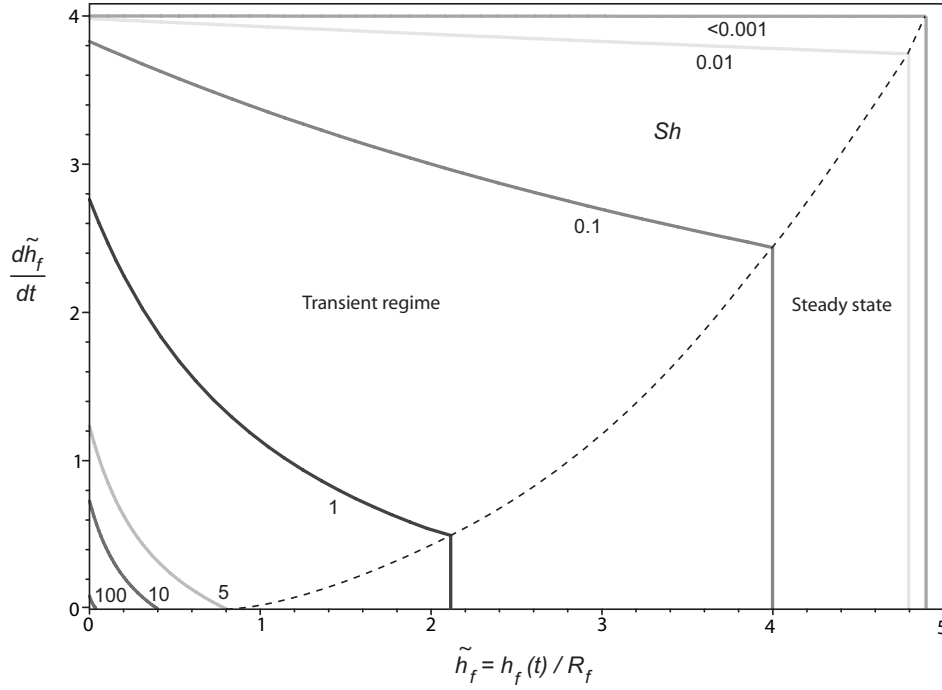
FIG. 7.4 – Velocity of fiber height growth as a function of fiber height ($A = 5$, $\widetilde{S}_t = 2$).

$$\frac{d\widetilde{h_f}}{d\widetilde{t}} = \frac{1}{1 + \widetilde{k}_y^{eff}(\widetilde{h_f})\,\widetilde{\delta_c}\,Sh} \left(\frac{A}{1 + \widetilde{h_f}\,Sh} - 1 \right) \tag{7.13}$$

with $\widetilde{t} = t/\tau$ (where $\tau = R_f/(C_0 k_f \upsilon_f)$ is a characteristic time of the problem), $\widetilde{\delta_c} = \delta_c/R_f$, and the initial condition for integration being $\widetilde{h_f}(t = 0) = 0$. The right hand side of equation (7.13), which is a complex function of $\widetilde{h_f}(t)$, is represented on figure 7.4 for different values of Sh and for $A = 5, \widetilde{S}_t = 2$ and $\widetilde{\delta_c} = 0.75$. In reaction-limited regime ($Sh < 0.001$), the growth velocity of $\widetilde{h_f}$ (noted $\widetilde{h_f}'$), being of course null by definition in steady state, is $A - 1$ in transient regime. When Sh increases, two effects have an influence on $\widetilde{h_f}'$: (i) the fact that $\widetilde{h_f}$ increases tends to increase the weak phase protection by the fiber and then decrease $\widetilde{h_f}'$ (term in parentheses in the right hand side part of equation (7.13)), (ii) the evolution of the effective concentration with the effective reactivity, which is linked to $\widetilde{h_f}$. The initial values of $\widetilde{h_f}'$ on figure 7.4 are representative of the second effect at $t = 0$. When ablation begins ($t > 0$), this second effect tends to increase $\widetilde{h_f}'$ when C_{eff} increases, that is, $\widetilde{k}_y^{eff}$ decreases. In the converse case, the opposite effect is observed. The decrease of $\widetilde{h_f}'$ is higher when diffusional effects increase, that is, when Sh increases. In the case for which the fibers are still flat-topped in steady state ($Sh > \sqrt{A^2 - 1}$), $\widetilde{h_f}'$ tends to zero when $\widetilde{h_f}$ tends to $\widetilde{h_f^s}$. Hence, in that case, the establishment of the steady state will be long despite $\widetilde{h_f^s}$ is low.

To express $\widetilde{h_f}$ as a function of time, one has to solve the differential equation (7.13). The complexity of the right hand side prevents from solving it analytically. An approximation is proposed to solve this equation. Since the shape of the curves of figure 7.4 are roughly
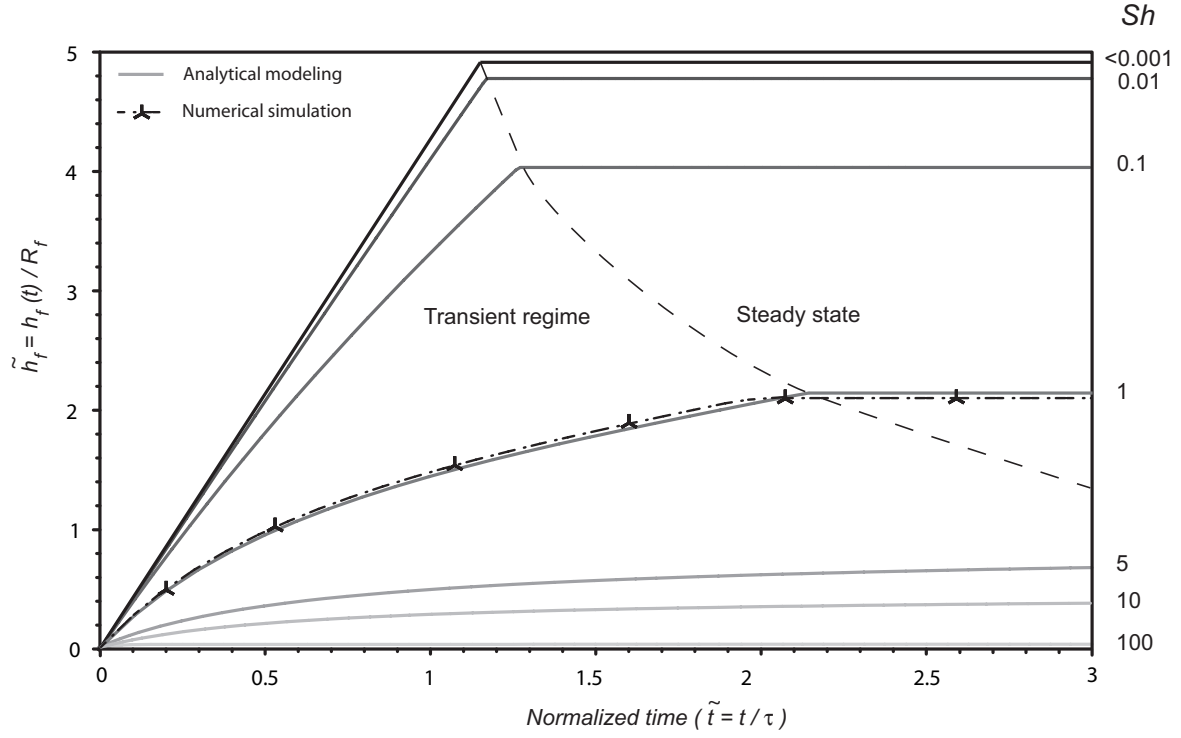
FIG. 7.5 – Fiber height versus time ($A = 5$, $\widetilde{S}_t = 2$).

parabolic, it is proposed to fit them by a second-order polynomial approximation. Equation (7.13) rewrites :

$$\frac{d\widetilde{h_f}}{d\widetilde{t}} = a + b\widetilde{h_f} + c\widetilde{h_f^2} \tag{7.14}$$

where a, b, and c are real constants, which are to be determined for each set of values (Sh, A, $\widetilde{S_t}, \widetilde{\delta_c}$). The solution of equation (7.14) is then :

if $4ac - b^2 > 0$

$$\widetilde{h_f}(\widetilde{t}) = \frac{1}{2c} \left(\Delta \tan \left(\frac{\Delta \widetilde{t}}{2} + \arctan(b/\Delta) \right) - b \right) \tag{7.15}$$

with $\Delta = \sqrt{4ac - b^2}$, else

$$\widetilde{h_f}(\widetilde{t}) = \frac{1}{2c} \left(-\Delta \, \mathcal{R}e \left(\tanh \left(\frac{\Delta \widetilde{t}}{2} + \frac{1}{2} \ln \left[\frac{\Delta - b}{\Delta + b} \right] \right) \right) - b \right) \tag{7.16}$$

with $\Delta = \sqrt{-4ac + b^2}$.

These equations are useful to assess the effective reaction rate as a function of time, since $\widetilde{k}_y^{eff}$ is a function of $\widetilde{h_f}(\widetilde{t})$. This resolution method may appear heavy, but for a given application, a single parameter set is generally used, then a single fit for the determination of a, b, and c is required. This method has been applied for various values of Sh (with $A = 5$, $\widetilde{S_t} = 2$). The resulting plots of $\widetilde{h_f}$ as a function of $\widetilde{t}$ are represented on figure 7.5. In reaction-limited regime, as expected, the growth rate of $\widetilde{h_f}$ is proportional to $\widetilde{t}$, the proportionality
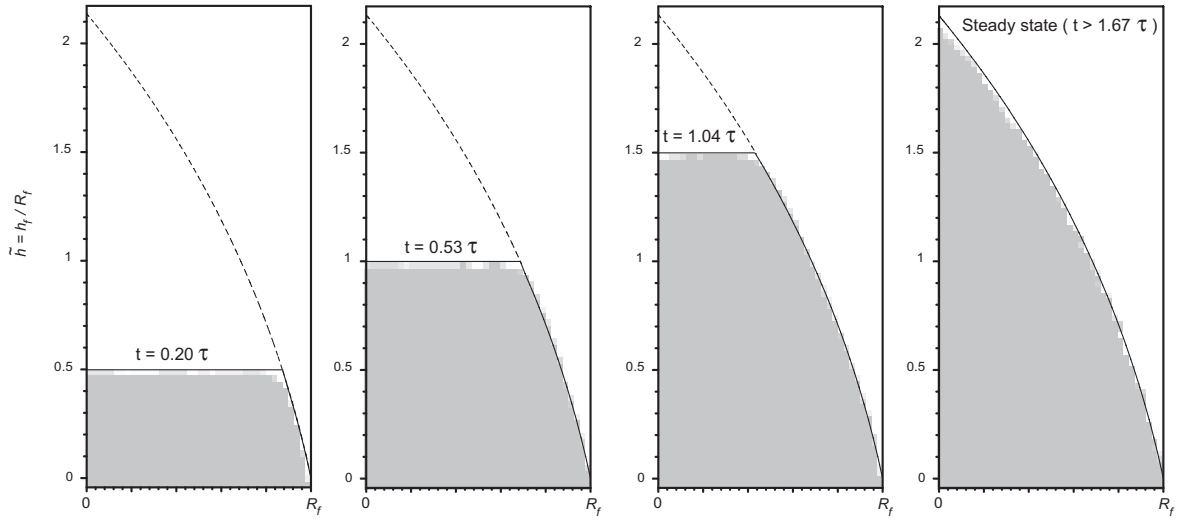
FIG. 7.6 – Fiber section morphology versus time : comparison of analytical (black lines) and numerical (grey pixels) results.

coefficient being $A - 1$. The duration of the transient regime in reaction limited-regime is given by the following equation :

$$t^s = \tau \, \widetilde{t^s} = \tau \, \frac{\sqrt{A^2 - 1}}{A - 1} \tag{7.17}$$

According to the remarks associated to equation (7.13), when diffusion effects appear, the scaled transient regime duration increases in spite of the fact that the reduced steady state height of the fibers is lower (see figure 7.5). Nevertheless, in the cases for which fibers present a plateau in steady state ($Sh > \sqrt{A - 1}$), this tendency is inverted. Indeed, while the transient regime duration is $\widetilde{t^s} = 7.7$ for $Sh = 5$, it shrinks to 5.4 for $Sh = 10$ and 3.9 for $Sh = 100$. On figure 7.6, the evolution of the fiber shape is represented as a function of time for $Sh = 1$ in continuous black lines. Dashed lines represent the steady state geometry, the fiber plateau position being given by figure 7.5. This method to assess the surface roughness as a function of time applies in all regimes.

7.3.2   Macroscopic scale

The mathematical bases of the mesoscopic scale model can be applied at macroscopic scale to address the second change of scale. The macroscopic scale physical hypotheses are the same than for mesoscopic scale [63]. However, the material architecture is different (see figures 7.1-a and b). The perpendicular yarns (y) are the macroscopic scale equivalents of the fibers at mesoscopic scale. They can be assumed homogeneous, isotropic, strictly perpendicular to the surface, and having a rectangular section surrounded by a weak phase, noted $wp - y$ [63]. Between the perpendicular yarns, the composite is made alternatively of parallel yarns ($y- \parallel$) and matrix octets (o). In steady state, the composite behavior is only driven by the weakest and the strongest phases, that is, the interphase and the perpendicular yarns [63]. In transient regime, the other phases display little influence on the material behavior if their reactivity

is equal to the average reactivity of perpendicular yarns and interphase weighted by their respective surfaces at initial time. This writes :

$$k_{y-\parallel} = k_o = \frac{k_y S_y + k_{wp-y} S_{wp-y}}{S_{wp-y} + S_y} \tag{7.18}$$

For the material of this study, this relation is quite well respected since $S_y \simeq 6 S_{wp-y}$ [61], $k_y \simeq 8 k_{wp-y}$ [63], and $k_{y-\parallel} \simeq k_o \simeq 2 k_y$ [64]. The macroscopic model of the composite architecture can then be simplified into a model similar to the mesoscopic one, apart from the facts that the perpendicular yarn has a square section (instead of circular) and the sizes are different. The geometry of a yarn is more efficiently described in cartesian coordinates : $S_y(x, y, z, t) = z - F(x, y, t) = 0$. The equation of the surface $z = F(x, y, t)$ can be derived using the method developed in subsection 7.3.1 [63]. In steady state, the yarns are shown to acquire a pyramidal shape. Their reduced height in steady state writes :

if $Sh_y < \sqrt{A_y^2 - 1}$

$$\widetilde{h_y^s} = \sqrt{Sh_y^{-2} + 2 Sh_y^{-1} \sqrt{A_y^2 - 1} - 1} - Sh_y^{-1} \tag{7.19}$$

else

$$\widetilde{h_y^s} = (A_y - 1)/Sh_y \tag{7.20}$$

where $\widetilde{h_y^s} = 2 h_y^s / l$ ($l/2$, one-half of the yarn edge size, is the homologue of R_f), $Sh_y = k_{wp-y} l / (2D)$ is the Sherwood number associated to the yarn, $A_y = (k_{wp-y} v_{wp-y})/(k_y v_y)$ the contrast in the reactivities for the perpendicular yarn. Let $\widetilde{\Lambda} = 2\Lambda/l$ be the homologue of R; its expression is given by equation (7.5), using the suitable dimensionless numbers. Then, converting the results of subsection 7.3.1, one obtains the normalized effective reactivity of the composite as a function of $\widetilde{h_y}(t)$:

$$\widetilde{k}_c^{eff}(\widetilde{h_y}) = \frac{\widetilde{\Lambda}^2(\widetilde{h_y})}{A_y \widetilde{S}_{t-y}} + \left(1 - \frac{\widetilde{\Lambda}^2(\widetilde{h_y})}{\widetilde{S}_{t-y}}\right) \frac{1}{1 + Sh_y \widetilde{h_y}} \tag{7.21}$$

with $\widetilde{k}_c^{eff} = k_c^{eff}/k_{wp-y}$, $\widetilde{S}_{t-y} = S_{t-y}/(l^2)$ (where S_{t-y} is the total surface of the cell), and $\widetilde{h_y} = 2 h_y(t)/l$.

Rewriting equation (7.13) for macroscopic scale, one obtains the following differential equation for $\widetilde{h_y}(t)$:

$$\frac{d\widetilde{h_y}}{d\widetilde{t}} = \frac{1}{1 + \widetilde{k}_c^{eff}(\widetilde{h_y}) \, \widetilde{\delta}_c^y \, Sh_y} \left(\frac{A_y}{1 + \widetilde{h_y} \, Sh_y} - 1\right) \tag{7.22}$$

with $\widetilde{t} = t/\tau_y$ (where $\tau_y = l/(2 C_0 k_y v_y)$ is a characteristic time of the macroscopic scale problem), $\widetilde{\delta}_c^y = 2\delta_c/l$, and the initial condition for integration being $\widetilde{h_y}(t = 0) = 0$.

Except the fact that the dimensionless variables have to be converted into the suitable macroscopic scale notations given below, all the results (equation, figures, discussions) presented for mesoscopic scale are appropriate for macroscopic scale.

7.3.3   Discussion on the validity of the second change of scale

For the second change of scale, the properties of the yarn are considered constant in space, but also in time. This latter assumption is correct if the duration of the transient regime at mesoscopic scale is low compared to that of the macroscopic scale. Let the validity of this hypothesis be evaluated in the case of the C/C composite of the study. The 3D C/C material of this study has been oxidized at $898\,K$ under dry air and atmospheric pressure. In these conditions, the oxidation rate of the carbon fibers and of the perpendicular yarns are respectively about $1.2\,10^{-5}m/s$ [62] and $3.8\,10^{-4}m/s$ [63]. The characteristic times of ablation are then found to lie around : $\tau = 5$ hours for mesoscopic scale and $\tau_y = 23$ hours for macroscopic scale. In this case, the regime is reaction-limited at both scales [63]. The contrast in the reactivities are : $A = 32$, $A_y = 8$ [63]. Then, according to equation (7.17), the theoretical durations of the transient regime are respectively 5 hours for mesoscopic scale and 26 hours for macroscopic scale. Then the hypothesis that had tacitly been done at macroscopic scale, that is, to consider that the duration of the transient regime at mesoscopic scale was negligible in front of that of the macroscopic scale, is not exact but acceptable.

7.4   3D numerical simulation

The aim of this section is to validate the vertical gradient hypothesis of the analytical model in transient regime using a numerical simulation code. First, the numerical simulation tool is briefly presented. Then, the mesoscopic scale model is solved with lesser assumptions and the results of the numerical simulation are compared to the analytical solution.

7.4.1   Presentation of AMA

An efficient numerical simulation code, named AMA, has been developed on a Monte-Carlo random-walk principle [64]. AMA, which is a C ANSI implementation, contains five main parts. (i) A 3-D image containing several phases (fluid/solids) is described by discrete cubic voxels (3D pixel) method. (ii) The moving fluid/solid interface is determined by a simplified marching cube approach [97]. (iii) Mass transfer by diffusion is simulated by a Brownian motion simulation technique [91], which is a continuum (grid-free) method to simulate diffusion in a continuous fluid. (iv) Heterogeneous first-order reaction on the wall is simulated by a sticking probability adapted to the Brownian motion simulation technique [67,82]. (v) A Dirichlet upper boundary condition is simulated using a buffer zone, where C is maintained constant [64]. AMA has been validated by comparison to a 1D analytical model in transient regime [67] and to the 3D mesoscopic scale model in steady state [64]. The transient regime has been simulated on the cell presented in subsection 7.3.1 for $A = 5$. The steady state is reached after a computing time lying around 48 hours with a $3.2\,GHz$ Xeon CPU computer.

7.4.2   Comparison of numerical and analytical results

As a whole, analytical and numerical results are in agreement. The error is found to be lower than 3% both on the transient regime duration evaluation and on the fiber height as a function or time. Let the comparison be illustrated in the most complex case, that is, in mixed regime : $Sh = 1$. The numerical points of the evolution of $\widetilde{h}_f$ as a function of time are reported on figure 7.5. The steady state height is 2.5% lower for the numerical simulation than for the analytical evaluation. This error can be attributed to the numerical simulation

code uncertainty which is also 2.5% [64]. The transient regime duration evaluation using the numerical simulation is 3% lower than the analytical prediction. This explains why the numerical simulation curve is slightly above the analytical curve in transient regime. Anyway, analytical and numerical evaluations of $\widetilde{h}_f$ as a function of time are in good agreement. Analytical and numerical fiber morphologies are compared on figure 7.6. The agreement is correct; the error is roughly equal to the voxel size. At initial time, since the fiber is less reactive, a 1D analytical model [63] shows that the concentration should be higher above the fiber than above the matrix. Horizontal diffusion effects tend to counterbalance this discrepancy. Hence, a horizontal concentration gradient appears on the fiber, the concentration above the center of the fiber tip being higher than on the edges. Then, the recession velocity of the center of the fiber should be higher, and the fiber tip plateau should appear slightly convex on figure 7.6 for $t = 0.2\tau$. Since it is not the case, this means the concentrations over the fiber and the matrix are homogeneous and equal to C_{eff}. The concentration gradient can then be assumed vertical at any time. Consequently, the assumptions of the analytical model are correct for the prediction of the composite behavior.

7.5   Application to 3D C/C

In this section, the above model is applied in transient regime to a 3D C/C composite, the steady state behavior of which has already been successfully modeled [63]. First, the surface roughness of the composite, which has been analyzed by SEM at different stages of oxidation, is qualitatively compared to the results of the model. Then, the mass loss of the sample, which has been followed versus time [62], is compared to a theoretical prediction.

7.5.1   Surface roughness in transient regime

The reactivities of the composite and of its components have been assessed either by direct experimental measurement (composites, fibers) [62] or by inverse analysis from the surface roughness morphologies in steady state (matrices, yarns) [63, 64]. The values obtained show that the regime is reaction-limited at both scales. Then, the morphologies are only functions of the reactivities contrast; one has $A = 32$ and $A_y = 8$ [63]. Experimental observations and numerical simulations at mesoscopic scale are represented on figure 7.7. The elementary numerical cell has been repeated by translation. It has been sectioned on the front part to highlight the surface roughness evolution. In the numerical cell, the bulk matrix is represented. Its reactivity is taken equal to that of the fibers. Images of the features obtained by SEM analysis, numerical simulation, and analytical computation are represented on figure 7.8 for transient regime and steady state. The results of the model are in correct agreement with experimental observations. This tends to support the idea that the fibers and the bulk matrix reactivities are equal.

At macroscopic scale, the morphology of the surface roughness strongly suggests that the steady state has not been reached at the end of the oxidation test. Indeed, the yarns are still truncated, whereas they should display a sharp tip in steady state according to the model, since the regime is reaction-limited (see figure 7.9-b and c). Moreover, it has been shown in section 7.3.3 that the theoretical duration of the transient regime was about 26 hours, while the experiment lasted only 17 hours [62]. Since in reaction-limited regime the yarn growth is proportional to time, the height of the yarns on micrographs 7.9-b and c should be around 65% of the final height h_y^s. With $A_y = 8$, one deduces from equation (7.19) that h_y^s lies around

| 0.05 | 0.3 | 0.7 | 1 |
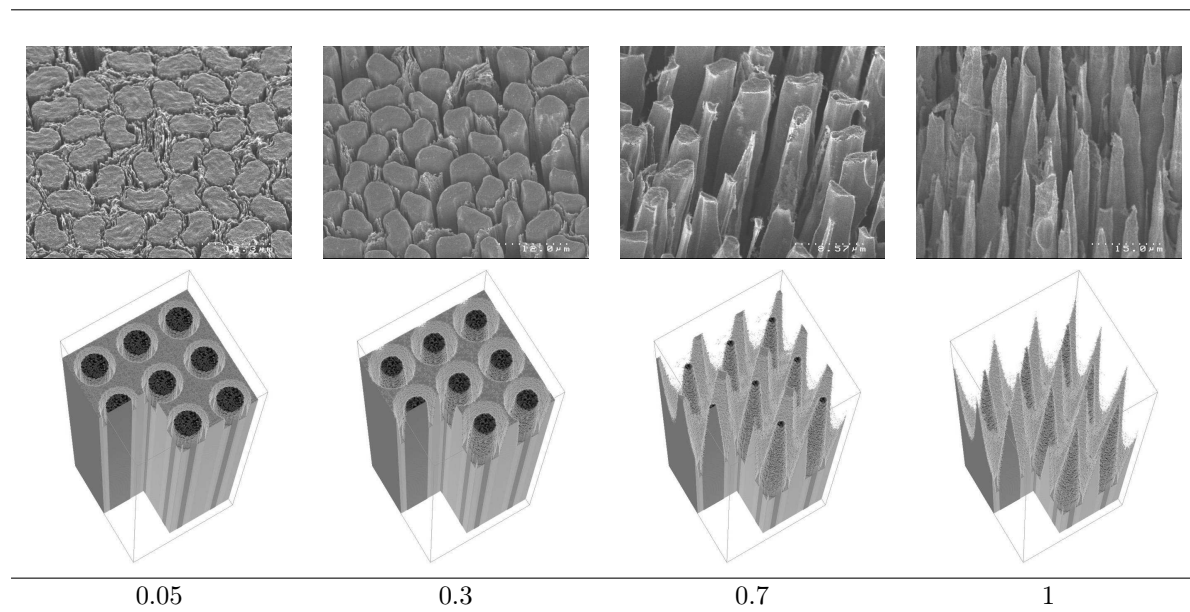
FIG. 7.7 – Experimental observations (SEM) vs. simulation results (AMA) as a function of h_f/h_f^s ($A = 30$, $Sh < 0.001$).

a) Transient regime : observation (SEM)   b) Transient regime : simulation (AMA)   c) Transient regime : analytic

d) Steady state : observation (SEM)   e) Steady state : simualtion (AMA)   f) Steady state : analytic
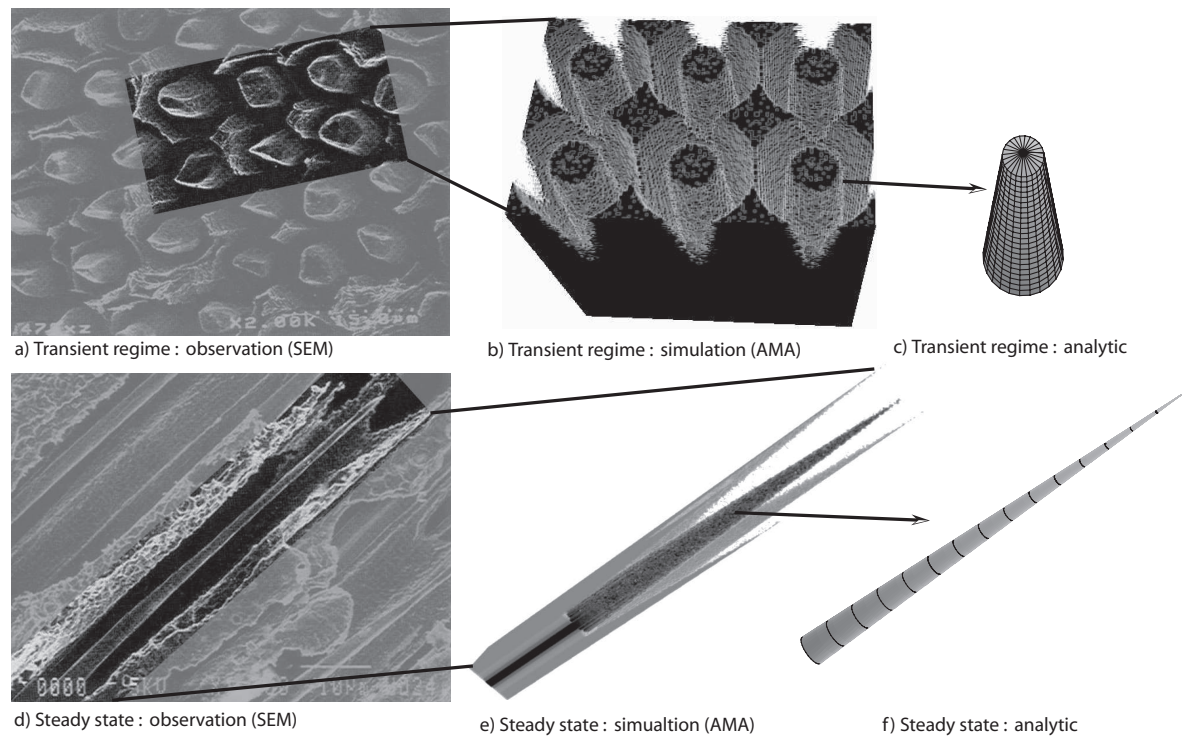
FIG. 7.8 – Comparison of experimental and theoretical results in transient regime and in steady state

a) Initial time (SEM)   b) End of the experiment (SEM) :   c) Zoom on a fiber bundle (SEM)
                              transient regime

d) Initial time :   e) Transient regime :   f) Transient regime :
Numerical cell (AMA)   Simulation (AMA)   Analytical computation

FIG. 7.9 – Comparison of experimental and theoretical morphologies at macroscopic scale

four times the yarn edge size (l). Hence, the truncated fiber height of figures 7.9-b and c should be around $2.5\,l$. This is in agreement with the micrographs ; note that the yarn height has to be measured from the bottom of the interphase to the yarn tip. Simulations have been carried out on the nu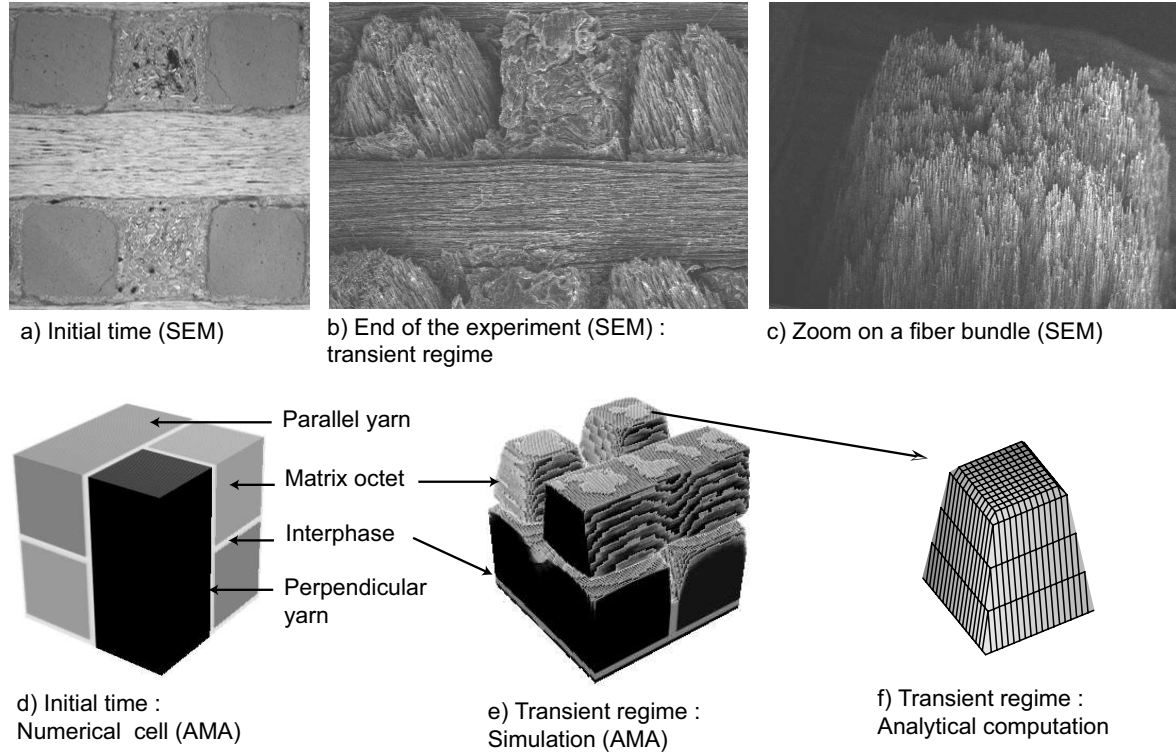merical cell presented on figure 7.9-b, designed according to micrograph 7.9-a. All the component densities have been taken equal to $2\,g.cm^{-3}$, except for the matrix octets which are porous ($1.6\,g.cm^{-3}$). The reactivity contrast between parallel and perpendicular yarns is about 1 [64]. The matrix octet reactivity is taken equal to that of the parallel yarns. The simulation result for an oxidation duration of 17 hours are presented on figure 7.9-e. On figure 7.9-f, the shape of a yarn calculated using the analytical model is shown. As a conclusion, the results of the model are in good agreement, qualitatively and quantitatively, with the experimental observations.

7.5.2   Mass loss in transient regime

The mass loss has been experimentally measured versus time from the initial time to the end of the experiment (17 hours). It is given in gram per minute in [62] for a sample of one square centimeter surface. On figure 7.10, the mass loss is plotted in dimensionless units ($\widetilde{m}$) as a function of the reduced time ($\widetilde{t} = t/\tau_y$). In the following, since the duration of the transient regime at mesoscopic scale is low in front of the duration of the transient regime at macroscopic scale, only the macroscopic scale is considered. The total mass loss at time t writes :

$$m(t) = \mathcal{M}_c S_{eff} \int_{u=0}^{u=t} k_c^{eff}(u)\, C_{eff}(u)\, du \tag{7.23}$$
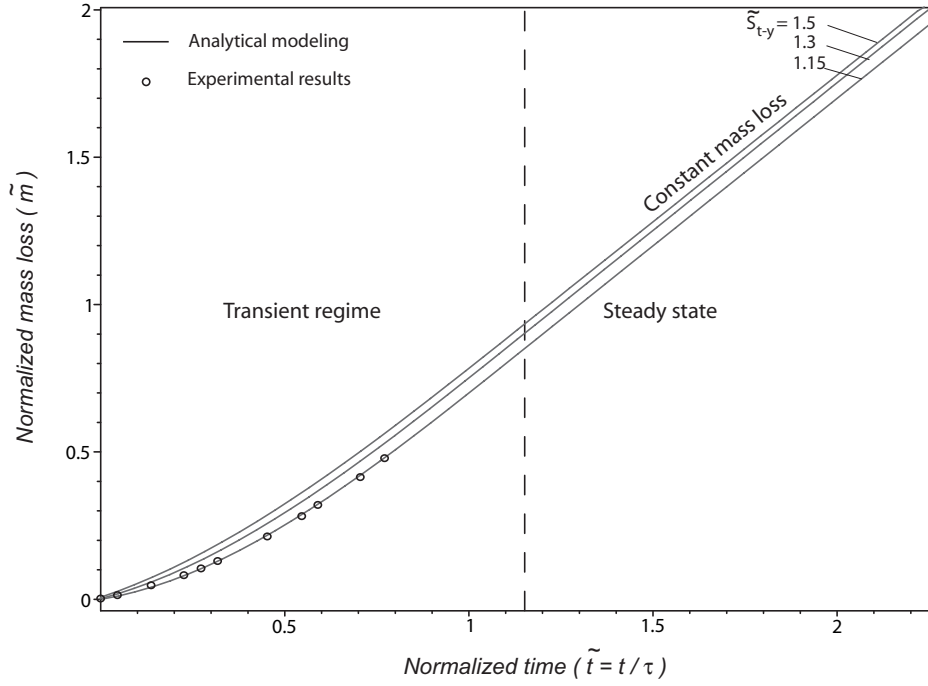
FIG. 7.10 – Comparison of experimental and theoretical mass loss (3DCC, dry air oxidation, $898\,K$)

where S_{eff} is the effective geometric surface of the sample and $\mathcal{M}_c$ the molar mass of carbon. In the present case, one can assume $C_{eff} = C_0$ [62]. Using this hypothesis, let equation (7.23) be rewritten under a dimensionless form :

$$\widetilde{m}(\widetilde{t}) = \int_{u=0}^{u=\widetilde{t}} \widetilde{k}_c^{eff}(u)\,du \tag{7.24}$$

with

$$\widetilde{m}(\widetilde{t}) = m(\widetilde{t}) \frac{k_y v_y}{k_{wp-y} \mathcal{M}_c S_{eff} l} \tag{7.25}$$

In order to plot the theoretical mass loss, the proportion of inter-yarn interphase when compared to perpendicular yarn has to be estimated. According to micrograph 7.9-a, $\widetilde{S}_{t-y}$ lies around 15%. The value of $\widetilde{S}_{t-y}$ is then about 1.15. The steady state mass loss is not a function of $\widetilde{S}_{t-y}$. However, at initial time, the proportion of weak phase has a neat influence on the mass loss rate (see figure 7.10). Using the measured value of 1.15, the agreement between experimental and theoretical results is excellent. At the end of the experiment (26 hours, or $\widetilde{t} = 0.75$), the mass loss rate seemed to be constant : that is why the experiment has been stopped. The fact that the oxidation rate looks constant before the end of the transient regime is also well represented by the curves of figure 7.10. This could be expected from figure 7.3, since the effective reactivity tends to a horizontal asymptote at the end of the transient regime. According to equation (7.21), which gives the slope of the curves of figure 7.10, at the end of the experiment the mass loss rate was only 90% of the theoretical mass loss rate in steady state. This theoretical results bring the opportunity to analyze the previous results.

First, the steady state reactivity of the 3D C/C is about 10% higher than measured, that is, its actual geometrical reactivity is $3.3\,10^{-3}m/s$ at $898\,K$, under dry air and atmospheric pressure [62]. Second, the morphological inverse analysis of part III [63] is erroneous by 10%; this is not surprising since the incertitude of the inverse analysis is estimated to lie around 30% for this material.

As a conclusion on the comparisons between experimental and theoretical results, one notes that all the tendencies are well represented and explained by the model. Moreover, a correct quantitative agreement is obtained on the mass loss and on the surface roughness morphology parameters.

7.6 Conclusion

The ablation of carbon/carbon (C/C) composites is shown to lead to a steady state behavior described and modeled elsewhere [61,63,64]. Here, the transient regime behavior of a 3D C/C composite is treated. A surface recession model is proposed to handle the surface evolution. The surface is supposed to recede due to a first order gasification process (for example oxidation). Mass transfer of reactants from the bulk of the fluid phase to the wall is taken into account. Under the assumption of a vertical concentration gradient of reactants, the model is solved analytically. Since the material is a multi-scale material, its modeling follows its structure through two changes of scales. First, the mesoscopic scale behavior of the composite (yarn) is inferred from the properties of the microscopic scale components (fiber, intra-yarn matrix). Second, the macroscopic scale behavior of the composite is obtained from that of the yarn and the inter-yarn components. A numerical simulation code, which simulates efficiently the receding surfaces, is used to validate the hypotheses of the analytical model. The agreement between numerical and analytical results is shown to be correct. The main outputs of the models are the description of surface roughness as a function of time, the prediction of the duration of the transient regime, and the determination of the effective reactivity of the composite versus time. Finally, the results of the model are compared to an ablation experiment carried out on a 3D C/C composite. A good agreement is obtained between the predictions of the model and the experimental observations on the three main outputs of the model. Interestingly, the study reveals that the material had not reached steady state when the experiment was stopped, even though the oxidation rate seemed constant. This validation case was in reaction-limited regime. An outlook of this work is to apply the results of the transient regime model to plasma-jet test or in higher temperature oxidation experiments for which the reaction regime is intermediate.

8 Conclusion

Le comportement ablatif des composites en carbone a été étudié, modélisé, et le modèle validé. L'étude s'est focalisée sur l'ablation physico-chimique (oxydation, sublimation), avec une approche originale de l'interaction pariétale matériau/environnement. L'attention a été portée simultanément sur l'architecture et la nature du matériau composite et sur le transport de masse en phase gazeuse. Un des points forts de cette étude a été l'interaction entre expérimentation et modélisation entretenue à toutes les étapes, permettant l'établissement d'une stratégie de modélisation multiéchelle basée sur des modèles réalistes puis sa validation. Du point de vue de la résolution des modèles, l'association de méthodes numériques et analytiques a permis d'élucider les couplages entre les phénomènes et d'apporter une compréhension fine du comportement des composites lors de l'ablation. Parallèlement, AMA, un code de simulation numérique 3D basé sur un principe Monte-Carlo Marche Aléatoire associé à un *Marching Cube* simplifié, a été développé et validé pour résoudre les problèmes de réaction/diffusion avec surface hétérogène récessive.

Le point de départ a été l'analyse du comportement du matériau et la mesure des réactivités intrinsèques des composites et de leurs composants. Afin de permettre une étude rigoureuse, un moyen d'essai modèle, dans lequel les conditions expérimentales sont complètement connues et maîtrisées, a été conçu. Il s'agit d'un réacteur d'oxydation isotherme fonctionnant à pression atmosphérique sous un flux d'air sec contrôlé. L'écoulement et les transferts de masse des gaz réactifs y ont été modélisés en 3D, et le modèle résolu numériquement en utilisant un code CFD commercial. L'intérêt de cette modélisation était de prévoir dans tous les régimes la concentration en gaz réactif sur un échantillon ayant une réactivité donnée. L'étude numérique a montré qu'au dessus de l'échantillon le transport de masse convectif était négligeable devant le transfert de masse par diffusion, ce dernier étant unidirectionnel et normal à la surface moyenne de l'échantillon. Une solution analytique 1D, prenant en compte le transfert de masse et la consommation à la paroi, permet, avec une bonne précision dans tous les régimes, d'approcher le champ de concentration en réactif au-dessus de l'échantillon. Les régimes réactifs et diffusifs ont pu être identifiés. Dans le cas des échantillons de cette étude, le régime était mixte, c'est-à-dire que sans apporter une limitation diffusive complète le transfert de masse ralentissait sensiblement la vitesse de réaction apparente de l'échantillon. Le modèle a permis d'extraire des données expérimentales brutes les réactivités géométriques effectives des échantillons, en soustrayant les effets diffusifs. Dans le cas des matériaux denses (composites C/C, matrices), cette réactivité effective correspond exactement à la réactivité géométrique intrinsèque nécessaire à la validation des modèles d'ablation. Pour les fibres de carbone, disposées en un empilement unidirectionnel dans un creuset, un modèle classique de milieu poreux a permis de remonter à leur réactivité géométrique effective. Un premier résultat est que la réactivité géométrique effective des composites n'est une propriété additive issue de celle de ses composants. Les couplages physico-chimiques qui interviennent, et qui

sont à l'origine de cette observation, sont l'objet de la partie modélisation.

Lors de l'ablation, une rugosité typique apparaît sur la surface des composites C/C. Une analyse multiéchelle qualitative (MEB) et quantitative (microtomographie) a été réalisée sur trois matériaux composites (un 3D C/C, un 2D C/R et un graphite polycristallin), chacun testé à l'aide du réacteur d'oxydation et d'un jet plasma. Les idées directrices pour la modélisation du comportement du matériau émergent de l'analyse de la rugosité :
  – la rugosité est fortement corrélée à l'architecture multiéchelle des matériaux : les modèles doivent inclure cette dernière ;
  – la rugosité est multiéchelle : la modélisation doit l'être également. Idéalement, le point de départ de la modélisation est le plan de graphène, entité élémentaire constitutive de tous les matériaux, et le point d'arrivée le composite homogénéisé.

La stratégie de modélisation retenue part des petites échelles pour remonter vers les grandes par changements d'échelle successifs. L'étude a été divisée en deux volets :
  1. Une étude fondamentale sur le lien entre la microstructure anisotrope des matériaux et leur comportement a été réalisée en partant des propriétés des plans de graphènes. Le point d'arrivée est le volume élémentaire réprésentatif isotrope.
  2. Une étude quantitative, donnant des résultats exploitables sur le comportement des composites pour les ingénieurs, part des propriétés des composants microscopiques des composites pour aboutir à celui des composites, après deux étapes d'homogénéisation.

A chaque échelle, partant d'une interface fluide/solide plane, les modèles intègrent le suivi du front d'ablation qui devient progressivement rugueux et qui est lié à la récession hétérogène de l'interface, propriété locale dépendant de la réactivité de la phase considérée et du transfert de masse associé.

Le premier volet inclut une interprétation de la réactivité anisotrope des plans de graphène, et l'intégration de celle-ci dans le code de simulation numérique AMA. Ensuite, deux changements d'échelles permettent de passer successivement au comportement des cristallites, puis à celui d'un matériau texturé. Le graphite polycristallin est utilisé comme matériau modèle dans cette démarche. Un accord qualitatif est obtenu. Pour parler des perspectives, il serait très profitable de poursuivre cette étude dans un objectif de modélisation quantitative. On a montré que deux données quantitatives d'alimentation, encore absentes de la littérature, doivent être obtenues : (i) les réactivités géométriques intrinsèques des plans de graphène (plan et bord de plan), (ii) la caractérisation précise de la texture des fibres et matrices par microscopie électronique à transmission. La validation quantitative sera alors obtenue après homogénéisation par comparaison aux réactivités géométriques des fibres et matrices et aux rugosités de surface expérimentales. Cette étude pourrait assurer le changement d'échelle entre les modélisations à l'échelle atomique (méthodes *ab initio* complétées par les simulations de type dynamique moléculaire [14]) et les modélisations partant de l'échelle microscopique (réactivités géométriques intrinsèques des fibres et matrices).

Le deuxième volet se concentre sur l'étude du 3D C/C et du 2R C/R. Le point de départ est l'échelle microscopique (fibres, matrices intra-fil). Un premier changement d'échelle a permis d'obtenir le comportement des fils : apparition de rugosité, réactivité effective. Une résolution numérique a permis de résoudre le problème dans le cas général (*i.e.* : toutes les orientations de fibres par rapport à la surface moyenne, transfert de masse 3D). Une étude paramétrique

a révélé que la réactivité effective du fil ne dépendait pas de l'orientation des fibres et que le transfert de masse était globalement 1D et perpendiculaire à la surface moyenne. Sous ces hypothèses, l'équation de l'évolution 3D de l'interface a pu être résolue analytiquement, permettant une compréhension fine des couplages qui sont liés à deux nombres sans dimension :

– le contraste de réactivité hétérogène entre les différents composants solides,
– un nombre de Sherwood relié à la taille caractéristique de ces composants.

La réactivité effective des fils a ensuite été utilisée pour effectuer le second changement d'échelle permettant d'obtenir le comportement du composite connaissant celui de la matrice intra-fil. La même démarche de résolution a été adoptée et les résultats sont analogues. La prédiction de l'évolution de la rugosité est en excellent accord à chaque échelle avec les observations expérimentales. Partant des réactivités expérimentales des composants microscopiques et après les deux changements d'échelle, la prédiction de la perte de masse du composite est en accord avec les mesures expérimentales dans le réacteur d'oxydation et permet d'en expliquer les tendances.

Le modèle, validé dans le cas de l'ablation par oxydation, est ensuite extrapolé et exploité pour l'analyse des essais plasma. L'analyse de la rugosité mésoscopique a permis d'évaluer les réactivités intrinsèques géométriques des fibres et de la matrice intra-fil dans les conditions des essais. Ce résultat est d'autant plus intéressant que les valeurs des réactivités des composants sont pour l'instant obtenues au prix d'expériences difficiles à des températures inférieures, ce qui nécessite en outre une extrapolation des données. A l'échelle macroscopique, les hypothèses du modèle développé pour les essais d'oxydation ne sont plus complètement valides. Cependant, utilisé qualitativement, le modèle permet de montrer que l'érosion thermomécanique joue alors un rôle non négligeable.

Trois axes de valorisation des modèles sont envisageables :
– amélioration des critères de conception, notamment lorsqu'une extrapolation s'avère nécessaire, par l'utilisation de modèles phénoménologiques du comportement des matériaux ;
– choix optimal des matériaux pour une application donnée en fonction de leur comportement attendu ;
– idées directrices pour l'amélioration des composites en fonction du domaine d'utilisation, via le renforcement du constituant faible (les interphases en régime réactif, c'est-à-dire à température modéré ; les fibres en régime diffusif, soit à haute température).

Une perspective constructive à court terme sera l'exploitation des modèles pour l'interprétation des résultats d'essais à plus haute température, pour lesquels l'érosion reste nulle ou négligeable :
– réacteur d'oxydation à haute température (essais modèles, LCTS) ;
– plasma à vitesse d'écoulement modérée (par exemple dispositif du Von Karman Institute, Belgique) ;
– essais de sublimation par chauffage radiatif (par exemple four à image d'arc, CEA-CESTA) ;
– analyse des parois des Tokamaks (ITER, CEA de Cadarache) ;
– analyse des parties non frottantes des freins d'avions (Groupe SAFRAN).

A moyen terme, il serait souhaitable de prendre en compte la convection et l'érosion thermomécanique pour la modélisation du comportement macroscopique des composites lors

des essais plasma à écoulement rapide.

Un problème scientifique de bien plus grande ampleur sera de modéliser en 3D un écoulement laminaire, puis turbulent, sur les géométries réalistes de rugosité présentées dans ce travail, d'abord en partant de la rugosité en régime permanent, puis en régime transitoire. Un couplage fort est attendu entre écoulement et évolution de l'état de surface, du fait des variations des coefficients de transfert.

Bibliographie

[1] J. D. Anderson. *Hypersonic and high temperature gas dynamics*. Mac Graw-Hill, New-York, 1989.

[2] Y. Aspa, J. Lachaud, G. Vignoles, and M. Quintard. Simulation of C/C composites ablation using a vof method with moving reactive interface. In J. Lamon and A. Torres-Marques, editors, *Proc. 12th European Conference on Composite Materials*, Biarritz, France, September 2006. AMAC. 8 p.

[3] Y. Aspa, M. Quintard, J. Lachaud, and G. L. Vignoles. Identification of microscale ablative properties of C/C composites using inverse simulation. In *Collection of technical papers - 9th AIAA/ASME Joint Thermophysics and Heat Transfer Conference Proceedings*, volume 1, pages 52–64, 2006.

[4] R. Backreedy, J. M. Jones, M. Pourkashanian, and A. Williams. A study of the reaction of oxygen with graphite : Model chemistry. *Faraday Discuss.*, 119 :385–394, 2001.

[5] R. L. Baker and P. G. Crowell. Graphite materials ablation performance in high thermal radiation environments. In *14th Thermophysics conference*, Orlando, Florida, June 1979. AIAA paper 79-1084.

[6] R. G. Batt and H. H. Legner. A review of roughness-induced nosetip transition. *AIAA Journal*, 21 :7–22, 1983.

[7] P. Baudry. *Etude du résidu carboné et de la liaison fibre/matrice lors de la pyrolyse de composites carbone/phénolique*. PhD thesis n°2879, Université Bordeaux I, 2004.

[8] N. Bertrand, J. Lachaud, G. Bourget, F. Rebillat, and G. L. Vignoles. Identification of intrinsic carbon fiber oxidation kinetics from experimental data and CFD modeling. In J. Lamon and A. Torres-Marques, editors, *Proc. 12th European Conference on Composite Materials*, Biarritz, France, September 2006. AMAC. 8 p.

[9] L. Bonnetain and G. Hoynant. *Oxydation des graphites aux températures moyennes*, volume 1 of *Les Carbones*, chapter 17, pages 277–382. Masson, Paris, 1965.

[10] V. Borie, J. Brulard, and G. Lengellé. An areothermochemical analysis of carbon-carbon nozzle regression in solid-propellant rocket motors. In *AIAA/ASME/SAE/ASEE 24th Joint Propulsion Conference*, Boston, MA, USA, 1988. AIAA paper 88-3346.

[11] V. Borie, Y Maisonneuve, D. Lambert, and G. Lengellé. *Ablation des matériaux de tuyère de propulseurs à propergol solide, Note technique*. ONERA, Châtillon, France, 1990.

[12] X. Bourrat. *Sciences of carbon materials*, chapter 1. Structure in carbons and carbon artifacts, pages 1–97. Universidad de Alicante, Alicante, 2000.

[13] T. Burtseva, A. Hassanein, I. Ovchinnikov, and V. Titiov. Study of brittle destruction and erosion mechanisms of carbon-based materials during plasma instabilities. *Journal of Nuclear Materials*, 290–293 :1059–1063, 2001.

[14] P. Chantrenne and S. Volz. Introduction à la dynamique moléculaire. *Techniques de l'ingénieur*, BE(8290) :1–20, 2002.

[15] M. W. Chase. NIST-JANAF Thermochemical Tables (4th ed.). *Journal of Physical Chemical Reference Data*, 14, 1985.

[16] P. Chassaing. *Mécanique des fluides*. Cépaduès, Paris, 2000. 450 p.

[17] D. Cho, J. Y. Lee, and B. I. Yoon. Microscopic observations of the ablation behaviours of carbon fibre/phenolic composites. *Journal of Materials Science Letters*, 12 :1894–1896, 1993.

[18] D. Cho and B. I. Yoon. Microstructural interpretation of the effect of various matrices on the ablation properties of carbon-fiber-reinforced composites. *Composites science and technology*, 61 :271–280, 2001.

[19] F. Christin. Design, fabrication, and application of thermostructural composites like C/C, C/SiC, and SiC/SiC composites. *Advanced Engineering Materials*, 4(12) :903–911, 2002.

[20] B. Chéron. *Théorie cinétique : gaz et plasmas*. Ellipses, physique université, Paris, 2001. 200 p.

[21] O. Coindreau, G. Vignoles, and P. Cloetens. Direct 3D microscale imaging of carbon-carbon composites with computed holotomography. *Nuclear Instruments and Methods in Physics Research B*, 200 :308–314, 2003.

[22] J. Couzi, J. de Winne, and B. Leroy. Improvements in ablation predictions for reentry vehicle nosetip. In *Proceedings of the third European symposium on aerothermodynamics for space vehicles*, pages 493–499, ESA, Noordwijk, The Nederlands, 1998.

[23] M. Dauchier and J.-C. Cavalier. Matériaux composites phénoliques ablatifs. *Techniques de l'ingénieur*, AM(5325) :1–9.

[24] P. Delhaès. Le polymorphisme des solides carbones. In : P. Bernier, S. Lefrant, editors. Le carbone dans tous ses états. Gordon and Breach Science Publishers, 1997.

[25] T. L. Dhami, L. M. Manocha, and O. P. Bahl. Oxidation behaviour of pitch based carbon fibers. *Carbon*, 29(1) :51–60, 1991.

[26] Y. I. Dimitrienko and I. D. Dimitrienko. Effect of thermomechanical erosion on heterogeneous combustion of composite materials in high-speed flows. *Combustion and flame*, 122 :211–226, 2000.

[27] T. A. Dolton, H. E. Goldstein, and R. E. Maurer. Thermodynamic performance of carbon in hyperthermal environments. In *3rd AIAA Thermophysics conference*, Los Angeles, California, June 1968.

[28] J. B. Donnet. Structure and reactivity of carbons : from carbon black to carbon composites. In *15th Biennal conference on carbon*, Philadelphia, PE, June 1981.

[29] E. Dourthe, A. Cosculluela, and D. Rousselle. Etude des propriétés d'ablation des graphites à l'aide d'une torche à plasma. Technical report, Rapport CEA-DAM CEB.III-DETN Service matériaux avancés, 1995.

[30] S. Drawin, M. P. Bacos, J. M. Dorvaux, and O. Lavigne. Oxidation model for carbon-carbon composites. In *4th International Aerospace Planes Conference*, Orlando, Florida, December 1992. AIAA paper 92-210.

[31] G. Duffa. *Ablation, Monographie*. CEA, Le Barp, France, 1996.

[32] G. Duffa, G. L. Vignoles, J.-M. Goyhénèche, and Y. Aspa. Ablation of C/C composites : Investigation of roughness set-up from heterogeneous reactions. *International Journal of Heat and Mass Transfer*, 48(16) :3387–3401, 2005.

[33] M. Dumont. *Composites C/C 3D densifiés par imprégnation/carbonisation de brai mésophasique*. PhD thesis n°2344, Université Bordeaux I, 2001.

[34] E. Duvivier. *Cinétique d'oxydation d'un composite carbone/carbone et influence sur le comportement mécanique*. PhD thesis n°1692, Université Bordeaux I, 1997.

[35] P. Ehrburger and J. Lahaye. Characterization of carbon-carbon composites : oxiation behavior. *Carbon*, 19 :7–10, 1981.

[36] A. Einstein. *Investigations on the theory of the brownian movement (Translated by A. D. Cowper)*. R. Fürth, Berlin, Dover edition, 1956.

[37] G. Federici, M. Mayer, G. Strohmayer, V. Chuyanov, and C. Day. Modelling of deposition of hydrocarbon films underneath the divertor and in the pumping ducts of ITER. *Journal of Nuclear Materials*, 337–339 :40–44, 2005.

[38] E. Fitzer and L. M. Manocha. *Carbon reinforcements and C/C composites*. Springer, 1998. 342 p.

[39] A. Gil and J. Segura. CA3D : a Monte Carlo code to simulate 3D buffered diffusion of ions in sub-membrane domains. *Computer Physics Communications*, 136 :269–293, 2001.

[40] W. H. Glime and J. D. Cawley. Oxidation of carbon fibers and films in ceramic matrix composites : a weak link process. *Carbon*, 33(8) :1053–1060, 1995.

[41] W. H. Glime, J. D. Cawley, and A. J. Eckel. The evolution of a non-planar oxidation front in receding carbon fibers. *Ceramic Transactions*, 46 :1039–1047, 1995.

[42] S. Goto, K. H. Han, and G. R. St-Pierre. A review on oxidation kinetics of carbon fiber/carbon matrix composites at high temperature. *Trans. Iron Steel Inst. Jpn.*, 26 :597–603, 1986.

[43] J.-M. Goyhénèche, G. L. Vignoles, and G. Duffa. Homogénéisation thermique d'interfaces rugueuses. Principe et application à différentes rugosités périodiques. In *Congrès Français de Thermique*, Presqu'île de Giens, France, 25-28 May 2004. SFT. 6 p.

[44] P. Grécias and R. Didier. *Chimie Spé. PC*, PC*. Lavoisier Tech et Doc, collection de sciences physiques, Paris, 1999.

[45] A. Grossman and P. Magnaud. Les défis thermiques pour ITER et la fusion thermonucléaire par confinement magnétique. In *Conférence Plénière du Congrès Français de Thermique*, Île de Ré, France, 16-19 Mai 2006. SFT.

[46] J. Guichard. Freinage à très hautes performances (exemple aéronautique). *Techniques de l'ingénieur*, B(5580) :1–21, 2000.

[47] J. R. Hahn. Kinetic study of graphite oxidation along two lattice directions. *Carbon*, 43 :1506–1511, 2005.

[48] J. C. Han, X. D. He, and S. Y. Du. Oxidation and ablation of 3D carbon-carbon composite at up to 3000˚C. *Carbon*, 33(4) :473–478, 1995.

[49] G. H. Hennig. Anisotropic reactivities of graphite - I. Reaction of ozone and graphite. *Carbon*, 3(2) :107–108, 1965.

[50] E. J. Hippo. The role of active sites in the inhibition of gas-carbon reactions. *Carbon*, 27(5) :689–695, 1989.

[51] F. P. Incropera and D. P. De Witt. *Fundamentals of Heat and Mass Transfer*. John Wiley and Sons, New-York, 5 th edition, 2002.

[52] N. S. Jacobson and D. M. Curry. Oxidation microstructure studies of reinforced carbon/carbon. *Carbon*, 44 :1142–1150, 2006.

[53] I. V. Katardjiev, G. Carter, M. J. Nobes, S. Berg, and H.-O. Blom. Three-dimensional simulation of surface evolution during growth and erosion. *Journal of Vacuum Science and Technology A*, 12(1) :61–68, 1994.

[54] J. A. Keenan. *Thermo-chemical ablation of heat shields under Earth reentry conditions.* PhD thesis, North Carolina State University, USA, 1994.

[55] J. A. Keenan and G. V. Candler. Simulation of ablation in earth atmospheric entry. In *AIAA 28th Thermophysics conference*, volume 93, Orlando, FL, July 1993.

[56] A. S. Kim and H. Chen. Diffusive tortuosity factor of solid and soft cake layers : A random walk simulation approach. *Journal of Membrane Science*, page 11 p., 2006.

[57] K. Kuo and S. Keswani. A comprehensive theoretical model for carbon-carbon composite nozzle recession. *Combustion Science and Technology*, 42 :177–192, 1986.

[58] S. Labruquère, X. Bourrat, R. Pailler, and R. Naslain. Structure and oxidation of C/C composites : role of the interface. *Carbon*, 39 :971–984, 2001.

[59] J. Lachaud, Y. Aspa, G. Vignoles, and G. Bourget. Experimental characterization and 3D modelling of carbon/carbon composites oxidation : role of the interphase. In J. Lamon and A. Torres-Marques, editors, *Proc. 12th European Conference on Composite Materials*, Biarritz, France, September 2006. AMAC. 8 p.

[60] J. Lachaud, Y. Aspa, G. Vignoles, and J.-M. Goyhénèche. 3D modeling of thermo-chemical ablation in carbon-based materials : effect of anisotropy on surface roughness onset. In M. Dinguirard and J. Kleiman, editors, *Proc. 10th International Symposium on Materials in a Space Environment*, volume SP-616, Collioure, France, September 2006. ESA. 10 p.

[61] J. Lachaud, G. L. Vignoles, J.-M. Goyhénèche, and J.-F. Epherre. Physico-chemical ablation of carbon-carbon composites : Multi-scale analysis of surface roughness. *Submitted to Carbon*. Chapter 3 of this manuscript.

[62] J. Lachaud, N. Bertrand, G. L. Vignoles, G. Bourget, F. Rebillat, and P. Weisbecker. Physico-chemical ablation of carbon-carbon composites : Experimental evaluation of intrinsic reactivities. *Submitted to Carbon*. Chapter 4 of this manuscript.

[63] J. Lachaud, Y. Aspa, and G. L. Vignoles. Physico-chemical ablation of carbon-carbon composites : Multi-scale analytical modeling in steady state. *Submitted to Int. J. of Heat and Mass Transfer*. Chapter 5 of this manuscript.

[64] J. Lachaud and G. L. Vignoles. Physico-chemical ablation of carbon-carbon composites : 3D numerical modeling of actual architectures in steady state. *Submitted to Journal of Computational Physics*. Chapter 6 of this manuscript.

[65] J. Lachaud, Y. Aspa, and G. L. Vignoles. Physico-chemical ablation of carbon-carbon composites : Analytical and 3D numerical modeling in transient regime. *Submitted to J. Appl. Phys.* Chapter 7 of this manuscript.

[66] J. Lachaud, Y. Aspa, G. L. Vignoles, and J.-M. Goyhénèche. Modélisation 3D de l'ablation thermochimique des composites C/C. In *Congrès Français de Thermique*, volume 1, pages 125–130, Île de Ré, France, 16-19 May 2006. SFT.

[67] J. Lachaud, G. L. Vignoles, J. M. Goyhénèche, and J. F. Epherre. Ablation in C/C composites : microscopic observations and 3D numerical simulation of surface roughness evolution. *Ceramic Transactions*, 191 :149–160, 2006.

[68] J. Lahaye, F. Louys, and P. Ehrburger. The reactivity of carbon-carbon composites. *Carbon*, 28(1) :137–141, 1990.

[69] N. R. Laine, F. J. Vastola, and P. R. Walker. The importance of active surface area in the carbon-oxygen reaction. *J. Phys. Chem.*, 67 :2030, 1963.

[70] F. Lamouroux, G. Camus, R. Naslain, and J. Thebault. Kinetics and mechanism of oxidation of 2D woven C/SiC composites : I - Experimental approach. *J. Am. Ceram. Soc.*, 77 :2049–2057, 1994.

[71] Y.-J. Lee and H. J. Joo. Investigation on ablation behavior of CFRC composites prepared at different pressures. *Composites : Part A*, 35 :1285–1290, 2004.

[72] R Luo, J Cheng, and T Wang. Oxidation behaviour and protection of carbon/carbon composites prepared using rapid directional diffused CVI techniques. *Carbon*, 40 :1965–1972, 2002.

[73] K. L. Luthra. Oxidation of C/C composites - A theoretical study. *Carbon*, 26(2) :217–224, 1988.

[74] D. W. McKee. Oxidation behavior and protection of carbon/carbon composites. *Carbon*, 25(4) :551–557, 1987.

[75] R. Naslain. *Introduction aux matériaux composites*, volume 2. IMC/Editions du CNRS, Bordeaux, 1985. Ecole d'été du CNRS (Bombannes 1979).

[76] A. Oberlin, J. Goma, and J. N. Rouzaud. Techniques d'étude des structures et texture (microtextures) des matériaux carbonés. *J. Chimie Physique*, 81(11) :701–710, 1984.

[77] J. K. Park, D. Cho, and T. J. Kang. A comparison of the interfacial, thermal and ablative properties between spun and filament yarn type carbon fabric/phenolic composites. *Carbon*, 42 :795–804, 2004.

[78] J. K. Park and T. J. Kang. Thermal and ablative properties of low temperature carbon fiber-phenol formaldehyde resin composites. *Carbon*, 40 :2125–2134, 2002.

[79] S. Pestchanyi, V. Safronov, and I. Landman. Estimation of carbon fibre composites as ITER divertor armour. *Journal of Nuclear Materials*, 329–333 :697–701, 2004.

[80] Robert C. Reid, John M. Prausnitz, and Bruce E. Poling. *The properties of gases and liquids*. McGraw Hill Book Company, New-York, 4th edition, 1987.

[81] J. Rodriguez-Mirasol, P. A. Thrower, and L. R. Radovic. On the oxidation resistance of carbon-carbon composites : importance of fiber structure for composite reactivity. *Carbon*, 33(4) :545–554, 1995.

[82] J. Sallès, J. F. Thovert, and P. M. Adler. Deposition in porous media and clogging. *Chemical Engineering Science*, 48 :2839–2858, 1993.

[83] E. Sandre. *Le carbone dans tous ses états*, chapter II- Structure électronique. Gordon and Breach Science Publishers, 1997.

[84] C. Sauder. *Relation microstructure/propriétés à haute température dans les fibres et matrices de carbone.* PhD thesis n°2477, Université Bordeaux 1, 2001.

[85] V. Z. Shemet, A. P. Pomytkin, and T. G. Protsenko. High-temperature oxidation of carbon-carbon composite materials in air. In I. N. Fridlyander and V. I. Kostikov, editors, *Moscou International Composites Conference*, pages 650–650. Elsevier Applied Science, 1990.

[86] I. W. Smith. The intrinsic reactivities of carbons to oxygen. *Fuel*, 57 :409–414, 1978.

[87] F. Stevens and T. P Beebe. Computer modeling of graphite oxidation : differences between monolayer and multilayer etching. *Computers and Chemistry*, 23 :175–183, 1999.

[88] D. Tandon, E. J. Hippo, H. Marsh, and E. Sebok. Surface topography of oxidized HOPG by scanning tunneling microscopy. *Carbon*, 35(1) :35–44, 1997.

[89] J. M. Thomas. Microscopic studies of graphite oxidation. *Chemistry and Physics of Carbon*, 1 :121–202, 1965.

[90] P. Tianyou and P. Weizhou. Microstructures in 3D C/C composites. *Ceramics International*, 24 :605–609, 1998.

[91] S. Torquato and I. Kim. Efficient simulation technique to compute effective properties of heterogeneous media. *Appl. Phys. Lett.*, 55 :1847–1849, 1989.

[92] F. Transvalidou and S. V. Sotirchos. Effective diffusion coefficients in square arrays of filament bundles. *AIChE J.*, 42(9) :2426–2438, 1996.

[93] K. A. Trick and T. E. Saliba. Mechanisms of the pyrolysis of phenolic resin in a carbon/phenolic composite. *Carbon*, 33(11) :1509–1515, 1995.

[94] J. M. Vallerot. *Matrices de pyrocarbone : propriétés, structure et anisotropie optique.* PhD thesis, Université Bordeaux 1, 2004.

[95] J-M. Vallerot, X. Bourrat, A. Mouchon, and G. Chollon. Quantitative structural and textural assessment of laminar pyrocarbons through raman spectroscopy, electron diffraction and few other techniques. *Carbon*, 44(9) :1833–1844, 2006.

[96] G. Vignoles, Y. Aspa, J. Lachaud, G. Duffa, J. M. Goyheneche, J. F. Epherre, N. T. H. Nguyen-Bui, M. Quintard, and B. Dubroca. Multiscale study of ablation in carbon/carbon composites : Surface roughness evolution and possible physicochemical causes. In *ESA Workshop on Ablation, ESTEC*, Noordwijk, The Netherlands, October 2005.

[97] G. L. Vignoles. Modelling binary, Knudsen, and transition regime diffusion inside complex porous media. *J. Phys. IV France*, C5 :159–166, 1995.

[98] G. L. Vignoles. Image segmentation for phase-contrast hard X-ray CMT of C/C composites. *Carbon*, 39 :167–173, 2000.

[99] G. L. Vignoles, F. Langlais, C. Descamp, A. Mouchon, A. Mouchon, H. Le Poche, N. Reuge, and N. Bertrand. CVD and CVI of pyrocarbon from various precursors. *Surface and Coatings Technology*, 188–189 :241–249, 2004.

[100] C. Vix-Guterl, G. Bekri, J. Dentzer, S. Manocha, L. M. Manocha, and P. Ehrburger. Reactivity in wet air of carbon-carbon composites with treated pitch. *Journal of Analytical and Applied Pyrolysis*, 67 :341–357, 2003.

[101] P. L. Walker, F. Rusinko, and L. G. Austin. Gas reactions of carbon. *Advances in Catalysis and Related Subjects*, 11 :133–217, 1959.

[102] B. E. Warren. X-ray diffraction in random layer lattices. *The Physical Review*, 59(9) :693–698, 1941.

[103] J. Weisse. Fusion thermonucléaire. *Techniques de l'ingénieur*, BN(3013), 2000.

[104] M. R. Wool. Summary of experimental and analytical results. Technical Report SAMSO-TR-74-86, Passive Nosetip Technology Program (PANT), January 1975.

[105] P. B. Wright, J. W. Davis, R. G. Macaulay-Newcombe, C. G. Hamilton, and A. A. Haasz. Chemical erosion of DIII-D divertor tile specimens. *Journal of Nuclear Materials*, 313–316 :158–162, 2003.

[106] H. Würz, B. Bazylev, I. Landman, S. Pestchanyi, and V. Safronov. Macroscopic erosion of divertor and first wall armour in future tokamaks. *Journal of Nuclear Materials*, 307–311 :60–68, 2002.

A Effect of carbon anisotropy on the onset of surface roughness

Ce chapitre est le texte intégral d'un article qui a fait l'objet d'une présentation en congrès international en juin 2006.

Auteurs : J. Lachaud[1], Y.Aspa[1,2], G. L. Vignoles[1] et J.-M. Goyhénèche[1]

Affiliations :

[1]Laboratoire des Composites ThermoStructuraux (LCTS)

UMR 5801 : CNRS-SAFRAN-CEA-UB1

Domaine Universitaire de Bordeaux – 3, Allée de La Boétie, 33600 Pessac, France

[2]Institut de Mécanique des Fluides de Toulouse (IMFT),

1, allée Prof. Camille Soula, 31000 Toulouse, France

Mots clés

Degradation models, Environment effects, Ablation modeling, Spacecraft materials, Carbon-based materials

Résumé en français

La modélisation de l'ablation est abordée du point de vue du matériau. Dans un premier temps, la rugosité multiéchelle de deux matériaux carbonés est analysée par microscopie et microtomographie. Ensuite, un modèle 3D pour les surfaces récessives, intégrant réaction hétérogène et diffusion, est établi dans l'idée d'interpréter les morphologies observées à l'échelle microscopique. Afin de prendre en compte la structure cristalline du graphite, le modèle a été enrichi par l'ajout d'une réactivité hétérogène anisotrope. Lorsque cela est possible, le modèle est résolu analytiquement ; sinon, un code de simulation numérique développé à cet effet est utilisé. Les résultats sont en accord qualitatif avec les observations expérimentales. Cette approche contribue à la compréhension (i) des phénomènes couplés intervenant lors de l'ablation et (ii) du comportement intrinsèque des matériaux.

Abstract

Ablation modeling is addressed from the material point of view. Multi-scale surface roughness of two ablated carbon-based materials is first analyzed by SEM and micro-tomography.

Then, a 3D reaction-diffusion model is set up and solved to explain the observed morphologies at micrometer scale. To take into account the complex crystalline structure of graphite, the model has been enriched by incorporation of an anisotropic heterogeneous reactivity. The models are solved either analytically or using a homemade simulation code. Results are in correct agreement with observations. This approach contributes to the understanding of the physico-chemical coupled phenomena involved in ablation and of the material intrinsic behavior.

A.1   Introduction

Spatial vehicles often encounter severe environments during atmospheric crossing. Since the speed can reach many km/s in dense atmospheres, the flow close to the nosetip can be hypersonic. In this case a thin bow shock surrounds an inviscid flow (eulerian flow), while a dynamic boundary layer develops in the vicinity of the wall [22]. It has been shown [22, 32] that the temperature of the flow may reach $7000\,K$ and it may lead to a maximal wall temperature of $4500\,K$ for pressures higher than $100\,bar$. For such an environment, the design of thermal protection systems relies on Carbon/Carbon (C/C) composites, which possess the best compromise between thermal, thermo-chemical and mechanical properties [38]. However, a high interfacial mass transfer, strongly coupled with boundary layer transfer phenomena, leads to surface recession. Indeed, C/C composites are progressively destroyed by oxidation, sublimation and, up to a certain extent, mechanical erosion. These physico-chemical phenomena, collected into the term *ablation*, are globally endothermic. Hence they reduce the wall temperature and the heat flux that penetrates the internal structure [32].

Ablation of C/C composites leads to a typical surface roughness which induces an enhancement of heat and mass transfer between the protection wall and the surrounding environment via two major phenomena : (i) it increases the chemically active surface of the wall; (ii) it contributes to the laminar-to-turbulent transition in the dynamic boundary layer. PANT program results show that the heat flux may be multiplied by a factor up to three in turbulent regime [104]. The obvious consequence is a considerable enhancement of global ablation velocity.

If general phenomenological tendencies are now well explained and simulated in the bulk fluid phase [22, 55], the understanding of the interaction between the material and the flow close to the wall has to be improved. In this work, the emphasis is set on surface roughness analysis and modeling for two carbon-based materials : a carbon/carbon composite (C/C) and a poly-crystalline graphite. First, the link between the structure of turbostratic carbons and the ablation behavior of carbon-based material is discussed. Second, a morphological analysis of multi-scale roughness features is briefly presented for these two materials. Then, a reaction-diffusion model, set up to explain microscopic roughness developed on C/C, and the associated results are summarized. To model efficiently the surface evolution of the poly-crystalline graphite, the crystalline structure is included in the model through an orientation-dependant gasification rate.

A.2   Link between turbostratic carbons structure and the ablation behavior of carbon-based materials

The components of ablative carbon-based materials are made of various kinds of turbostratic carbons [84], which differ from graphite by a less organized and extended crystalline

structure [12] (see figure A.1). At atomic scale, this difference arises from a lack of pure sp^2 carbon atoms, as compared to graphite ; this fact might be explained by the presence of sp^3-like defects [95] or 5 or 7 membered rings [99]. They tends to disorientate graphene planes inside graphene layers, which can be slightly curved [95] or exhibit an inter-plane average length up to ten percent larger than in graphite [84]. The change of inter-plane average length (X-ray diffraction measurement of d_{002}) reduces the local density. d_{002} generally decreases with graphitization degree [76]. The extension of graphene planes and the size of graphene stacks increase with graphitization degree [12, 76]. Consequently, the local density increases with graphitization degree [84]. The way the graphene stacks are connected together has also a strong effect on density, as it can lead to a more or less optimized space occupation. The size of the representative elementary volume for the global density evaluation is about ten times the size of individual graphene stacks.

The gasification rates (oxidation or sublimation) of the graphene planes increase with plane perimeter to plane surface ratio [28]. Indeed, the reactivity of the edges, whose atoms conformations constitute active sites [50], is three orders of magnitude higher than the reactivity of the surface [49], which contains few defects and then few active sites. (In this work, this effect of the defects on reactivity is not modeled : it is the field of study of *ab initio* computations or molecular dynamics simulations [14].) As a consequence the gasification resistance of turbostratic carbons is strengthened with the graphitization rate [38], as graphitization tends to expand the graphene planes. Consequently, the gasification rate of turbostratic carbons generally decreases as local density increases [24].

The local recession velocity of the surface depends on the local reactivity. This effect leads to the establishment of surface roughness on composite materials, which are heterogeneous materials made of several kinds of turbostratic carbons. This phenomenon can be balanced by a mass transfer limitation in the fluid phase. This competition between mass transfer and heterogeneous reaction can explain a large part of the roughness features observed on the material surface [67]. In some cases, especially when surface roughness size is of the order of magnitude of the graphene plane, the crystalline structure has to be included in the model through an anisotropic gasification rate.
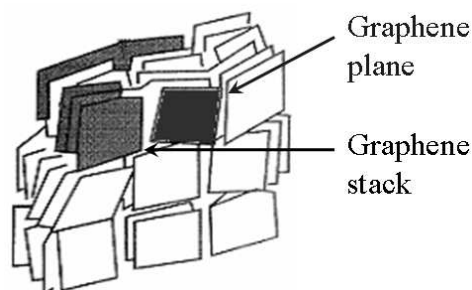

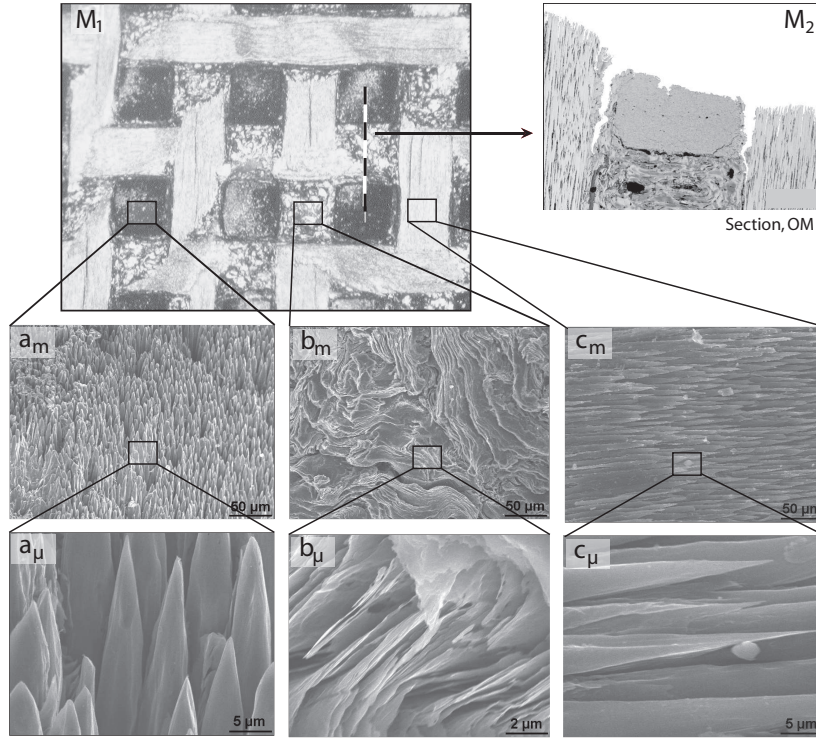FIG. A.1 – Sketch of the structure of turbostratic carbon [12].

FIG. A.2 – SEM micrographs of 3D C/C surface after plasma jet ablation

A.3   Analysis of surface roughness

A.3.1   C/C composite

C/C composite samples, made from a 3D ex-PAN carbon fiber woven preform and a pitch-based carbon matrix, have been submitted to arc-jet ground tests in stagnation point configuration. The material temperature was high enough $(3000\,K)$ to enable both oxidation and sublimation. However, the efficient C/C architecture prevents the sample from being notably eroded mechanically during ablation. Surface roughness has mainly been observed by optical microscope (OM), scanning electron microscopy (SEM) and phase-contrast synchrotron X-ray microtomography (SXMT). Let us briefly depict the micrographs of figure A.2 which feature the multi-scale surface roughness [67] :

– A macroscopic (M) surface roughness takes place on the lattice of the composite (micrograph M_1). It seems to result from the difference of reactivity between bundles and extra-bundle pitch-based matrix. Notches appear between emerging bundles (micrograph M_2). The section of emerging bundles (tangent or perpendicular to surface) is slightly undulating (micrograph M_2). Indeed, if edges of initially square section of bundles are emerging, creating crenel-like features, they are smoothed out to a wavy form by ablation. Mechanical erosion sporadically occurs through the detachment of an extrabundle matrix octet.

– A mesoscopic (m) surface roughness develops at the end of emerging bundles, and looks like "needle clusters" (micrograph a_m) -resp. "needle layers" (micrograph c_m)- for bundles perpendicular -resp. parallel- to material surface. In the literature, many micrographs

show such roughness features on carbon-based composites during ablation by oxidation [17, 34] or both oxidation and sublimation [18, 48, 71]. Due to an important recession of the intrabundle matrix, fibers, which are less reactive, are partially stripped, become thinner, and acquire a needle shape. As shown on figure b_m, the surface roughness of the extrabundle pitchbased matrix can be neglected at this scale.

– A microscopic (μ) surface roughness appears on the fibers and on the extra-bundle matrix. Fiber tips are faceted (micrograph a_μ and c_μ). The extrabundle pitch-based matrix shows parallel denuded layers (micrograph b_μ). This is coherent with its pseudo-crystalline structure.

A.3.2 Polycrystalline graphite

The studied poly-crystalline graphite, named EDM3, is an isostatic graphite from Poco Inc. To reduce the residual porosity, the material is impregnated with pitch, which is then carbonized and graphitized. The grain size distribution approximatively obeys a gaussian law with a mean value of $4\,\mu m$ and a standard deviation of $1\,\mu m$. The density value is 1.78 [29]. This material has been submitted to plasma jet ablation [29, 32] and to an oxidation test (this work). The surfaces roughnesses resulting from the two processes are not distinguishable at microscopic and mesoscopic scales. At macroscopic scale, mechanical erosion can occur with plasma jet facilities. X-ray computed microtomography has been carried out on EDM3 after the oxidation test (dry air at atmospheric pressure at 625°C). The tomograph has been performed at ESRF (European Synchrotron Radiation Facility) in Grenoble (France) on a coherent X-ray source. The resolution is $0.3\,\mu m$. This study reveals the complex multi-scale three-dimensional structure of EDM3 :

– A macroscopic porosity, visible on the left hand side of the microtomograph (figure A.3), is likely to arise from macro-pores poorly filled by the pitch matrix. The diameter of these pores is around $10\,\mu m$. Consequently, they lead to a macroscopic surface roughness when they are opened by ablation. The mark of a macro-pore, which has been uncovered by ablation, can be observed on the surface of the front corner of the tomograph.

– A mesoscopic surface roughness is shown on SEM micrographs of figure A.3. It arises from the difference of reactivity between the grains according to their orientation to surface. The more parallel (resp. perpendicular) to surface the graphene planes are, the more resistant (resp. weak) the grains are. This surface roughness size is of the order of the grain size. Moreover, the pitch-based matrix seems to have a higher oxidation rate, as it is not observed on the micrographs.

– At microscopic scale, a lamellar surface roughness appears on the grains (bottom micrograph of figure A.3). It is probably correlated to the lamellar structure of the grains.

A.3.3 Synthesis

From the above presented descriptions and classifications, it appears that ablation-related geometrical features of the rough surface mainly follow the material structure. Accordingly, it will be called structural roughness to make a difference with a purely physical roughness which has already been observed on homogeneous materials and modeled [32]. This physical roughness consists in scalloped morphologies and is not correlated to material structure [96]. The cause seems to be a dynamical effect based on the concurrence between bulk transfer and heterogeneous transfer, be it of mass or heat. In addition to such a competition, possible physical phenomena leading to structural roughness appear to be reactivity differences between
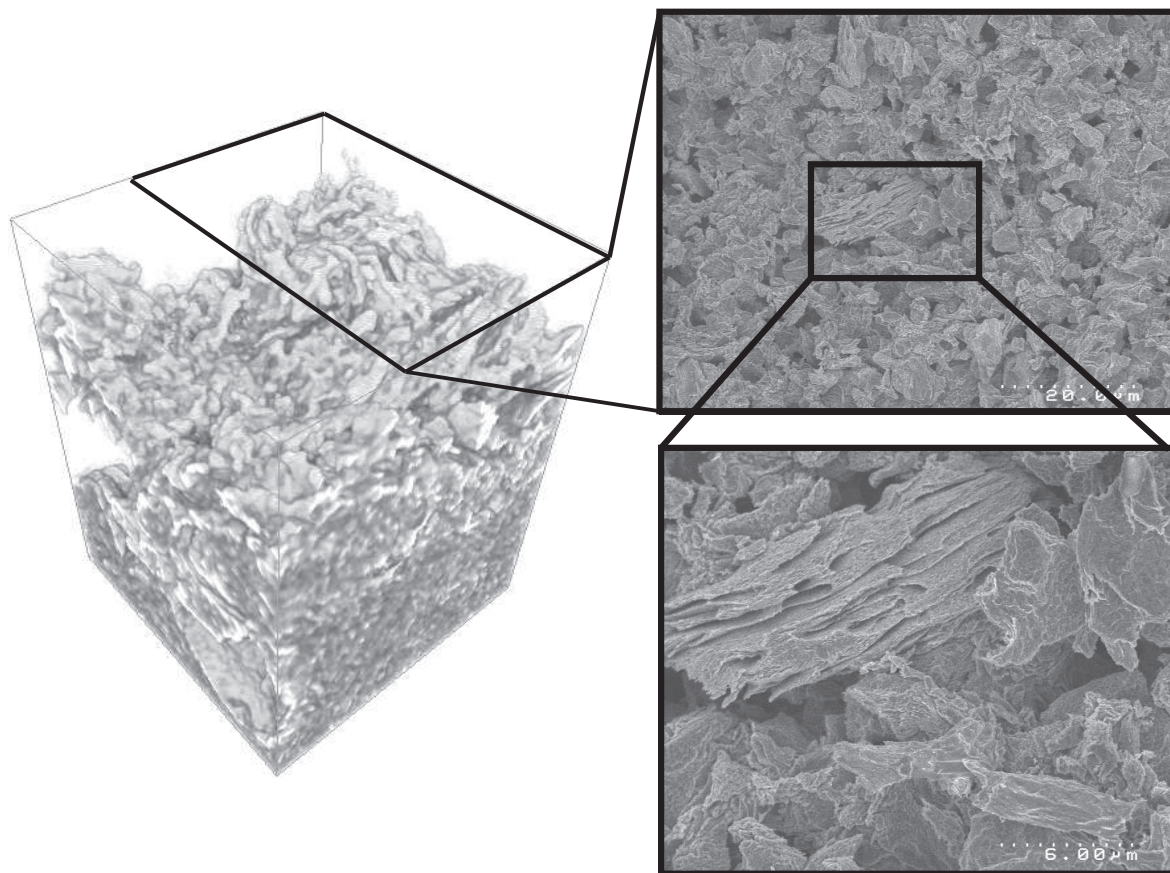
Fig. A.3 – X-ray microtomograph (left) and SEM micrographs (right) of EDM3 graphite surface after ablation

phases. As a result, models including structure and physics have to be taken in consideration. Moreover, to model accurately poly-cristalline graphite behavior, the material anisotropy has to be taken into account.

A.4   Modeling of meso-scale surface roughness

A.4.1   Heterogeneous isotropic materials : C/C composites bundles

The evolution described in section A.3.1 of the pointed fibers has been sketched in 2D by Han [48]. We recently succeeded in modeling it in transient regime and to solve it using a simulation code [67]. The model has been solved analytically in steady state [59]. Let us summarize the hypotheses and the results of these works, as they constitute the physical basis of the model of the following part.

As specified in the previous section, the C/C composite bundles are heterogeneous. They are made of fibers and matrix, which are assumed homogeneous and isotropic. They are ablated following either a first order oxidation process or sublimation. These two cases are mathematically equivalent considering either reactant diffusion to the wall or vaporized carbon
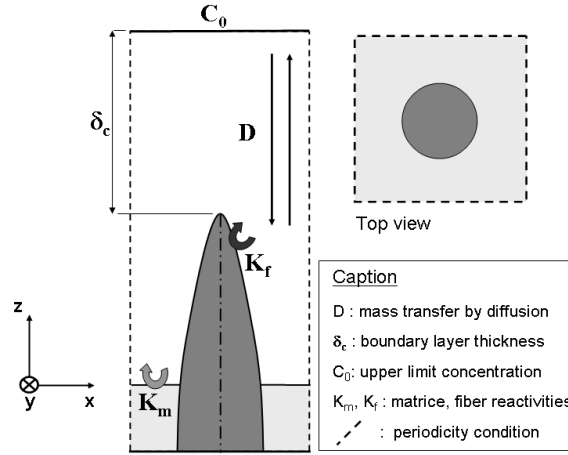
FIG. A.4 – Scheme of the elementary pattern and of the proposed model

diffusion from the wall and a Knudsen-Langmuir law [32]. The gasification rate of the fibers (k_f) is lower than for the matrix (k_m).

The proposed model is sketched on figure A.4. On this scheme the stationary rough surface is represented ; however at initial time, the fluid/solid interface is flat. This profile has therefore to be obtained using a moving fluid/solid interface modeling.

Let us write mass conservation of the reactant (of molar concentration C) in the fluid phase :

$$\frac{\partial C}{\partial t} + \nabla \cdot (-D\nabla C) = 0 \tag{A.1}$$

Boundary conditions relative to the model domain are :
– On boundary layer top : $C = C_0$;
– At the fluid/solid interface the oxidation molar rate r writes :

$$J = (-D\nabla C) \cdot \mathbf{n} = -k_i C \tag{A.2}$$

where $\mathbf{n}$ is the normal to the surface, and k_i (m/s) the reaction kinetic constant of matrix $(i = m)$ or fibers $(i = f)$;
– Periodicity on the lateral boundaries (the bundle section is supposed infinite in transverse directions).

The interface position $(S(x, y, z, t))$ is given by the simultaneous resolution of equations (A.1-A.2) and of [32] :

$$\frac{\partial S}{\partial t} + \mathbf{v} \cdot \nabla S = 0 \tag{A.3}$$

where $\mathbf{v} = v_s J\mathbf{n}$ is the surface local normal velocity , with v_s the solid molar volume.

The resolution of this model in steady state for an axi-symmetric fiber gives the geometry of the fiber after ablation as a function of two dimensionless numbers (figure A.5) : (i) the Sherwood number $(Sh = R_f k_f / D)$, which is relevant of reaction versus diffusion competition, (ii) the reactivity contrast between matrix and fibers $(A = \frac{k_m v_m}{k_f v_f})$ [59]. The model has been validated using independent feeding and validation data [8,59]. The comparison of the micrographs of figure A.2 to the results of the model (figure A.5) shows that the Sherwood number is low for the plasma jet test, as fibers are conical. This means that ablation is limited by reaction.
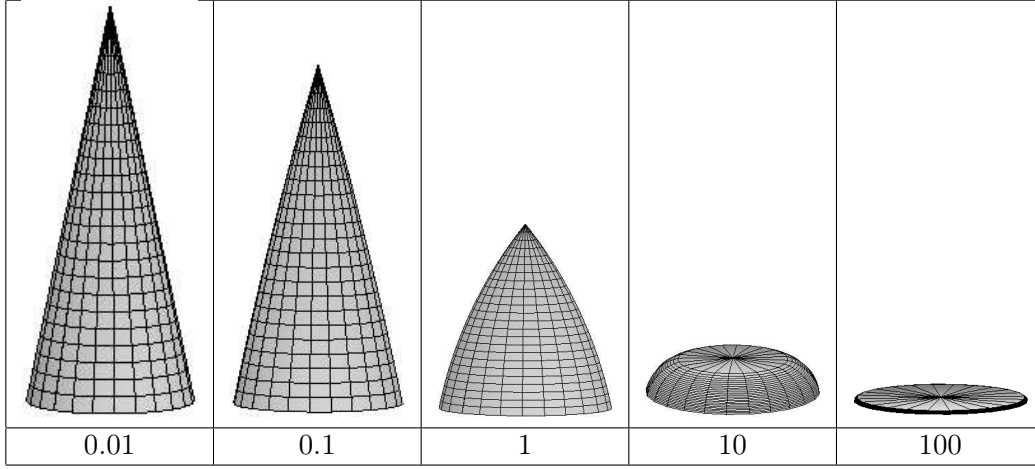
| 0.01 | 0.1 | 1 | 10 | 100 |

FIG. A.5 – Fiber morphology at steady state as a function of Sh (with $A = 5$).

A.4.2   Anisotropic materials : EDM3 and C/C composite inter-bundle matrix

As introduced in section A.2, the turbostratic carbons possess a complex multi-scale structure. EDM3 has been first tackled in this work due to its repetitive structure and to the direct equivalence between graphene stacks and grains (see subsection A.4.2.3). The C/C composite inter-bundle matrix shows an anisotropic structure leading to a microscopic surface roughness (figure A.2) which is of interest ; unfortunately, its structure is quite complex and irregular. Nevertheless, the results of this section could be applied to the matrix modeling.

First the graphene plane is analyzed ; then, two successive changes of scales are performed.

A.4.2.1   Interpretation of the graphene plane reactivity

The starting point of the modeling is the graphene plane. For the materials of the study, the graphene plane curvature is negligible since either the turbostratic carbons possess few defects (poly-crystalline graphite case) or the extension of the graphene planes is small (C/C case) [84]. Graphene edge reactivity is known to be about three orders of magnitude larger than in the perpendicular direction (see section A.2). A sticking probability is then assigned to the perpendicular direction, noted $P_\perp$, and one to the edge, noted $P_\parallel$ (figure A.6). This property can be modeled by an orthotropic sticking probability. Using the notations of the figure A.6 it writes :

$$\underline{\underline{P}} = \begin{pmatrix} P_\parallel & 0 & 0 \\ 0 & P_\parallel & 0 \\ 0 & 0 & P_\perp \end{pmatrix}_{(\mathbf{i},\mathbf{j},\mathbf{k})}$$

The interface of a graphene stack is made of a series of surfaces alternately parallel ($S_\parallel$ with a sticking event probability $P_\parallel$) and perpendicular ($S_\perp$ with a sticking probability $P_\perp$) to the graphene plane (figure A.6). Let us assume that the average sticking probability, noted $\tilde{P}$, is the arithmetic average of $P_\parallel$ and $P_\perp$ with respect to their real surfaces to effective surface ratio. Let θ be the angle between the normal $\mathbf{n}$ to the material effective surface and

k, the local orientation of graphene planes (figure A.6). The sticking probability, which can be regarded as a projection of $\underline{P}$ on the effective surface, is then a function of θ :

$$\tilde{P}_\theta = \frac{P_\parallel |\sin\theta| + P_\perp |\cos\theta|}{|\sin\theta| + |\cos\theta|} \tag{A.4}$$
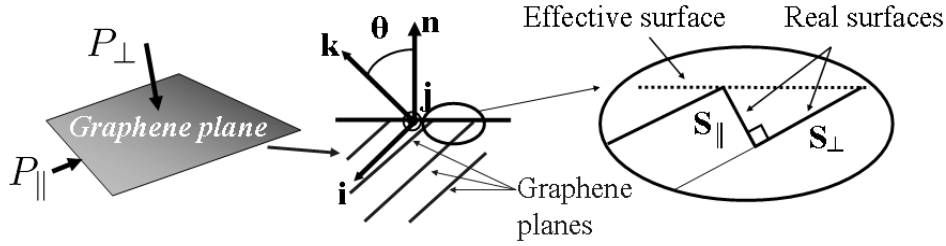

FIG. A.6 – Sketches and notations for the interpretation of graphene plane reactivity

A.4.2.2 First change of scale : graphene plane to graphene stack

The change of scale is numerical. Indeed, one has to model the complex behavior of a reactive crystalline material. As introduced in section A.2 and represented on figure A.7, the graphene stack is considered as a perfect lamellar crystallite, constituted of flat graphene planes. Under these hypotheses, the graphene stack retains the orthotropic property of graphene planes. Consequently, the direction **k** fully describes the stack orientation. The surface reactivity is a function of graphene stack orientation compared to the interface orientation. Let α be the angle between **k** and **n**. Note that for rough surfaces α is different from θ, as θ is affected by a local orientation, while α arises from a global interface orientation.
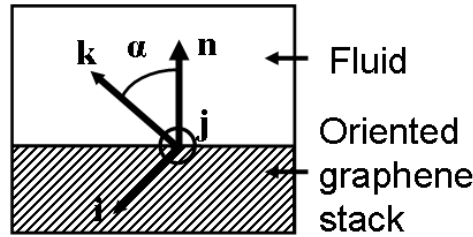

FIG. A.7 – Sketches and notations for graphene stack modeling

To solve this problem in 3-D and in non-stationary regime, an efficient numerical simulation code, named AMA, has been developed on a Monte-Carlo random-walk principle. AMA, which is a C ANSI implementation, contains five main parts. (i) A 3-D image containing several phases (fluid/solids) is described by discrete cubic voxels method. (ii) The moving fluid/solid interface is determined by a simplified marching cube approach [97]. (iii) Mass transfer by diffusion is simulated by a Brownian motion simulation technique [91], which is a continuum (grid-free) and rapidly converging method to simulate diffusion in a continuous fluid. (iv) Heterogeneous anisotropic first-order reaction on the wall is simulated by a sticking probability ($\tilde{P}'_\theta$) adapted to the Brownian motion simulation technique [67]. AMA has been

validated by comparison to a 1D analytical model in transient regime [67] and to the axi-symmetrical model presented above in steady state [59].
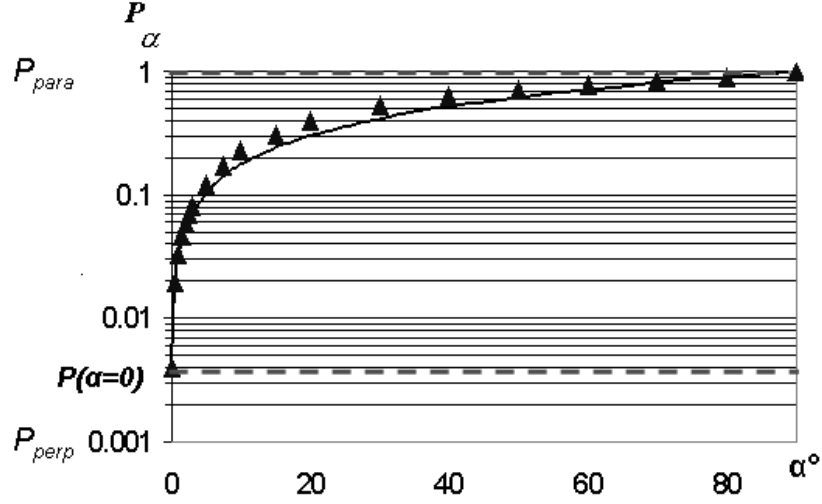

FIG. A.8 – Effective sticking probability of a stack as a function of its relative orientation to the surface
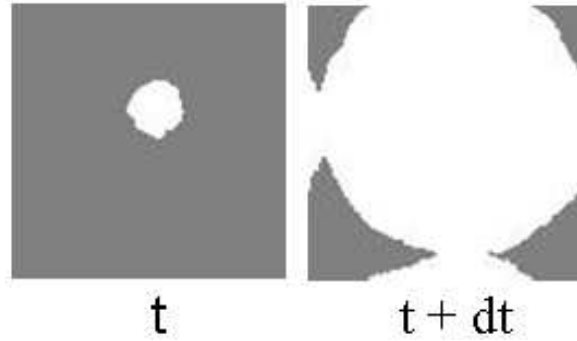

FIG. A.9 – Pitting on a graphene stack for $\alpha = 0$: pit growth. Surface top view.

In the literature, the actual gasification rates of parallel and perpendicular direction are never quantitatively reported. In the scope of reproducing larger scale behavior and to progress in turbostratic carbon modeling before carrying out difficult experiments, the parallel to perpendicular ratio has been fixed to 1000. Then, the Damköhler number has been taken very low. Indeed, this assumption seems to be correct in the field of the considered applications (see subsection A.4.1). The effective sticking probability, P_{α}, is reported as a function of graphene stack orientation to surface α, on figure A.8, where the sticking probabilities have been normalized. The filled triangles are the simulation points. The curve is a representation of an approximation of the numerical result; this approximation ($P_{\alpha} = a + b\,\alpha^{0.8}$, where a and b are two constants) is used in the following to compute the next change of scale. Note that the lower sticking probability, $P_{(\alpha=0)}$, is no longer $P_{\perp}$. This fact is due to the ability of the random walk code to simulate random events. In particular, the pitting of a graphene plane

followed by a pit extension in the perpendicular direction is taken into account in the effective reactivity evaluation. This phenomenon, experimentally observed [47] and already simulated in 2D [87], is simulated in 3D in this work (figure A.9). Thus, the effective sticking event in perpendicular direction is increased by this phenomenon.

A.4.2.3 Second change of scale : graphene stack to material

In the case of EDM3 poly-crystalline graphite, the graphene stack can be assimilated to the grain. Two poly-crystalline graphites have been randomly processed following the EDM3 gaussian law of grain repartition (see subsection A.3.2). The first one is an ideal graphite : the grains are well connected (see figure A.10). In a more realistic way, the second one includes a pitch-based matrix joining the grains (see figure A.11). The matrix is a homogeneous material. Its reactivity value is taken equal to the arithmetic average of P_α. Each grain orientation is chosen by a random process according to a normal law for the angle ; on the figure, the gray scale values span from black ($\alpha = 0°$) to white ($\alpha = 90°$). These materials are globally isotropic. The sticking probability law P_α is used to simulate the graphite ablation. A steady state regime, with a stabilized surface roughness height, is obtained after the ablation of approximatively ten grain levels. The surface roughness is linked to material structure. It is of the order of magnitude of the grain size for the chosen reactivity ratio between perpendicular and parallel directions. Two qualitative results tend to validate the model. First, the surface roughness simulation is in correct agreement with observations. The agreement may be improved with a more realistic modeling of the material. Second, the sensitivity of the model to grain size (or graphene plane extension) is in agreement with the experimental results of the literature (see section A.2).

A.5 Conclusion and outlooks

In this work, the origin and development of surface roughness on a 3D-C/C composite and on a poly-crystalline graphite during ablation are addressed. First, the link between turbostratic carbons structure and the ablation behavior of carbon-based materials is analyzed : it underlies the overall ablation phenomena. Second, using as references arc-jet test and oxidation test samples, multi-scale roughness is observed, classified and briefly analyzed for these two materials. Then the focus is set on the well-known "needle clusters" roughness features which develop on emerging bundles of C/C composites. A simple heterogeneous reaction/diffusion model is presented and the results of an analytical solution in steady state are summarized. The model, which has been experimentally validated, opens a broad understanding of the material behavior at this scale. However, at lower scales the anisotropic structure has a strong effect on surface roughness and material behavior. To progress in this study, the poly-crystalline graphite is used as a model material.

In order to model the ablation behavior of the poly-crystalline graphite, which is a particular turbostratic carbon, an anisotropic reactivity is included in the model. It takes into account its turbostratic structure. The starting point of the model is the graphene plane. An interpretation of graphene reactivity as a function of its parallel and perpendicular reactivities is proposed. Then, two successive changes of scales following the material structure are processed (graphene plane $\Rightarrow$ graphene stack (or grain) $\Rightarrow$ material). These changes of scales are done using a homemade simulation code, which handles efficiently anisotropic reactivities. At each scale, the sensitivity of the model to the study parameters are consistent with

literature data. At the largest scale, simulation results can be compared to SEM and CMT observations : a correct qualitative agreement is obtained. The model could be improved by a better description of the material. Despite a lack of nano-scale feeding data for a quantitative validation, results are promising, since the proposed model can qualitatively explain roughness development on graphite. To progress in the turbostratic carbon modeling, experimental studies have to be carried out to determine graphene plane reactivities.
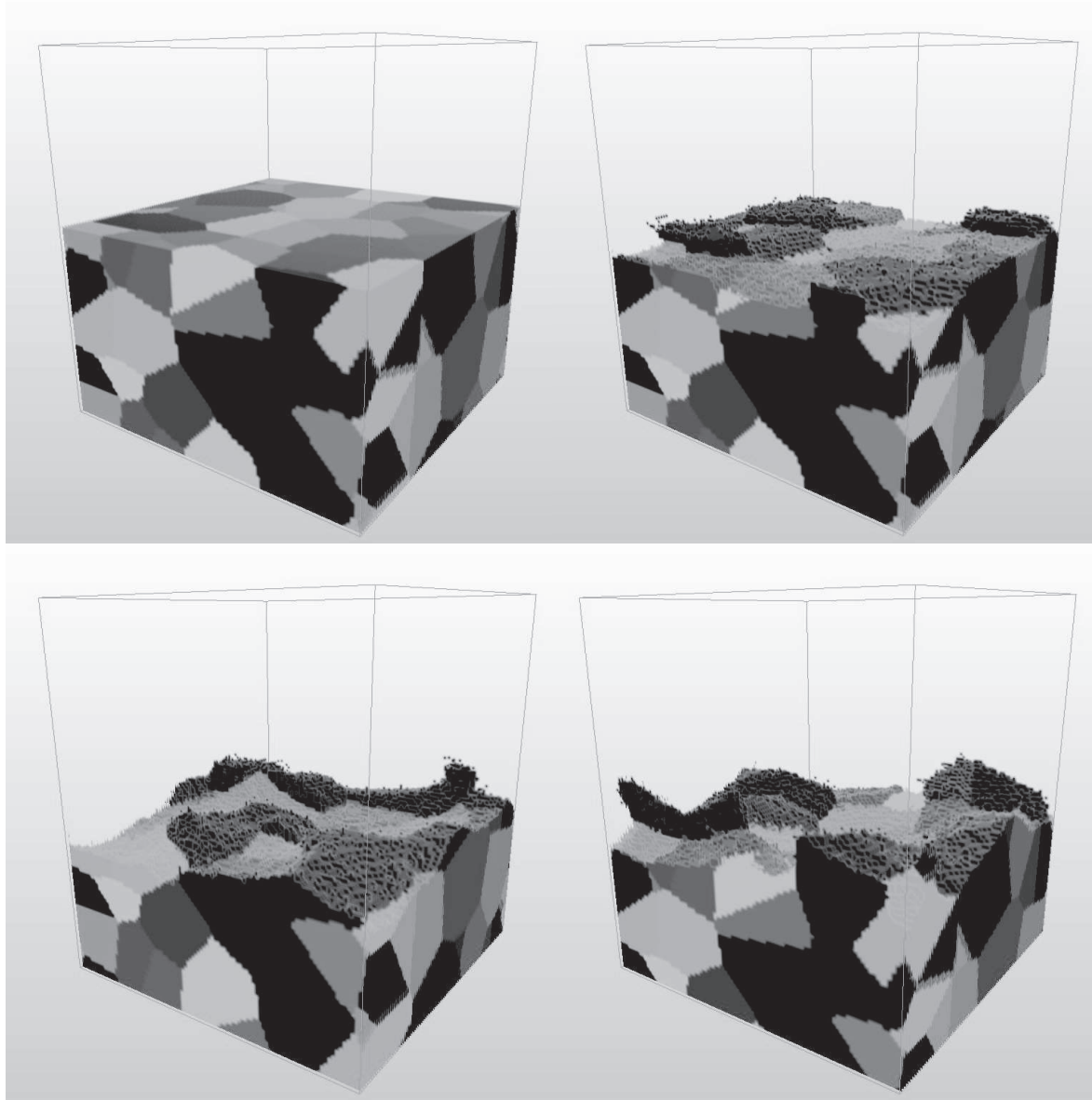

FIG. A.10 – Simulation of the surface evolution of an ideal poly-crystalline graphite during ablation
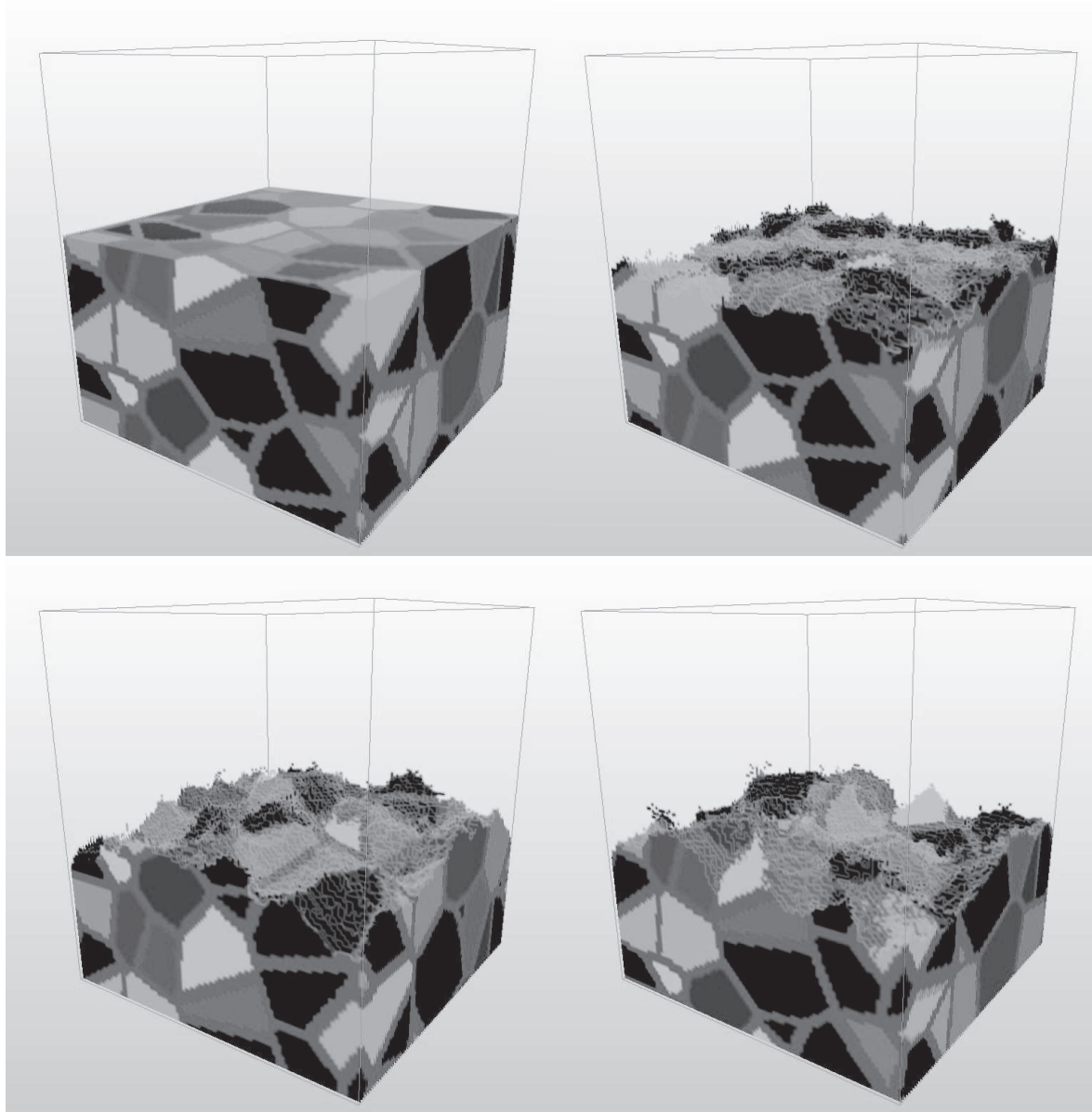
FIG. A.11 – Simulation of the surface evolution of a poly-crystalline graphite with grain boundaries during ablation

B Publications

Une partie de ce travail de thèse a été présentée à des congrès nationaux et internationaux avec actes publiés. En voici la liste :

1   J. Lachaud, Y. Aspa, G. L. Vignoles, J.-M. Goyhénèche. *3D Modelling of thermo-chemical ablation in carbon-based materials : effect of anisotropy on surface roughness onset.* 10th International Symposium on Materials in a Space Environment, Collioure, France, 2006. ESA special publication, vol. 616, 10 p.

2   G. Vignoles, J. Lachaud, Y. Aspa. *Roughness evolution in ablation of carbon-based materials : multi-scale modelling and material analysis.* 5th European Symposium on Thermal Protection Systems and Hot Structures, Noordwijk, The Netherlands, 2006. ESA special publication, vol. 631, 10 p.

3   Y. Aspa, J. Lachaud, G. Vignoles, M. Quintard. *Identification of microscale ablative properties of C/C composites using inverse simulation.* 9th AIAA/ASME Joint Thermophysics and Heat Transfer Conference, San Fransisco, CA, USA, 2006. AIAA paper 2006-291, 12 p.

4   J. Lachaud, Y. Aspa, G. Vignoles, G. Bourget. *Experimental characterization and 3D modeling of carbon/carbon composites oxidation : role of the interphase.* 12th European Conference on Composite Materials (ECCM12), Biarritz, France, 2006. J. Lamon and A. Torres-Marques Eds., AMAC, 8 p.

5   N. Bertrand, J. Lachaud, G. Bourget, G. L. Vignoles, F. Rebillat. *Identification of intrinsic carbon fiber oxidation kinetics from experimental data and CFD modeling.* ECCM12, 8p.

6   Y. Aspa, J. Lachaud, G. Vignoles, M. Quintard. *Simulation of C/C composites ablation using a VOF method with moving reactive interface.* ECCM12, 8p.

7   G. Vignoles, J. Lachaud, Y. Aspa, J.-M. Goyhénèche. *Ablation of carbon-based materials : multiscale roughness modeling.* ECCM12, 8p.

8   J. Lachaud, G. Vignoles, Y. Aspa, J.-F. Epherre. *Ablation of carbon/carbon composites : 3D multi-scale simulation of surface roughness evolution.* 1st International ARA Days : Atmospheric Reentry Systems Missions and Vehicles, Arcachon, France, 2006. T. Leuveugle Ed., EADS, 10 p.

9   Y. Aspa, J. Lachaud, G. Vignoles, M. Quintard. *Effective Surface Approach for the Design of Ablative Composites.* 1st International ARA Days, 10 p.

10   J. Lachaud, Y. Aspa, G. Vignoles, J.-M. Goyhénèche. *Modélisation 3D de l'ablation thermochimique des composites C/C.* Congrès Français de Thermique 2006, Bois-plage, France. SFT, 1 : 125–130, 2006.

11   J. Lachaud, G. L. Vignoles, J.M. Goyhénèche, J.-F. Epherre. *Ablation in carbon/carbon composites : microscopic observations and 3D numerical simulation of surface roughness evolution.* PacRim 6, Maui, HI, USA, 2005. Ceramic Transactions, 191 : 149–160, 2006.

Résumé

Les matériaux composites en carbone sont employés dans des conditions extrêmes : Tokamaks, corps de rentrée atmosphérique, tuyères de fusées, freins d'avions. Leurs parois subissent alors une récession, appelée ablation, en majeure partie due à des phénomènes physico-chimiques de gazéification (oxydation, voire sublimation). Ce travail contribue à l'amélioration de la compréhension de l'interaction pariétale matériau/environnement et à sa modélisation.

Des expériences originales de gazéification ont été réalisées, modélisées et analysées quantitativement ; un comportement multiéchelle complexe des matériaux est observé : il s'exprime à travers leur vitesse moyenne de récession et l'acquisition d'une rugosité liée à leur structure hétérogène anisotrope. Ces analyses ont conduit à l'élaboration d'une stratégie de modélisation s'articulant sur les diverses échelles caractéristiques des matériaux : nanoscopique (texture du carbone), microscopique (fibre, matrice inter-fibres), mésoscopique (fil, matrice inter-fils), macroscopique (composite homogénéisé). A chaque échelle, les modèles intègrent notamment la récession locale de la paroi couplée à un transfert de masse avec changement de phase. Un code de simulation numérique, de type Monte-Carlo Marches Aléatoires associé à un Marching Cube simplifié pour la description de l'interface, a été développé, validé et utilisé pour leur résolution.

Sous des hypothèses validées numériquement, une solution analytique a été obtenue ; elle permet une analyse fine des phénomènes d'ablation. Elle apporte notamment la prédiction quantitative du comportement macroscopique des matériaux en fonction des propriétés de leurs composants microscopiques via deux changements d'échelle successifs. Les résultats des modèles phénoménologiques ont été validés par comparaison aux essais en laboratoire et appliqués à l'analyse de cas industriels. Ils permettent la formulation de critères pour le choix ou la fabrication de matériaux optimaux.

Mots clefs

Matériaux composites, modélisation de procédés, ablation, transfert de masse avec changement de phase, interfaces mobiles, Monte-Carlo Marches Aléatoires, changement d'échelle, réactivité effective.

Abstract

Carbon-based composites are used in extreme conditions : Tokamaks, re-entry bodies, nozzle throats, plane brakes. Their walls undergo a surface recession, called ablation, mainly due to some gasification phenomena (oxidation or even sublimation). This work is a contribution to the improvement of the understanding of the near-wall material/environment interaction and to its modeling.

Some original gasification experiments have been carried out, modeled, and quantitatively analyzed ; a complex multiscale behavior of the materials is observed through their average recession velocity and a surface roughness onset mainly caused by their heterogeneous anisotropic structure. In order to explain these observations, a multiscale modeling strategy has been set up ; it follows the characteristic scales of the composites : nanoscopic (carbon texture), microscopic (fiber, inter-fiber matrix), mesoscopic (yarn, inter-yarn matrix), and macroscopic (homogenized composite) scales. The proposed models notably integrate the local recession of the wall, the heterogeneous gasification reactions, and mass transfer. A numerical simulation tool, based on Monte-Carlo Random Walks with Simplified Marching Cubes for the front tracking, has been implemented, validated, and used to solve these models.

Using some numerically validated hypotheses, an analytical solution has been obtained ; it provides a comprehensive understanding of ablation phenomena. It provides the effective behavior of the composites from that of their microscopic components through two changes of scale. The results of these phenomenological models have been validated by comparison to the laboratory experiments and applied for the analysis of actual applications. Physics-based criterions are made available for the choice or the fabrication of ideal materials.

Key words

Composite materials, process modeling, ablation, mass transfer, front tracking, Monte-Carlo Random Walk, change of scale, effective reactivity.

2006 | N° 3291

Modélisation physico-chimique de l'ablation
de matériaux composites en carbone

Jean LACHAUD